

University of Naples Federico II
Naples, Italy



**NUMERICAL AND EXPERIMENTAL
INVESTIGATION OF UNSTEADY
PLANE LIQUID JETS**

Alessandro Della Pia

**THESIS FOR THE DEGREE OF
DOCTOR OF PHILOSOPHY
IN INDUSTRIAL ENGINEERING
CYCLE XXXV**

Supervisors:

prof. Luigi de Luca
dr. Matteo Chiatto

Coordinator:

prof. Michele Grassi

December 2022

*Nothing in life is to be feared, it is
only to be understood.*

Maria Skłodowska Curie

To my family

NUMERICAL AND EXPERIMENTAL INVESTIGATION OF UNSTEADY PLANE LIQUID JETS

Ph.D. Thesis presented
for the purpose of obtaining the Degree of Doctor of Philosophy
in Industrial Engineering
by

ALESSANDRO DELLA PIA

December 2022



Supervisors:

prof. Luigi de Luca

dr. Matteo Chiatto

University of Naples Federico II

Ph.D. Program in Industrial Engineering

XXXV cycle - Coordinator: prof. Michele Grassi

Abstract

This work deals with the numerical and experimental investigation of unsteady plane liquid jets interacting with an external gaseous environment. Two flow configurations are analyzed: the gravitational liquid sheet (curtain) flow issuing into still air, and the planar air-water mixing layer developing past a splitter plate.

The curtain flow is mainly investigated through theoretical and numerical methodologies, including volume-of-fluid simulations, linear stability analysis based on a simplified theoretical model, and data-driven modal decomposition techniques. Air-water mixing layers are characterized through time-resolved particle image velocimetry measurements, performed simultaneously in gas and liquid phases.

As regards the major results, three flow regimes are distinguished in the curtain dynamics: supercritical, transcritical, and subcritical regimes (depending on the Weber number), each of them revealing different features and stability properties. In particular, a discontinuity of the flow natural frequency is found numerically and experimentally in transcritical conditions. The mixing layer configuration is characterized by the presence of a wake region just behind the splitter plate, which is strongly affected by both gas and liquid physical parameters. The flow dynamics exhibits a rich variety of unsteady behaviours, including global mode oscillations at high gas Reynolds numbers and air-water dynamic pressure ratios.

Keywords: curtain flows, two-phase mixing layers, splitter plate, volume-of-fluid simulation, modal analysis, particle image velocimetry.

Contents

Abstract	i
Acknowledgements	vii
List of Figures	ix
List of Tables	xxv
List of Publications	xxix
1 Introduction	1
1.1 Motivations and objectives	2
1.2 Outline	3
2 Layout of plane liquid jets	5
2.1 Gravitational liquid curtains	5
2.1.1 Unconfined curtain in critical conditions	6
2.1.2 Subcritical regime	9
2.1.3 Theoretical and numerical modelling	10
2.2 Two-phase mixing layers	24
2.2.1 Local linear stability theory	25
2.2.2 Numerical-experimental comparisons	26
2.2.3 Physical mechanisms of instability	28

2.2.4	Towards global stability analysis	28
3	Numerical and experimental methodologies	31
3.1	Direct numerical simulations	31
3.1.1	One-fluid formulation	32
3.1.2	Volume-of-fluid method in BASILISK	33
3.2	Linear stability analysis	35
3.3	Data-driven decomposition techniques	38
3.3.1	Spectral proper orthogonal decomposition	39
3.3.2	Dynamic mode decomposition	40
3.4	Curtain flows experimental setup	44
3.4.1	Natural oscillation frequency detection	44
3.5	Mixing layers experimental investigation	46
3.5.1	Experimental apparatus	46
3.5.2	Two-phase particle image velocimetry	51
4	Results	57
4.1	Gravitational liquid curtains	57
4.1.1	Base case configuration	57
4.1.2	Supercritical regime	66
4.1.3	Supercritical-to-subcritical flow transition	96
4.1.4	Subcritical regime	104
4.2	Two-phase mixing layers	121
4.2.1	Mean flow field characterization	121
4.2.2	Unsteady dynamics analysis	140
4.2.3	Global oscillatory behaviour	143
5	Conclusion	149
5.1	Conclusions	150

5.1.1	Gravitational liquid curtains	150
5.1.2	Two-phase mixing layers	152
5.2	Recommendations for future work	154
A	Insights into liquid curtains numerical treatment	155
A.1	Boundary conditions in subcritical regime	155
A.2	Viscous modification of the eigenvalues analysis	157
B	Details of the mixing layer experimental apparatus	159
B.1	Experiment core	159
B.2	Air circuit	162
B.2.1	Air blower power estimation	165
B.3	Liquid circuit	168
B.3.1	Overflowing tank design	170
B.3.2	Liquid pump power estimation	171
B.4	Final assembly	173
	References	175

Acknowledgements

The study presented in this dissertation has been financially supported by Università degli Studi di Napoli “Federico II” and Compagnia di San Paolo, and it has been carried out under the supervision of prof. Luigi de Luca and dr. Matteo Chiatto. In the framework of the STAR Program 2020, part of the work has been done at Delft University of Technology, under the supervision of prof. Marios Kotsonis and dr. Theodoros Michelis. The candidate is deeply grateful to his Supervisors for the human and scientific guidance they have provided during the whole time of the Ph.D. activity, and to dr. Onofrio Semeraro and prof. Yves Le Guer for their suggestions in reviewing the Ph.D. thesis.

List of Figures

2.1	Sketch of an unperturbed gravitational liquid curtain of length L^* issuing into a quiescent gaseous ambient. Gravity is directed along the x^* axis, and the gas-liquid interface is represented in blue.	7
2.2	Sinuus dynamics of a gravitational liquid curtain issuing into a quiescent gaseous ambient.	11
2.3	Sketch of sinuous (a) and varicose (b) disturbances.	13
2.4	Aerodynamic damping coefficients in Eqs. (2.20)-(2.21): U (black dotted line); $RU \int_0^1 U(\cdot) \ln x - \xi d\xi$ (coloured dashed lines). Solid lines represent the total damping coefficient: $r_\rho = 0.001$ (blue curve); 0.01 (black); 0.05 (red).	17
2.5	Froude number effect on the fast (panel (a)) and slow (panel (b)) wave crossing times t_{cross}^\pm as a function of the Weber number. In panel (b), coloured dashed lines denote the values We_{th} as a function of Fr , while the curve $We = 1$ is represented as a black dot-dashed line.	19

2.6	Sketch of the gas-liquid mixing layer flow developing past a splitter plate (black). Details of gas (red) and liquid (blue) channels are highlighted.	25
2.7	Typical mixing layer base flow velocity profile with (red dashed curve) and without (black curve) velocity defect. The gas-liquid interface is located at $y = 0$. Adapted from Fuster <i>et al.</i> [48].	26
2.8	Numerical prediction of the most unstable frequency f as a function of M in convective ($M < M_c$) and absolute ($M > M_c$) instability regimes. The red line represents the convective-absolute transition threshold $M = M_c$. Adapted from Fuster <i>et al.</i> [48].	27
3.1	Volume fraction $C(x, y)$ contour representation of a two-dimensional liquid jet injected in still air: $C = 1$ (red region) in liquid phase ($\rho = \rho_l$), 0 (blue region) in the gaseous ambient ($\rho = \rho_g$).	33
3.2	Adaptive grid structure employed to obtain the numerical solution shown in Fig. 3.1.	35
3.3	Typical eigenvalue spectrum obtained from Eq. (3.8) (left panel) in supercritical conditions ($We > 1$), with zoom around the least stable part (right panel). . . .	37
3.4	Sketch of the apparatus for curtain flows experiments. Details of the two-dimensional liquid sheet and the nozzle are reported on the right. The red spot in the curtain plane denotes the measuring point.	45

3.5	Overall schematic representation (panel (a)) and two-dimensional sketch close to the nozzle exit section (panel (b)) of the experimental setup.	47
3.6	Air flow experimental characterization in terms of turbulence intensity level (u'_{rms}/\bar{u} , panel (a)) and inlet gas vorticity thickness (δ_g , panel (b)) variations with Reynolds number Re_{H_g} . Comparisons with literature results (Fuster <i>et al.</i> [48], Matas <i>et al.</i> [50], Raynal <i>et al.</i> [39]) are also provided in panel (b).	49
3.7	Pictures of the PIV measurement setup.	52
3.8	Velocity field measurement workflow: acquired raw image (a), pre-processing (b), phases separation (c)-(d), and post-processing (e).	54
3.9	Velocity profile in air at different streamwise stations upstream of the injection section ($x/H_g = 0$) and Reynolds number Re_{H_g} values: $Re_{H_g} = 0.67 \cdot 10^4$ (black curves), $0.96 \cdot 10^4$ (red), $Re_{H_g} = 1.62 \cdot 10^4$ (blue). The numerical solution of the fully-developed turbulent channel flow obtained by Kim <i>et al.</i> [100] at Reynolds number equal to 13750 is also reported for comparison (green curve).	56
4.1	Schematic of computational domain (left) and of adaptive grid (right). The sheet of length L^* falls under gravity along x^* direction. Red lines define the initial interface shape, which is magnified by a factor of 10 along y^* direction in left panel.	58

4.2	Grid convergence analysis of the contraction ratio $CR = H_f^*/H_i^*$ for the steady solution. From right to left: $\Delta x^*/H_i^* = 0.0976$ (10 grid cells in H_i^*); $\Delta x^*/H_i^* = 0.0488$ (20 grid cells in H_i^*); $\Delta x^*/H_i^* = 0.0244$ (40 grid cells in H_i^*). Flow parameters specified in Tables 4.1 and 4.2.	62
4.3	Steady field in terms of u velocity component (top), sheet interface (middle), and pressure p (bottom) along the axial direction $y = 0$. Numerical solution (black curve); Torricelli's solution (red dashed curve).	63
4.4	Steady solution of u (left), v (middle) and p (right) y -distribution at different x stations: $x = 0$ (black continuous curve); 0.05 (black dashed); 0.15 (red continuous); 0.3 (red dashed); 0.5 (blue continuous); 0.8 (blue dashed).	65
4.5	Steady velocity field and interface shape (red line) of the liquid sheet.	65
4.6	Steady u velocity component (black continuous curve) and one-dimensional reduction using Eq. (4.4) for $\phi = u$ (black dashed curve).	67
4.7	Sequence of instantaneous average v distributions extracted from the VOF simulation. From left to right, top to bottom: $t = 0, 0.05, 0.21, 0.52$. $We = 2.5$, $Fr = 0.33$, $r_\rho = 0.01$	68
4.8	Sequence of instantaneous meanline distributions extracted from the VOF simulation. From left to right, top to bottom: $t = 0, 0.05, 0.21, 0.52$. $We = 2.5$, $Fr = 0.33$, $r_\rho = 0.01$	68

4.9	Instantaneous v velocity component and meanline ℓ distributions at $t = 0.05$ extracted from the VOF simulation (black curve) and computed by Eqs. (2.13)-(2.14) (blue). $We = 2.5$, $Fr = 0.33$, $r_\rho = 0.01$	69
4.10	Fast Fourier Transform (FFT) of the sheet meanline deflection extracted from VOF simulations at different x stations. The red line represents the least stable frequency $\lambda_i = 3.78$ arising from stability analysis. From left to right, top to bottom: $x = 0.2, 0.4, 0.6, 0.8$. $We = 2.5$, $Fr = 0.33$, $r_\rho = 0.01$	70
4.11	Inner eigenvalues of the spectrum (left), with a zoom of the upper branch around the least stable part (right). $We = 2.5$, $Fr = 0.33$, $r_\rho = 0.01$	71
4.12	Reynolds number Re effect at different values of the density ratio r_ρ on the inner eigenvalues of the spectrum: $r_\rho = 0.001$ (panel (a)); 0.005 (panel (b)); 0.01 (panel (c)); 0.02 (panel (d)). $Re = \infty$ (black filled circle); 400 (red open circle); 40 (blue asterisk); 20 (green filled circle). $We = 2.5$, $Fr = 0.16$	73
4.13	Temporal evolution of the two-dimensional volume fraction field C computed via VOF simulations for $r_\rho = 0.01$ (panels (a), (c), (e)) and $r_\rho = 0.02$ (panels (b), (d), (f)). $We = 2.5$, $Fr = 0.16$, $Re = 20$	74

4.14	Density ratio r_ρ effect on the temporal evolution of the energy budgets. From left to right: $r_\rho = 0.001, 0.01, 0.02$. The fast and slow waves expulsion times are $t = 0.25$ and $t = 0.60$, respectively. Note that all the terms have been scaled with respect to the initial total energy E_{t_0} . For a detailed explanation of the terms, see Eq. (2.33) in Section 2.1.3. $We = 2.5, Fr = 0.16, Re = 20$	75
4.15	Comparison between the pressure power L_p and the total energy time derivative dE_t/dt for unstable conditions ($r_\rho = 0.02$). For a detailed explanation of the terms, see Eq. (2.33) in Section 2.1.3. $We = 2.5, Fr = 0.16, Re = 20$	77
4.16	Instantaneous view of the volume fraction C (top) and ambient-phase velocity components u_a^*/U_i^* (middle) and v_a^*/U_i^* (bottom) fields in unstable conditions. In all the panels the interface is the black contour line.	78
4.17	$u'(x, y)$ evolution of a random initial disturbance ($0 < x < 1, -0.75 < y < 0.75$). $We = 2.5, r_\rho = 0.01$. Field variables have been normalized with respect to the corresponding maximum.	81
4.18	Data driven BiGlobal spectrum. $We = 2.5, r_\rho = 0.01$. Black dots refer to the 2D simulations, red circles represent 1D model results. Letters denote selected modes.	82
4.19	Spatial distributions of the DMD modes A (panels (a)-(c)) and B (panels (d)-(f)) in xy plane ($0 < x < 1, -0.75 < y < 0.75$). $We = 2.5, r_\rho = 0.01$. The black dashed line represents the interface location.	83

4.20	Varicose component of DMD $u'(x, y)$ modes corresponding to the eigenvalues C, D, E ($0 < x < 1$, $-0.75 < y < 0.75$). $We = 2.5$, $r_\rho = 0.01$. The black dashed line represents the interface location.	86
4.21	Energy distribution for the modes C (panel (a)), D (panel (b)) and E (panel (c)) in xy plane ($0 < x < 1$, $-0.75 < y < 0.75$). $We = 2.5$, $r_\rho = 0.01$. The black dashed line represents the interface location.	87
4.22	Schematic representation of the three-dimensional computational domain. The gravity g is directed along the streamwise x direction, y is the lateral coordinate, z the spanwise one.	88
4.23	Three-dimensional view of the liquid sheet interface (a), spanwise velocity field w in xz plane (b) and $w(z)$ profiles at different streamwise x stations (c). $AR = 40$, $We = 2.5$	90
4.24	Interface shape in yz planes located at different x stations (panel (a)); maps of spanwise w (panel (b)) and transverse v (panel (c)) liquid velocity components at $x = 15$. $AR = 40$, $We = 2.5$	92
4.25	Map in xy plane of the streamwise velocity u (panel (a)); x -variation of the axial velocity $u(x, y = 0)$ and y -averaged trend $\langle u(x, y) \rangle$ (b). The reference Torricellian velocity u_{torr} and the calculated convergence length L_c are also reported. $AR = 40$, $We = 2.5$. . .	95
4.26	Convergence length L_c variation with Weber number. The theoretical prediction L_c^{th} is also reported.	96

- 4.27 Combined $We-Fr$ effect on the eigenvalues, panels (a) and (b), and on the normalized least stable eigenfunction, panel (c): $(We, Fr) = (1.2, 0.08)$, black filled dot and continuous black line; $(1.05, 0.07)$, black open dot and dashed black line; $(0.95, 0.06)$, red filled dot and continuous red line; $(0.8, 0.05)$, red open dot and dashed red line. Panel (b) shows a zoom of the inner part of the spectra reported in panel (a). The characteristic frequencies $\Delta\lambda_i^+$ and $\Delta\lambda_i^-$, whose values are listed in Table 4.8, are indicated respectively in panels (a) and (b). 98
- 4.28 Normalized power spectral density of the vibrometer recordings acquired at different values of the Weber number. 100
- 4.29 Comparison between numerical (f_n^* , continuous curves) and experimental (f_e^* , filled circles) natural frequencies in supercritical (black) and subcritical (red) regimes. The numerical frequency associated with the fast branch of spectrum in supercritical conditions is also reported (black dashed curve). The error bars represent the standard deviation of the experimental measurements. 102
- 4.30 Weber number effect on the sheet centreline deflection, ℓ , as a function of the streamwise station, x , at different fractions of oscillation period T : $t = 0 \cdot T$ (black); $0.25 \cdot T$ (red); $0.5 \cdot T$ (blue); $0.75 \cdot T$ (green). The dashed line denotes the centreline of the unperturbed curtain. From top to bottom: $f^* = 1, 5$ and 20 Hz. . 103

- 4.31 Reynolds number Re effect on the meanline maximum oscillation amplitude A_ℓ as a function of the streamwise direction x at different forcing frequencies f^* (left column) and of the forcing frequency at different streamwise stations (right column). Left column: $f^* = 15$ (green curve); 20 (brown); 25 (black); 30 (red); 35 (blue); 45 (orange); 55 (purple) Hz. Right column: $x = 0.05$ (black); 0.13 (blue); 0.2 (red); 0.4 (purple); 0.6 (green); 0.8 (orange). Natural frequency predicted by the theoretical model: $f_n^* = 26.26$ Hz. From top to bottom: $Re = 20, 40, 400, 800, 1600$ 107
- 4.32 Reynolds number Re effect on the maximum oscillation amplitude of transverse velocity component A_v as a function of the streamwise direction x at different forcing frequencies f^* (left column) and of the forcing frequency at different streamwise stations (right column). Left column: $f^* = 15$ (green curve); 20 (brown); 25 (black); 30 (red); 35 (blue); 45 (orange); 55 (purple) Hz. Right column: $x = 0.05$ (black); 0.13 (blue); 0.2 (red); 0.4 (purple); 0.6 (green); 0.8 (orange). Natural frequency predicted by the theoretical model: $f_n^* = 26.26$ Hz. From top to bottom: $Re = 20, 40, 400, 800, 1600$ 108
- 4.33 Normalized SPOD spectra at $We = 0.75$ for different Reynolds number Re values. The spectra report only the frequency content of the first 2 modes. Forcing frequency $f^* = 25$ Hz ($St = 0.076$). 111

4.34	Cumulative energy distribution of SPOD modes at $We = 0.75$ for different Reynolds number Re values.	112
4.35	Panel (a): sketch of sinuous disturbance. The red lines denote the interface of the mean field. Panel (b): streamlines pattern as viewed by an observer moving with the mean flow. The colour map refers to $C'(x, y)$ mode ($0 < x < 1, -1 < y < 1$).	112
4.36	Panel (a): sketch of varicose disturbance. The red lines denote the interface of the mean field. Panel (b): streamlines pattern as viewed by an observer moving with the mean flow; the colour map refers to the varicose part of $C'(x, y)$ mode ($0 < x < 1, -1 < y < 1$).	113
4.37	Decomposition in sinuous and varicose components of the flow field at $We = 0.75, Re = 1600$. $C'(x, y)$ mode (left panel) and its varicose (middle panel) and sinuous (right panel) components ($0 < x < 1, -0.75 < y < 0.75$).	114
4.38	Spatio-temporal evolution of the transverse velocity perturbation $v(x, t)$ for $We = 0.8$ (panel (a)) and $We = 0.4$ (panel (b)): $t = 0.25$ (black line), 2.5 (blue line) and 7.5 (red line). The magenta curve in both panels represents the initial perturbation (4.5). $We_{th} = 0.63$	116
4.39	Temporal evolution of the energy budgets for $We = 0.8$ (panels (a)-(d)) and $We = 0.4$ (panels (e)-(h)). All the terms are scaled with respect to the initial total energy E_{t_0} . For a detailed explanation of the terms, see Eq. (2.33) in Section 2.1.3. $We_{th} = 0.63$	118

4.40	Temporal evolution of meanline oscillations amplitude at $x = x_p$ for $We = 0.8$ (panel (a)) and $We = 0.4$ (panel (b)): $Re = 41.3$ (continuous black curve); 413 (continuous red curve); ∞ (continuous blue curve). The dot-dashed curves represent algebraic ($\sim t^{\frac{1}{3}}$, red) and exponential ($\sim e^{\frac{1}{3}t}$, blue) growths. $We_{th} = 0.63$.	119
4.41	Inner eigenvalues of the spectrum (panel (a)) with a zoom on the unstable part (panel (b)). The curve $\lambda_r = 1/3$ (dot-dashed blue line) is also reported. $Re = \infty$, $We_{th} = 0.63$.	120
4.42	Overview of the air-water mixing layer testing conditions in terms of M values as a function of the gas velocity U_g , at different values of the liquid velocity U_l .	122
4.43	Time-averaged velocity magnitude \bar{V}/U_g contour (a) with zoom next to the nozzle exit section (b). In both panels, the splitter plate location is highlighted in black, and velocity vectors are reported. REF case of Table 4.12.	122
4.44	Time-averaged streamwise $\bar{u}(\tilde{y})/U_g$ velocity component profiles at different \tilde{x} stations: $\tilde{x} = 0.55$ ($\text{---}\circ\text{---}$); 10.88 ($\text{---}\blacklozenge\text{---}$); 21.76 ($\text{---}\blacksquare\text{---}$); 32.10 ($\text{---}\blackstar\text{---}$); 42.98 ($\text{---}\blacktriangle\text{---}$); 53.31 ($\text{---}\circ\text{---}$). The dashed and dotted lines represent the values $\bar{u}/U_g = 0$ and 1, respectively, while error bars denote the average measurement uncertainty. REF case of Table 4.12.	124

- 4.45 Velocity profiles $\bar{u}(\tilde{y})/U_g$ at different \tilde{x} stations (a) with zoom near the liquid phase (b) and velocity defect $(\bar{u}_{min} - U_l)/U_g$ streamwise distribution (c). The vertical red line in panel (c) denotes the wake region length \tilde{x}_w , while error bars represent the average measurement uncertainty. REF case of Table 4.12. 125
- 4.46 Time-averaged streamwise $\bar{u}(\tilde{x})/U_g$ (a) and vertical $\bar{v}(\tilde{x})/U_g$ (b) velocity component profiles at different \tilde{y} stations. REF case of Table 4.12. 127
- 4.47 Contour of $\overline{u'u'}/U_g^2$ (a), $\overline{v'v'}/U_g^2$ (b) and $\overline{u'v'}/U_g^2$ (c). The white circles in panel (b) denote monitoring locations employed for the analysis of unsteady velocity fluctuations in Section 4.2.2. REF case of Table 4.12. 128
- 4.48 Profiles of $\overline{u'u'}/U_g^2$ (a), $\overline{v'v'}/U_g^2$ (b) and $\overline{u'v'}/U_g^2$ (c) at different streamwise stations: $\tilde{x} = 0.55$ ($\text{---}\circ\text{---}$); 10.88 ($\text{---}\color{red}\diamond\text{---}$); 21.76 ($\text{---}\color{blue}\square\text{---}$); 32.10 ($\text{---}\color{black}\blacktriangleright\text{---}$); 42.98 ($\text{---}\color{red}\blacktriangleright\text{---}$); 53.31 ($\text{---}\color{blue}\circ\text{---}$). Panel (d) reports $\overline{u'u'}/U_g^2$ profiles at different vertical stations \tilde{y} . REF case of Table 4.12. 129
- 4.49 Theoretical-experimental comparison of velocity profiles inside (panels (a)-(b)) and outside ((c)-(d)) the wake region of length $\tilde{x}_w = 17.5$. REF case of Table 4.12. 131
- 4.50 Weber number We_l effect on \bar{V}/U_g flow field. The splitter plate is highlighted in black, and velocity vectors are reported. WElo (a), REF (b), WEme (c) and WEhi (d) cases of Table 4.12. 133

4.51	Weber number We_l effect on the time-averaged stream-wise $\bar{u}(\tilde{y})/U_g$ velocity component at different \tilde{x} stations: $\tilde{x} = 0.55$ (—○—); 10.88 (—◆—); 21.76 (—■—); 32.10 (—★—); 42.98 (—▲—); 53.31 (—◇—). REF (a) and WEhi (b) cases of Table 4.12.	134
4.52	Reynolds number Re_g effect on the time-averaged velocity magnitude \bar{V}/U_g . The splitter plate is highlighted in black, and velocity vectors are reported. RElo (a), REF (b), REme (c) and REhi (d) cases of Table 4.12.	136
4.53	Reynolds number Re_g effect on the time-averaged stream-wise $\bar{u}(\tilde{y})/U_g$ velocity component at different \tilde{x} stations: $\tilde{x} = 0.55$ (—○—); 10.88 (—◆—); 21.76 (—■—); 32.10 (—★—); 42.98 (—▲—); 53.31 (—◇—). RElo (a), REF (b), REme (c) and REhi (d) cases of Table 4.12.	137
4.54	Profiles of $\overline{u'u'}/U_g^2$ at $\tilde{y} = 0$ for different values of the Reynolds number. REF (black curve), REtr (red curve) and REhi (blue curve) cases of Table 4.12. . .	138
4.55	Reynolds number Re_g effect on the wake region length \tilde{x}_w at different We_l values. The vertical red line corresponds to $Re_g = 493$	138
4.56	Dynamic pressure ratio M effect on the wake region length \tilde{x}_w at different values of the Reynolds number Re_g	139

4.57	We_l and Re_g effects on the FFT of vertical velocity component fluctuation $v'(t)/U_g$ at $(\tilde{x}, \tilde{y}) = (0.55, 5.44)$, i.e. in air flow immediately downstream of the splitter plate. $M = 5.78$ (a), 1.45 (b), 17.00 (c), 4.25 (d), 25.56 (e), 6.64 (f).	141
4.58	Dynamic pressure ratio M effect on the peak (dimensionless) frequency of the FFT of $v'(t)$ at $(\tilde{x}, \tilde{y}) = (0.55, 5.44)$ for different values of the Reynolds number Re_g	142
4.59	FFT of $v'(t)$ at different (\tilde{x}, \tilde{y}) locations: $\tilde{y} = 8.16$ (black curve); 5.44 (red); 2.72 (blue). REgl case of Table 4.12.	144
4.60	POD analysis of the REgl case of Table 4.12. Energy distribution (panel (a)); leading u' modes (each scaled with respect to its maximum, panels (b)-(f)). In each panel, the splitter plate is highlighted in grey, and the mean interface location is denoted by the white dashed line.	146
4.61	Power spectral density (PSD) of the temporal coefficients a_i associated to the leading POD modes shown in Fig. 4.60. The vertical red dashed lines denote the peak frequency $f\delta_g/U_g = 2.8 \cdot 10^{-4}$ and its first superharmonic $f\delta_g/U_g = 5.6 \cdot 10^{-4}$	147
B.1	Block diagram representation (top) and three dimensional sketch (bottom) of the experiment core components. The splitter plate separates the gas and liquid ducts.	160

B.2	Main views of the experiment core components.	161
B.3	Picture of the experiment core realized in Plexiglas. The test section is also shown (on the right).	162
B.4	Block diagram representation (top) and three dimensional sketch (bottom) of the gas circuit (plus the core) components. The air flow seeding and the pressure taps are not represented.	164
B.5	Picture of the connection component between the blower (on the right) and the air duct (on the left).	165
B.6	Block diagram representation (top) and three dimensional sketch (bottom) of the final version of the experimental apparatus. The flowmeter, the pressure taps, the regulating valve and the flows seeding are not represented.	169
B.7	Picture of the final assembly of the experimental apparatus components.	174

List of Tables

3.1	Relevant geometrical quantities of the two-phase mixing layer experimental setup (see also Fig. 3.5(b)). . .	50
4.1	Dimensional physical quantities involved in the problem, reporting the values referring to the base case. . .	61
4.2	Dimensionless parameters corresponding to the base case of Table 4.1.	61
4.3	Summary of results for the base case in terms of VOF-1D model comparison. $We = 2.5$, $Fr = 0.33$, $r_\rho = 0.01$	72
4.4	Selected eigenvalues for the case of $We = 2.5$, $r_\rho = 0.01$	84
4.5	Sinusoidal and varicose energy contributions of the selected DMD modes. $We = 2.5$, $r_\rho = 0.01$	85
4.6	Comparison between theoretical (L_c^{th}) and numerical (L_c) values of the convergence length by varying Weber and Froude numbers. The relative percentage spread is defined as $\epsilon_c = 100 \cdot (L_c - L_c^{th})/L_c$. $AR = 40$	94
4.7	Dimensionless parameters involved in the numerical analysis of supercritical-to-subcritical flow transition.	99

4.8	Global frequency in supercritical ($\Delta\lambda_i^-$, $We > 1$) and subcritical ($\Delta\lambda_i^+$, $We < 1$) flow regimes.	100
4.9	Experimental and numerical values of the natural frequency varying the Weber number. The relative percentage spread ϵ is defined as $\epsilon = 100 \cdot (f_n^* - f_e^*)/f_n^*$. The last column reports the standard deviation of the experimental measurements.	101
4.10	Dimensionless parameters involved in the subcritical regime analysis.	105
4.11	Dimensional quantities corresponding to the REF case.	123
4.12	Overview of the main cases considered in the analysis. Dimensionless parameters are defined in Eq. (4.15). .	123
B.1	Gas and liquid ducts dimensions. Each duct has a rectangular cross section (in yz plane); the area occupied by each phase (gas or liquid) is $A_{yz} = h \cdot w$	162
B.2	Splitter plate dimensions. It has a $e \times w$ rectangular cross section (in yz plane). Parameters values: $l = 500$ mm; $h = w = 100$ mm; $e = 2$ mm.	163
B.3	Gas and liquid nozzles dimensions. Each nozzle has a contoured cross section (in yz plane) with contraction ratio $H^i/H^f = 5$. Parameters values: $l = 500$ mm; $h = w = 100$ mm; $e = 2$ mm.	163
B.4	Minor losses coefficients for the air circuit: data from Munson <i>et al.</i> [129] and White [130]. In particular, the estimation $K = 4$ is taken from Chapter 8 of [129]. .	166

B.5	Gas circuit head losses varying the working velocity U_g . The required power P_e is calculated assuming a precautionary value of $\eta = 0.75$ for the blower efficiency.	166
B.6	Minor losses coefficients relative to the first part of the liquid circuit (from the overflowing tank to the nozzle): data from Munson <i>et al.</i> [129], White [130]. * The ball valve head loss coefficient $K = 0.05$ is taken from Chapter 8 of [129]. ** The head loss coefficient $K = 10$ is purely indicative; it can vary in a range [1;100] depending on the type of flowmeter and the operating conditions [131]. *** The honeycomb head loss coefficient $K = 4$ is taken from Chapter 8 of Munson <i>et al.</i> [129].	172

List of Publications

Published journal articles:

- A. Colanera, A. Della Pia and M. Chiatto, *Data-driven global stability of vertical planar liquid jets by DMD on random perturbations*, Physics of Fluids, 34, 122101 (2022);
- M. Chiatto and A. Della Pia, *Natural frequency discontinuity of vertical liquid sheet flows at transcritical threshold*, Journal of Fluid Mechanics, 945, A32 (2022);
- A. Della Pia, A. Colanera and M. Chiatto, *Surface tension-induced instability in spatially developing subcritical liquid curtains*, Physics of Fluids, 34, 042122 (2022);
- A. Della Pia, A. Colanera, M. Chiatto and L. de Luca, *Energy insights into the unsteady dynamics of a viscous gravitational liquid sheet*, Physics of Fluids, 33, 092118 (2021);
- A. Colanera, A. Della Pia, M. Chiatto, L. de Luca and F. Grasso, *Modal decomposition analysis of unsteady viscous liquid sheet flows*, Physics of Fluids, 33, 092117 (2021);

- A. Della Pia, M. Chiatto and L. de Luca, *Receptivity to forcing disturbances in subcritical liquid sheet flows*, Physics of Fluids, 33, 032113 (2021);
- A. Della Pia, M. Chiatto and L. de Luca, *Global eigenmodes of thin liquid sheets by means of Volume-of-Fluid simulations*, Physics of Fluids, 32, 082112 (2020).

Journal articles in preparation:

- A. Della Pia, T. Michelis, M. Chiatto, M. Kotsonis and L. de Luca, *Experimental analysis of two-phase wake-mixing layer flow behind a plane splitter plate*, in preparation for Journal of Fluid Mechanics;
- A. Della Pia, M. R. Acquaviva, A. Colanera, M. Chiatto and L. de Luca, *Flow topology and hole-induced dynamics of a three-dimensional gravitational liquid curtain*, in preparation for Physical Review Fluids.

Conference proceedings:

- A. Della Pia, L. Grande, A. Colanera, M. Chiatto and L. de Luca, *Volume-of-fluid simulation of three-dimensional gravitational liquid sheet flows*, European Congress on Computational Methods in Applied Sciences and Engineering (ECCO-MAS 2022), Oslo (Norway), 5-9 June 2022;
- A. Colanera, A. Della Pia, M. R. Acquaviva, M. Chiatto and L. de Luca, *Modal analysis of a 3D gravitational liquid sheet*,

European Congress on Computational Methods in Applied Sciences and Engineering (ECCOMAS 2022), Oslo (Norway), 5-9 June 2022;

- A. Della Pia, *Numerical and experimental investigation of unsteady two-phase flows*, 1st Ph.D. day of European students in Aerospace Engineering (AIDAA 2021), Pisa (Italy), Virtual Congress 15 February 2021;
- A. Della Pia, M. Chiatto and L. de Luca, *Unsteady dynamics of free-interface gravitational liquid sheet flows*, European Congress on Computational Methods in Applied Sciences and Engineering (ECCOMAS 2020), Paris (France), Virtual Congress 11-15 January 2021.

Chapter 1

Introduction

The comprehension of two-phase (and more in general multiphase) flows dynamics is matter of critical engineering and scientific importance, due to the huge variety of industrial applications involving multiphase flows of one sort or another (Tryggvason, Scardovelli and Zaleski [1]). From a mathematical point of view, two-phase flow problems are notoriously difficult: not only the equations governing the fluid flow in both phases are highly nonlinear, but the position of the phase boundary must generally be found as a part of the solution. Exact analytical solutions, therefore, exist only for the simplest problems. The need for numerical solutions of the governing equations, as well as experimental investigations, has thus been felt by the multiphase research community since its origin.

The present thesis deals with the numerical and experimental investigation of two unsteady two-phase flow systems. The configurations analyzed are both plane liquid jets interacting with an external gaseous environment: i) the gravitational liquid sheet (curtain) flow; and ii) the planar air-water mixing layer developing past a splitter plate. In the first configuration, the liquid jet velocity is relatively low and gravitational effects on the flow dynamics are relevant; the mixing layer flow is instead characterized by a relatively high velocity of the liquid jet, thus making dominant the aerodynamic instability due to the interaction with the gaseous phase.

1.1 Motivations and objectives

The first flow configuration here investigated consists of a thin sheet of liquid issuing vertically into an unconfined quiescent gaseous environment, under the influence of the gravitational field. The study of such a flow system is motivated by the variety of its scientific and technological applications, including coating deposition (Weinstein and Ruschak [2]), paper making (Soderberg and Alfredsson [3]), and dam safety (Lodomez *et al.* [4]) to name a few. Notwithstanding the large amount of research efforts, several aspects of the unsteady dynamics of liquid sheet flows are the object of ongoing studies, in particular those related to the physical mechanisms driving the liquid sheet towards instability. Therefore, a main target of the present research activity is a combined theoretical-numerical-experimental investigation of the stability properties of gravitational planar liquid sheet flows interacting with an unconfined gaseous environment. Such flow configurations have been investigated by means of direct numerical simulations based on the volume-of-fluid (VOF) method, linear stability analysis of a simplified low-dimensional theoretical model, data-driven modal decomposition techniques, and experiments. The main objective is to summarize a broad theoretical background allowing in future to establish connections between theoretical-numerical results of the present investigation and three-dimensional observations of real occurrence.

The second flow configuration is related to the instability of an atomizing jet, and thus it is of particular importance to model phenomena of industrial interest, such as fuel injection in air-blast atomizers (Lefebvre [5]). In the planar configuration here considered, two parallel co-flowing gas and liquid phases are initially separated by a splitter plate and, when they meet at its trailing edge, the velocity difference existing between them triggers a shear instability on the gas-liquid interface. Despite extensive research dedicated to the topic, a comprehensive understanding of the physical mechanisms governing the two-phase mixing layer instabilities has not been

achieved yet, making the modelling and control of two-phase mixing layers still challenging tasks nowadays. In particular, one of the most imperative requests is the accurate knowledge of the flow in the near-field region, which could then be used for a global stability analysis to improve the capability to predict the flow dynamics in most of the experimental conditions. For this reason, another aim of the present work is the characterization of two-phase mixing layers through two-dimensional flow field measurements. An experimental investigation based on time-resolved particle image velocimetry (TR-PIV) has been performed, aimed at disclosing new aspects of the mean flow topology and unsteady dynamics in the near-field region of the flow. This part of the Ph.D. research activity is the result of a collaboration between the research group in which the candidate worked in Naples and the Flow Stability & Control research group at Delft University of Technology, where the candidate spent a Visiting Scholar period of one year during his Ph.D. Program.

1.2 Outline

The rest of the thesis is structured as follows. Chapter 2 discusses more in detail the gas-liquid interfacial flow systems which are object of this study, namely gravitational liquid sheet (curtain) flows (Section 2.1) and planar air-water mixing layers (Section 2.2). Chapter 3 (together with Appendices A and B) contains a detailed description of the theoretical, numerical and experimental methodologies and set-ups employed to obtain data described along the thesis. Chapter 4 is dedicated to the results: the physical mechanisms governing the curtain flow dynamics in stable and unstable conditions are first investigated in Section 4.1; the air-water mixing layer experimental characterization is then reported in Section 4.2. The thesis ends with Chapter 5, containing a summary of the main findings and suggestions for possible future research activities.

Chapter 2

Layout of plane liquid jets

The gas-liquid interfacial flow configurations representing the object of this study are detailed discussed in this chapter. Section 2.1 is dedicated to gravitational liquid sheet (curtain) flows issuing into a still gaseous environment, while two-phase mixing layers are described in Section 2.2.

2.1 Gravitational liquid curtains

Liquid sheet flows issuing into a gaseous environment have been studied since the middle of the last century (Squire [6]), due to their wide scientific and industrial interest, which involves coating deposition (Weinstein and Ruschak [2]), paper making (Soderberg and Alfredsson [3]), space industry (Chubb *et al.* [7]), dam safety and waterfall noise reduction (Lodomez *et al.* [4]), and other applications. The literature includes a wide variety of geometrical and physical configurations, which span both planar (Barlow *et al.* [8], Weinstein *et al.* [9]) and round (Duke *et al.* [10]) geometries, both high (Zandian *et al.* [11]) and low speed (gravitational) (Lhuissier *et al.* [12], Girfoglio *et al.* [13]) flows (in the latter case the term *curtain* is often used), both quiescent (de Luca and Costa [14]) and co-flowing air (Tammisola *et al.* [15]) ambient, which refers to an enclosure located

on one side of the sheet (De Rosa *et al.* [16]), or can be considered unconfined on all sides of it (Barlow *et al.* [17]).

Notwithstanding the large amount of research efforts, which are comprehensively summarized in the literature reviews reported within the historical works by de Luca [18], Finnicum *et al.* [19], Lin and Jiang [20], Soderberg [21], and in the more recent contribution by Torsey *et al.* [22], several aspects of the unsteady dynamics of gravitational liquid curtain flows are the object of ongoing studies and remain currently open. Among them, the present work focuses on the unconfined liquid sheet behaviour in supercritical conditions ($We > 1$), across the supercritical-to-subcritical flow transition ($We = \mathcal{O}(1)$, transcritical regime), and in subcritical regime ($We < 1$). The Weber number We is a main governing parameter of the flow system, here defined as the ratio between inertia and capillary forces within the liquid phase. Depending on the We value, each of the three regimes introduced above is characterized by different features and stability properties.

The open questions in the literature directly related to the present investigation are discussed in the following Sections 2.1.1 and 2.1.2, further highlighting motivations and objectives of this study. Later on, a theoretical model developed within this work for the analysis of unconfined liquid curtain flows is presented in Section 2.1.3.

2.1.1 Unconfined curtain in critical conditions

It is known that a liquid plane jet (sheet, curtain) interacting with an unconfined gaseous environment and subjected to gravity effects does not merely breakup due to the amplification of modal disturbances. As a matter of fact, experimental evidence shows that the sheet breaks up (when the flow rate is reduced) below the critical threshold $We = 1$, as a consequence of phenomena such as the formation of holes involving two unsteady oscillating free-edges in the three-dimensional plane (Brown [23], de Luca and Meola [24], Roche *et al.* [25], Kacem *et al.* [26]). The parameter We is here defined as

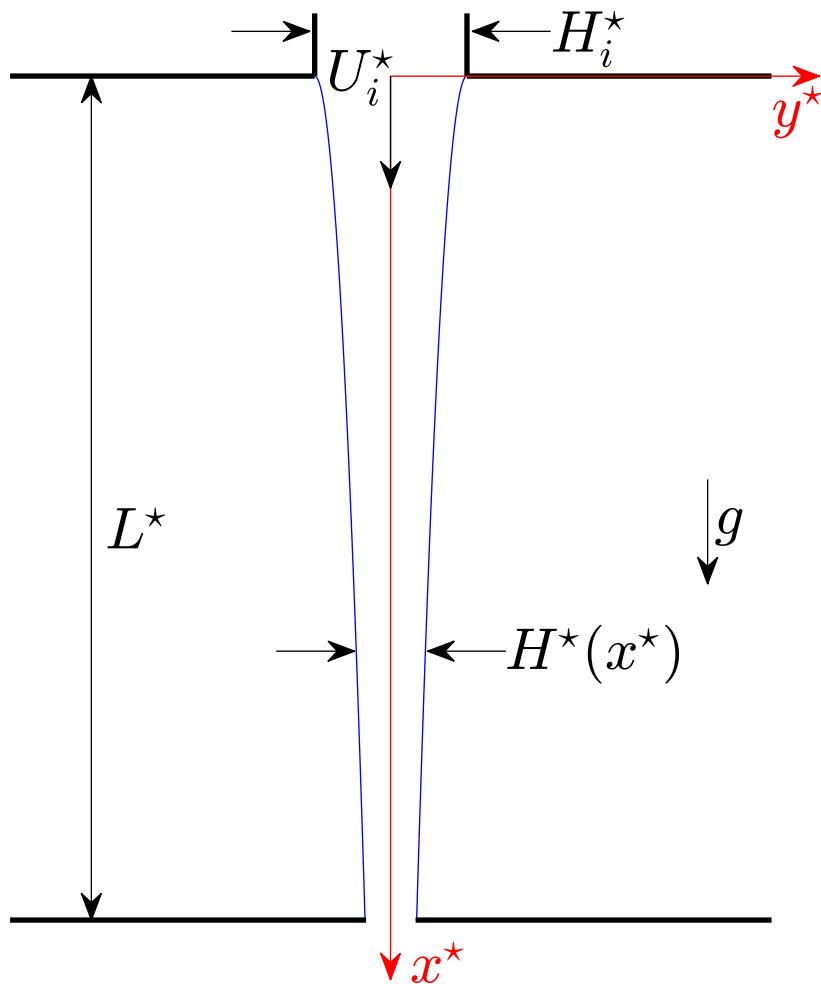


Figure 2.1. Sketch of an unperturbed gravitational liquid curtain of length L^* issuing into a quiescent gaseous ambient. Gravity is directed along the x^* axis, and the gas-liquid interface is represented in blue.

the ratio between inertia and capillary forces at the slot section of thickness H_i^* (i.e. where the liquid flow issues and the sheet starts to form, see Fig. 2.1), $We = \rho_l U_i^{*2} H_i^* / (2\sigma)$, U_i^* being the inlet mean liquid velocity ($Q_i^* = U_i^* H_i^*$ is the flowrate), ρ_l and σ the fluid density and the surface tension coefficient, respectively. Therefore, an exhaustive study of the rupture would require a fully three-dimensional approach, and it is clear that it must be based on a well-defined physical modelling of the different curtain flow regimes; results of direct numerical simulations have to be interpreted on the basis of this physical knowledge. The theoretical study of unconfined liquid sheets dynamics involves the resolution of a singularity appearing in the governing equations of low order modelling (Finnicum *et al.* [19], Weinstein *et al.* [27], Girfoglio *et al.* [13]) when the Weber number crosses the critical threshold $We = 1$, i.e. when the supercritical ($We > 1$) to subcritical ($We < 1$) flow transition occurs. On this research line, the analysis of the singularity exhibited by the equation governing the unsteady subcritical behaviour of the so called liquid nappe, namely the freely falling liquid sheet interacting with a one-sided closed air chamber, has been fully accomplished only a few years ago by Girfoglio *et al.* [13]. The flow of waterfalls, generated by the overflow of water over long crests of dams or weirs, represents a typical example of such a configuration. The noise produced by the oscillation of the waterfall can be radiated far away from the source and may cause vibrations in windowpanes of buildings nearby, and even structural damages to the dam itself (Erpicum *et al.* [28], Lodomez *et al.* [29]).

A modelling study aimed at predicting the oscillatory dynamics of the flow configuration in both supercritical ($We > 1$) and subcritical ($We < 1$) regimes is still missing in literature, and thus represents a major objective of this work. The topic is also important from the technological aspect, because unconfined two-dimensional planar liquid sheets falling under gravity are often employed to deposit liquid layers on a solid moving surface during coating processes (Weinstein and Ruschak [2]).

2.1.2 Subcritical regime

One of the pioneering experimental investigations focusing on the sheet rupture mechanisms was carried out by Brown [23], who stated that a condition for the curtain breakup is $We < 1$. Brown found the minimum liquid flow rate to guarantee the stability of the sheet by noticing that equilibrium must be maintained at a free edge between the inertia forces and the surface tension, and that when a free edge appears because of the formation of a hole, such a hole does not grow if the sheet is in supercritical conditions ($We > 1$), otherwise it does produce the curtain disintegration. On the other hand, the historical work by Finnicum *et al.* [19] reports that stable liquid curtains can be experimentally observed under a wide range of flow conditions, spanning both the supercritical and subcritical regimes. Still on the experimental side, Le Grand-Piteira *et al.* [30] studied subcritical liquid sheets falling from a horizontal wet tube and maintained between two vertical wires. These authors showed that when We reduces below the unity, the curtain is able to self-sustain a characteristic chessboard pattern of sinuous waves, whose propagation velocity is equal to half of the liquid speed at the transonic line, namely at the vertical station along the curtain where the local (dimensionless) velocity equals the Weber number, and does not depend on the vertical location on the curtain, arguing this behaviour could be related to global mode oscillations. The latter work provides an experimental investigation of the curtain response to perturbations near breakup, outlining different behaviours between $We > 1$ and $We < 1$ conditions, the latter scenario being characterized by possible holes expansions leading to the liquid sheet rupture.

From theoretical and numerical points of view, the stability condition $We > 1$ found by Brown [23] was retrieved in the works by Lin [31], de Luca and Costa [14], Lin and Roberts [32], and Barlow *et al.* [17]. In particular, [17] showed through a local spatio-temporal linear stability analysis that subcritical plane liquid sheets can experience absolute instability, with algebraic temporal growth of sinuous

modes superposed on the main flow, in agreement with the previous investigation by de Luca and Costa [14].

The present work thus aims at representing a further step towards a deeper understanding of gravitational liquid sheets dynamics. Based on the derivation of a simplified linear model of the curtain flow (Section 2.1.3), its stability properties are elucidated, outlining relevant physical mechanisms and providing comparisons with two-dimensional direct numerical simulations, data-driven modal analysis, and experiments. The main objective is to summarize a broad theoretical background allowing in future to establish connections between theoretical-numerical results of the present investigation and three-dimensional observations of real occurrence.

2.1.3 Theoretical and numerical modelling

A sketch of the analyzed flow configuration is reported in Fig. 2.2, where the gravitational sheet is represented with the x^* axis vertically oriented. In the unperturbed condition, the liquid flows along the gravity direction with a steady velocity and two symmetrical free interfaces (blue thin lines in Fig. 2.2, where H^* represents the unperturbed local thickness). The definitions of centreline ℓ^* location and thickness h^* of the sheet are given in terms of the interface positions $y^{*\pm}$ as

$$\ell^*(x^*, t^*) = \frac{y^{*+}(x^*, t^*) + y^{*-}(x^*, t^*)}{2}, \quad (2.1a)$$

$$h^*(x^*, t^*) = y^{*+}(x^*, t^*) - y^{*-}(x^*, t^*), \quad (2.1b)$$

where superscripts \pm refer to right and left interfaces, respectively.

The assumption of a thin sheet with respect to the wavelength of a disturbance allows one to consider local plug-type velocity profiles across the liquid sheet thickness for both the velocity components. Starting from the two-dimensional Euler equations (the inviscid assumption is made in what follows; a derivation of the governing equations accounting for viscous effects is reported at the end of this

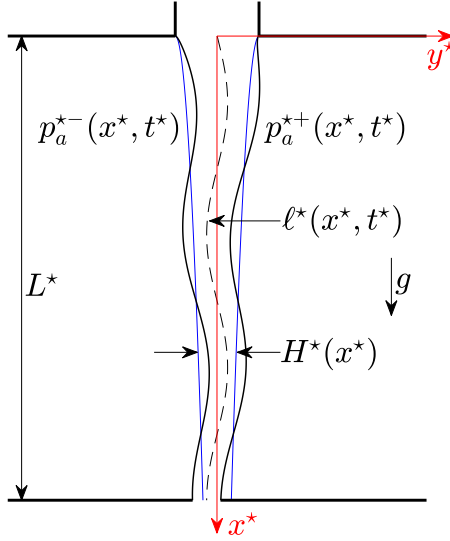


Figure 2.2. Sinuous dynamics of a gravitational liquid curtain issuing into a quiescent gaseous ambient.

section) closed by kinematic and dynamic conditions imposed at the free interfaces, the following procedure has been adopted to derive the governing equations of a one-dimensional model of the curtain dynamics (see also Girfoglio *et al.* [13]). The mass and x^* -momentum balances are formulated over a generic slice of the curtain of length dx^* ; the y^* -momentum equation is integrated along the lateral coordinate y^* ; the unsteady quantities are considered as the sum of a steady contribution and a perturbation (or fluctuation):

$$u^* = U^* + u'^*, \quad (2.2)$$

$$v^* = V^* + v'^*, \quad (2.3)$$

$$p^* = P^* + p'^*, \quad (2.4)$$

$$h^* = H^* + h'^*, \quad (2.5)$$

$$y^{*\pm} = Y^{*\pm} + y'^{\pm}, \quad (2.6)$$

where capital letters denote basic (steady) quantities, while the su-

perscript *prime* the corresponding fluctuation. Under the assumption of small perturbations, and $V^* = 0$, the linearized forms of boundary kinematic condition and y^* -momentum equation are written, respectively:

$$v'^* = \frac{\partial \ell'^*}{\partial t^*} + U^* \frac{\partial \ell'^*}{\partial x^*}, \quad (2.7)$$

$$\frac{\partial v'^*}{\partial t^*} + U^* \frac{\partial v'^*}{\partial x^*} - \frac{2\sigma}{\rho_l H^*} \frac{\partial^2 \ell'^*}{\partial x^{*2}} = -\frac{1}{\rho_l H^*} (p_a'^{*+} - p_a'^{-}), \quad (2.8)$$

where all dimensional quantities except the fluid material properties (liquid density ρ_l , surface tension coefficient σ) are denoted with the superscript \star . In particular, ℓ'^* represents the meanline deflection (dashed line in Fig. 2.2), U^* and H^* the base flow velocity and thickness distributions, x^* and t^* the spatial and temporal coordinates. It is worth noting that the linearization allows for the separation between anti-symmetric and symmetric (or varicose) modes; Eqs. (2.7)-(2.8) describe sinuous ones, while the latter are obtained from the continuity equation and x^* -momentum balance, and read

$$\frac{\partial h'^*}{\partial t^*} = -\frac{\partial}{\partial x^*} (U^* h'^* + H^* u'^*), \quad (2.9)$$

$$\frac{\partial u'^*}{\partial t^*} + \frac{\partial}{\partial x^*} (U^* u'^*) = -\frac{1}{\rho_l} \frac{\partial \bar{p}'^*}{\partial x^*} + \frac{\sigma}{2\rho_l} \frac{\partial^2}{\partial x^{*2}} \left[\frac{\partial h'^*}{\partial x^*} \right], \quad (2.10)$$

where

$$\bar{p}'^* = \frac{p_a'^{*+} + p_a'^{-}}{2}.$$

Fig. 2.3(a)-(b) reports the sketch to illustrate the sinuous and varicose disturbances, respectively, together with the relevant physical quantities involved. As outlined by Girfoglio *et al.* [13], the varicose modes are not able to sustain any oscillating wave pattern under the assumptions made to derive the present configuration (namely, the pressure terms at the right hand side of Eq. (2.10) are of ε^2 order, where ε is the sheet slenderness ratio defined later in this section), and

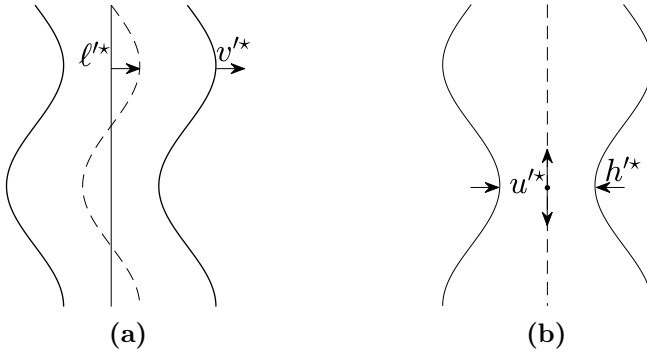


Figure 2.3. Sketch of sinuous (a) and varicose (b) disturbances.

thus only the sinuous modes will be the object of the modal analysis. This statement is consistent with a previous study made by Weinstein *et al.* [27], who found that pressure variations do not interact with the varicose response, and therefore to the order of the approximations considered in their paper, *pressure disturbances induce a deflection of the curtain without any associated thickness variations; that is, the front and back interfaces are perturbed in precisely the same way to preserve the local thickness of the undisturbed curtain.* Of course this basic result holds for the inviscid linear analysis. However, direct numerical simulations reported in Section 4.1.4 will show that, although the perturbations have small amplitudes and the flow is stable, for relatively low forcing frequencies and high Reynolds numbers, a non-linear interaction between anti-symmetric (sinuous) and symmetric (varicose) modes can occur.

The right hand side of Eq. (2.8) describes the pressure jump between the liquid and the gaseous fields due to the surface tension σ , and the variation of the pressure of the external ambient surrounding the sides of the sheet. By employing the unsteady Bernoulli's equation, in the absence of air velocity, the pressure variation of the

external ambient can be evaluated as (Kornecki *et al.* [33])

$$p_a^{l*+} - p_a^{l*-} = -\frac{2}{\pi} \rho_a \int_0^{L^*} \frac{\partial^2 \ell'^*}{\partial t^{*2}} \ln \left| \frac{x^* - \xi^*}{L^*} \right| d\xi^*, \quad (2.11)$$

where ρ_a denotes the air density and L^* the sheet length. The integral in Eq. (2.11) yields the evaluation of the local pressure variation due to the influence of the whole sheet deformation. For any $x^* = \xi^*$ the integrand is singular, and its evaluation requires a suited treatment (De Rosa [34]).

Travelling-wave features of the theoretical solution

By employing the following reference quantities (subscript r)

$$L_r^* = L^*, \ell_r^* = H_i^*, U_r^* = U_i^*, v_r^* = \varepsilon U_i^*, t_r^* = L^*/U_i^*, \quad (2.12)$$

where the sheet slenderness ratio $\varepsilon = H_i^*/L^*$ has been introduced, the dimensionless form of Eqs. (2.7)-(2.8) is obtained:

$$\frac{\partial \ell}{\partial t} + U \frac{\partial \ell}{\partial x} = v, \quad (2.13)$$

$$\frac{\partial v}{\partial t} + U \frac{\partial v}{\partial x} = \frac{1}{WeH} \frac{\partial}{\partial x} \frac{\partial^2 \ell}{\partial x^2} - (p_a^+ - p_a^-), \quad (2.14)$$

where the superscript *prime* for the perturbations quantities has been suppressed, and

$$p_a^+ - p_a^- = -\frac{2}{\pi} \frac{\rho_a}{\rho_l} \frac{1}{\varepsilon} \frac{1}{H} \int_0^1 \frac{\partial^2 \ell}{\partial t^2} \ln |x - \xi| d\xi. \quad (2.15)$$

Based on the works by Weinstein *et al.* [27] and Finnicum *et al.* [19], the Torricelli's free-fall solution is considered as the steady main flow

in Eqs. (2.13)-(2.14),

$$U = \sqrt{1 + 2\frac{x}{Fr}}, \quad UH = 1, \quad P = 0, \quad (2.16)$$

being $Fr = U_i^{\star 2}/(gL^{\star})$ the Froude number. Note also that hereafter dimensionless quantities will be denoted without apex \star . It is useful to recast the system of Eqs. (2.13)-(2.14) as a single second order integro-differential equation

$$\begin{aligned} \frac{\partial^2 \ell}{\partial t^2} - \frac{2}{\pi} \frac{1}{\varepsilon} \frac{\rho_a}{\rho_l} \frac{1}{H} \int_0^1 \frac{\partial^2 \ell}{\partial t^2} \ln|x - \xi| d\xi + \\ + 2U \frac{\partial^2 \ell}{\partial x \partial t} + U \left(U - \frac{1}{We} \right) \frac{\partial^2 \ell}{\partial x^2} + U \frac{\partial U}{\partial x} \frac{\partial \ell}{\partial x} = 0. \end{aligned} \quad (2.17)$$

In terms of substantial derivative, Eq. (2.17) can be conveniently rewritten as

$$\frac{D^2 \ell}{Dt^2} - \frac{2}{\pi} \frac{1}{\varepsilon} \frac{\rho_a}{\rho_l} \frac{1}{H} \int_0^1 \frac{\partial^2 \ell}{\partial t^2} \ln|x - \xi| d\xi - \frac{U}{We} \frac{\partial^2 \ell}{\partial x^2} = 0, \quad (2.18)$$

which is analogous to the classic one representing transverse vibrations of a finite length tensional string. Therefore, for $\rho_a = 0$, Eq. (2.18) features two real and distinct characteristics on the entire physical domain, which are physically represented by travelling waves with velocities $\pm\sqrt{U/We}$ relative to that of the basic flow U (Weinstein *et al.* [27], Girfoglio *et al.* [13]). It is worth noting that, for $\rho_a \neq 0$, the system (2.13)-(2.14) is not rigorously hyperbolic due to the integral term (2.15). However, numerical integrations of the equations shown later in Section 4.1 reveal solutions represented by travelling waves with phase velocities and corresponding crossing times in strict agreement with those obtained for $\rho_a = 0$. Based on this consideration, Eqs. (2.13)-(2.14) are equipped with two boundary conditions imposed at the inlet section ($x = 0$) for $We > 1$ (two downstream-oriented characteristic curves), while for $We < 1$, due to

the upstream-oriented curve $U - \sqrt{U/We}$, only one constraint can be retained at $x = 0$. The boundary conditions assignment to properly close the system (2.13)-(2.14) in both supercritical and subcritical regimes is addressed in detail in Section 3.2.

A physical interpretation of the sheet dynamics

A different rearrangement of the system (2.13)-(2.14) leads to

$$\begin{aligned} \frac{\partial^2 \ell}{\partial t^2} + U \frac{\partial^2 \ell}{\partial t \partial x} + RU \int_0^1 U \frac{\partial^2 \ell}{\partial t \partial x} \ln |x - \xi| d\xi - \frac{1}{We_l H} \frac{\partial^2 \ell}{\partial x^2} = \\ -U \frac{\partial v}{\partial x} + RU \int_0^1 \frac{\partial v}{\partial t} \ln |x - \xi| d\xi, \end{aligned} \quad (2.19)$$

where the parameter $R = \frac{2 r_\rho}{\pi \varepsilon}$ has been introduced ($r_\rho = \rho_a / \rho_l$ is the density ratio), and the substitution $U = 1/H$ from Eq. (2.16) has been made. According to Eq. (2.19), the oscillatory dynamics of the average sheet displacement ℓ appears forced by terms containing the lateral velocity v , which basically depend on the base flow U . The second and third terms at the left hand side, namely

$$U \frac{\partial^2 \ell}{\partial t \partial x}, \quad (2.20)$$

$$RU \int_0^1 U \frac{\partial^2 \ell}{\partial t \partial x} \ln |x - \xi| d\xi, \quad (2.21)$$

represent aerodynamic damping terms, since they contain the first time derivative of the displacement ℓ . Note that the two damping coefficients, namely the basic flow velocity U and the integral operator in Eq. (2.21), have opposite sign and, depending on the magnitude of the parameter R , the total damping coefficient can be negative, as reported in Fig. 2.4. As will be shown in Section 4.1.2, in supercritical conditions ($We > 1$) this makes the system unstable, which, in the absence of nonlinear saturation, manifests an exponential ampli-

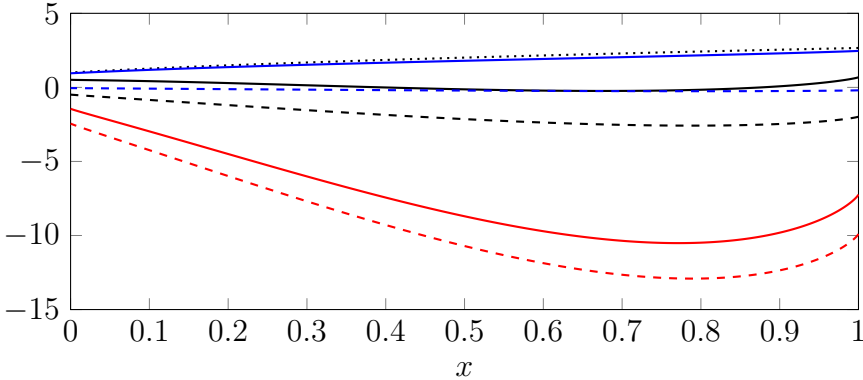


Figure 2.4. Aerodynamic damping coefficients in Eqs. (2.20)-(2.21): U (black dotted line); $RU \int_0^1 U(\cdot) \ln|x - \xi| d\xi$ (coloured dashed lines). Solid lines represent the total damping coefficient: $r_\rho = 0.001$ (blue curve); 0.01 (black); 0.05 (red).

fication of disturbances.

From supercritical to subcritical regime

It has been previously observed in this section that Eq. (2.17) exhibits two real and distinct characteristics curves on the entire physical domain, which are physically represented by travelling waves with velocities $\pm\sqrt{U/We}$ relative to that of the basic flow U . It is therefore possible to define the crossing time of each wave as

$$t_{cross}^\pm = \int_0^1 \frac{dx}{U \pm \sqrt{U/We}}, \quad (2.22)$$

namely the time needed for the fast and slow wave, denoted by t_{cross}^+ and t_{cross}^- , respectively, to cross the entire sheet length. As shown by Girfoglio *et al.* [13], the two integrals of Eq. (2.22) can be analytically

evaluated as

$$t_{cross}^{\pm} = 2Fr \left[\frac{1}{2} (U|_1 - 1) \mp \frac{1}{\sqrt{We}} (\sqrt{U|_1} - 1) \right] + \left[\frac{1}{We} \log \frac{\sqrt{U|_1} \pm \frac{1}{\sqrt{We}}}{1 \pm \frac{1}{\sqrt{We}}} \right], \quad (2.23)$$

where $U|_1 = \sqrt{1 + 2/Fr}$. The fast and slow wave crossing time variation with the Weber number are reported in Fig. 2.5 for three different values of the Froude number, namely $Fr = 0.5, 1.0$ and 2.0 . The analysis of Fig. 2.5 reveals that, while t_{cross}^+ is a continuous monotonic function in both supercritical ($We > 1$) and subcritical ($We < 1$) ranges, t_{cross}^- has a distinctive different behaviour: it exhibits two singularities at $We = 1$ and $We = We_{th}$, where

$$We_{th} = \frac{1}{U|_1} = \frac{1}{\sqrt{1 + \frac{2}{Fr}}}. \quad (2.24)$$

Moreover, t_{cross}^- is a positive, or negative, decreasing function for $We > 1$, or $We < We_{th}$, respectively. Of course the formally negative time refers to a crossing time for a negative velocity. For $We > 1$ both the fast and slow travelling waves have positive velocity, i.e. they travel downstream towards the right end of the curtain, and they are both characterized by formally positive crossing times. As the Weber number decreases below the unity, but it is still greater than We_{th} , the fast wave velocity does not change in sign, while the slow one becomes negative in the region $0 < x < x_s$, where x_s is the critical station, i.e. the location where the local Weber number equals the unity, given by

$$x_s = \frac{Fr}{2} \left(\frac{1}{We^2} - 1 \right). \quad (2.25)$$

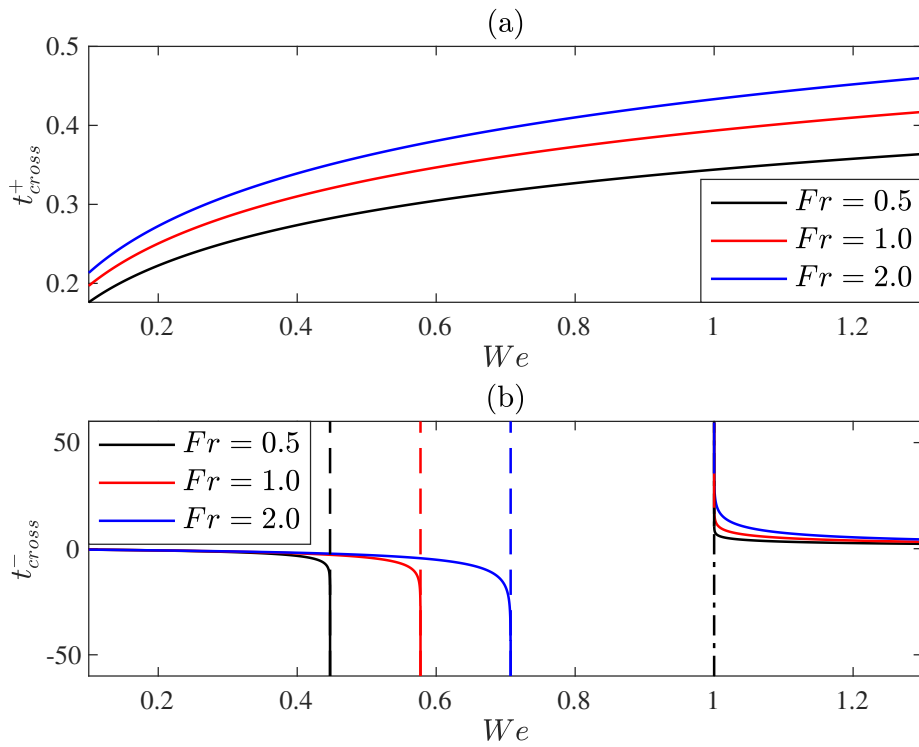


Figure 2.5. Froude number effect on the fast (panel (a)) and slow (panel (b)) wave crossing times t_{cross}^{\pm} as a function of the Weber number. In panel (b), coloured dashed lines denote the values We_{th} as a function of Fr , while the curve $We = 1$ is represented as a black dot-dashed line.

For $We_{th} < We < 1$, only the fast (right-travelling) wave determines the asymptotic liquid sheet dynamics: the associated crossing time t_{cross}^+ is the only one physically relevant (Fig. 2.5(a)), whereas t_{cross}^- is not defined (Fig. 2.5(b)). As a consequence, by applying linear stability analysis (Section 3.2) two branches of spectrum in supercritical regime and just one branch for $We_{th} < We < 1$ will be predicted, as confirmed by results reported in Section 4.1.3. Furthermore, when the Weber number decreases below the threshold $We = We_{th}$, that is the flow Weber number for which the critical station is located at the exit section, substituting Eq. (2.24) into Eq. (2.25) it is obtained that $x_s > 1$, namely the entire liquid sheet is subcritical. It will be shown in Section 4.1.4 that, as in supercritical conditions, for $We < We_{th}$ the crossing time t_{cross}^- is related to a physically relevant wave-propagation mechanism, and formally assumes negative values being associated to an upstream-travelling disturbance (Fig. 2.5(b)); two branches of spectrum will thus arise also for $We < We_{th}$.

Energy budgets equations

The derivation of the energy budgets which will be reported in Section 4.1 starts from the following Eqs. (2.26)-(2.27),

$$v'^* = \frac{\partial \ell'^*}{\partial t^*} + U^* \frac{\partial \ell'^*}{\partial x^*}, \quad (2.26)$$

$$\begin{aligned} \frac{\partial v'^*}{\partial t^*} + U^* \frac{\partial v'^*}{\partial x^*} = \\ \frac{2\sigma}{\rho_l H^*} \frac{\partial^2 \ell'^*}{\partial x^{*2}} + \frac{2\rho_a}{\pi \rho_l H^*} \int_0^{L^*} \frac{\partial^2 \ell'^*}{\partial t^{*2}} \ln \left| \frac{x^* - \xi^*}{L^*} \right| d\xi^* + \frac{\mu_l}{\rho_l} \frac{\partial^2 v'^*}{\partial x^{*2}}, \end{aligned} \quad (2.27)$$

which are the same as Eqs. (2.7)-(2.8) previously introduced in this section, except for the viscous term $\frac{\mu_l}{\rho_l} \frac{\partial^2 v'^*}{\partial x^{*2}}$ (μ_l is the liquid viscosity). Note that all the dimensional quantities, except the fluid material properties ($\rho_a, \rho_l, \mu_l, \sigma$), are denoted with the superscript \star .

Let us now define preliminarily the kinetic, E_c^* , and surface tension, E_σ^* , energies per unit length of the perturbed field (Olsson and Henningson [35]), respectively the quantities

$$E_c^* = \frac{\rho_l}{2} \int_0^L H^* v'^{*2} dx^*, \quad E_\sigma^* = \sigma \int_0^L \left(\frac{\partial \ell'^*}{\partial x^*} \right)^2 dx^*. \quad (2.28)$$

Multiplying Eq. (2.27) by $\rho_l H^* v'^*$ and integrating between 0 and L^* yield the evolution equation of the sinuous perturbation energy:

$$\begin{aligned} \rho_l \int_0^L H^* \frac{\partial v'^*}{\partial t^*} v'^* dx^* + \rho_l \int_0^L U^* H^* \frac{\partial v'^*}{\partial x^*} v'^* dx^* = \\ 2\sigma \int_0^L \frac{\partial}{\partial x^*} \left(\frac{\partial \ell'^*}{\partial x^*} \right) v'^* dx^* - \int_0^L \Delta p_a'^* v'^* dx^* + \\ \mu_l \int_0^L H^* \frac{\partial^2 v'^*}{\partial x^{*2}} v'^* dx^*. \end{aligned} \quad (2.29)$$

Integrating by parts and taking into account the kinematic condition (Eq. (2.26)), one can rearrange Eq. (2.29) in the form of an energy budget equation:

$$\begin{aligned} \frac{d}{dt^*} (E_c^* + E_\sigma^*) = & -\rho_l U^* H^* \frac{1}{2} [v'^{*2}]_0^L - \sigma \left[U^* \left(\frac{\partial \ell'^*}{\partial x^*} \right)^2 \right]_0^L + \\ & + 2\sigma \left[v'^* \frac{\partial \ell'^*}{\partial x^*} \right]_0^L - \int_0^L \Delta p_a'^* v'^* dx^* + \\ & - \sigma \int_0^L \frac{\partial U^*}{\partial x^*} \left(\frac{\partial \ell'^*}{\partial x^*} \right)^2 dx^* + \mu_l \int_0^L H^* \frac{\partial^2 v'^*}{\partial x^{*2}} v'^* dx^*. \end{aligned} \quad (2.30)$$

The time variation of the total energy, $E_t^* = E_c^* + E_\sigma^*$, is thus determined by:

- the exchanges of kinetic, E_c^* , and surface tension, E_σ^* , energies

through the domain boundaries (first and second terms at the right hand side of Eq. (2.30));

- the work per time unit of the external forces, namely the surface tension, σ , and the pressure difference, Δp_a^* , caused by the sheet velocity, v^* (third and fourth terms);

- a production term depending on the surface tension and related to the interaction between the perturbation, $\partial \ell^*/\partial x^*$, and the base flow stretching, $\partial U^*/\partial x^*$ (fifth term);

- a dissipation term related to liquid viscous effects (last term).

By employing the reference (dimensional) quantities previously introduced in this section (Eq. (2.12)), the dimensionless form of Eq. (2.30) is obtained:

$$\begin{aligned} \frac{d}{dt}(E_c + E_\sigma) &= -\frac{1}{2} [v^2]_0^1 - \frac{1}{2We} \left[U \left(\frac{\partial \ell}{\partial x} \right)^2 \right]_0^1 + \frac{1}{We} \left[v \frac{\partial \ell}{\partial x} \right]_0^1 \\ &+ \frac{2}{\pi} \frac{r_\rho}{\varepsilon} \int_0^1 \left(\int_0^1 \left(\frac{\partial v}{\partial t} - U \frac{\partial^2 \ell}{\partial t \partial x} \right) \ln |x - \xi| d\xi \right) v dx \\ &- \frac{1}{2We} \int_0^1 \frac{\partial U}{\partial x} \left(\frac{\partial \ell}{\partial x} \right)^2 dx + \frac{\varepsilon}{2Re} \int_0^1 \frac{\partial^2 v}{\partial x^2} \frac{v}{U} dx, \end{aligned} \quad (2.31)$$

where the superscript *prime* for the perturbation quantities has been suppressed. Note that in Eq. (2.31) the Reynolds number $Re = \frac{\rho_l U_i^* H_i^*}{2\mu_l}$ has been introduced, and that Eq. (2.26) has been used to simplify the second order time derivative in the pressure term. The dimensionless forms of the kinetic and surface tension energies read respectively

$$E_c = \frac{1}{2} \int_0^1 \frac{v^2}{U} dx, \quad E_\sigma = \frac{1}{2We} \int_0^1 \left(\frac{\partial \ell}{\partial x} \right)^2 dx. \quad (2.32)$$

Finally, the energy budget equation can be conveniently rearranged

in a more compact form:

$$\frac{d}{dt}(E_c + E_\sigma) = \Delta F_c + \Delta F_\sigma + L_\sigma + L_p + P + D, \quad (2.33)$$

where the following notations have been introduced:

$$\Delta F_c = -\frac{1}{2} [v^2]_0^1;$$

$$\Delta F_\sigma = -\frac{1}{2We} \left[U \left(\frac{\partial \ell}{\partial x} \right)^2 \right]_0^1;$$

$$L_\sigma = \frac{1}{We} \left[v \frac{\partial \ell}{\partial x} \right]_0^1;$$

$$L_p = \frac{2r_\rho}{\pi \varepsilon} \int_0^1 \left(\int_0^1 \left(\frac{\partial v}{\partial t} - U \frac{\partial^2 \ell}{\partial t \partial x} \right) \ln |x - \xi| d\xi \right) v dx;$$

$$P = -\frac{1}{2We} \int_0^1 \frac{\partial U}{\partial x} \left(\frac{\partial \ell}{\partial x} \right)^2 dx;$$

$$D = \frac{\varepsilon}{2Re} \int_0^1 \frac{\partial^2 v}{\partial x^2} v dx.$$

An energy budget equation for viscous liquid sheets was also derived by Lin *et al.* [36], in the framework of parallel flow, which allowed the authors to introduce a spatial Fourier decomposition in wavenumbers, and the energy budgets were evaluated per unit of wavelength. On the contrary, the energy budgets are here evaluated for the entire sheet extension, for comparisons with the global stability analysis developed in Section 3.2.

2.2 Two-phase mixing layers

Investigations of the physical mechanisms determining the interfacial instability in gas-liquid mixing layer flows date back to two centuries ago (Helmholtz [37], Thomson [38]). Typical industrial configurations where this kind of two-phase flow system can be encountered are air-blast atomizers, where a relatively low-speed liquid jet (density ρ_l , velocity U_l) is sheared by a faster parallel co-flowing gaseous phase (ρ_g , U_g), after the two streams meet downstream a separator (or splitter) plate at the end of an injection nozzle (Raynal *et al.* [39], Ben Rayana *et al.* [40], Eggers and Villermaux [41]); a sketch is reported in Fig. 2.6. The velocity difference existing between the two phases triggers a shear instability at the separating interface, leading to the generation of a liquid wave which is in turn affected by secondary instabilities, determining the formation, corrugation and finally breaking of ligaments into droplets (primary atomization). The last process leads to the generation of mutually interacting gas-droplets mixtures, in the so called secondary atomization, i.e. the last stage of this “instability cascade” (Marmottant and Villermaux [42]). Among many others, the application of such a flow configuration to fuel injection, where the quality of combustion and then pollutant generation crucially depend on the characteristics of the atomization process (Lefebvre [5]), makes the topic of primary interest for both automotive and aerospace industrial sectors, and it has been leading scientific research through extensive theoretical, experimental and numerical investigations for decades. However, a comprehensive understanding of the physical mechanisms governing the different stages of the instability cascade has not been achieved yet, making the modelling and control of two-phase mixing layer flows still challenging tasks nowadays. An overview of selected works directly relevant to the aim of this study, concerning planar air-water mixing layers, is reported in the following Sections 2.2.1-2.2.3. Motivations and objectives of the work on this research line are further highlighted in Section 2.2.4.

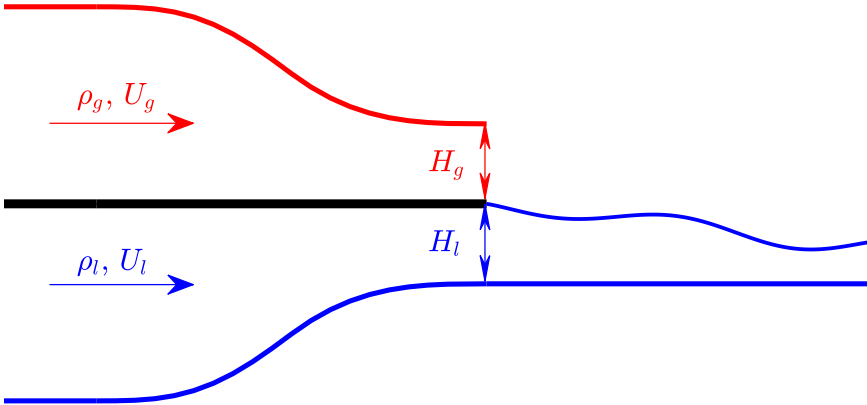


Figure 2.6. Sketch of the gas-liquid mixing layer flow developing past a splitter plate (black). Details of gas (red) and liquid (blue) channels are highlighted.

2.2.1 Local linear stability theory

The gas-liquid interfacial wave dynamics in proximity of the injection section (i.e., in the near-field region) has been conventionally investigated through linear stability analysis of small perturbations superposed on a properly selected base flow, within the parallel (or quasi-parallel) flow approximation, with the aim of determining the most unstable frequency and wavelength of the instability. First investigations were carried out assuming inviscid regime for both the base flow and the evolution of perturbations (Marmottant and Villermaux [42], Eggers and Villermaux [41], Matas *et al.* [43]). Later on, Matas *et al.* [43] included a velocity defect in the base flow (i.e. they considered a viscous base flow, see Fig. 2.7, where y is the spatial coordinate normal to the splitter plate direction x) to mimic the splitter plate effect on the near-field flow region. They found that accounting for the velocity defect is crucial to obtain reasonable quantitative agreement between inviscid stability analysis predictions and experimental measurements of the interface oscillations frequency, although the spatial growth rate is significantly underestimated with this ap-

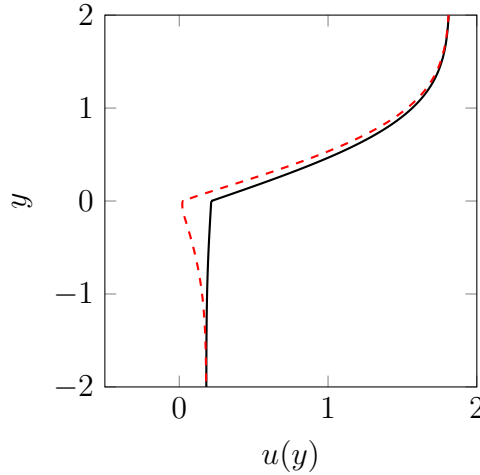


Figure 2.7. Typical mixing layer base flow velocity profile with (red dashed curve) and without (black curve) velocity defect. The gas-liquid interface is located at $y = 0$. Adapted from Fuster *et al.* [48].

proach. On the other hand, a good quantitative match between measured and theoretically predicted spatial growth rates of the unstable wave can be obtained including viscous effects in the temporal linear stability analysis, i.e. by formulating an Orr-Sommerfeld problem for the two-phase shear layer (Yecko *et al.* [44], Boeck and Zaleski [45]), but then frequencies become overestimated.

2.2.2 Numerical-experimental comparisons

To obtain a more satisfactory and systematic agreement between stability analysis predictions and experimental measurements, Otto *et al.* [46] developed a spatio-temporal linear stability approach, improving the match between theoretical and experimental values for both frequency and spatial growth rate. Moreover, their method provided for the first time evidence of a transition from convective to absolute instability (Huerre and Monkewitz [47]) for the injection conditions reported in the work by Matas *et al.* [43], with experi-

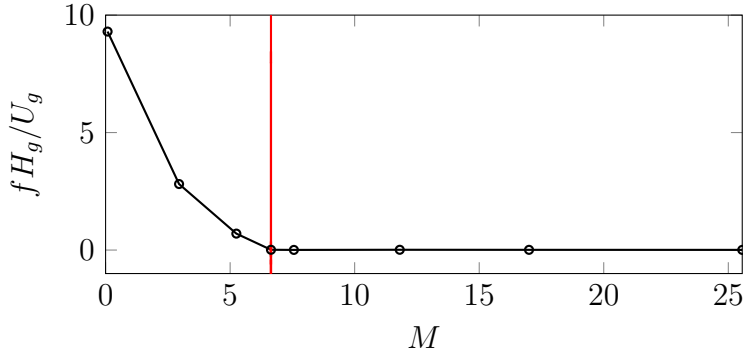


Figure 2.8. Numerical prediction of the most unstable frequency f as a function of M in convective ($M < M_c$) and absolute ($M > M_c$) instability regimes. The red line represents the convective-absolute transition threshold $M = M_c$. Adapted from Fuster *et al.* [48].

mental data spanning both the instability regimes. This aspect was further clarified by Fuster *et al.* [48], who showed that the transition from convective to absolute unstable behaviour of the flow crucially depends on the dynamic pressure ratio parameter $M = \rho_g U_g^2 / (\rho_l U_l^2)$ (Fig. 2.8). In particular, the absolute instability regime found by the authors was strongly affected by the splitter plate thickness separating the two streams before the injection, and Bozonnet *et al.* [49] pointed out that it was determined by a resonance mechanism between an upstream-travelling surface capillary wave and the main downstream-oriented shear wave. In this respect, Matas *et al.* [50] outlined that surface tension becomes the physical mechanism triggering the flow absolute instability for a sufficiently low interfacial velocity. It is interesting to note that a surface tension-induced global instability was also found by Tammissola *et al.* [51] for two-dimensional planar jet and wake flows of two immiscible fluids with different velocities, which has been recently confirmed by nonlinear two-phase direct numerical simulations (Schmidt *et al.* [52]).

2.2.3 Physical mechanisms of instability

Apart from surface tension acting at the separating fluids interface, another physical mechanism has been recently discovered to play a key role in triggering the two-phase mixing layer absolute instability: the confinement effect, represented by the finite thicknesses of gas and liquid streams (Matas [53]). As explained in the more general framework of jet/wake flows by Juniper [54, 55] and retrieved for an air-water mixing layer configuration in the combined experimental, theoretical and numerical analysis by Bozonnet *et al.* [49], confinement is able to determine absolute instability. This is possible through a resonance mechanism taking place between velocity perturbations cross-stream spatial oscillations within the gaseous phase, which are induced by the streamwise liquid wave development, and the confinement length (i.e. the gas stream injection thickness H_g). While both the convective mode of instability (triggered by viscosity differences across the interface, see Yih [56] and Boeck and Zaleski [45]) and the surface tension-induced absolute mode (Fuster *et al.* [48]) are characterized by relatively small wavelengths, the confinement absolute mode reveals a smaller wave number, which better matches most of the experimental conditions (Matas [53]). A map of the different mixing layer flow regimes has been recently proposed by Matas *et al.* [50], outlining that the velocity defect induced in the near-field region by the splitter plate has an impact on both the surface tension and confinement induced absolute instability.

2.2.4 Towards global stability analysis

The literature review summarized above reveals that one of the most challenging requests to enhance the agreement between the theoretical and experimental findings is the accurate knowledge of the relevant flow field. Numerical simulations of the flow performed both in three (Agbaglah *et al.* [57], Ling *et al.* [58, 59]) and two-dimensional (Fuster *et al.* [48], Bozonnet *et al.* [49]) scenarios have shown that the two-phase mixing layer is characterized by strong spatial variations

in the near-field region, where the flow is basically two-dimensional. The (locally) parallel flow assumption usually done for linear stability calculations is thus generally not accurate. As pointed out by Bozonnet *et al.* [49], a global stability analysis, or several local stability studies, should be performed on linear and/or nonlinear mean flows to improve the capability to predict the flow dynamics in most of the experimental conditions.

As a matter of fact, the two-phase mean flow characterization of such a mixing layer configuration, and more in general of free surface flows in presence of a wavy interface, poses severe challenges from an experimental point of view (Sanchis and Jensen [60], Ayati *et al.* [61], Andr e and Bardet [62], Buckley and Veron [63], Kosiwczuk *et al.* [64]). In most cases, when studying interfacial phenomena through particle image (PIV) or particle tracking (PTV) velocimetry, the illuminating light sheet is oriented perpendicular to the interface, eventually causing undesirable reflections in the form of bright spots. Dynamic masking techniques can be used to detect the separating fluids interface in such cases, as done in Sanchis and Jensen [60] by applying the Radon transform algorithm to PIV images of a stratified air-water flow in a circular pipe, obtaining also the velocity field within the liquid phase. The large difference in refractive index between phases can also lead to glare and prevent optical access. Moreover, particular care must be taken to ensure that the flow tracers do not modify interface properties such as surface tension and viscosity. Finally, the huge difference in the two phases mean injection velocities (about two order of magnitude in mixing layer configurations of practical interest, where the water stream is slower) makes the simultaneous PIV characterization of the phases a severe issue when using a single-laser single-camera measuring configuration. Combined particle image velocimetry and laser-induced fluorescence systems have been recently used to perform the interface detection and mean flow measurements in the gaseous phase over wind driven surface waves (Buckley and Veron [63]), while both phases of a stratified air-water flow in a horizontal pipe (Ayati *et al.* [61]) and for a turbulent spray mixture

(Kosiwczuk *et al.* [64]) have been characterized by means of sophisticated multi-camera ([64], [61]) and multi-laser ([63]) instrumentation. PIV measurements of the mean gaseous velocity field have also been performed by Descamps *et al.* [65] for a planar air-water mixing layer configuration.

As an important step to assist future global stability studies, this work provides a detailed experimental characterization of the two-dimensional air-water wake/mixing layer flow developing downstream of a splitter plate, which initially separates the two currents. The experiments are designed in such a way that the ratio of the plate to the air vorticity thickness is greater than one. By means of a proper light sheet optics arrangement, two-components time-resolved particle image velocimetry (TR-PIV) measurements are performed simultaneously in air and water streams (Section 3.5.2). The two-phase mean (time-averaged) and unsteady features of the flow are thus characterized for several injection conditions, spanning both the convective and the absolute instability regimes discussed above. Although several studies reported in literature show the possibility to apply PIV methods to mixing layer flows (Descamps *et al.* [65]), to more general interfacial flows (Sanchis and Jensen [60], Ayati *et al.* [61], André and Bardet [62], Buckley and Veron [63], Li *et al.* [66]), and even to turbulent spray mixtures (Kosiwczuk *et al.* [64]), a TR-PIV characterization of a planar mixing layer performed simultaneously in gas and liquid phases is still lacking in literature, and therefore represents a major novel contribution of the present investigation.

Chapter 3

Numerical and experimental methodologies

The present chapter is dedicated to the numerical and experimental investigation approaches employed in this work. Direct numerical simulation and linear stability analysis for two-phase flows are first described (Sections 3.1 and 3.2), with emphasis on the flow configurations introduced in Chapter 2. The modal decomposition techniques applied to numerical data are then presented (Section 3.3), and the experimental methodologies finally discussed in Sections 3.4 and 3.5.

3.1 Direct numerical simulations

The accurate prediction of multiphase flows dynamics is of crucial industrial and scientific interest, representing a problem into which computer simulations are giving unprecedented insights nowadays (Tryggvason, Scardovelli and Zaleski [1]). Direct numerical simulation of two-phase flows based on the so called *one-fluid* formulation is briefly recalled hereafter, providing examples inspired from results later discussed in Section 4.1 regarding gravitational liquid sheet flows.

3.1.1 One-fluid formulation

The mathematical modelling of the interface separating immiscible fluids is a crucial aspect to obtain accurate numerical predictions of multiphase flows behaviour. A modern approach consists in deriving the governing equations for two-phase flows following the single-phase formulation (Scardovelli and Zaleski [67]). Given the assumption of incompressible flow, and restricting the attention to a two-dimensional case within the xy Cartesian space to simplify notations, continuity and momentum equations in the one-fluid formulation read (in Einstein notation) as

$$\frac{\partial u_i}{\partial x_i} = 0, \quad (3.1a)$$

$$\rho \left(\frac{\partial u_i}{\partial t} + u_j \frac{\partial u_i}{\partial x_j} \right) = -\frac{\partial p}{\partial x_i} + \frac{\partial}{\partial x_j} \left[\mu \left(\frac{\partial u_i}{\partial x_j} + \frac{\partial u_j}{\partial x_i} \right) \right] + F_S, \quad (3.1b)$$

with $(u_1, u_2)^T = (u, v)^T$ representing the velocity vector, p the pressure, $(x_1, x_2)^T = (x, y)^T$ the spatial coordinates, ρ the density, μ the dynamic viscosity. The term F_S represents the surface tension force acting at the separating fluids interface, and it reads as $F_S = \sigma \kappa n_i \delta_S$, where κ is the mean interface curvature, $(n_1, n_2)^T = (n_x, n_y)^T$ the outward pointing normal vector, and σ the surface tension coefficient.

The phase boundary is the only region of the domain where the term F_S is different from zero. Indeed δ_S is a Dirac distribution function, equal to 1 at the interface, 0 otherwise. Therefore, density and viscosity fields are evaluated as

$$\rho = \rho_g + (\rho_l - \rho_g)C, \quad (3.2a)$$

$$\mu = \mu_g + (\mu_l - \mu_g)C, \quad (3.2b)$$

where subscripts g and l respectively refer to the gas and liquid interacting flow phases, and $C(x, y, t)$ is the volume fraction, a (dimensionless) Heaviside function equal to the liquid-to-total volume ratio. Computational cells where $C = 1$ are located in the liquid phase and

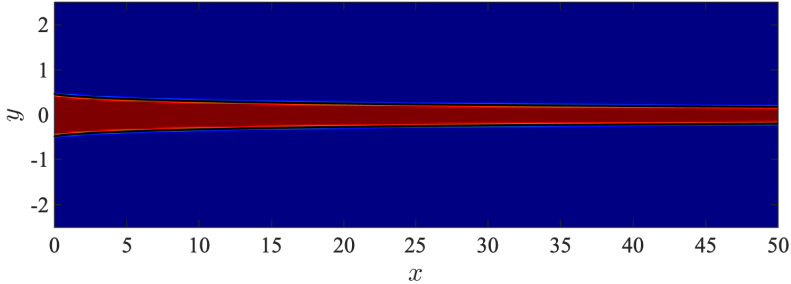


Figure 3.1. Volume fraction $C(x, y)$ contour representation of a two-dimensional liquid jet injected in still air: $C = 1$ (red region) in liquid phase ($\rho = \rho_l$), 0 (blue region) in the gaseous ambient ($\rho = \rho_g$).

cells with $C = 0$ are situated in the gaseous phase; $0 < C < 1$ for cells crossing the interface (see Fig. 3.1).

An additional equation is required to localize the interface, namely the volume fraction advection equation

$$\frac{\partial C}{\partial t} + \frac{\partial C u_i}{\partial x_i} = 0, \quad (3.3)$$

which, coupled with the system (3.1a)-(3.1b), closes the problem.

3.1.2 Volume-of-fluid method in BASILISK

The equations introduced in Section 3.1.1 are numerically solved using the finite volume method in BASILISK, an open-source code suitable for the solution of partial differential equations on adaptive Cartesian meshes, originally developed by Popinet (basilisk.fr). The salient features of the code are briefly summarized hereafter: for a detailed description of the implemented numerical schemes, the reader can refer to Popinet [68, 69].

The governing equations are solved, as is usual for incompressible flows, by the so-called projection method, where a temporary velocity field is firstly found by ignoring the pressure gradient, and, in the

second step, it is projected onto a space of divergence-free velocity fields by adding the appropriate pressure gradient information. The interface is tracked with the Volume-Of-Fluid (VOF) method [70], solving Eq. (3.3) for the volume fraction advection. With the velocity field known, a one-dimensional scheme is used to advect the volume fraction field along each coordinate direction. The local volume fraction fluxes are calculated from the local velocities, and the geometric reconstruction of the interface is realized in each cell by knowledge of the corresponding volume fraction value. The interface in each cell is a segment described by $n_1x_1 + n_2x_2 = c$, where n_i is the partial derivative of C with respect to the corresponding spatial coordinate x_i , and c represents the shortest distance from the segment to the current coordinate below it. In practice, an analytical formula can be used to determine c (Scardovelli and Zaleski [67]).

The surface tension term in Eq. (3.1b) is evaluated using a balanced Continuum Surface Force (CSF) formulation (see Francois *et al.* [71]), which adopts a height-function method to estimate the interface curvature with second-order accuracy (Cummins *et al.* [72]). A momentum conserving scheme is used for the advection term in Eq. (3.1b) for small density ratios (e.g. air/water flow) to avoid numerical instabilities.

Apart from a classic uniform structured grid, BASILISK allows the generation of a hierarchical quad-tree adaptive grid structure (an example is shown in Fig. 3.2) to dynamically refine the grid at each time step according to user-defined adaptation criteria. The dynamic grid helps the user to retain a high resolution in the flow field region of interest, while simultaneously allowing for coarse resolution away from it, that decreases the computational cost of the entire simulation. The refinement of a generic grid cell is performed at each iteration reducing by one and then increasing again its grid level, resulting in a down- and up-sampling of the stored scalar fields. Therefore, the error $\chi = \|\phi - \phi^+\|$ between the original ϕ and the up-sampled ϕ^+ field can be estimated; the cell is refined if $\chi > \beta$ and coarsened if $\chi < \beta$, where β is the error threshold of the specific scalar field. For

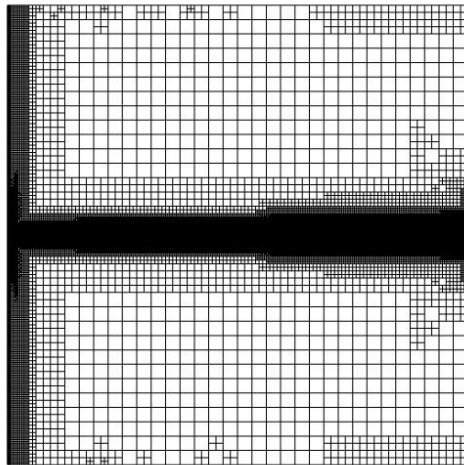


Figure 3.2. Adaptive grid structure employed to obtain the numerical solution shown in Fig. 3.1.

a detailed explanation of the adaptive grid-strategy implemented in BASILISK, the reader is referred to van Hooft *et al.* [73].

3.2 Linear stability analysis

To determine the asymptotic behaviour of a flow system, and to provide comparisons with results arising from direct numerical simulations and experiments, a boundary value eigenvalues problem can be formulated. For the case of a gravitational liquid sheet flow (Section 2.1), this has been carried out starting from Eqs. (2.13)-(2.14) of the linear inviscid one-dimensional theoretical model presented in Section 2.1.3.

By eliminating the second time derivative from Eq. (2.14), one

obtains the following system

$$\frac{\partial v}{\partial t} - RU \int_0^1 \left(\frac{\partial v}{\partial t} - U \frac{\partial^2 \ell}{\partial t \partial x} \right) \ln |x - \xi| d\xi = -U \frac{\partial v}{\partial x} + \frac{U}{We} \frac{\partial^2 \ell}{\partial x^2}, \quad (3.4)$$

$$\frac{\partial \ell}{\partial t} = v - U \frac{\partial \ell}{\partial x}, \quad (3.5)$$

where the substitution $1/H = U$ (Eq. (2.16)) has been made in Eq. (3.4). The classic global temporal modes position is then enforced assuming the following form of the disturbances:

$$\ell(x, t) = \hat{\ell}(x) \cdot e^{\lambda t}, \quad (3.6)$$

$$v(x, t) = \hat{v}(x) \cdot e^{\lambda t}, \quad (3.7)$$

where $\hat{\ell}$ and \hat{v} are eigenfunctions and λ is the complex eigenvalue. This permits one to recast the governing equations into the following matrix form

$$\lambda \mathcal{M} \begin{pmatrix} \hat{v} \\ \hat{\ell} \end{pmatrix} = \mathcal{A} \begin{pmatrix} \hat{v} \\ \hat{\ell} \end{pmatrix}, \quad (3.8)$$

where the temporal operator is the block matrix

$$\mathcal{M} \equiv \begin{pmatrix} \mathcal{I} - RU \cdot \mathcal{I} \mathcal{N} \mathcal{T} & RU \cdot \mathcal{I} \mathcal{N} \mathcal{T} \cdot U \cdot \mathcal{D} \\ \mathcal{O} & \mathcal{I} \end{pmatrix},$$

and the spatial operator is the block matrix

$$\mathcal{A} \equiv \begin{pmatrix} -U \cdot \mathcal{D} & U/We \cdot \mathcal{D}^2 \\ \mathcal{I} & -U \cdot \mathcal{D} \end{pmatrix},$$

with \mathcal{I} denoting the identity operator, $\mathcal{O} = 0 \cdot \mathcal{I}$, \mathcal{D} (\mathcal{D}^2) is the first (second) spatial derivative operator, and $\mathcal{I} \mathcal{N} \mathcal{T}$ represents the

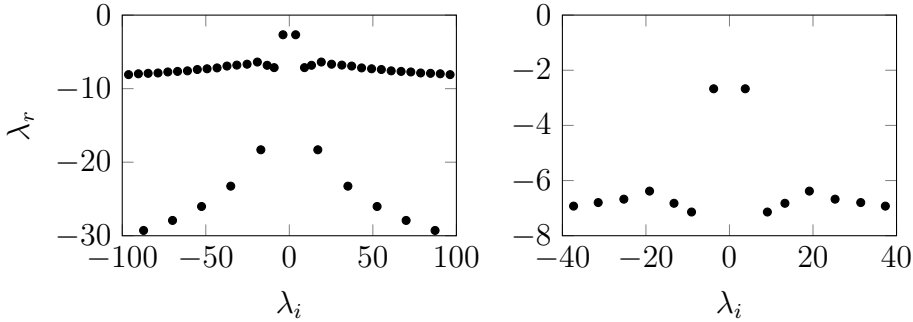


Figure 3.3. Typical eigenvalue spectrum obtained from Eq. (3.8) (left panel) in supercritical conditions ($We > 1$), with zoom around the least stable part (right panel).

integral $\int_0^1(\cdot) \ln|x - \xi| d\xi$.

Eigenvalues and eigenfunctions are numerically computed by a Chebyshev collocation method in the MATLAB environment, with both differential and integral terms being spectrally accurate. As anticipated in Section 2.1.3, a countable set of separated modes is found in the spectrum, which in supercritical conditions ($We > 1$) appears clustered in two separated branches, each one being characterized by eigenvalues with different real λ_r (i.e. growth rate) and evenly spaced imaginary λ_i (i.e. frequency) coefficients; an example is reported in Fig. 3.3. In supercritical regime, two boundary conditions are required at the inlet section to close the system (3.8), i.e.

$$\hat{\ell}(0) = 0, \quad (3.9)$$

$$\left. \frac{\partial \hat{\ell}}{\partial x} \right|_0 = 0. \quad (3.10)$$

On the contrary, for subcritical cases, $We < 1$, due to the upstream directed wave characteristic velocity $U - \sqrt{U/We}$ (see again Section 2.1.3), the condition $\hat{\ell} = 0$ can only be retained at the inlet

boundary. On the other hand, the system (3.8) becomes singular, and the condition removing the singularity constitutes the required second constraint to calculate the spectrum in subcritical regime ($We < 1$). This aspect is detailed in Appendix A.1, together with the proper modifications required to account for viscous effects within the liquid sheet (Appendix A.2).

3.3 Data-driven decomposition techniques

The comprehension of complex flows takes advantage from the recognition of physically important features, associated with modes characterizing the spatial topology. Modes can also be used to construct reduced-order modelling and to control the flow itself as shown in Schmidt and Colonius [74]. Several techniques have been developed to extract the main flow features, as reported in the reviews by Rowley and Dawson [75], Taira *et al.* [76], Towne *et al.* [77]. Proper orthogonal decomposition (POD, Berkooz *et al.* [78]), Spectral POD (Towne *et al.* [77]), and dynamic mode decomposition (DMD, Schmid [79] and Tu *et al.* [80]) are the most used techniques for this purpose. In particular, the POD provides the minimal number of basis functions (the modes) to capture as much energy as possible, the SPOD allows one to characterize the spatial and temporal evolution of coherent structures through the decomposition in the frequency domain of the flow in various modes, ordered by their energy content, whereas DMD is based on the eigendecomposition of a best-fit linear operator that approximates the dynamics present in the data.

Recent works on this topic have been carried out to extract the features of swirling coaxial jets (Kadu *et al.* [81]) and of the flow around a square-section building (Zhang *et al.* [82]), to characterize the dynamics of flows past finite curved cylinders by Chiatto *et al.* [83], and the dynamics of actively controlled flow past a backward facing ramp by the same authors [84]. In the present context, the SPOD and DMD techniques are applied to numerical data of

two-dimensional liquid sheets flow fields computed by means of the two-phase code BASILISK (Section 3.1.2).

3.3.1 Spectral proper orthogonal decomposition

Defining the fluctuation of a stochastic field $\mathbf{q}(\mathbf{x}, t)$, with \mathbf{x} the position and t the discrete time, as

$$\mathbf{q}'(\mathbf{x}, t) = \mathbf{q}(\mathbf{x}, t) - \bar{\mathbf{q}}(\mathbf{x}), \quad (3.11)$$

where $\bar{\mathbf{q}} = E \{ \mathbf{q}(\mathbf{x}, t) \}$ is the ensemble average (and $E \{ \cdot \}$ the expectation operator), in accordance with the works by Towne *et al.* [77], the SPOD decomposition provides the best representation of $\mathbf{q}'(\mathbf{x}, t)$, with the least number of modes, in the space-time domain (Schmidt and Colonius [74]).

The SPOD modes satisfy the eigenvalue problem of the cross-spectral density tensor \mathbf{S} , and are computed with Welch method [74]. Accordingly, the flow snapshots (each snapshot representing a flow field realization at a given time instance) are grouped in N_b blocks of equal length N_f (N_f being the number of snapshots per block): $\mathbf{Q}^{(j)} = [\mathbf{q}_1^{(j)}, \mathbf{q}_2^{(j)}, \dots, \mathbf{q}_{N_f}^{(j)}]$, with $j = 1, \dots, N_b$. For clarity, the superscript $\{ \cdot \}'$ (which represents the fluctuation) has been removed. Each block overlaps with adjacent ones (a 50% overlap has been used herein).

For each block j , the weighted discrete Fourier transform $\hat{\mathbf{Q}}^{(j)} = \mathcal{F} \{ \mathbf{Q}^{(j)} \mathbf{W}_T \}$ (where \mathbf{W}_T is the matrix of window weights) is first computed (Welch [85]). Then all Fourier transform realizations at the same k^{th} frequency are collected in matrices as $\hat{\mathbf{Q}}_k$, which are defined as $\hat{\mathbf{Q}}_k = [\hat{\mathbf{q}}_k^{(1)}, \hat{\mathbf{q}}_k^{(2)}, \dots, \hat{\mathbf{q}}_k^{(N_b)}]$, and the cross-spectral density tensor $\mathbf{S}_k = \hat{\mathbf{Q}}_k \hat{\mathbf{Q}}_k^*$ is computed one frequency at a time, thus obtaining the SPOD modes (Φ_k) and eigenvalues (Λ_k).

Once the SPOD modes have been identified, a low rank reconstruction of the fluctuation field can be obtained through the inverse

weighted (discrete) Fourier transform $\mathbf{Q}^{(j)} = \mathcal{F}^{-1} \left\{ \hat{\mathbf{Q}}^{(j)} \mathbf{W}_T^{-1} \right\}$ to come back in the time domain. This approach was recently presented by Nekkanti and Schmidt [86] and applied by Chiatto *et al.* [84] to reconstruct the flow past a backward facing ramp (with and without active flow control) considering a limited number of SPOD modes. More in detail, the Fourier realizations matrix is expressed as $\hat{\mathbf{Q}}_k = \mathbf{\Phi}_k \mathbf{\Lambda}_k \mathbf{\Psi}_k^*$, where $\mathbf{\Psi}_k^*$ is the matrix containing the eigenvectors of $\hat{\mathbf{Q}}_k^* \hat{\mathbf{Q}}_k$. For low rank reconstruction only r eigenvalues are retained and $\hat{\mathbf{Q}}_k$ is approximated as

$$\hat{\mathbf{Q}}_k \approx \tilde{\mathbf{\Phi}}_k \tilde{\mathbf{\Lambda}}_k \tilde{\mathbf{\Psi}}_k^*, \quad (3.12)$$

where $\tilde{\mathbf{\Phi}}_k$ and $\tilde{\mathbf{\Psi}}_k$ are, respectively, the first r columns of $\mathbf{\Phi}_k$ and $\mathbf{\Psi}_k$.

As previously stated, once the reconstruction procedure of the $\hat{\mathbf{Q}}_k$ has been completed, the Fourier realizations are re-arranged into the blocks form $\hat{\mathbf{Q}}^{(j)} = \left[\hat{\mathbf{q}}_1^{(j)}, \hat{\mathbf{q}}_2^{(j)}, \dots, \hat{\mathbf{q}}_{N_f}^{(j)} \right]$, and the snapshots in the time domain are obtained through an inverse weighted Fourier transform. Particular attention needs to be paid to avoid the ambiguity for the snapshots belonging to two different blocks. To solve the ambiguity, as proposed by Nekkanti and Schmidt [86], the snapshot with the higher windowing weight $w(j)$ is chosen.

3.3.2 Dynamic mode decomposition

The DMD technique is applied in this work to VOF simulations (Section 3.1) data of gravitational liquid sheet flows, to obtain insights into the two-dimensional global spectrum of the system, and to give comparisons with results of a classic linear stability analysis performed on the simplified one-dimensional curtain model (Section 3.2).

In the framework of two-phase flows, it is convenient to define the state vector \mathbf{q} (see Eq. (3.11)) by stacking the velocity components and the volume fraction at every time instance. With this assumption, the governing equations (system (3.1a)-(3.1b) and Eq. (3.3))

can be recast in the form of a classic first order dynamical system,

$$\dot{\mathbf{q}} = f(\mathbf{q}), \quad (3.13)$$

with f being a non-linear operator depending on \mathbf{q} . By means of the decomposition represented by Eq. (3.11), it is possible to obtain the linearized form of Eq. (3.13):

$$\dot{\mathbf{q}}' = \mathbf{L}_{\bar{\mathbf{q}}}\mathbf{q}', \quad (3.14)$$

with $\mathbf{L}_{\bar{\mathbf{q}}}$ being the Jacobian operator evaluated at the base flow.

The computation of $\mathbf{L}_{\bar{\mathbf{q}}}$ is numerically prohibitive; in the hypothesis of small perturbations, Theofilis [87] and Bagheri *et al.* [88] showed that its evaluation can be simplified when based on instantaneous \mathbf{q}' fields (i.e. snapshots), obtained by a high-order solver (in the present case, the code BASILISK). Moreover, following Gomez *et al.* [89] a proper set of snapshots is constructed through the Fréchet derivative:

$$\dot{\mathbf{q}}' = \mathbf{L}_{\bar{\mathbf{q}}}\mathbf{q}' = \left. \frac{\partial f(\mathbf{q})}{\partial \mathbf{q}} \right|_{\bar{\mathbf{q}}} \mathbf{q}' \approx f(\bar{\mathbf{q}} + \mathbf{q}') - f(\bar{\mathbf{q}}), \quad (3.15)$$

that when integrated from a generic time instance $t = t_n$ to $t = t_n + \Delta t$ leads to

$$\mathbf{q}'_{n+1} = e^{\mathbf{L}_{\bar{\mathbf{q}}}\Delta t} \mathbf{q}'_n = \mathbf{A}\mathbf{q}'_n \approx \int_{t_n}^{t_n+\Delta t} f(\bar{\mathbf{q}} + \mathbf{q}') dt - \int_{t_n}^{t_n+\Delta t} f(\bar{\mathbf{q}}) dt. \quad (3.16)$$

The inspection of Eq. (3.16) highlights the linear relationship between two subsequent snapshots \mathbf{q}'_n and \mathbf{q}'_{n+1} through the matrix \mathbf{A} . More in details, $\mathbf{A}\mathbf{q}'_n$ is approximated by the difference between the perturbed and the base flow fields variation. The base flow $\bar{\mathbf{q}}$ has been assumed coincident with the flow field after an evolving time $t_0 = 6t_r$, with $t_r = L^*/U_i^*$ (see Eq. (2.12) in Section 2.1.3). The perturbed field has been obtained by adding a purely random perturbation to the base flow at $t = t_0$. In particular, the perturbation

is modelled as white noise, with an amplitude equal to $0.01U_i^*$ for the velocity components (u and v), and 0.01 for the volume of fraction in the interface region.

The matrix \mathbf{A} has been obtained by means of the DMD technique (Ranjan *et al.* [90]), which decomposes time-resolved data into modes with distinct frequencies and growth rates. Considering a standard DMD algorithm (Tu *et al.* [80]), it is convenient to define a physically meaningful norm for \mathbf{q}' related to the fluctuations energy of the velocity components and of C' . In particular, the norm is $\|\mathbf{q}'\|_{\mathbf{P}}^2 = \mathbf{q}'^* \mathbf{P} \mathbf{q}'$, where $(\cdot)^*$ denotes the conjugate transpose operator and \mathbf{P} represents a weight matrix, whose elements have been computed according to Chu [91]. This provides the following energy norm:

$$E = \int_{\Omega} \left[\bar{\rho} (u'^2 + v'^2) + (\bar{u}^2 + \bar{v}^2) \frac{\Delta \rho^2}{\bar{\rho}} C'^2 \right] d\Omega, \quad (3.17)$$

being Ω the entire flow field region. In this way, \mathbf{P} takes into account the integration quadratures and appropriate scaling of heterogeneous variables of the problem. Finally, a Cholesky decomposition $\mathbf{P} = \mathbf{F}^* \mathbf{F}$, has been computed to obtain $\|\mathbf{q}'\|_{\mathbf{P}}^2 = \mathbf{q}'^* \mathbf{F}^* \mathbf{F} \mathbf{q}' = \|\mathbf{F} \mathbf{q}'\|_2^2$. The DMD algorithm considers the snapshots ($\mathbf{F} \mathbf{q}'_k$) collected as columns in the matrices \mathbf{Q}_1 and \mathbf{Q}_2 ,

$$\mathbf{Q}_1 = \mathbf{F} \begin{bmatrix} | & & | & & | \\ \mathbf{q}'_1 & \cdots & \mathbf{q}'_k & \cdots & \mathbf{q}'_M \\ | & & | & & | \end{bmatrix}, \quad (3.18)$$

$$\mathbf{Q}_2 = \mathbf{F} \begin{bmatrix} | & & | & & | \\ \mathbf{q}'_2 & \cdots & \mathbf{q}'_{k+1} & \cdots & \mathbf{q}'_{M+1} \\ | & & | & & | \end{bmatrix}, \quad (3.19)$$

where $\mathbf{Q}_1, \mathbf{Q}_2 \in \mathbb{R}^{N \times M}$, N being the cardinality of the state vector \mathbf{q}' and M the number of snapshots. In this view, the linear operator approximates the temporal dynamics of the data such that

$$\mathbf{Q}_2 \approx \Theta \mathbf{Q}_1. \quad (3.20)$$

It is worth noting that the matrix Θ is related to the matrix \mathbf{A} by $\Theta = \mathbf{F}\mathbf{A}\mathbf{F}^{-1}$; it shares the same eigenvalues of \mathbf{A} and its eigenvectors are scaled by \mathbf{F} . Moreover, snapshots collected within the matrices \mathbf{Q}_1 and \mathbf{Q}_2 can also refer to several simulations with different random initializations (Herrmann *et al.* [92]). The present analysis considers 200 simulations, each one of 200 snapshots, with $\Delta t = 0.003 t_r$.

The leading coherent structures (namely the DMD modes) are evaluated through the SVD decomposition of \mathbf{Q}_1 , according to which $\mathbf{Q}_1 = \mathbf{U}\Sigma\mathbf{V}^*$. In this way, Eq. (3.20) becomes $\Theta = \mathbf{Q}_2\mathbf{V}\Sigma^{-1}\mathbf{U}^*$, which generally requires a large computational cost. To mitigate this effort, it is convenient to introduce the matrix $\tilde{\Theta} = \mathbf{U}^*\mathbf{Q}_2\mathbf{V}\Sigma^{-1}$ that shares the same non-zero eigenvalues of Θ (and of \mathbf{A}), but it has a lower dimension and thus requires a reduced numerical cost. Finally, the DMD modes Φ are retrieved as $\Phi = \mathbf{Q}_2\mathbf{V}\Sigma^{-1}\mathbf{W}$, with \mathbf{W} being the matrix of eigenvectors of $\tilde{\Theta}$. The dimensionless spectrum of the underlying linear operator $\mathbf{L}_{\bar{q}}$ is thus computed as

$$\lambda_k = \lambda_r + i\lambda_i = \frac{\log(\mu_k)}{\Delta t} 2\pi t_r, \quad (3.21)$$

where μ_k is the k^{th} (complex) eigenvalue of $\tilde{\Theta}$, λ_r the growth rate, and λ_i the frequency.

The convergence and the saturation of the DMD algorithm are evaluated by means of the L_2 norm of the residual \mathbf{r} . Indeed, considering the qr factorization of the snapshots matrix ($\mathbf{Q}_1 = \mathbf{S}\mathbf{R}$) the residual \mathbf{r} is defined as:

$$\mathbf{r} = \mathbf{q}'_{M+1} - \mathbf{Q}_1\mathbf{R}^\dagger\mathbf{S}^*\mathbf{q}'_{M+1}, \quad (3.22)$$

in which \mathbf{q}'_{M+1} is the last snapshot and $(\cdot)^\dagger$ is the pseudoinverse operator. Note that \mathbf{r} is the reconstruction error field of the last snapshot \mathbf{q}'_{M+1} , and it simply represents how well the last snapshot can be approximated as a linear combination of the first M ones.

3.4 Curtain flows experimental setup

The experimental setup realized to perform curtain flows experiments is a remake of that described in detail by de Luca and Meola [24]; a sketch is reported in Fig. 3.4. Starting from an overflow tank and through flexible tubes, the liquid fluid goes into a stagnation chamber equipped with a perforated plate, and it is ejected by means of a stainless steel nozzle. The flow rate is controlled with a regulating valve and a flow meter. Two lateral Plexiglas plates, placed at each end of the nozzle, facilitate the formation of the sheet and guarantee the two-dimensionality of the base motion; details of the experimental sheet and the nozzle cross-section are reported on the right in Fig. 3.4. Particular care is taken to eliminate any vibration source and to control the ambient air to be quite still. The liquid is collected in a reservoir below the test section and then pumped back to the tank. Tests are carried out on liquid sheets issuing from a nozzle with a horizontal exit section, 180 mm long, having discharge width H_{in}^* equal to 2 mm.

To enhance the optical detection of the sheet oscillations as described in Section 3.4.1, the working fluid was obtained by diluting a very small amount of white ink (Lefranc & Bourgeoi coloured drawing ink) in water, so as to obtain a low-concentration aqueous solution with 1% of ink. The characterization of the solution has been carried out by measuring the fluid properties: the nominal (or bulk) surface tension has been obtained by means of a tensiometer through the pendant drop method, and it is equal to 0.0605 N/m; the fluid density is 0.998 Kg/m³, and a falling-sphere viscometer has provided a value of the dynamic viscosity equal to $1.05 \cdot 10^{-3}$ Pa·s. The temperature in the room was stable and equal to 20° during the experiments.

3.4.1 Natural oscillation frequency detection

Time-resolved measurements of the sheet oscillations in the lateral plane xy (normal to the nozzle spanwise direction z) are carried

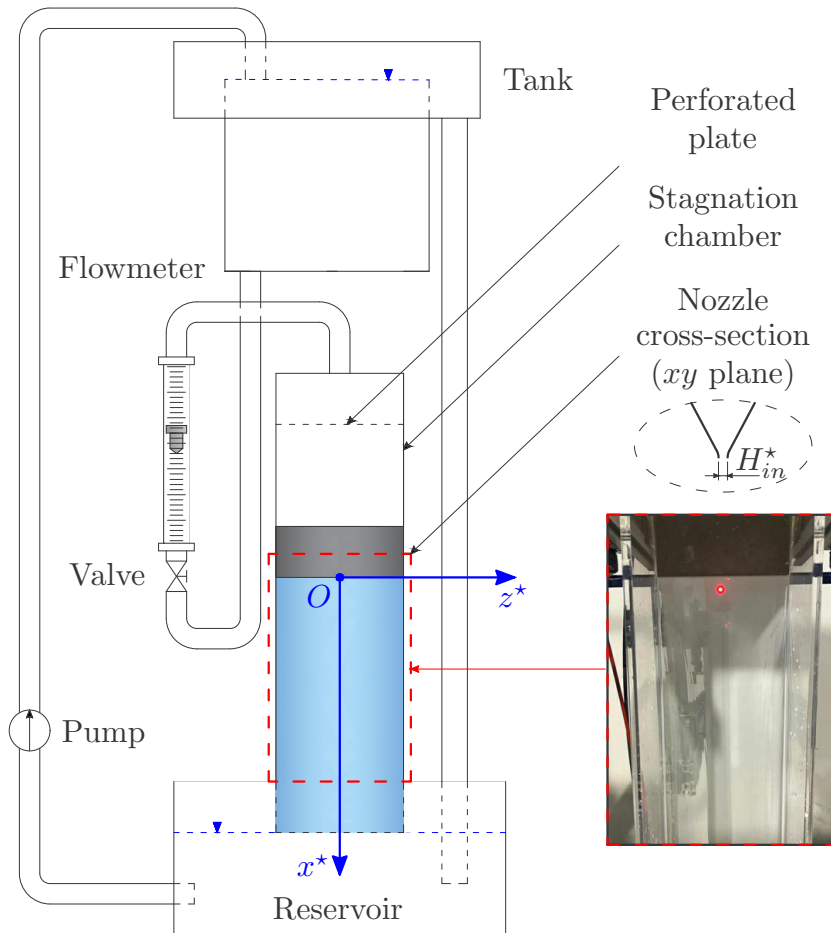


Figure 3.4. Sketch of the apparatus for curtain flows experiments. Details of the two-dimensional liquid sheet and the nozzle are reported on the right. The red spot in the curtain plane denotes the measuring point.

out by recording the transverse velocity signal $v(t)$ by means of a scanning Laser Doppler Vibrometer (LDV) (Polytec PSV400–H4) at a proper measuring point, located 20 mm downstream of the nozzle exit section, as indicated by the red spot on the right in Fig. 3.4. The acquired frequency does not depend on the measuring point location. The frame-rate of acquisition is equal to 256 Hz, and 2048 samples are taken for each measurement. The aqueous solution of white ink is necessary to make the test fluid opaque, thus allowing the laser measurements. The curtain oscillations are excited through the impulse motion of a thin plate, 0.5 mm in thickness, moving in the horizontal yz plane, 0.2 mm below the nozzle exit section. This contact method, used to set the curtain in motion, does not disrupt the sheet for all the test conditions.

3.5 Mixing layers experimental investigation

The apparatus employed to perform air-water mixing layer experiments (inspired by previous works from Ben Rayana *et al.* [40], Raynal *et al.* [39], Matas *et al.* [43]) is presented in Section 3.5.1, followed by a description of the measurement technique used to characterize the two-phase flow (Section 3.5.2). Further details regarding the design and realization of the apparatus are reported in Appendix B.

3.5.1 Experimental apparatus

A schematic representation of the air-water wind tunnel employed in experiments is shown in Fig. 3.5(a)-(b). The first panel gives an overview of all the main components, including the measurement setup (later discussed in Section 3.5.2), while the second focuses on the near-field flow region of the mixing layer, i.e. immediately after the nozzle exit section, which is located at $x = 0$. A water stream flows along the streamwise x direction below a parallel faster air

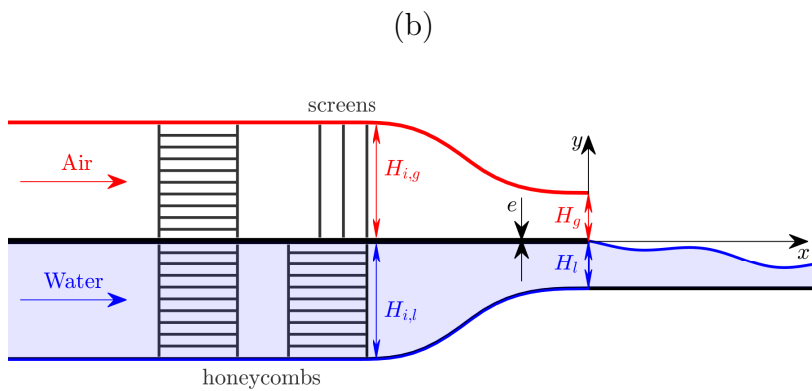
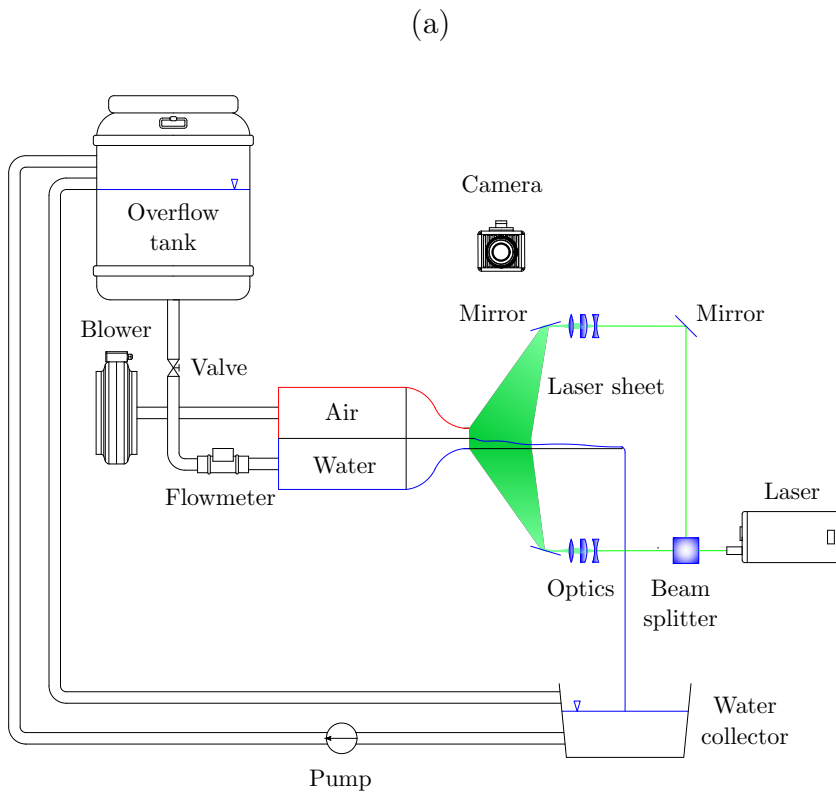


Figure 3.5. Overall schematic representation (panel (a)) and two-dimensional sketch close to the nozzle exit section (panel (b)) of the experimental setup.

current, the two fluids being separated by a stainless steel splitter plate with thickness $e = 2$ mm (Fig. 3.5(b)). The shape of water and air channels is the same: walls are made in Plexiglas, the cross-sectional area (in yz plane) is initially 100×100 mm² (y and z are the normal-to-flow and spanwise coordinates, respectively), then a two-dimensional converging nozzle reduces the channel height from 100 mm to $H_g = H_l = 20$ mm at $x = 0$, where the flows issue into a test section (see Table 3.1). Three-dimensional effects due to the later confinement of the test section walls on the liquid jet are negligible in the near-field region of the flow, where the two-dimensional PIV measurements are realized. An overflowing tank (Fig. 3.5(a)), positioned 1.5 m above the splitter plate, drives the liquid flow by gravity, and it is continuously filled up by a pump (T.I.P. TVX 12000 Dompelpomp), thus realizing a closed-loop circuit for the water stream. The flowrate, which is kept constant during each experiment, is regulated by means of a valve located upstream of the water channel entry; different values measured by a LVB-25-A vortex flowmeter are obtained, corresponding to liquid inlet velocities (i.e. at $x = 0$) in the range $U_l \in [0.10, 0.30]$ m/s. The air stream is generated by a blowing machine (ruck Ventilatoren RS315LEC) allowing to obtain injection velocities between $U_g = 2$ m/s and $U_g = 15$ m/s, as measured by a Pitot tube located at the gas nozzle exit section midpoint (i.e. at $x = 0$, $y = 10$ mm), and cross-checked by static pressure probes positioned at inlet ($x = -250$ mm) and outlet ($x = 0$) sections of the gas nozzle. Flow conditioners are used both in liquid and gas currents to damp velocity fluctuations; two 50 mm long hexagonal cells Aluminum honeycombs (aluNID from Alucoat) are employed in the liquid phase, while a combination of the same honeycomb and screens is used in the air channel.

Particular care is taken in designing the flow conditioners for the gas phase to control its turbulence intensity level, which has been shown to affect the mixing layer development both in experimental (Matas [53]) and numerical (Jiang and Ling [93, 94]) studies, and that strongly depends on screen geometrical properties and relative

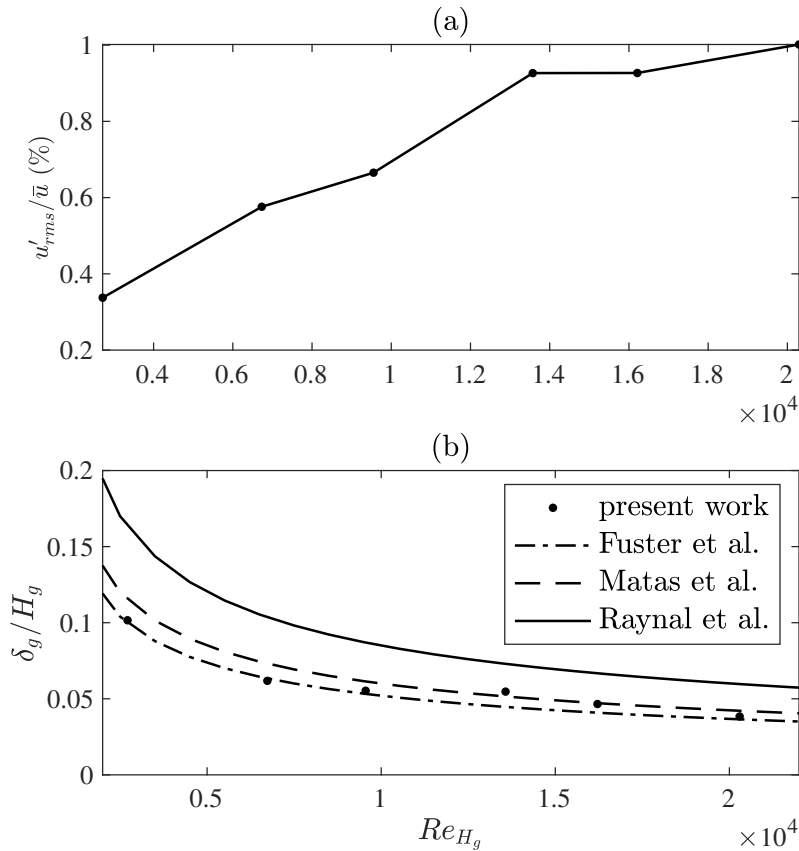


Figure 3.6. Air flow experimental characterization in terms of turbulence intensity level (u'_{rms}/\bar{u} , panel (a)) and inlet gas vorticity thickness (δ_g , panel (b)) variations with Reynolds number Re_{H_g} . Comparisons with literature results (Fuster *et al.* [48], Matas *et al.* [50], Raynal *et al.* [39]) are also provided in panel (b).

Name	Variable	Value	Unit
Gas nozzle inlet height	$H_{i,g}$	100	mm
Gas nozzle outlet height	H_g	20	mm
Liquid nozzle inlet height	$H_{i,l}$	100	mm
Liquid nozzle outlet height	H_l	20	mm
Splitter plate thickness	e	2	mm

Table 3.1. Relevant geometrical quantities of the two-phase mixing layer experimental setup (see also Fig. 3.5(b)).

streamwise spacing in a multiple screens configuration (see for example the works by Mehta and Bradshaw [95], Marhsall [96], Groth and Johansson [97]). Following [97], a combination of three screens was chosen (Fig. 3.5(b)), with mesh size progressively decreasing from 1 mm (coarse screen) to 0.5 mm (fine) and constant relative spacing equal to 20 mm, while a distance of 50 mm was selected between the honeycomb and the more upstream coarse screen. This configuration gives a turbulence intensity level below 1% for all the testing conditions, as reported in Fig. 3.6(a). The turbulence intensity is quantified in terms of root-mean-square of the gas velocity fluctuation $u'(t) = u(t) - \bar{u}$, where $u(t)$ is the streamwise velocity component measured (with liquid stream turned off) by a hot-wire located at the gas nozzle exit section midpoint, and \bar{u} its time-averaged value. Reynolds number values reported in Fig. 3.6(a) correspond to $U_g = 2, 5, 7, 10, 12$ and 15 m/s, the Reynolds number here being defined as $Re_{H_g} = \rho_g U_g H_g / \mu_g$, ρ_g and μ_g being respectively the gas density and dynamic viscosity. The inlet gas vorticity thickness δ_g , which is defined as $\delta_g = \Delta \bar{u} / (d\bar{u}/dy)|_{max}$ ($\Delta \bar{u} = \bar{u}(y = H_g/2) - \bar{u}(y = e/2)$) and is known to play a crucial role in the mixing layer instability selection mechanisms (Matas *et al.* [43], Fuster *et al.* [48]), has also been measured positioning the hot-wire at a downstream distance equal to

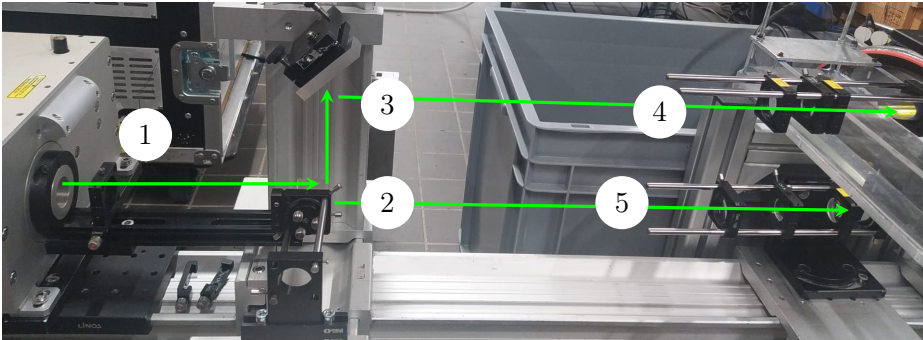
$x = e/2$. The obtained values are reported in Fig. 3.6(b), revealing good agreement with analogous results selected from literature.

3.5.2 Two-phase particle image velocimetry

The single-laser single-camera measurement system designed to achieve the TR-PIV characterization of the flow simultaneously in the two phases is schematically shown in Fig. 3.5(a), while pictures of the experimental setup highlighting its main components are reported in Fig. 3.7(a)-(b). As previously discussed in Section 2.2.4, performing this type of measurement is challenging, and other strategies such as combining PIV with laser-induced fluorescence (Buckley and Veron [63]) or multi-camera multi-laser configurations (Ayati *et al.* [61], Kosiwczuk *et al.* [64]) have been employed to date. Among other reasons, the major issues are related to the laser light reflection and refraction across the interface, and to the high relative velocity between the two phases (about two order of magnitude).

In the present work, to enlighten simultaneously air and water flows overcoming light reflections at the fluids interface, a Continuum Mesa PIV 532-120M laser (item 1 in Fig. 3.7) with pulse at 2 kHz repetition rate (pulse energy 18 mJ) is used to generate a light beam, which is separated in two by a beam splitter (item 2). A first beam (horizontal green arrow between items 2 and 5) goes through a combination of two spherical and one cylindrical lenses (item 5) and a mirror (item 7), thus becoming a thin sheet enlightening the liquid phase (item 9). A second beam (vertical arrow between items 2 and 3) is rotated horizontally by a mirror (item 3), and it is transformed into an analogous sheet for the air flow (superposed on the sheet for water, item 8) by the same combination of lenses and mirror (items 4 and 6). A high speed (2 kHz repetition rate in double exposure mode) camera (Photron, Fastcam SA-1, 1024×1024 pixels, item 10), whose axis is orthogonal to the laser sheets plane, and a programmable timing unit (LaVision, HSC, not shown in Figs. 3.5 and 3.7), complete the measurement setup. Liquid particles (mean diameter $1 \mu\text{m}$) are

(a)



(b)

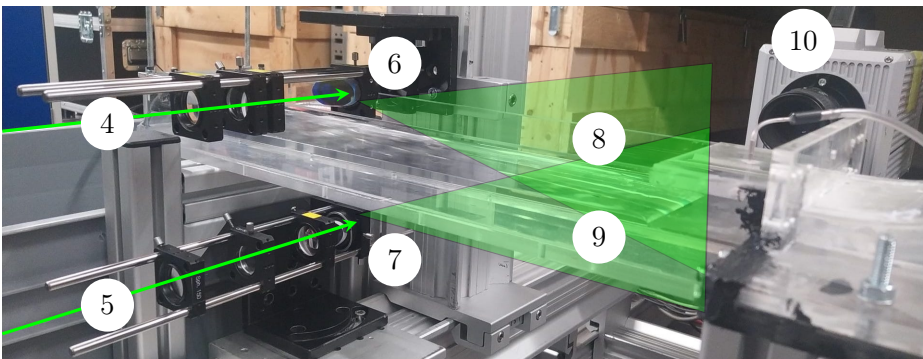


Figure 3.7. Pictures of the PIV measurement setup.

seeded in the air channel by a fog generator (SAFEX, Fog 2010+) using a working fluid of water–glycol mixture, while a 20 μm polyamide Vestosint powder is used to seed the liquid phase.

A $54e \times 18e$ ($e = 2 \text{ mm}$) field of view is imaged by mounting a 105 mm objective (Nikon, Micro-Nikkor) on the high-speed camera, thus giving a two-dimensional $x \in [-18, 108] \times y \in [-18, 18] \text{ mm}^2$ region of interest within the plane positioned midway from the channel side walls. By adjusting the camera focus, particle images approximately 2–3 px in diameter are obtained in both liquid and gas phases, as shown in the raw image reported in Fig. 3.8(a). A pre-processing algorithm written in MATLAB is used to clean the raw images (panel (b)) and separate air and water phases (panels (c)-(d)), which are then post-processed separately through LaVision Davis 10 (the same software is also used in the acquisition process). An iterative multi-grid cross-correlation scheme with window deformation (Scarano and Riethmuller [98]) is used to compute velocity fields, and results are post-processed with the universal outlier detection algorithm (Westerbeel and Scarano [99]). The time delay between two successive frames in air is adjusted from $\Delta t_g = 200 \mu\text{s}$ to $70 \mu\text{s}$ for $U_g \in [2, 15] \text{ m/s}$, while values ranging from $\Delta t_l = 10.5 \text{ ms}$ to 1.2 ms are employed for cross-correlation in water (U_l varying between 0.10 m/s to 0.30 m/s), to guarantee a peak particle displacement of approximately 10 pixels in both phases. For each couple of U_g and U_l values, the time delay for cross-correlation in water Δt_l is simply adjusted by skipping the number of frames necessary to achieve the same peak particle displacement as in air (i.e. $U_l \Delta t_l = U_g \Delta t_g$). In the final pass of cross-correlation operation, the interrogation window size and the overlapping ratio are $16 \text{ px} \times 16 \text{ px}$ and 50%, respectively, leading to a spatial resolution of 1 mm/vector. Mean quantities are estimated based on 8000 realizations (acquisition rate equal to 2 kHz), with average measurement uncertainty on the streamwise and vertical velocity components respectively in the range $[0.62, 9.43]\%$ and $[0.71, 6.28]\%$ of the injection velocities (increasing value moving towards walls). A qualitative representation of a typical velocity field

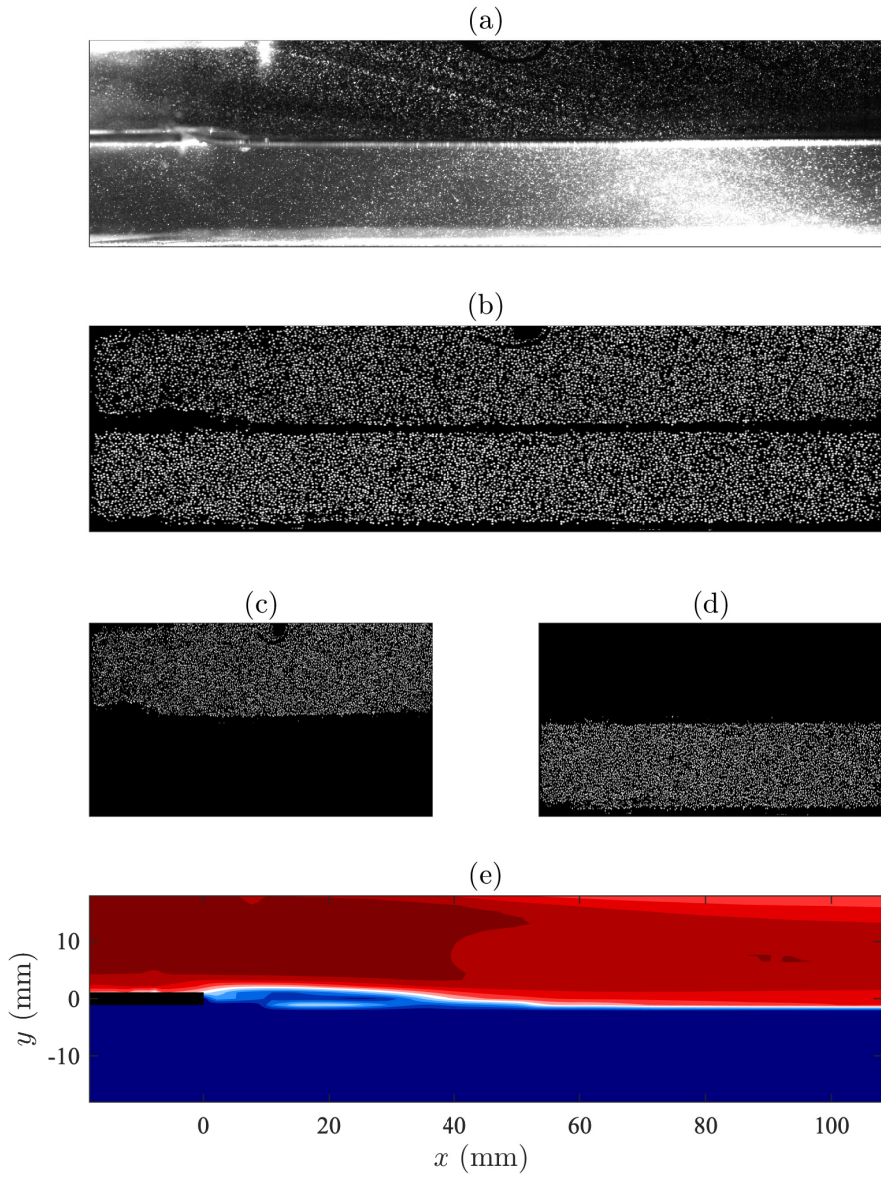


Figure 3.8. Velocity field measurement workflow: acquired raw image (a), pre-processing (b), phases separation (c)-(d), and post-processing (e).

thus obtained is reported in Fig. 3.8(e), which reveals the presence of a wake region behind the splitter plate separating air and water currents (red and dark blue regions, respectively).

The PIV measurements allow to complete the air stream characterization in terms of inflow conditions as shown in Fig. 3.9. In particular, the mean streamwise velocity component profile \bar{u} (defined by Eq. (4.16) in Section 4.2.1) is shown at three different streamwise stations upstream of the injection section: $x/H_g = -1$ (panel (a)), $x/H_g = -0.5$ (b) and $x/H_g = -0.1$ (c). Note that the normal-to-flow coordinate y has been vertically shifted by $e/2$ ($y^* = y - e/2$), such that $\bar{u} = 0$ at $y^* = 0$, and that U_g here denotes the mean velocity at each station. Three velocity profiles are reported in each panel, corresponding to $Re_{H_g} = 6.7 \cdot 10^3$ (black curves), $9.6 \cdot 10^3$ (red) and $16.2 \cdot 10^3$ (blue), and the numerical solution of the fully-developed turbulent channel flow obtained by Kim *et al.* [100] at Reynolds number equal to 13750 is also reported for comparison (green curve). The velocity profiles denote a progressive transition towards turbulent inflow conditions by increasing Re_{H_g} . This occurrence seems to be confirmed by the trend of the turbulence intensity reported in Fig. 3.6(a), showing an initially increasing behaviour followed by a plateau. Note also that the non symmetric velocity profiles with respect to the y direction are due to the non symmetric shape of the exit nozzle, limited by the flat splitter plate and the converging lateral wall (where the boundary layer is thinner).

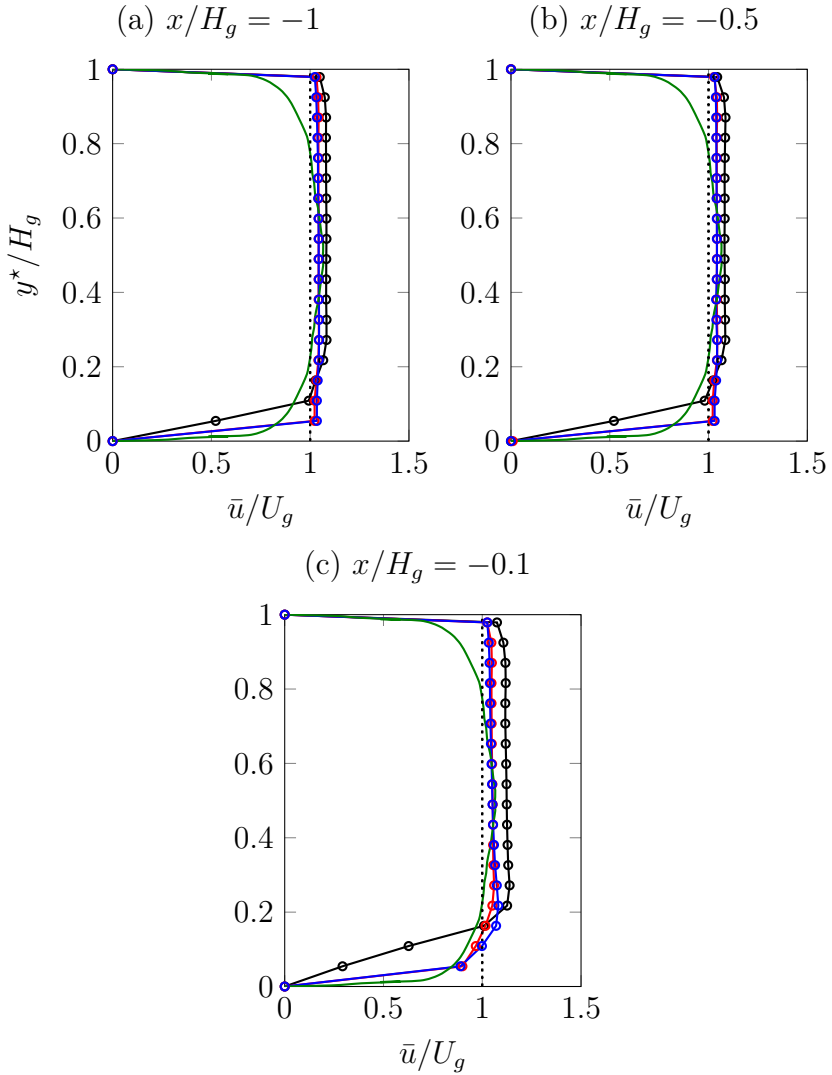


Figure 3.9. Velocity profile in air at different streamwise stations upstream of the injection section ($x/H_g = 0$) and Reynolds number Re_{H_g} values: $Re_{H_g} = 0.67 \cdot 10^4$ (black curves), $0.96 \cdot 10^4$ (red), $Re_{H_g} = 1.62 \cdot 10^4$ (blue). The numerical solution of the fully-developed turbulent channel flow obtained by Kim *et al.* [100] at Reynolds number equal to 13750 is also reported for comparison (green curve).

Chapter 4

Results

The flow configurations presented in Chapter 2 are here investigated by means of the theoretical, numerical and experimental methodologies described in Chapter 3. Section 4.1 is dedicated to the study of gravitational liquid sheet flows, while air-water mixing layers are analyzed in Section 4.2.

4.1 Gravitational liquid curtains

The aim of the present section is the investigation of the spatio-temporal evolution of a perturbed planar liquid sheet, interacting with an unconfined gaseous ambient located on the sides of the liquid phase. The analysis is performed in supercritical ($We > 1$, Sections 4.1.1 and 4.1.2), transcritical ($We = \mathcal{O}(1)$, Section 4.1.3), and subcritical ($We < 1$, Section 4.1.4) conditions.

4.1.1 Base case configuration

A sketch of the flow configuration has been previously reported in Fig. 2.2 (Section 2.1.3), where the gravitational sheet is represented with the x^* axis vertically oriented. In the unperturbed condition, the liquid flows along the gravity direction with a steady velocity and

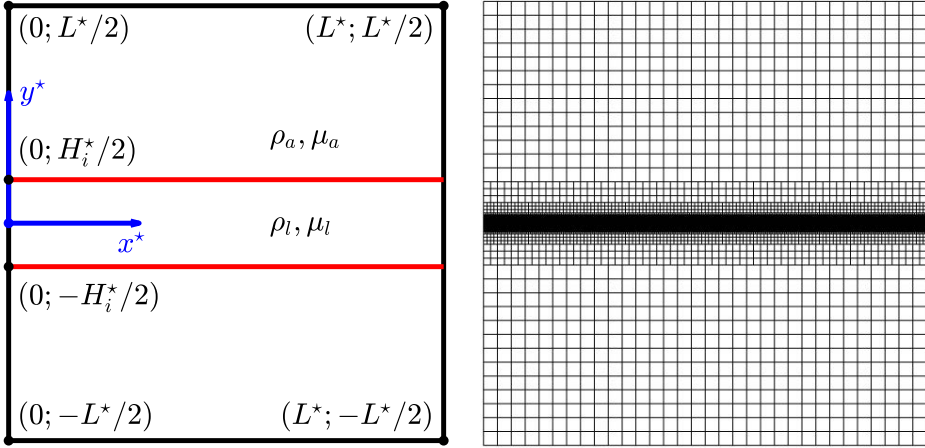


Figure 4.1. Schematic of computational domain (left) and of adaptive grid (right). The sheet of length L^* falls under gravity along x^* direction. Red lines define the initial interface shape, which is magnified by a factor of 10 along y^* direction in left panel.

two symmetrical free interfaces (thin blue lines in Fig. 2.2).

VOF computational layout

A schematic description of the VOF computational domain is reported in the left panel of Fig. 4.1, where for computational convenience the gravity direction x^* is represented horizontally. The computational domain is a square whose side length is equal to the liquid sheet length $L^* = 50H_i^*$, where H_i^* is the inlet sheet thickness, which is located at the centre of the left boundary. The origin of the reference frame Ox^*y^* coincides with the mean point of the inlet sheet thickness, while the red lines define the initial rectangular shape of the interface, employed to start the computation. Dirichlet boundary conditions are enforced at the inlet: in the liquid region, around the symmetry axis, a fully developed parabolic velocity profile

is imposed, and the conditions read

$$u^* = \frac{3}{2}U_i^* \left[1 - \left(\frac{2y^*}{H_i^*} \right)^2 \right], \quad (4.1a)$$

$$v^* = 0, \quad (4.1b)$$

$$C = 1, \quad (4.1c)$$

where U_i^* represents the mean liquid velocity at the inlet. On the remaining part of the left edge (gaseous phase) a no-slip condition is imposed. The top and lower edges are equipped with Neumann boundary conditions for all variables. At the right edge a standard outflow condition

$$\frac{\partial u^*}{\partial x^*} = \frac{\partial v^*}{\partial x^*} = \frac{\partial C}{\partial x^*} = p^* = 0, \quad (4.2)$$

is considered. The liquid sheet region is initialized with a rectangular interface shape, and the same Poiseuille velocity profile adopted as inlet boundary condition is used throughout the entire sheet length. Note that the outlet condition for the differential pressure reproduces the far downstream condition, meaning that the atmospheric pressure is recovered at large downstream stations.

The physical quantities involved in the problem are listed in Table 4.1, where a set of numerical values is also specified, representing the base case considered in the present investigation. Following the Buckingham π theorem, the dimensional parameters can be arranged in 6 dimensionless quantities: a possible choice is reported in Table 4.2. Furthermore, assuming that the liquid phase is water, the liquid density and viscosity, ρ_l and μ_l , as well as, to within a certain approximation, the surface tension coefficient σ , are fixed. Note that the surface tension is a chemical property, and thus its value can be assumed independent of the gas-liquid pair of phases (see for example Tammissola *et al.* [51]). If also the gas viscosity μ_a is considered constant, the independent dimensionless parameters reduce to:

$$\bullet \quad We = \frac{\rho_l U_i^{*2} H_i^*}{2\sigma}, \quad Fr = \frac{U_i^{*2}}{gL^*}, \quad \varepsilon = \frac{H_i^*}{L^*}, \quad r_\rho = \frac{\rho_a}{\rho_l},$$

where the slenderness parameter ε is intrinsically a small quantity whose order generally ranges from $\mathcal{O}(10^{-3})$ to $\mathcal{O}(10^{-2})$. If not differently specified, it has been assumed $\varepsilon = 0.02$ for all the computations reported in the present section. On the other hand, for the standard case of $g = 9.81 \text{ m/s}^2$, the corresponding dimensional parameters are:

$$\bullet \quad U_i^*, H_i^*, L^*, \rho_a.$$

It is clearly evident that there exists a 1:1 correspondence between the set of governing dimensionless numbers and the set of physical parameters. This correspondence will be considered in the subsequent parametric investigation, which will be carried out by hypothesizing the variation of one physical parameter at a time (for instance the liquid velocity), leading to the variation of the related dimensionless parameters. Accordingly, the physical quantities can be conveniently made dimensionless by employing the reference quantities introduced in Section 2.1.3 (Eq. (2.12)); note that hereafter dimensionless quantities will be denoted without apex \star . This section is concluded by describing the grid adopted in the computations, shown in the right panel of Fig. 4.1. It is a quadtree-structured grid which retains its maximum level of refinement in a rectangular region containing the entire liquid sheet: $-0.5 < y^*/H_i^* < 0.5$, $0 < x^*/L^* < 1$. The maximum resolution is limited to $N = 11$ levels of refinement, corresponding to a minimum dimensionless cell edge length of $\Delta x^*/H_i^* = 0.0244$ (40 grid cells within H_i^*). A grid convergence analysis has been performed, and results in terms of thickness contraction ratio, which is a global parameter defined as the ratio of the outlet to the inlet sheet thickness, $CR = H_f^*/H_i^*$, are reported in Fig. 4.2: no variations between the two finest grid levels are detected.

The simulation time-step is evaluated at each iteration as

$$\Delta t^* = \min \left(\frac{0.5\Delta x^*}{u^*}, \sqrt{\frac{\rho_l + \rho_a}{2} \frac{\Delta x^{*3}}{\pi\sigma}} \right), \quad (4.3)$$

Table 4.1. Dimensional physical quantities involved in the problem, reporting the values referring to the base case.

Name	Variable	Value	Unit
Gas density	ρ_a	9.97	Kg m ⁻³
Liquid density	ρ_l	997	Kg m ⁻³
Gas viscosity	μ_a	$1.84 \cdot 10^{-5}$	Kg m ⁻¹ s ⁻¹
Liquid viscosity	μ_l	$8.90 \cdot 10^{-4}$	Kg m ⁻¹ s ⁻¹
Gravity acceleration	g	9.81	m s ⁻²
Inlet liquid mean velocity	U_i^*	0.49	m s ⁻¹
Inlet sheet thickness	H_i^*	$1.5 \cdot 10^{-3}$	m
Sheet length	L^*	$75 \cdot 10^{-3}$	m
Surface tension coefficient	σ	$72.5 \cdot 10^{-3}$	N m ⁻¹

Table 4.2. Dimensionless parameters corresponding to the base case of Table 4.1.

Name	Relation	Value
Gas-to-liquid density ratio	$r_\rho = \rho_a/\rho_l$	0.01
Gas-to-liquid viscosity ratio	$r_\mu = \mu_a/\mu_l$	0.02
Sheet slenderness ratio	$\varepsilon = H_i^*/L^*$	0.02
Reynolds number	$Re = \rho_l U_i^* H_i^*/(2\mu_l)$	420
Froude number	$Fr = U_i^{*2}/(gL^*)$	0.33
Weber number	$We = \rho_l U_i^{*2} H_i^*/(2\sigma)$	2.5

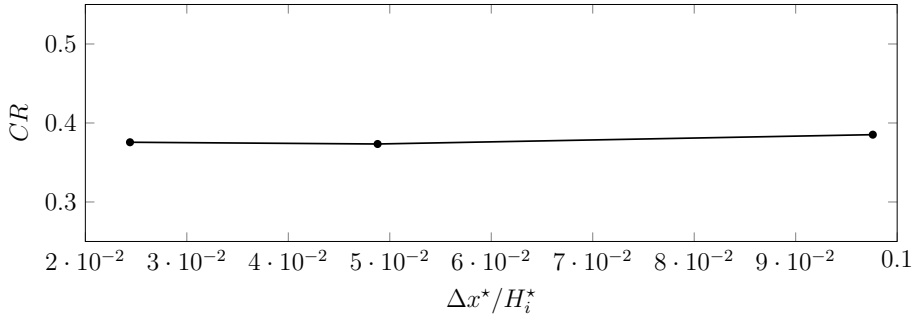


Figure 4.2. Grid convergence analysis of the contraction ratio $CR = H_f^*/H_i^*$ for the steady solution. From right to left: $\Delta x^*/H_i^* = 0.0976$ (10 grid cells in H_i^*); $\Delta x^*/H_i^* = 0.0488$ (20 grid cells in H_i^*); $\Delta x^*/H_i^* = 0.0244$ (40 grid cells in H_i^*). Flow parameters specified in Tables 4.1 and 4.2.

which is the minimum value between the CFL-based time-step and the oscillation period of the smallest capillary wave that can be captured by the grid. The adopted mesh structure has been obtained thanks to the adaptive-grid feature implemented in the BASILISK solver. A detailed description of the adaptive grid refinement strategy is given in van Hooft *et al.* [73].

Steady solution achievement

The steady solution of the falling liquid sheet is obtained starting from the initial condition shown in Fig. 4.1, which corresponds to a rectangular interface shape with a parallel Poiseuille velocity profile enforced along the entire length. For the base case parameters specified in Tables 4.1 and 4.2, a computational time equal to $t_s = 1.5$ was required to reach the steady configuration.

The computed flow field is represented in Fig. 4.3 in terms of u velocity component, interface shape, and p distribution along the liquid sheet centreline. As a reference, the free-fall Torricelli's solution is also reported (Eq. (2.16) in Section 2.1.3). As expected, velocity,

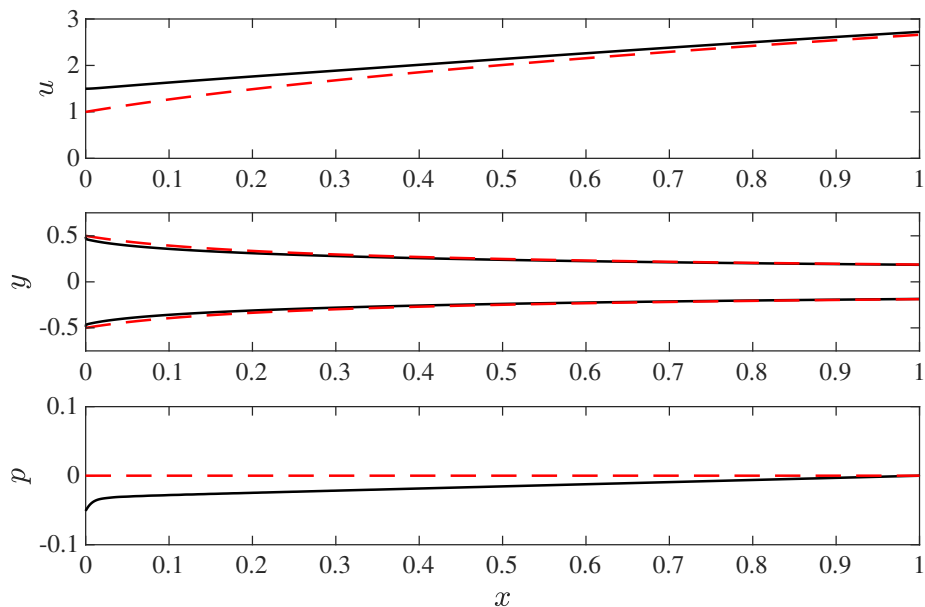


Figure 4.3. Steady field in terms of u velocity component (top), sheet interface (middle), and pressure p (bottom) along the axial direction $y = 0$. Numerical solution (black curve); Torricelli's solution (red dashed curve).

interface shape, and pressure profiles tend to the inertia-gravity Torricelli's model as the distance from the inlet increases. In the initial part of the sheet the velocity appears slightly greater than the reference solution; in agreement with this finding the interface shape restricts (remember that the Reynolds number is relatively high) and the pressure is lower (it attains negative relative values). Far downstream the flow accelerates under the gravity effect and then approaches the free-fall model, where viscous and surface tension effects, related to the sheet interface curvature, become negligible. Fig. 4.4 depicts lateral profiles of velocity components and pressure. Axial u velocity profiles clearly show that the initial parabolic trend tends to relax towards a quite plug distribution as the distance from inlet increases. The maximum values of transverse velocity component v profiles accordingly are reduced towards the bottom section. Note explicitly that v values appear magnified by the adopted scale: $v = v^*/(\varepsilon U_i^*)$. The present velocity profiles well agree with the corresponding numerical and experimental results reported in Fig. 2 of Soderberg [21] and Fig. 5 of Soderberg and Alfredsson [3]. The experimental data were obtained for Reynolds number $Re = 700$ and Weber number $We = 12.5$, both greater but comparable with the present simulation data, while the numerical solutions were obtained neglecting both surface tension and inertia effects of the surrounding gas [3]. Moreover, the numerical solutions reported in [3] were computed including an entrance length for the liquid phase, which somehow helps the flow to relax towards the plug profile. Regarding the p profile, for which to our knowledge there are neither experimental nor numerical data to compare with, it is possible to observe the jump in pressure distribution due to the surface tension effect at $x = 0$, where the liquid sheet curvature is maximum. Moving along the liquid sheet, the interface shape becomes nearly parallel to x axis and consequently pressure y -distributions become quite uniform, across both liquid and gas phases. The simulated two-dimensional velocity field shown in Fig. 4.5 allows one to appreciate the phenomenon of gas entrainment.

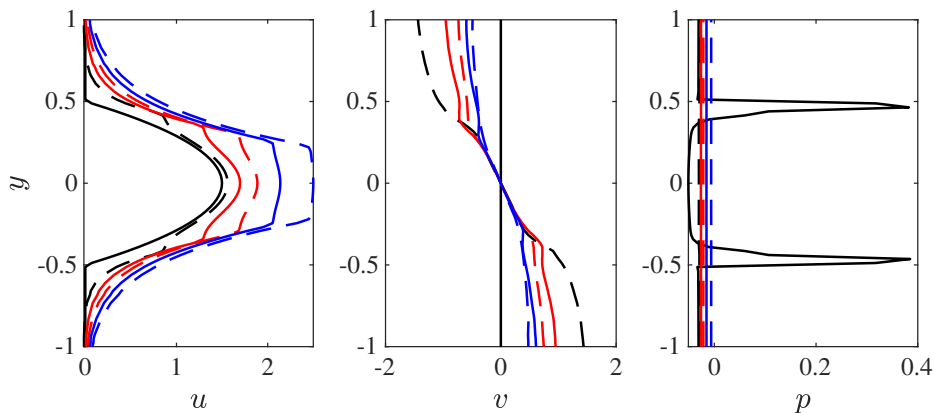


Figure 4.4. Steady solution of u (left), v (middle) and p (right) y -distribution at different x stations: $x = 0$ (black continuous curve); 0.05 (black dashed); 0.15 (red continuous); 0.3 (red dashed); 0.5 (blue continuous); 0.8 (blue dashed).

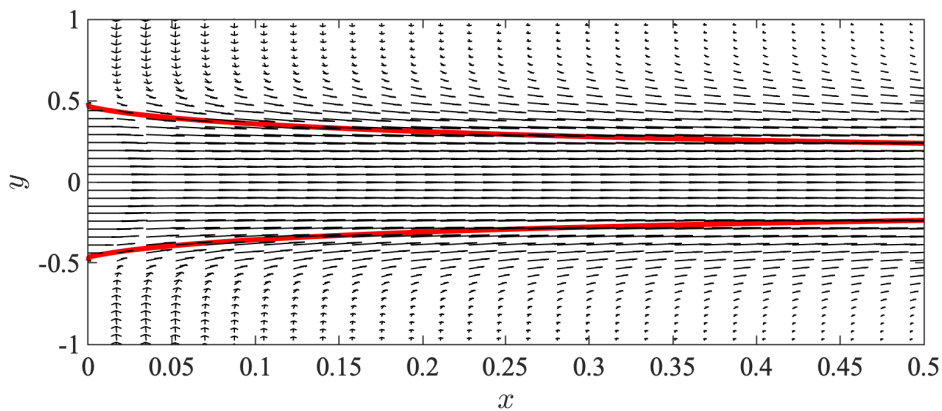


Figure 4.5. Steady velocity field and interface shape (red line) of the liquid sheet.

One-dimensional data reduction

A one-dimensional reduction of VOF data is required to compare the numerical results with predictions of the linear theoretical approach introduced in Section 3.2, which is based on a simplified one-dimensional model of the flow system. This reduction is based on the relationship

$$\phi_{1D} = \frac{\sum_{i=1}^{N_y} C_i \phi_i}{\sum_{i=1}^{N_y} C_i}, \quad (4.4)$$

where ϕ_{1D} is the spatial-averaged value over the lateral y direction, evaluated at every x station, of the generic physical quantity ϕ ; N_y is the total number of grid cells at the selected x station, while C_i is the volume fraction in the cell i . In particular, for $\phi = y$, the average deflection (meanline) of the sheet is obtained. Note that the implementation of Eq. (4.4) allows one to extract the average value of ϕ for the liquid phase only, being $C_i = 0$ in the gas phase. As an example, Fig. 4.6 shows the result obtained for $\phi = u$ for the steady configuration. Observe that the centreline u velocity component (solid line) converges towards the one-dimensional reduced mean value (dashed line) as x increases, in agreement with considerations concerning the convergence of the field towards the Torricelli's solution made above in this section (Figs. 4.3 and 4.4).

4.1.2 Supercritical regime

The unsteady behaviour of the liquid sheet forced by an impulse perturbation for the base (supercritical) configuration (Tables 4.1 and 4.2 of Section 4.1.1) represents the main topic of the present section. Results of the two-dimensional VOF simulations are treated according to the 1D reduction technique illustrated in Section 4.1.1, and they are compared with corresponding findings from the linear stability theory (Section 3.2). Features of the flow system in a realistic three-dimensional configuration are finally discussed.

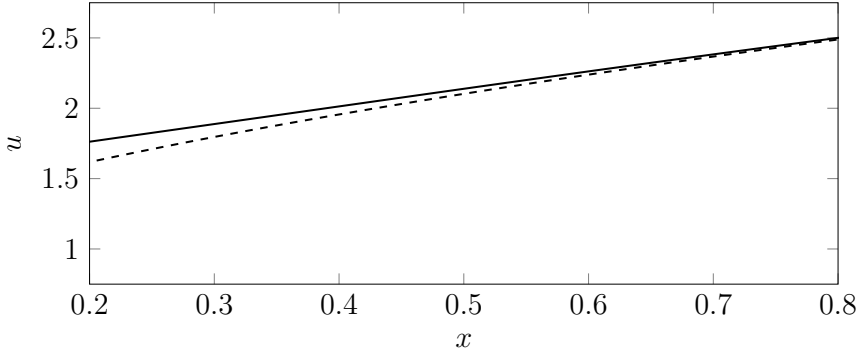


Figure 4.6. Steady u velocity component (black continuous curve) and one-dimensional reduction using Eq. (4.4) for $\phi = u$ (black dashed curve).

Travelling-waves dynamics

The computation via VOF of the unsteady response of the fluid system is performed forcing at the initial instant the steady configuration by means of an impulse disturbance applied at a specified x station. The adopted perturbation is a Gaussian bump in v velocity component

$$v_f = A e^{-\frac{1}{2}\left(\frac{x-x_0}{\Delta}\right)^2}, \quad (4.5)$$

where A is the amplitude, x_0 the peak station, and Δ^2 represents the variance of the Gaussian function. To guarantee a linear response, at least at the initial instants after the forcing, the following typical parameters have been adopted for all the computations: $A = 5\varepsilon$, $\Delta = 0.1\varepsilon$, $x_0 = 0.3$. Figs. 4.7 and 4.8 depict the x trends of average lateral velocity v and sheet meanline ℓ , extracted from the VOF simulation, at various time instants. The first panel of both figures reproduces the initial condition. The sequence of panels of Fig. 4.7 clearly shows that the initial v perturbation splits in two down-winding travelling wave fronts, which leave the domain through the right exit section at $t = 0.22$ and $t = 0.53$, respectively. Comparing these results with the expulsion times provided by the theoretical one-dimensional model

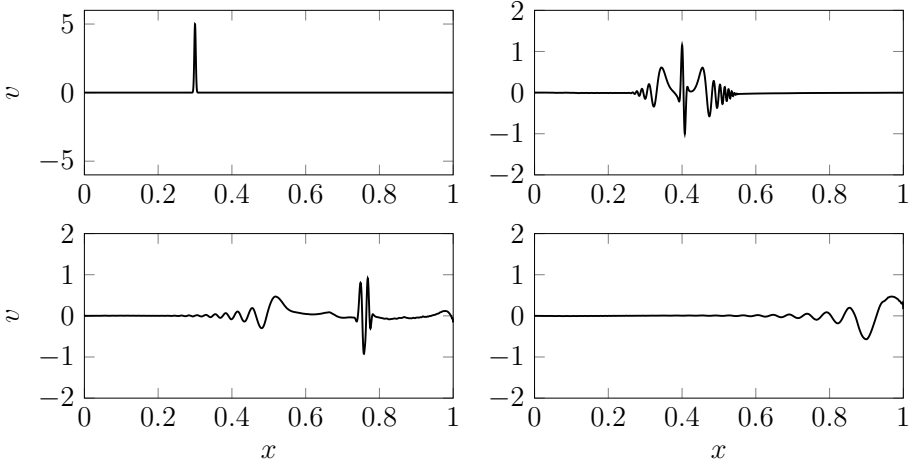


Figure 4.7. Sequence of instantaneous average v distributions extracted from the VOF simulation. From left to right, top to bottom: $t = 0, 0.05, 0.21, 0.52$. $We = 2.5$, $Fr = 0.33$, $r_\rho = 0.01$.

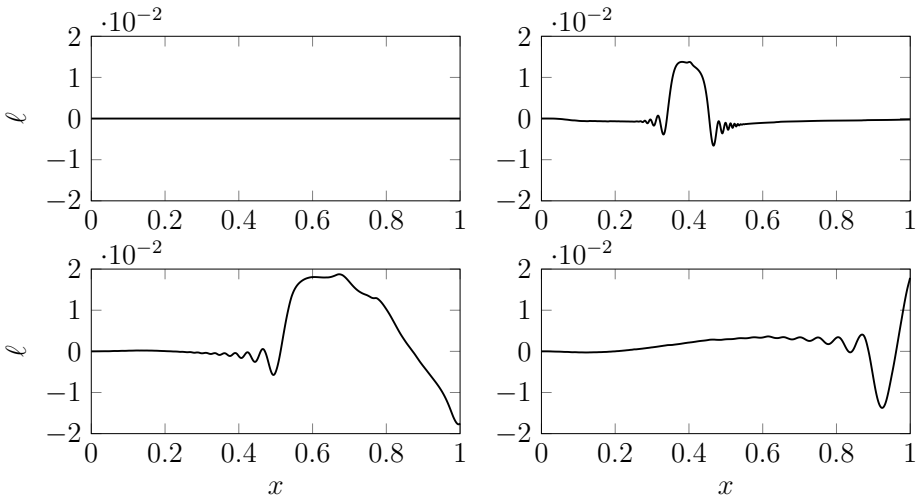


Figure 4.8. Sequence of instantaneous meanline distributions extracted from the VOF simulation. From left to right, top to bottom: $t = 0, 0.05, 0.21, 0.52$. $We = 2.5$, $Fr = 0.33$, $r_\rho = 0.01$.

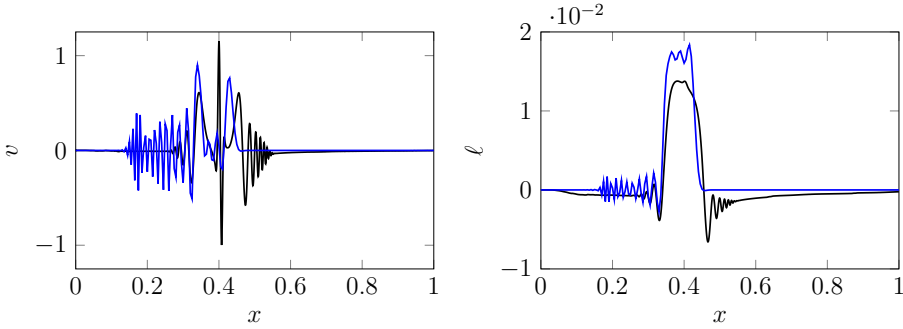


Figure 4.9. Instantaneous v velocity component and meanline l distributions at $t = 0.05$ extracted from the VOF simulation (black curve) and computed by Eqs. (2.13)-(2.14) (blue). $We = 2.5$, $Fr = 0.33$, $r_\rho = 0.01$.

(Section 2.1.3) a good agreement is found, with differences of 2% and 7% for the fast and the slow travelling waves, respectively. The expulsion times of fast and slow waves, of wave speed respectively equal to $U \pm \sqrt{U/We}$, are analytically evaluated as

$$t_{exp\pm} = \int_{x_0}^1 \frac{dx}{U \pm \sqrt{U/We}}, \quad (4.6)$$

$x_0 = 0.3$ being the station where the impulse perturbation is introduced (see also Eq. (2.22) in Section 2.1.3). As regards the meanline evolution, Fig. 4.8 shows that the perturbation in v produces a corresponding deformation of the meanline shape. This induced perturbation does not split in two wave fronts, as for the v signal, but it exhibits a compact front whose ends travel downstream with the two characteristic speeds, which determines the enlargement of the perturbation front as t increases. Fig. 4.9 shows the snapshots of v and l perturbations obtained by numerical integration in MATLAB environment of Eqs. (2.13)-(2.14) of the theoretical model, superimposed on VOF results. It has to be stressed that the features presented in previous Figs. 4.7 and 4.8 are recovered, with a relatively small delay

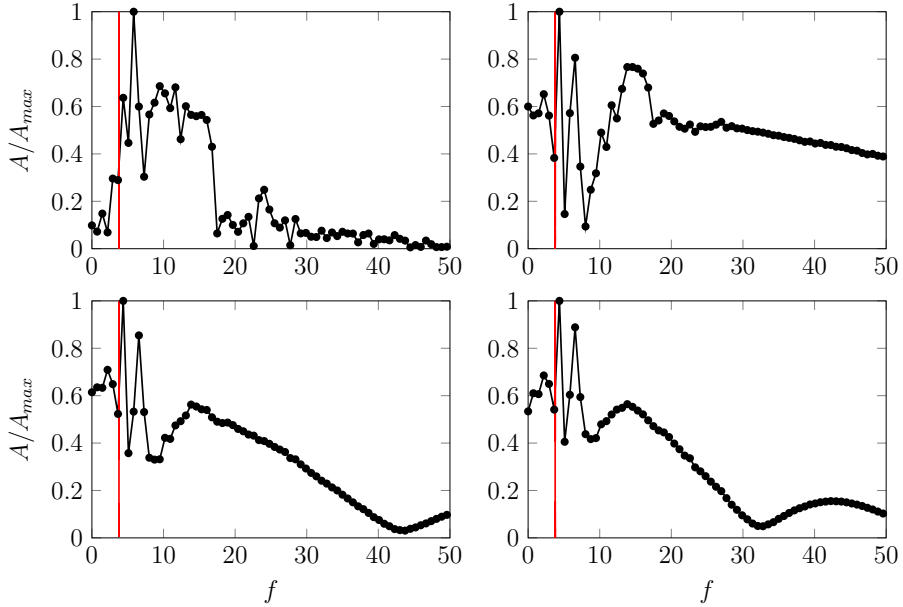


Figure 4.10. Fast Fourier Transform (FFT) of the sheet meanline deflection extracted from VOF simulations at different x stations. The red line represents the least stable frequency $\lambda_i = 3.78$ arising from stability analysis. From left to right, top to bottom: $x = 0.2, 0.4, 0.6, 0.8$. $We = 2.5$, $Fr = 0.33$, $r_\rho = 0.01$.

of the theoretical signals with respect to VOF data. This result represents a validation of the VOF simulation, which is able to capture the underlying physics of the system under consideration.

Natural frequency prediction

One of the main findings of the present investigation is that, after the complete expulsion of the perturbation from the computational domain, the meanline time evolution is characterized by low frequency sinuous oscillations. This oscillatory behaviour has been investigated by performing simulations for a final time equal to $t = 8$ and computing frequency spectra of meanline temporal signals stored

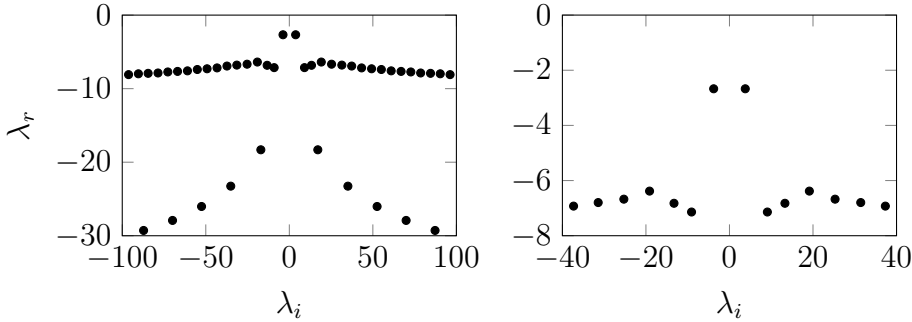


Figure 4.11. Inner eigenvalues of the spectrum (left), with a zoom of the upper branch around the least stable part (right). $We = 2.5$, $Fr = 0.33$, $r_\rho = 0.01$.

at different x stations along the liquid sheet. The results are shown in Fig. 4.10, which reports frequency spectra computed with the Fast Fourier Transform (FFT) algorithm. The presence of two low-frequency peaks is clearly detected at all the stations considered. In particular, for $x = 0.2$ the highest peak occurs for $f_{max} = 5.83$, but it moves to $f_{max} = 4.37$ for $x = 0.4$, and then it remains constant for all the other stations. In panels of Fig. 4.10 the frequency of the least stable eigenvalue predicted by linear stability is also represented as a red vertical line, while Fig. 4.11 shows a wide part of the spectrum of complex conjugate eigenvalues. Note the presence of two branches corresponding to the slow (upper) and fast (lower) travelling waves, exhibiting an almost constant spacing between the frequencies. This spacing is associated with the corresponding crossing time, $\Delta\lambda_i = 2\pi/t_{cross}$, where t_{cross} is given by Eq. (2.23) (Section 2.1.3).

The low-frequency peak detected from VOF simulations via FFT analysis differs from the frequency of the least stable eigenvalue of the stability analysis, belonging to the upper branch of the spectrum, by a relative spread of 14%. Moreover, it is also interesting to evaluate the ratio between the frequency of the leading eigenvalue and the spacing $\Delta\lambda_i$ of the relevant branch. This ratio is equal to 0.67 for the

Table 4.3. Summary of results for the base case in terms of VOF-1D model comparison. $We = 2.5$, $Fr = 0.33$, $r_\rho = 0.01$.

Variable	VOF simulation	1D model	Relative spread
t_{cross}	0.97	1.07	9%
$2\pi/t_{cross}$	6.48	5.86	9%
f_{max}	4.37	3.78	14%
$\frac{f_{max}}{2\pi/t_{cross}}$	0.67	0.64	4%
f_{max}^*	4.56 Hz	3.95 Hz	14%

VOF data and 0.64 for the stability analysis, with a 4% spread. This occurrence is reminiscent of the *integer-plus-one-quarter* resonance criterion of forced transverse vibrations of the nappe-string, already uncovered by De Rosa *et al.* [16] in the absence of surface tension, and by Girfoglio *et al.* [13] considering this effect. For the present case of a free-free interface liquid sheet, a modified criterion is proposed, providing the possible natural frequencies with the relationship

$$f = \frac{2\pi}{t_{cross}} \left(n + \frac{2}{3} \right), \quad (4.7)$$

where n is an integer ($n \geq 0$). Table 4.3 summarizes the comparison of the characteristic parameters of frequency response obtained with VOF simulation and the theoretical one-dimensional model. Data referring to the slow wave crossing time show a 9% spread, which is also the spread of the associated frequency, namely the almost constant spacing between the frequencies of the spectrum, $\Delta\lambda_i = 2\pi/t_{cross}$. The VOF crossing time reported in Table 4.3 has been computed applying the integral of Eq. (4.6) to simulation data for $x_0 = 0$, i.e. by integration along the entire sheet length.

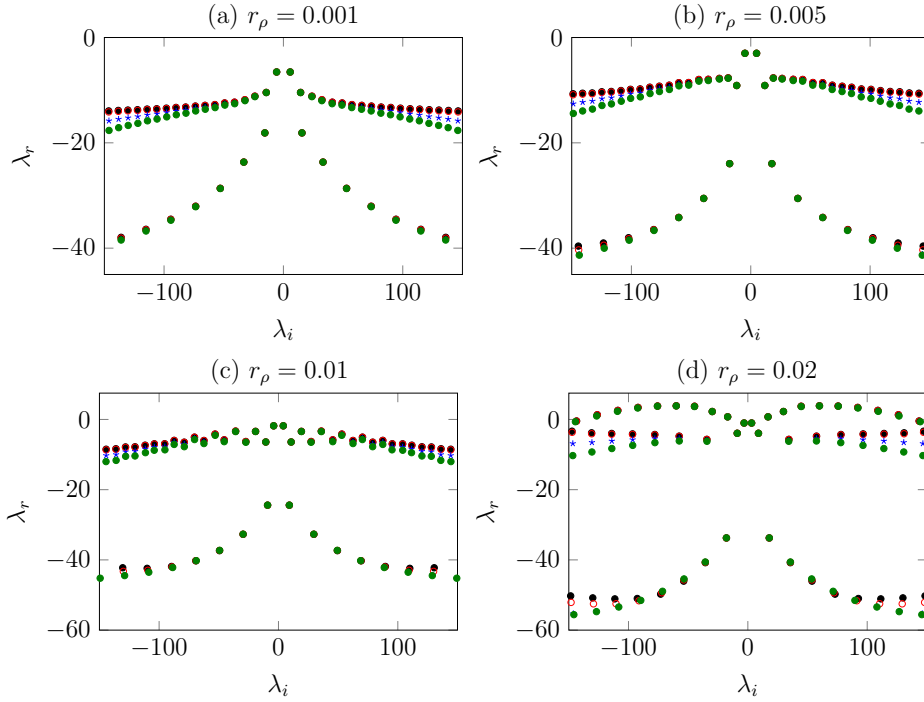


Figure 4.12. Reynolds number Re effect at different values of the density ratio r_ρ on the inner eigenvalues of the spectrum: $r_\rho = 0.001$ (panel (a)); 0.005 (panel (b)); 0.01 (panel (c)); 0.02 (panel (d)). $Re = \infty$ (black filled circle); 400 (red open circle); 40 (blue asterisk); 20 (green filled circle). $We = 2.5$, $Fr = 0.16$.

Supercritical unstable behaviour

The gas-to-liquid density ratio r_ρ effect on the spectral properties of the flow (for $We = 2.5$, $Fr = 0.16$) is reported in Fig. 4.12: each panel corresponds to a different r_ρ value, which is in turn analyzed in the range $Re \in [20; \infty[$, therefore including viscous effects in the simplified theoretical analysis (see Appendix A.2). The inviscid flow ($Re = \infty$) becomes unstable when the density ratio increases. In particular, when the onset of instability is approaching, pairs of inner eigenvalues move towards each other (Fig. 4.12(b)), and then for

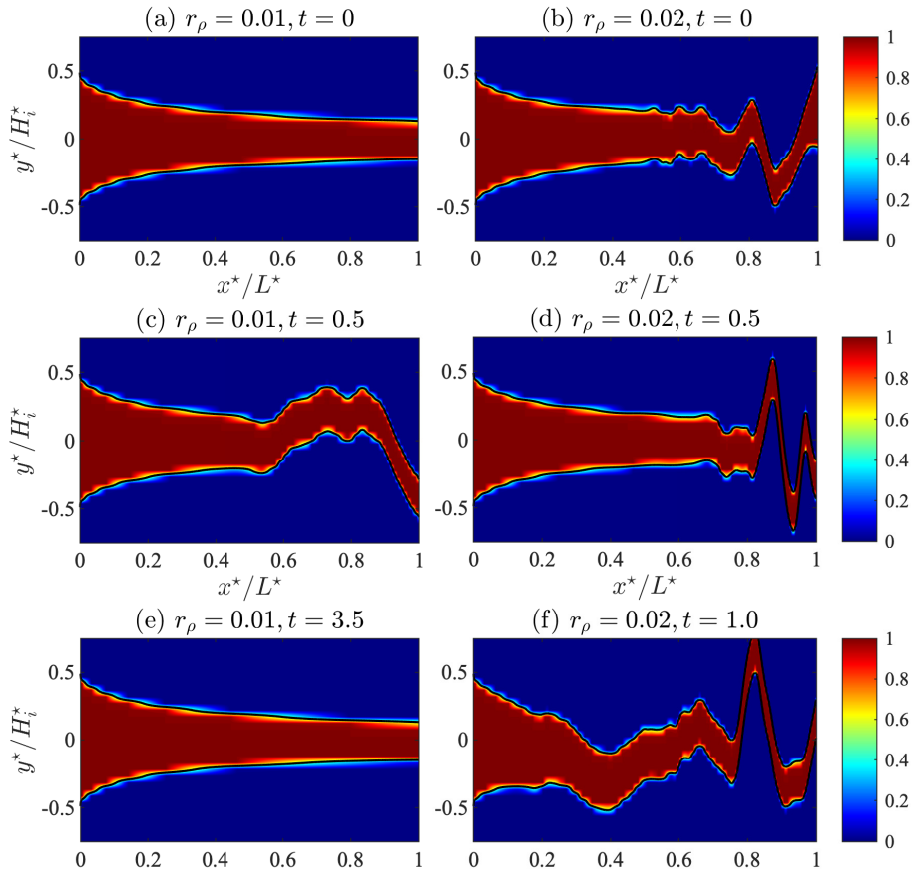


Figure 4.13. Temporal evolution of the two-dimensional volume fraction field C computed via VOF simulations for $r_\rho = 0.01$ (panels (a), (c), (e)) and $r_\rho = 0.02$ (panels (b), (d), (f)). $We = 2.5$, $Fr = 0.16$, $Re = 20$.

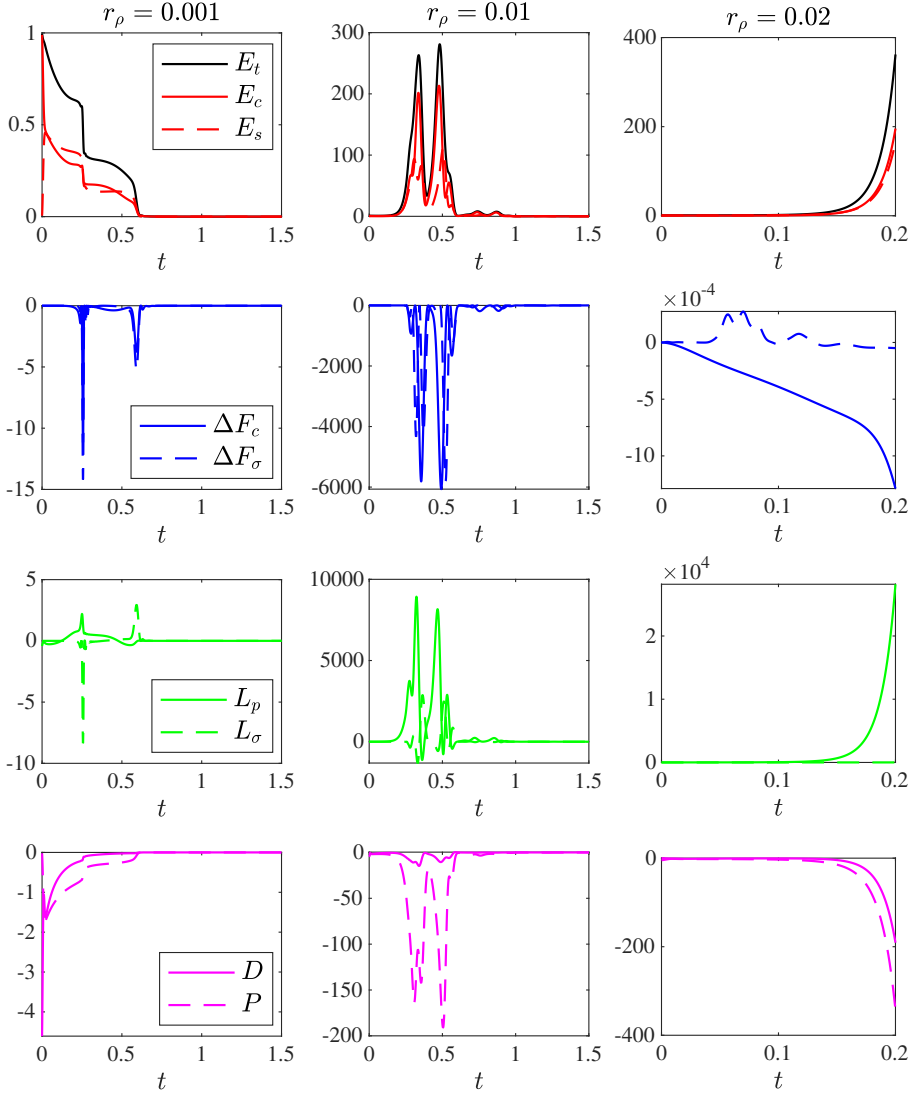


Figure 4.14. Density ratio r_ρ effect on the temporal evolution of the energy budgets. From left to right: $r_\rho = 0.001, 0.01, 0.02$. The fast and slow waves expulsion times are $t = 0.25$ and $t = 0.60$, respectively. Note that all the terms have been scaled with respect to the initial total energy E_{t_0} . For a detailed explanation of the terms, see Eq. (2.33) in Section 2.1.3. $We = 2.5$, $Fr = 0.16$, $Re = 20$.

each couple the growth rate of an eigenvalue remarkably increases (Fig. 4.12(c)), until the slow wave branch of the spectrum appears as divided into two distinct sub-branches, one of the two containing some unstable eigenvalues having positive real part (Fig. 4.12(d)). It can be also noted that the fast and slow branches of the spectrum become hardly distinguishable when unstable conditions are reached. The viscous analysis ($Re \neq \infty$) clearly retrieves the previous results, recovering the flow instability also for low values of the Reynolds number. Moreover, viscous results make clearer the distinction between the two slow sub-branches of the spectrum: the stable one behaves like the fast branch and undergoes the viscous damping, the other one is almost unaffected by viscosity and contains unstable eigenvalues. The unstable temporal behaviour at high density ratios r_ρ is retrieved in VOF simulations, as can be appreciated by looking at Fig. 4.13. In particular, a transient growth of perturbations (panel (c)) followed by damping at relatively long time (panel (e)) at $r_\rho = 0.01$, and an unstable evolution at $r_\rho = 0.02$ (panels (b), (d), (f)) followed by breakup for $t > 1$ (not shown here) are highlighted by the VOF analysis.

To shed light on the physical mechanisms determining the flow unstable dynamics outlined by both the eigenvalues and VOF analyses, a budgets decomposition of the total energy of the system (Eq. (2.33) in Section 2.1.3) is performed. Results are reported in Fig. 4.14 in terms of the energy budgets temporal evolution, for the three values of density ratio so far considered. The first row of panels shows that the total energy evolution E_t , which is stable at $r_\rho = 0.001$, undergoes transient growths at $r_\rho = 0.01$ in the time interval $t \in [0.25; 0.60]$, and then rapidly decreases to zero, which is in agreement with the asymptotic temporal stability prediction (Fig. 4.12) and VOF results (Fig. 4.13). For $r_\rho = 0.02$, the unstable behaviour can be recovered in the exponential growth of the total energy and its two contributions, E_c and E_σ , reaching values of $\mathcal{O}(100)$ before the waves expulsion ($t \approx 0.2$). The decomposition of E_t into budgets allows one to identify the physical mechanism that drives the system towards the in-

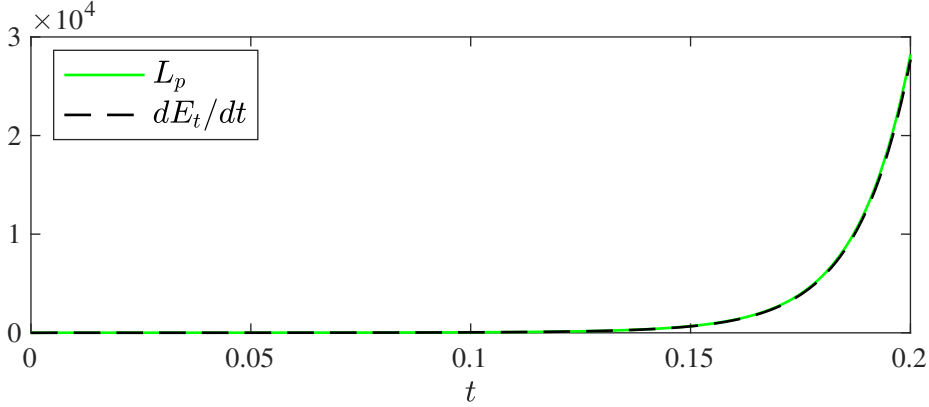


Figure 4.15. Comparison between the pressure power L_p and the total energy time derivative dE_t/dt for unstable conditions ($r_\rho = 0.02$). For a detailed explanation of the terms, see Eq. (2.33) in Section 2.1.3. $We = 2.5$, $Fr = 0.16$, $Re = 20$.

stability: it is basically related to L_p term, which represents the work per time unit exchanged between the liquid sheet and the gaseous environment, interacting through the ambient pressure field. Looking at the green continuous curves shown in Fig. 4.14, one can indeed detect that L_p plays an increasing destabilizing role ($L_p > 0$, meaning that the work is undergone by the liquid sheet, which drains energy from the interacting environment) as r_ρ increases. The destabilizing effect of the pressure power L_p is balanced by the other (stabilizing) contributions (ΔF_c and ΔF_σ , blue curves, P and D , magenta curves) until $r_\rho = 0.01$, whereas these are completely overwhelmed by L_p in unstable conditions ($r_\rho = 0.02$). In other terms, the flow features a convective amplification of the perturbation as it travels downstream. For low density ratio values, these amplifications are eventually expelled at the downstream domain exit leaving the flow globally stable; for high density ratios, the large convective amplification cannot be expelled from the domain and the flow suffers of a global instability. These results agree with previous findings by de Luca and Costa [14] and Barlow *et al.* [17]. The comparison between the total energy

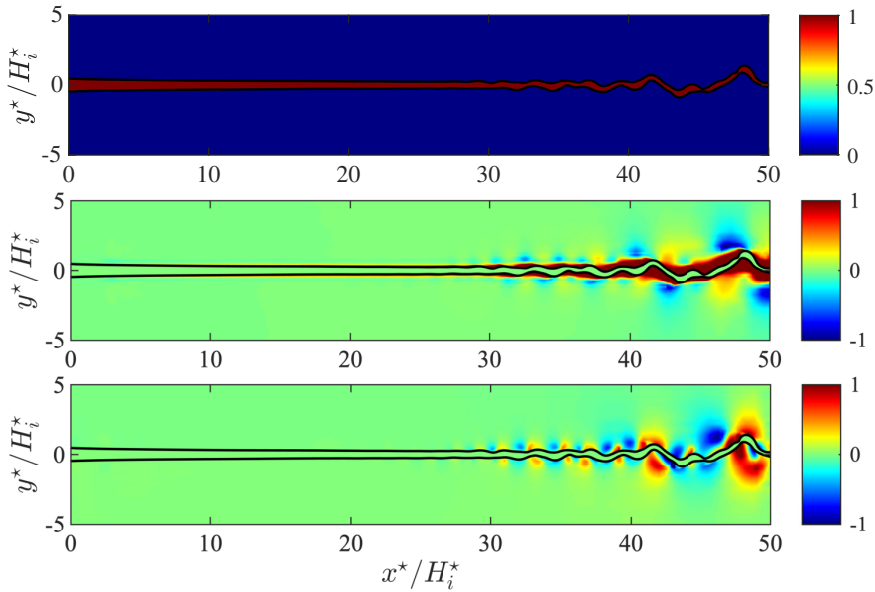


Figure 4.16. Instantaneous view of the volume fraction C (top) and ambient-phase velocity components u_a^*/U_i^* (middle) and v_a^*/U_i^* (bottom) fields in unstable conditions. In all the panels the interface is the black contour line.

time derivative dE_t/dt and L_p reported in Fig. 4.15 better clarifies the dominant role of the latter term in unstable conditions; it completely dominates the exponential temporal energy evolution, as can be appreciated by the almost perfect superposition between black and green curves.

This section is concluded providing an analogy between the global unstable behaviour exhibited by the liquid sheet as the density ratio r_ρ increases, and the surface tension-induced global instability found by Tammisola *et al.* [51]. These authors computed two-dimensional linear temporal global modes of planar jet and wake flows of two immiscible fluids with different velocities, and found that surface tension can induce global instability for large enough values of the shear ratio Λ , which measures the external flow velocity effect, being the under-

lying physical mechanism located in the shear layer. Apart from the differences in the two physical configurations, the role of the shear ratio parameter Λ underlined by [51] (when surface tension is present) can be related to the density ratio effect r_ρ in the present analysis, where the relatively strong entrainment effect of high density gas plays the destabilizing role. This analogy is also supported by the good qualitative agreement between Fig. 11 of [51], reporting global eigenmodes for a wake flow ($\Lambda < 1$) for different values of the Weber number, and Fig. 4.16 reported herein, showing the unstable liquid sheet shape together with the distributions of velocity components u_a and v_a of the ambient gaseous phase.

The oscillatory flow pattern exhibited by the u eigenmode at $We = 5$ in Fig. 11(e) of [51] can be recovered in the u_a distribution shown by the middle panel of Fig. 4.16, in particular for $30 < x^*/H_i^* < 40$, which is the liquid sheet region where the amplification of disturbances is not yet significantly affected by nonlinear effects. Furthermore, remember that in Section 2.1.3 it has been observed, Eq. (2.19), that the oscillatory dynamics of the average sheet displacement ℓ resembles that of a tensional string forced by terms containing the lateral velocity v , and subjected to a total damping coefficient which can assume negative values. Accordingly, one can argue that the distribution of the ambient velocity component v_a , showed in the bottom panel of Fig. 4.16, represents the forcing term which leads the system towards the instability when, for relatively high density ratios r_ρ , the total damping coefficient becomes negative.

The comparison with wake rather than jet flows of [51] is motivated by the observation that the inner stream acceleration and interface contraction experienced by wake flows (Fig. 1 of [51]), due to the shear effect of the higher velocity outer stream, can be regarded as the counterpart of the gravity effect considered in the present work. On the other hand, the analogy seems to fail in the initial part of the sheet, where the shear-induced velocity of the gaseous phase is weaker.

Data-driven global stability by DMD on random perturbations

The methodology described in Section 3.3.2 is here applied to VOF data, providing an estimation of the BiGlobal spectrum in a non-intrusive way, namely without the linearization of the governing equations. The analysis is performed in stable supercritical conditions ($We = 2.5$, $r_\rho = 0.01$); further details regarding the data-driven global spectrum in subcritical regime and for unstable conditions can be found in Colanera, Della Pia and Chiatto [101]. As discussed in Section 3.3.2, a random perturbation (white noise) in both the velocity components and volume fraction fields is superposed at $t = 0$ on the base (steady) flow. The temporal evolution of the axial velocity perturbation field $u'(x, y)$ is shown in Fig. 4.17 ($x = x^*/L^*$, $y = y^*/H_i^*$). Panel (a) contains the white noise added to the base flow; panels (b) and (c) show the evolution of these disturbances that, while reducing in amplitude, excite dynamics characterized by different scales.

The DMD technique is exploited to obtain the global spectrum. In this case, 200 simulations, corresponding to 40000 snapshots, have been used for the analysis. The DMD spectrum of the base case is reported in Fig. 4.18, together with the corresponding one (e.g. in the same flow conditions) given by the 1D model (red circles) for a direct comparison. Here, only 400 DMD modes are reported, which retain more than the 99.9% of the POD total energy, avoiding the introduction of spurious modes (Schmid [79]).

Generally speaking, the BiGlobal spectrum highlights a wider frequency content than the 1D results, and it exhibits a further branch between the upper and lower branches previously discussed. All the eigenvalues have a negative real part due to the stable nature of the flow; the less damped eigenvalues are located at low frequencies. The leading mode, labelled A, is equal to $\lambda = -0.54 + i3.64$, which perfectly matches the value predicted by the low order analysis. Other interesting eigenvalues are highlighted with blue circles in the spec-

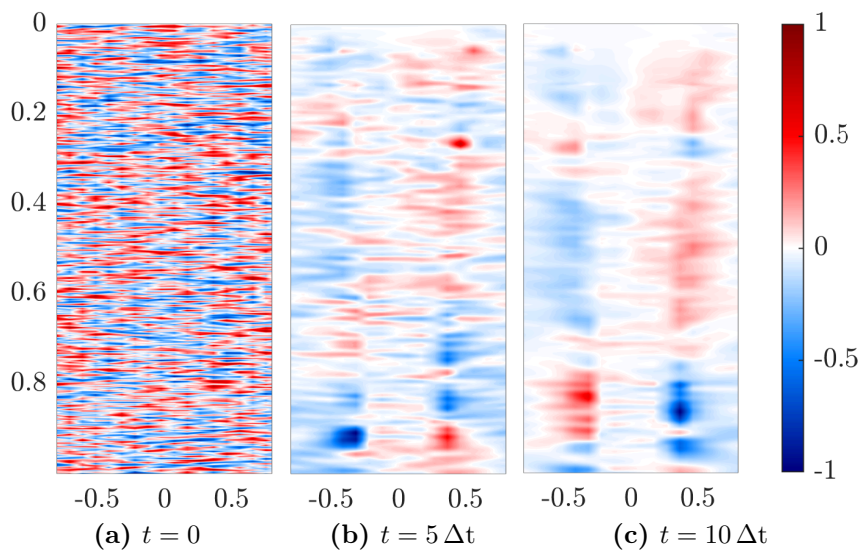


Figure 4.17. $u'(x, y)$ evolution of a random initial disturbance ($0 < x < 1$, $-0.75 < y < 0.75$). $We = 2.5$, $r_\rho = 0.01$. Field variables have been normalized with respect to the corresponding maximum.

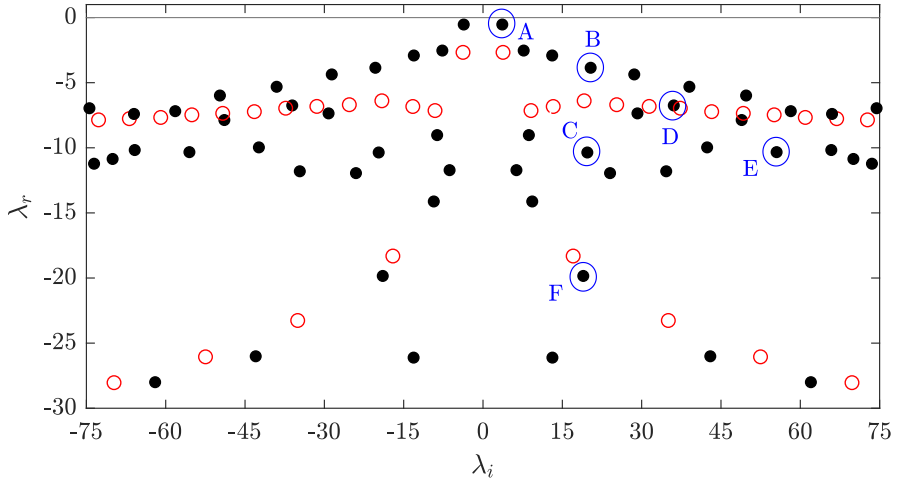


Figure 4.18. Data driven BiGlobal spectrum. $We = 2.5$, $r_\rho = 0.01$. Black dots refer to the 2D simulations, red circles represent 1D model results. Letters denote selected modes.

trum and are located on different branches: modes A and B belong to the upper branch, modes C, D and E are on the middle one, and mode F lies on the lower branch. The corresponding values are reported in Table 4.4.

The DMD technique also provides insights on the topology of the flow through the analysis of the coherent structures associated with the main modes. In particular, for the liquid sheet flow under study, the DMD provides the spatial distributions of both velocity components (u' , v') and volume fraction (C'). Fig. 4.19 reports the real part of the structures corresponding to modes A and B, scaled with respect to their maximum. Note that the black dashed line represents the interface location due the mode's action, that is computed considering only the correspondent mode in the C' reconstruction according to Tu *et al.* [80] and Schmid [79]. Panels (a) and (c) show antisymmetric distributions of u' and C' , while panel (b) contains a symmetric distribution of v' , as is typical for a sinuous motion. The v' distribution (panel (b)) along the axis $y = 0$ features an almost monotonic

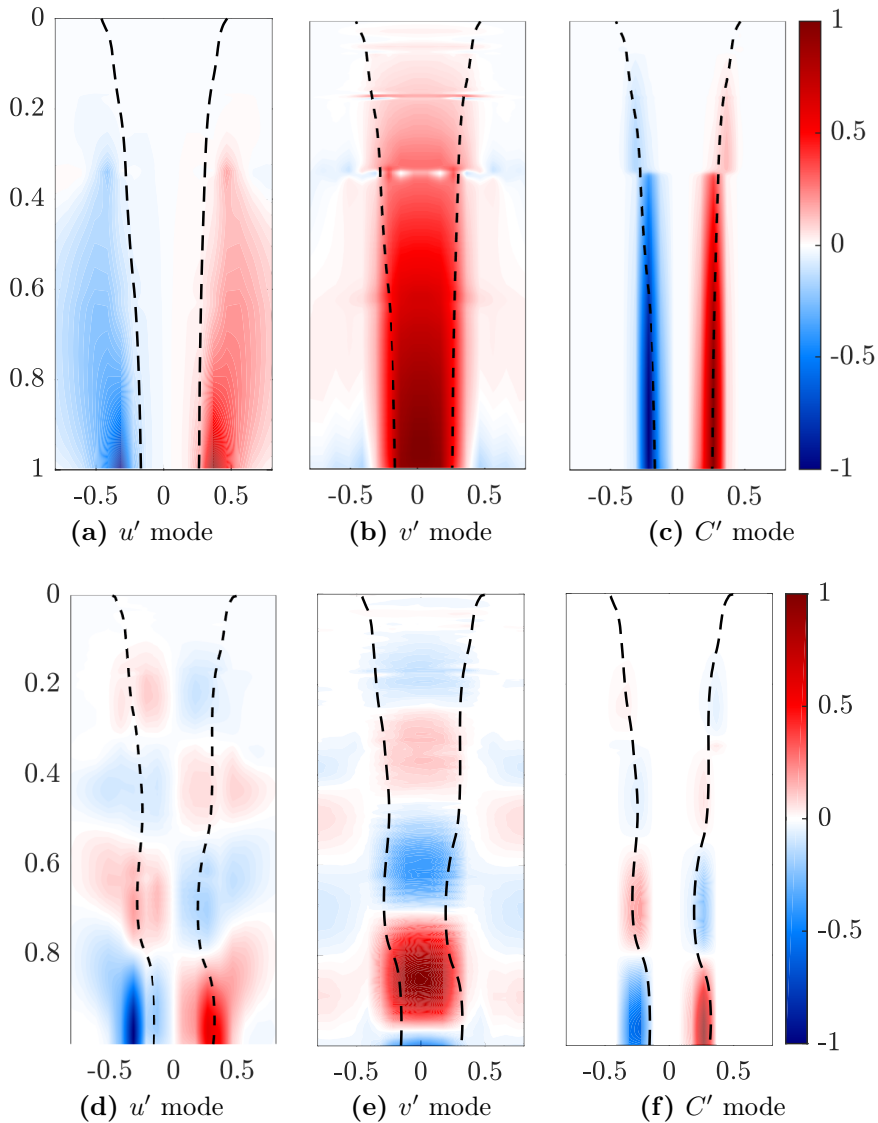


Figure 4.19. Spatial distributions of the DMD modes A (panels (a)-(c)) and B (panels (d)-(f)) in xy plane ($0 < x < 1$, $-0.75 < y < 0.75$). $We = 2.5$, $r_\rho = 0.01$. The black dashed line represents the interface location.

Table 4.4. Selected eigenvalues for the case of $We = 2.5$, $r_\rho = 0.01$.

	λ	
A	-0.54	+ i 3.64
B	-3.86	+ i 20.36
C	-10.36	+ i 19.73
D	-6.75	+ i 36.08
E	-10.33	+ i 55.51
F	-18.96	+ i 19.84

increase along the downstream direction. A similar behaviour can be also observed for the mode B, which is a generic mode representative of the flow topology in this branch. Indeed, panels from (d) to (f) report structures with smaller spatial scales with respect the previous ones, but still characterized by a sinuous motion. The topology described above is retrieved, with different scales, in all modes of this branch, which is therefore characterized by a purely sinuous behaviour. The same characteristics are obtained for the mode F (not reported herein) belonging to the lower branch. Bearing in mind that the 1D model is purely sinuous, it is not surprising that for these two sinuous branches there is a good agreement between the 1D and 2D spectra.

As will be detailed in the following, the additional 2D middle branch is associated with a varicose flow behaviour, which could not be predicted by the 1D model, accounting for the sinuous dynamics only. To proceed further with the discussion of the spectrum, it is convenient to decompose each mode φ_j in sinuous and varicose contributions:

$$\varphi_j(x, y) = \varphi_j^s(x, y) + \varphi_j^v(x, y), \quad (4.8)$$

being $\varphi_j^s(x, y)$ and $\varphi_j^v(x, y)$ the sinuous and varicose components of the mode, respectively. $\varphi_j^s(x, y)$ contains the antisymmetric part (with respect to the axis $y = 0$) of u' and C' modes and the symmetric

Table 4.5. Sinuous and varicose energy contributions of the selected DMD modes. $We = 2.5$, $r_\rho = 0.01$.

λ	$E^s(\%)$	$E^v(\%)$
A	93.5%	6.5%
B	93.5%	6.5%
C	78.0%	22.0%
D	47.9%	52.1%
E	22.9%	77.1%
F	89.0%	11.0%

one of v' , while $\varphi_j^v(x, y)$ represents the complementary distributions. Note that sinuous and varicose components are orthogonal to each other by definition. This decomposition can be directly extended to the perturbations energy E (see Eq. (3.17) in Section 3.3.2). In this way, the energy reads $E = E^s + E^v$, where E^s and E^v represent the sinuous and varicose contributions, respectively. Table 4.5 reports the energy contents for the selected DMD modes. One can note that, as expected, the first two modes (A and B) contain a sinuous energy contribution around the 93%; a similar value can be observed also for the mode F, for which $E^s = 89\%$. Different energy contents are observed in the central branch for increasing frequencies; indeed, modes C, D and E exhibit a growing varicose energy content, respectively equal to $E^v = 22.0\%$, 52.1% and 77.1% .

Bearing in mind the previous energy distributions, Fig. 4.20 reports the varicose component of u' modes for the eigenvalues C, D and E. The black dashed line represents the interface location, highlighting the cross-section area variation in varicose regime. Moving from C to E, a frequency increase is accompanied by a global decrease of the spatial scales. The resulting wavelength reduction determines a more uniform energy distribution along the sheet length. This can be inferred considering the spatial distributions of the modes' am-

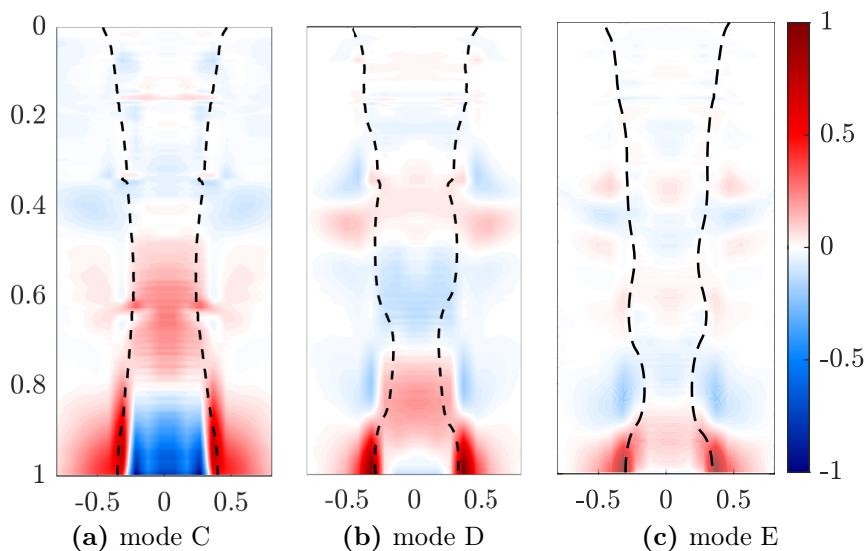


Figure 4.20. Varicose component of DMD $u'(x, y)$ modes corresponding to the eigenvalues C, D, E ($0 < x < 1$, $-0.75 < y < 0.75$). $We = 2.5$, $r_\rho = 0.01$. The black dashed line represents the interface location.

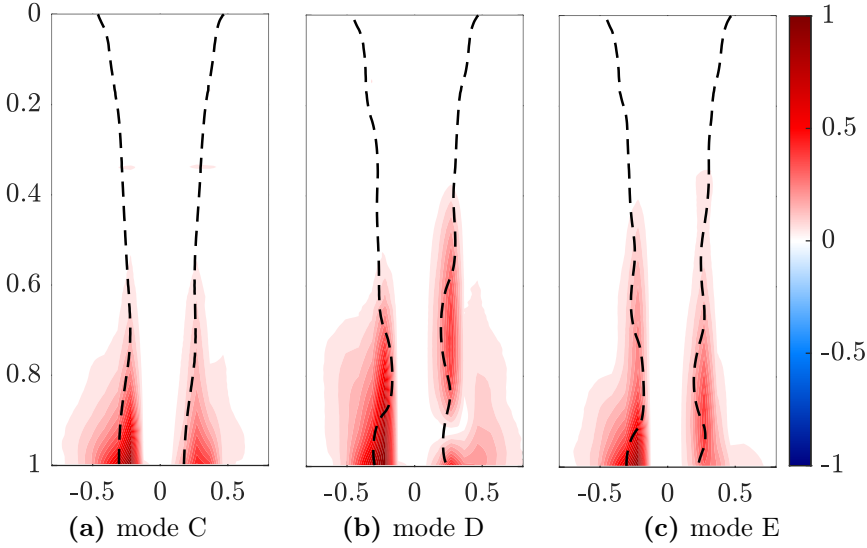


Figure 4.21. Energy distribution for the modes C (panel (a)), D (panel (b)) and E (panel (c)) in xy plane ($0 < x < 1$, $-0.75 < y < 0.75$). $We = 2.5$, $r_\rho = 0.01$. The black dashed line represents the interface location.

plitude, which represents the local contribution of the mode to the energy defined in Eq. (3.17). The corresponding energy distributions are reported in Fig. 4.21; the energy of the mode C is mainly concentrated downstream of the station $x = 0.6$, whereas the modes D and E show a more homogeneous distribution starting from $x = 0.5$ and 0.4 , respectively.

The procedure applied herein to evaluate the BiGlobal spectrum of the flow in supercritical conditions applies straightforward to the subcritical regime, revealing the presence of both sinuous and varicose modes in the spectrum also for $We < 1$. Further details are given in Colanera, Della Pia and Chiatto [101].

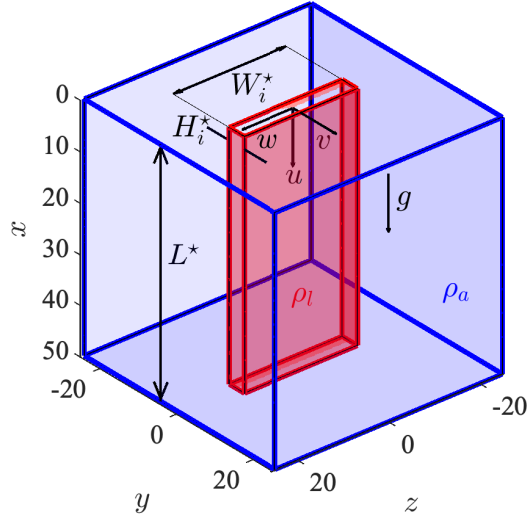


Figure 4.22. Schematic representation of the three-dimensional computational domain. The gravity g is directed along the streamwise x direction, y is the lateral coordinate, z the spanwise one.

Three-dimensional flow simulations

A schematic description of the computational domain employed to simulate a three-dimensional liquid curtain is reported in Fig. 4.22. It consists in a cubic region $[0, L^*] \times [-L^*/2, L^*/2] \times [-L^*/2, L^*/2]$ extending in the x (streamwise), y (transverse) and z (spanwise) directions, respectively. In dimensionless terms the spatial coordinates x , y and z have been scaled here with respect to the inlet sheet thickness H_i^* , while the corresponding streamwise u , transverse v and spanwise w velocity components have been made dimensionless with respect to the inlet mean liquid velocity U_i^* ($u = u^*/U_i^*$, $v = v^*/U_i^*$, $w = w^*/U_i^*$). The curtain issues into an initially quiescent gaseous environment (blue region in Fig. 4.22) from a rectangular slot of dimensions $H_i^* \times W_i^*$, representing the initial thickness (along the transverse y coordinate) and width (along the spanwise z direction) of the sheet, respectively. The origin of the reference

frame coincides with the centre of the slot, and the curtain shape is initialized as a parallelepiped $L^* \times H_i^* \times W_i^*$ (red region in Fig. 4.22, where $C(x, y, z, 0) = 1$), which is employed to start the computation. Dirichlet boundary conditions are enforced at the inlet: following Kacem [102], in the liquid region (i.e., for $-1/2 < y < 1/2$ and $-AR/2 < z < AR/2$, being $AR = W_i^*/H_i^*$ the sheet aspect ratio) a fully developed parabolic velocity profile with a proper error function modification at the slot boundaries (i.e., at $y = \pm 1/2, z = \pm AR/2$) is imposed, and the conditions read

$$u = \frac{3}{2} (1 - 4y^2) \operatorname{erf} \left(\frac{AR}{2} - z \right) \operatorname{erf} \left(\frac{AR}{2} + z \right), \quad (4.9a)$$

$$v = w = 0, \quad (4.9b)$$

$$C = 1, \quad (4.9c)$$

while on the remaining part of the inlet plane, namely within the gaseous phase, a no-slip condition is imposed. The four lateral boundary planes ($y = \pm 25, z = \pm 25$) are equipped with Neumann boundary conditions for all variables, and on the outlet plane ($x = 50$) a standard outflow condition is considered (analogously to the two-dimensional case). No symmetry conditions are thus employed to reduce the computational domain. The same $u(y, z)$ profile adopted as inlet boundary condition (Eq. (4.9a)) is used as initial velocity distribution throughout the entire sheet length. The computational domain is discretized with an adaptive mesh up to a maximum number of 2^9 grid points along each spatial dimension, corresponding to a minimum mesh size $\Delta^* \approx H_i^*/11$, and approximately 134 million cells if an uniform grid was used. Note that a lower resolution of $\Delta^*/H_i^* \approx 6$ has been recently shown to be effective in capturing holes expansion and collision in a thin ($H_i^* = 25 \cdot 10^{-6}$ m) liquid sheet by Agbaglah [103].

A typical three-dimensional curtain flow steady solution is shown in Fig. 4.23 in terms of three-dimensional interface shape (a), surface distribution of spanwise velocity component $w(x, z)$ in $y = 0$ plane

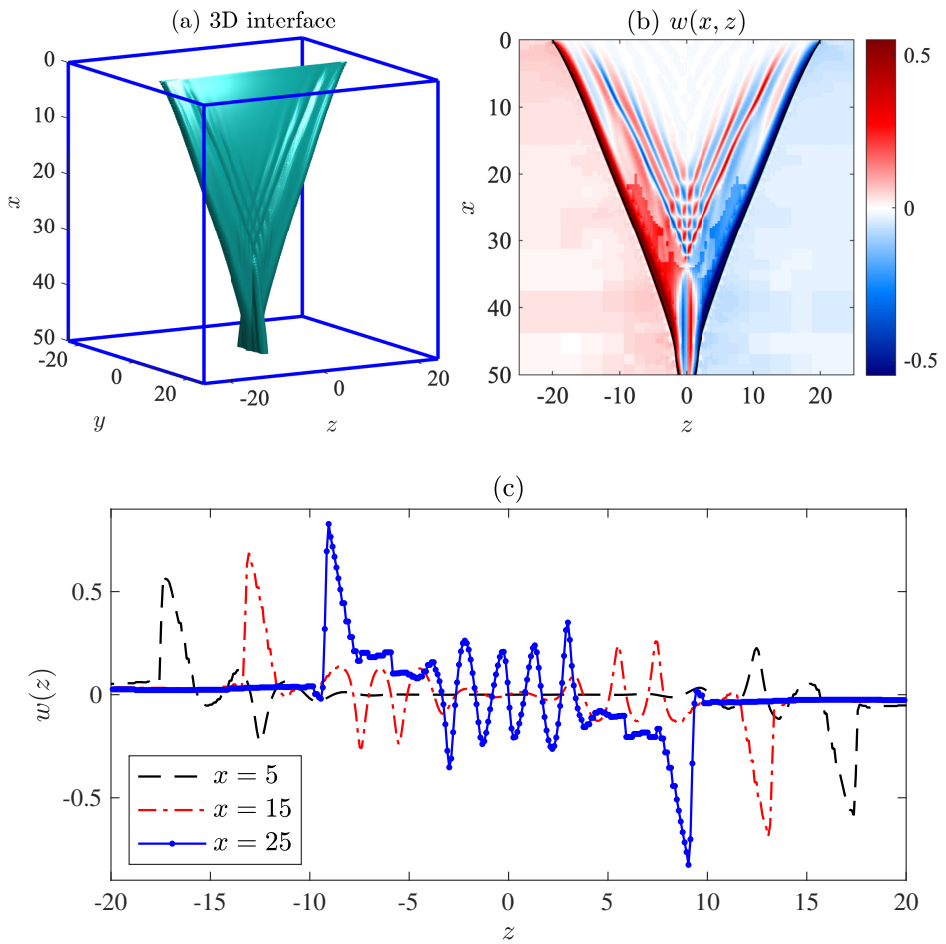


Figure 4.23. Three-dimensional view of the liquid sheet interface (a), spanwise velocity field w in xz plane (b) and $w(z)$ profiles at different streamwise x stations (c). $AR = 40$, $We = 2.5$.

(b), and $w(z)$ profiles at different streamwise x stations within the same plane. Fig. 4.23(a) depicts the typical shape assumed by the curtain once steady conditions are achieved starting from the parallelepiped initial condition previously described. It exhibits the characteristic triangular shape outlined by previous theoretical and experimental analyses (among others, notable are the works by Chubb and White [104], Chubb and Calfo [105], Chubb *et al.* [106, 7], Kacem *et al.* [26], Jaber and Tadjfar [107]), due to the edges retraction and convergence towards the central axis ($x = 0$) under the effect of surface tension. By inspection of the three-dimensional interface, it is possible to observe striped patterns indicating the presence of surface capillary waves, which manifest as stationary ripples in the transition area between the lateral rims and the planar part of the sheet, resulting from the competition between viscous and capillary forces. The dimensionless parameter representing the relative importance of viscous and surface tension effects is the Ohnesorge number $Oh = \mu/\sqrt{2H_i^* \rho_l \sigma}$, which in the present case is equal to $Oh = 0.0019 \ll 1$, leading to the formation of capillary waves near the rims as theoretically and numerically predicted by Sunderhauf *et al.* [108], Savva and Bush [109], Pierson *et al.* [110], Deka and Pierson [111], Karim *et al.* [112], and experimentally observed by Kacem *et al.* [26].

The spatial evolution of ripples is quantified by showing the spanwise velocity component $w(x, z)$ distribution (Fig. 4.23(b)) and the profiles $w(z)$ at different x stations (panel (c)) in $y = 0$ plane. At $x = 5$ (black curve in panel (c)), it can be seen that the velocity oscillates between negative and positive values after it drops down steeply in the region between the rim and the inner part of the curtain; the same behaviour was highlighted by Sunderhauf *et al.* [108] in the study of the edge retraction of a planar liquid sheet for low Oh values (see in particular Fig. 8 in [108]). Moving along the streamwise x direction, further crests appear starting from the curtain rims, which are displaced towards the central part of the sheet due to the rim retraction (as depicted by the black, red and blue curves

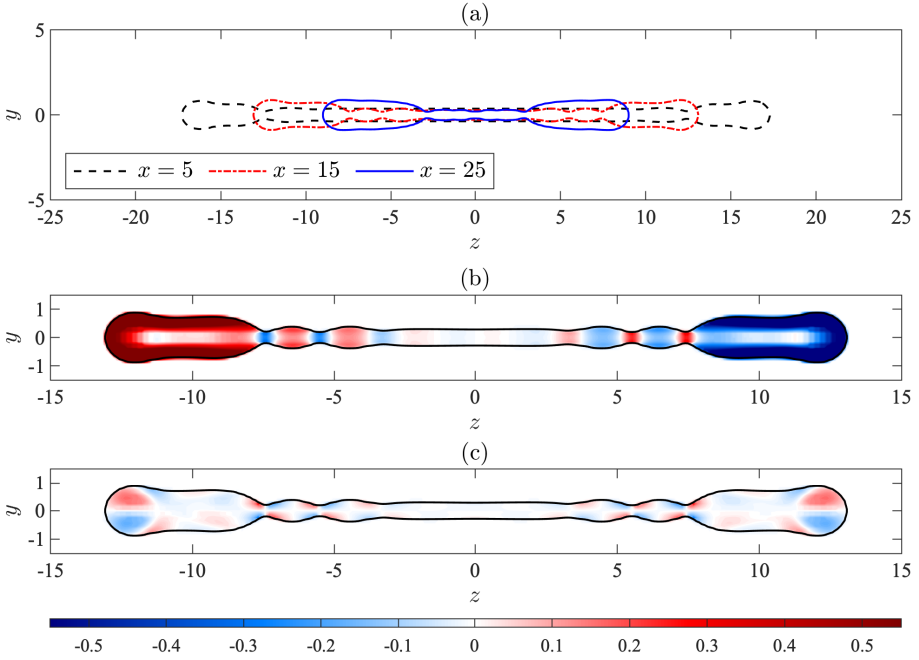


Figure 4.24. Interface shape in yz planes located at different x stations (panel (a)); maps of spanwise w (panel (b)) and transverse v (panel (c)) liquid velocity components at $x = 15$. $AR = 40$, $We = 2.5$.

in Fig. 4.23(c)). As a combined effect of gravity acceleration and rims retraction, the waves coming from the edges interfere with each other for $x > 20$, producing a criss-cross pattern, as also found experimentally by Kacem *et al.* [26]. Moreover, the competition between gravity and surface tension forces determines a streamwise variation of w at the rims, with values ranging from 0.5 to 0.9 for $x \in [5; 25]$; the order of magnitude agrees with the theoretical prediction of rim retraction velocity given by the classic Culick formula (Culick [113]), $u_c = \frac{1}{U_i^*} \sqrt{\frac{2\sigma}{\rho_l H_i^*}} = 0.63$, a reference value which does not take into account the vertical gravity acceleration nor viscous effects.

From Fig. 4.23(b)-(c), it can be also noted that the ripples wave-

length λ_c , estimated as the distance between two successive peak values of w in the central part of the sheet (blue curve in panel (c) for $-5 < z < 5$) is approximately equal to 1.85, in good agreement with the capillary length $l_c = \frac{1}{H_i^*} \sqrt{\frac{\sigma}{\rho_l g}} = 1.81$, representing a typical length scale in flows driven by capillary effects. It is interesting to note that a similar value equal to $\lambda_c = 1.63$ has been recently found in the study of an axisymmetric filament retraction at low Oh and high aspect ratio values [110] (see the discussion on page 8 of Pierson *et al.* [110]), being the wavelength scaled with respect to the filament diameter. Furthermore, from Fig. 4.23(c) it can be appreciated that the sheet evolution perturbs the initially quiescent ambient phase, which manifests the phenomenon of gas entrainment, that is to say $w < 0$ (> 0) for $z > 0$ (< 0) outside the curtain, respectively.

The overall flow topology is further elucidated by observing the curtain interface shapes in three cross sections taken with planes parallel to $x = 0$ plane, namely $x = 5, 15$ and 25 (Fig. 4.24(a)), together with the colour maps of spanwise w and transverse v velocity components within the liquid phase at $x = 15$ (panels (b) and (c) of Fig. 4.24, respectively). It can be seen that, as the curtain width reduces along the streamwise direction, the rims thicken (panel (a)) and the capillary ripples are displaced towards the curtain centre, thus producing varicose patterns (i.e., symmetric with respect to $y = 0$ axis) and associated transverse v velocity distributions in yz planes.

The distribution of the streamwise velocity component $u(x, y)$ in $z = 0$ plane within the liquid phase is reported in Fig. 4.25 (panel (a)), while the comparison between various estimates of the centreline streamwise velocity is illustrated in Fig. 4.25 (panel (b)). In particular the latter compares the u streamwise trend for $y = 0$ (red line) with the y -averaged velocity in xy plane, $\langle u(x, y) \rangle$, defined as

$$\langle u(x, y) \rangle = \frac{1}{\int_{-L/2}^{L/2} C(x, y) dy} \cdot \int_{-L/2}^{L/2} C(x, y) u(x, y) dy, \quad (4.10)$$

Table 4.6. Comparison between theoretical (L_c^{th}) and numerical (L_c) values of the convergence length by varying Weber and Froude numbers. The relative percentage spread is defined as $\epsilon_c = 100 \cdot (L_c - L_c^{th})/L_c$. $AR = 40$.

We	Fr	L_c^{th}	L_c	ϵ_c
2.5	0.41	27.96	32.19	13.14 %
2.25	0.37	26.76	29.94	10.62 %
2.0	0.33	25.46	28.18	9.65 %
1.75	0.29	24.10	26.32	8.43 %
1.5	0.25	22.65	24.66	8.15 %

where $L = L^*/H_i^*$ (black continuous line), and the free-fall Torricelli's theoretical solution $u_{torr} = \sqrt{1 + (2x)/(ARFr)}$ is indicated by the black dashed line.

The analysis of Fig. 4.25 allows one to distinguish three different regions of the flow field. In the first one, extending from $x = 0$ to approximately $x = 20$, the flow develops nearly two-dimensional in the plane xz ; due to gravity action, the sheet thickness reduces and the streamwise velocity increases. The initial parabolic velocity profile tends to relax towards a quite plug distribution, as shown by the convergence between the axial value of the velocity $u(x, y = 0)$ and the one-dimensional reduction $\langle u(x, y) \rangle$, which well agrees with the theoretical value u_{torr} as x increases. The second region is located in the range $20 < x < L_c$ (with $L_c \approx 32$), where the streamwise velocity displays an oscillating trend (see the superposition of red and black continuous curves) as a result of the interference between right-rim and left-rim incoming capillary waves, producing the characteristic criss-cross pattern already discussed (Fig. 4.23(b)). Finally, in the third region ($x > L_c$), downstream of the rims con-

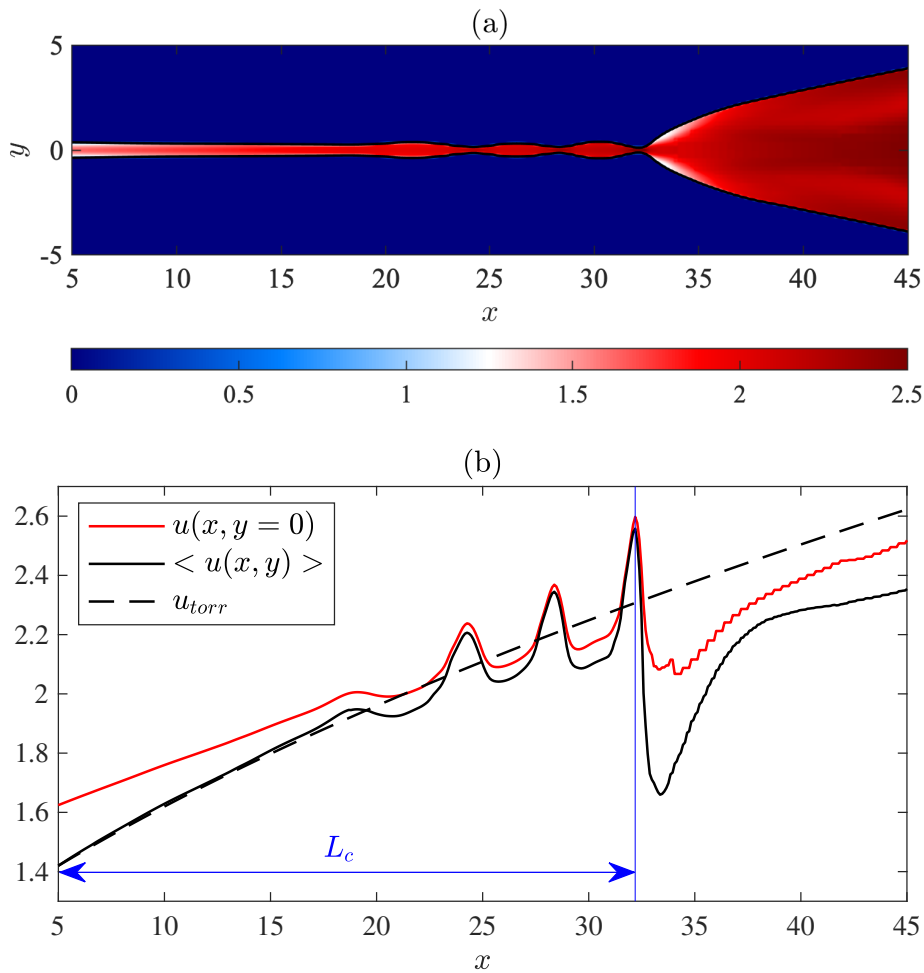


Figure 4.25. Map in xy plane of the streamwise velocity u (panel (a)); x -variation of the axial velocity $u(x, y = 0)$ and y -averaged trend $\langle u(x, y) \rangle$ (b). The reference Torricellian velocity u_{torr} and the calculated convergence length L_c are also reported. $AR = 40$, $We = 2.5$.

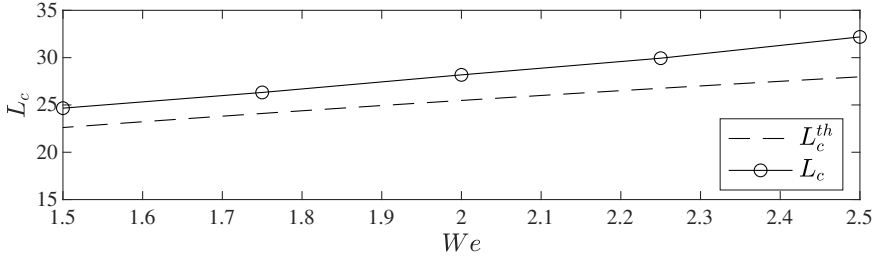


Figure 4.26. Convergence length L_c variation with Weber number. The theoretical prediction L_c^{th} is also reported.

vergence (see again Fig. 4.25(a)) the sheet is characterized by a tail with increasing thickness in xy plane denoting a switching axis effect. Note that L_c has been calculated as the x value corresponding to the maximum of $u(x, y = 0)$. It is interesting to observe that the present estimate of L_c agrees with the theoretical prediction made with the simplified model by Chubb *et al.* [7],

$$L_c^{th} = \frac{FrAR}{2} \left[\left(1 + \frac{3}{2Fr} \sqrt{\frac{We}{8}} \right)^{\frac{4}{3}} - 1 \right]. \quad (4.11)$$

Table 4.6 shows that the relative percentage spread $\epsilon_c = 100 \cdot (L_c - L_c^{th})/L_c$ in the range $We \in [1.5, 2.5]$ is less than 15%. Note that the numerical simulations at different Weber number values are performed by decreasing the inlet velocity U_i^* , thus determining a corresponding reduction of the Froude number as highlighted in Table 4.6. The variation of the convergence length with the Weber number is also shown in Fig. 4.26, together with the theoretical prediction L_c^{th} .

4.1.3 Supercritical-to-subcritical flow transition

The free and forced responses of gravitational liquid sheet flows interacting with an unconfined air ambient are hereafter analysed nu-

merically and experimentally in transcritical conditions, namely for Weber number values traversing from supercritical ($We > 1$) to subcritical ($We < 1$) regime. The numerical investigation is based on the linear inviscid one-dimensional model presented in Section 2.1.3. The eigenvalues analysis (Section 3.2) is employed to determine numerically the natural response, while the numerical integration of the governing equations (Eqs. (2.13)-(2.14) in Section 2.1.3), equipped with an inlet boundary condition including a harmonically oscillating transverse velocity, gives the forced behaviour of the sheet. Experimental tests are performed to measure the free response of the flow system (Section 3.4) and provide comparisons with numerical predictions.

Natural frequency discontinuity

Results of the spectral analysis for Weber numbers around unity are hereafter presented to shed light on the natural response of the flow when crossing the critical regime. Fig. 4.27, panels (a) and (b), compares spectra obtained in supercritical and subcritical conditions, with panel (b) depicting a zoom of the spectrum inner part; the relevant dimensionless parameters are listed in Table 4.7. Since the Weber number is modified by varying the inlet velocity, the Froude number accordingly changes, ranging from $Fr = 0.08$ to 0.05 as the Weber number varies from $We = 1.2$ to 0.8 .

As discussed by Girfoglio *et al.* [13] for the nappe problem, and recovered in Section 4.1.2 for the present liquid sheet configuration, the supercritical regime is characterized by the presence of two branches exhibiting an almost constant spacing $\Delta\lambda_i$ between the imaginary part of the eigenvalues (frequency), which is directly associated with the crossing time of slow (upper branch, $\Delta\lambda_i^-$) and fast (lower branch, $\Delta\lambda_i^+$) travelling waves (i.e., with velocity $\mp\sqrt{U/We}$ relative to that of the base flow U , respectively) featuring the solution of Eqs. (2.13)-(2.14). On the other hand, when the Weber number is reduced below the unity, the spectrum reveals the fast branch only; therefore, for

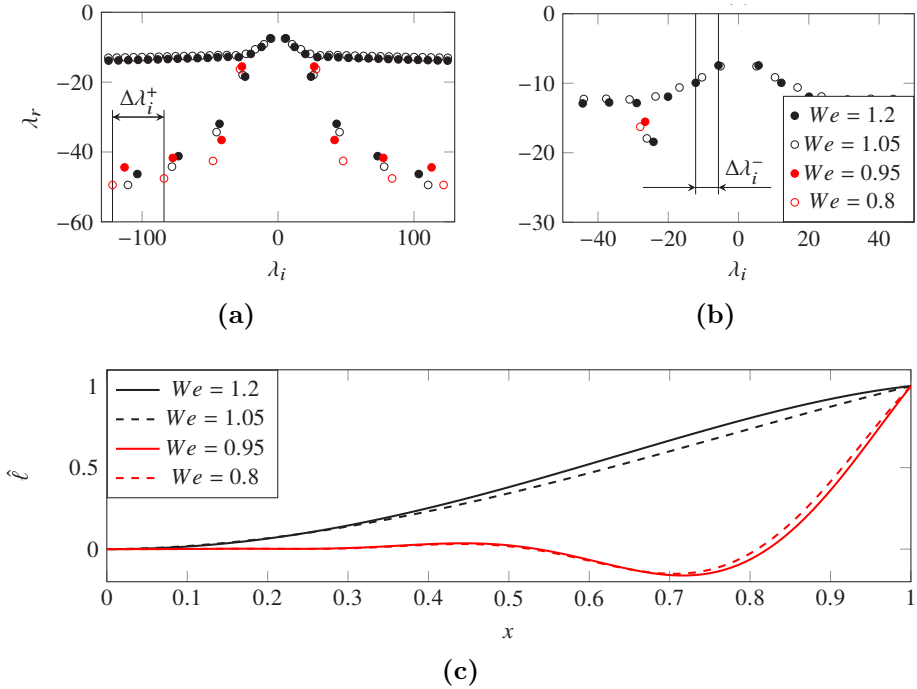


Figure 4.27. Combined We - Fr effect on the eigenvalues, panels (a) and (b), and on the normalized least stable eigenfunction, panel (c): $(We, Fr) = (1.2, 0.08)$, black filled dot and continuous black line; $(1.05, 0.07)$, black open dot and dashed black line; $(0.95, 0.06)$, red filled dot and continuous red line; $(0.8, 0.05)$, red open dot and dashed red line. Panel (b) shows a zoom of the inner part of the spectra reported in panel (a). The characteristic frequencies $\Delta\lambda_i^+$ and $\Delta\lambda_i^-$, whose values are listed in Table 4.8, are indicated respectively in panels (a) and (b).

Variable	Value
r_ρ	0.001
ε	0.01
Fr	0.08, 0.07, 0.06, 0.05
We	1.2, 1.05, 0.95, 0.8

Table 4.7. Dimensionless parameters involved in the numerical analysis of supercritical-to-subcritical flow transition.

$We = 1.05$ the characteristic frequency of the system, $\Delta\lambda_i^- = 6.16$, is associated with the crossing time of the slow wave, whilst for $We = 0.95$ it is $\Delta\lambda_i^+ = 33.80$ (Fig. 4.27 and Table 4.8), thus exhibiting a jump when traversing the critical regime (Table 4.8). An analogous discontinuity was found by Girfoglio *et al.* [13] for the nappe configuration; note also the continuous trend of $\Delta\lambda_i^+$ around the We critical threshold. The natural frequency discontinuity corresponds to an abrupt change in the eigenmode shape $\hat{\ell}$ associated with the least stable frequency of the spectrum, which is reported in Fig. 4.27(c) for We progressively reduced from $We = 1.2$ to $We = 0.8$. Note that each curve is normalized with respect to its maximum, which for all cases occurs at the domain exit section, such that $\hat{\ell}(1) = 1$. It is worth noting that the theoretical prediction of the liquid sheet natural frequency, and therefore its jump when the supercritical-to-subcritical flow transition occurs, strongly relies on two features of the curtain flow model here employed (Eqs. (2.13)-(2.14)): accounting for the sheet-ambient interaction via Eq. (2.15) (see Section 2.1.3), and considering a sheet of finite length L^* . As a matter of fact, if one neglects the pressure term (2.15) in case of a finite length curtain, the linear stability analysis yields an empty spectrum, i.e. no natural frequency is detected, and consequently no frequency discontinuity. On the other hand, if a curtain of infinite length is considered, the

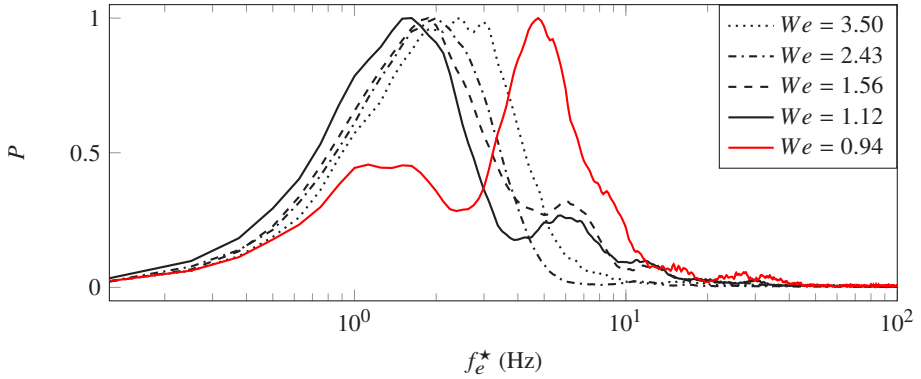


Figure 4.28. Normalized power spectral density of the vibrometer recordings acquired at different values of the Weber number.

We	1.2	1.05	0.95	0.8
$\Delta\lambda_i^-$	7.22	6.16	—	—
$\Delta\lambda_i^+$	29.83	31.99	33.80	36.88

Table 4.8. Global frequency in supercritical ($\Delta\lambda_i^-$, $We > 1$) and subcritical ($\Delta\lambda_i^+$, $We < 1$) flow regimes.

natural frequency predicted by the theoretical analysis vanishes; the latter question is addressed in detail by Chiatto and Della Pia [114] and not reported herein.

Results of the natural flow response experimental investigation are presented in Fig. 4.28, which reports the normalized power spectral density (PSD) of the signals acquired by the vibrometer for the following Weber number values: $We = 3.50, 2.43, 1.56, 1.12, 0.94$. The lowest value of We corresponds to the minimum flow rate allowing to maintain a stable two-dimensional liquid sheet. For each test condition, the measurement was repeated 20 times. At $We = 3.5$ the flow is fully in supercritical conditions, and the PSD exhibits a peak at $f_e^* = 2.38$ Hz. When We decreases, according to the stability

We	f_e^* (Hz)	f_n^* (Hz)	ϵ	s
3.50	2.38	2.52	5.56 %	16.4 %
2.43	2.00	2.30	13.04 %	10.2 %
1.56	1.88	2.00	6.00 %	11.0 %
1.12	1.63	1.67	2.40 %	11.8 %
0.94	4.75	4.84	1.86 %	8.0 %

Table 4.9. Experimental and numerical values of the natural frequency varying the Weber number. The relative percentage spread ϵ is defined as $\epsilon = 100 \cdot (f_n^* - f_e^*) / f_n^*$. The last column reports the standard deviation of the experimental measurements.

analysis predictions, the PSD peak moves towards lower f_e^* values, while a higher frequency dynamics is excited, as revealed by the secondary peak at $f_e^* \approx 6$ Hz for $We = 1.12$. A further decrease in the Weber number determines the flow transition from supercritical to subcritical regime, with the measured peak frequency undergoing a jump from $f_e^* = 1.63$ Hz ($We = 1.12$) to $f_e^* = 4.75$ Hz ($We = 0.94$). Table 4.9 and Fig. 4.29 show the agreement between experimental values (f_e^*) and numerical predictions (f_n^*) of the natural frequency, and confirm the occurrence of the discontinuity at $We = 1$. Note that the error bars reported in Fig. 4.29 and in last column of Table 4.9 represent the standard deviation (s) of the experimental measurements, whose values vary between 8% and 16% of the corresponding mean quantities. The reference frequency employed to convert the numerical data $\Delta\lambda_i^\pm$ in dimensional form f_n^* is $f_r^* = U_i^* / (2\pi L^*)$.

Forced dynamic response

The forced oscillatory dynamics of the sheet centreline is shown in Fig. 4.30 for supercritical ($We = 1.05$, left panels) and subcritical

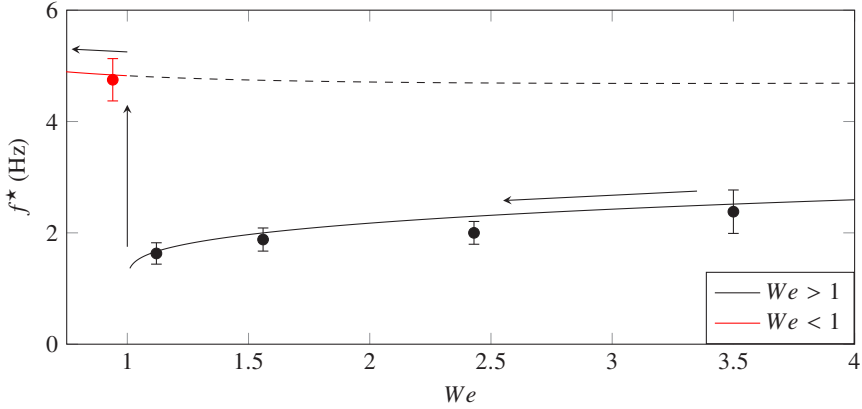


Figure 4.29. Comparison between numerical (f_n^* , continuous curves) and experimental (f_e^* , filled circles) natural frequencies in supercritical (black) and subcritical (red) regimes. The numerical frequency associated with the fast branch of spectrum in supercritical conditions is also reported (black dashed curve). The error bars represent the standard deviation of the experimental measurements.

($We = 0.95$, right panels) conditions. Results are obtained by solving Eqs. (2.13)-(2.14) enforcing the following boundary conditions

$$\ell(0, t) = 0, \quad (4.12)$$

$$v(0, t) = v_f(t) = A \sin(2\pi ft). \quad (4.13)$$

Three (dimensional) forcing frequencies f^* are considered in the analysis, namely $f^* = 1, 5, 20$ Hz, while the prescribed oscillation amplitude is $A = 5$ (corresponding to 5% of the inlet velocity magnitude U_i^* in the scale adopted). The initial unperturbed sheet centreline, $y = 0$, is denoted as a dashed line, while the solid lines indicate the centreline shapes at fixed times expressed as fractions of (dimensionless) oscillation period T . A transient solution is present in the domain after the forcing is introduced via the boundary condition (4.13) at $t = 0$. However, after less than one reference time ($t = 1$), the transient is expelled, and the sheet oscillations converge

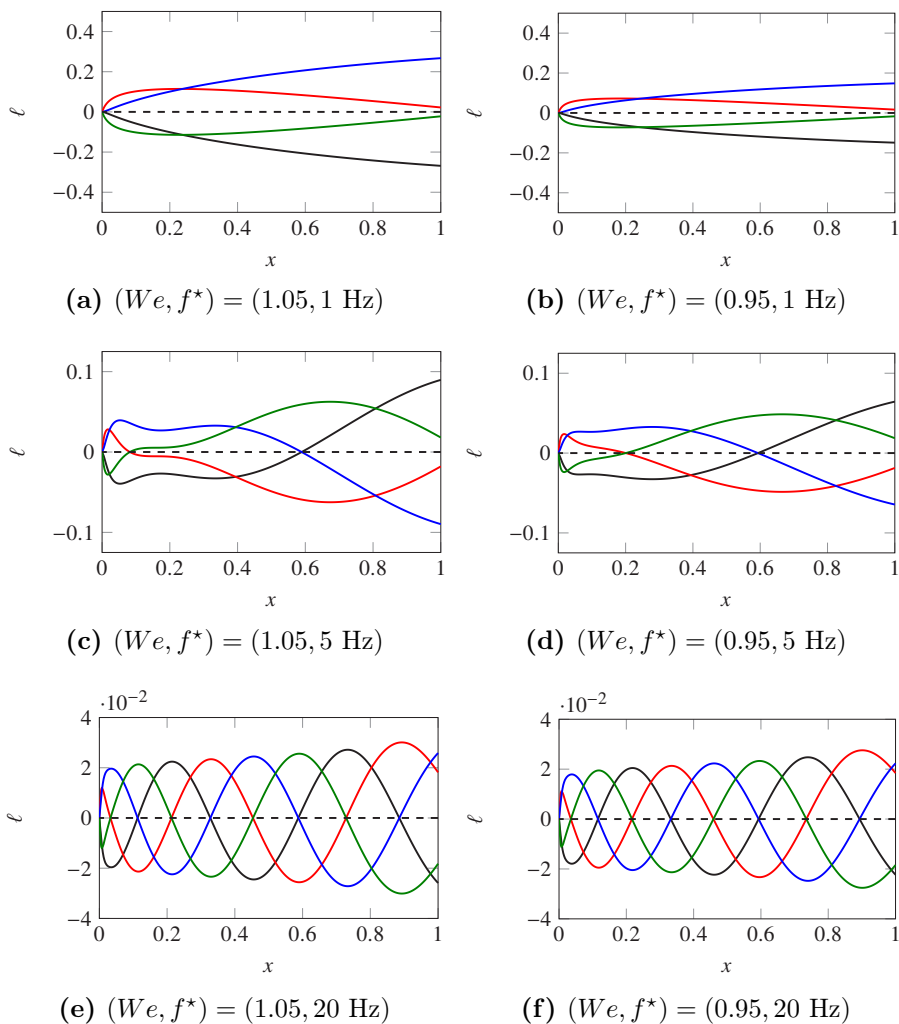


Figure 4.30. Weber number effect on the sheet centreline deflection, ℓ , as a function of the streamwise station, x , at different fractions of oscillation period T : $t = 0 \cdot T$ (black); $0.25 \cdot T$ (red); $0.5 \cdot T$ (blue); $0.75 \cdot T$ (green). The dashed line denotes the centreline of the unperturbed curtain. From top to bottom: $f^* = 1, 5$ and 20 Hz .

to periodic solutions for all the forcing frequencies considered, which are the ones reported in Fig. 4.30. Moreover, it has been verified that the converged values of the curtain centreline amplitude within each oscillation cycle do not depend on the specific boundary condition initial value, $v(x = 0, t = 0)$, i.e. on the forcing phase.

For all f^* and We values investigated, one observes that as the forcing frequency is increased the oscillation wavenumber also increases, whilst the maximum amplitude of sheet deflection correspondingly decreases. An analogous behaviour has been recently highlighted by Torsey *et al.* [22]. At the highest forcing frequency, panels (e)-(f), the sheet response shows a convective character and a shorter wavelength. As a major result of the analysis of the forced oscillatory curtain dynamics, it is possible to appreciate that, for each f^* value, the sheet response varies continuously when the flow undergoes the supercritical-to-subcritical transition, with both the sheet shapes and amplifications being quite similar for $We = 1.05$ and $We = 0.95$. Considering the analogous result found by Torsey *et al.* [22] in case of an infinite liquid sheet subjected to imposed ambient pressure disturbances not coupled with the curtain motion, one can infer that the continuous behaviour of the finite length curtain forced dynamics at the transcritical threshold does not depend on the specific curtain-ambient interaction model employed. The latter consideration is further corroborated by the analysis provided in Chiatto and Della Pia [114], where it is shown that, even neglecting the coupling (2.15) in Eqs. (2.13)-(2.14), the forced oscillatory dynamics varies continuously between $We > 1$ and $We < 1$.

4.1.4 Subcritical regime

The major aim of this section is to report on direct numerical simulations of subcritical liquid curtains continuously forced by a sinuous perturbation in lateral velocity. The forcing is applied at the sheet inlet section and basically excites sinuous modes of the system related to the natural impulse response, whose properties have

Parameter	Value
r_ρ	0.01
r_μ	0.02
ε	0.02
Re	20, 40, 400, 800, 1600
Fr	0.329
We	0.75

Table 4.10. Dimensionless parameters involved in the subcritical regime analysis.

been characterized in previous Sections 4.1.2 and 4.1.3. However, it will be shown through the application of the SPOD technique (Section 3.3.1) to numerical data that, in particular resonance conditions, also varicose modes are triggered due to nonlinear effects of interaction among modes. A surface tension-induced instability of the flow in highly subcritical regime is finally highlighted, by means of the energy budget decomposition of numerical data (Section 2.1.3) and linear stability analysis (Section 3.2).

Forced behaviour

Volume-of-fluid simulations of the forced curtain subcritical dynamics are performed for flow conditions specified in Table 4.10. Note that the critical station x_s (Eq. (2.25) in Section 2.1.3) and the natural frequency f_n^* predicted by the inviscid theoretical analysis in these conditions are respectively equal to $x_s = 0.13$ and $f_n^* = 26.26$ Hz. The sheet oscillations are excited via Eq. (4.13), i.e. by a time-continuous forcing introduced in the lateral velocity at inlet ($x = 0$), and different Reynolds number Re are considered. The oscillatory signals are post-processed through the FFT algorithm; results are

first presented in Fig. 4.31, where the left panels show the mean-line maximum oscillation amplitude A_ℓ as a function of the streamwise direction x for various forcing frequencies f^* , and right panels as a function of the forcing frequency at several stations. Depending on the Reynolds number, two different dynamical behaviours are observed (right panels). At low Reynolds numbers, $Re \leq 40$, the high viscosity effect makes the system overdamped, being the oscillation amplitude monotonically decreasing with the forcing frequency as is usual for standard forced-damped oscillators of low degrees-of-freedom. As Re increases, $Re \geq 800$, for which the inviscid conditions are approaching, the frequency response exhibits a resonance frequency which closely agrees with the natural frequency predicted by the linear stability analysis. Furthermore, the envelope of oscillation amplitudes (left panels) is quite uniform along the streamwise extent of the sheet at the higher Reynolds numbers, whilst it exhibits remarkably greater values towards the tail of the sheet at the lower Re . From one hand, this is due to the fact that the tail region is practically locally inviscid. On the other hand, as discussed later by application of the SPOD technique, in resonance conditions at high Re numbers the sheet thickness displays a varicose shape, that reduces the envelope amplitude. Fig. 4.31 shows that the resonance frequency occurs in a global way, i.e. it is the same at all the sheet stations, when the Reynolds number is progressively increased from $Re = 20$ to $Re = 1600$. As a global resonance frequency, it can be therefore actually compared with the global natural frequency predicted by the inviscid model.

To shed light on the mechanisms producing the resonance phenomenon as the Reynolds number varies, the frequency response of the one dimensional reduced transverse velocity field (Eq. (4.4) in Section 4.1.1 applied to $v(x, y)$ field) has also been investigated by applying the FFT technique. Results in terms of oscillation amplitude of lateral velocity, A_v , are reported in Fig. 4.32, as a function of x for various forcing frequencies (left column), and as a function of the forcing frequency f^* for various stations x (right column). The

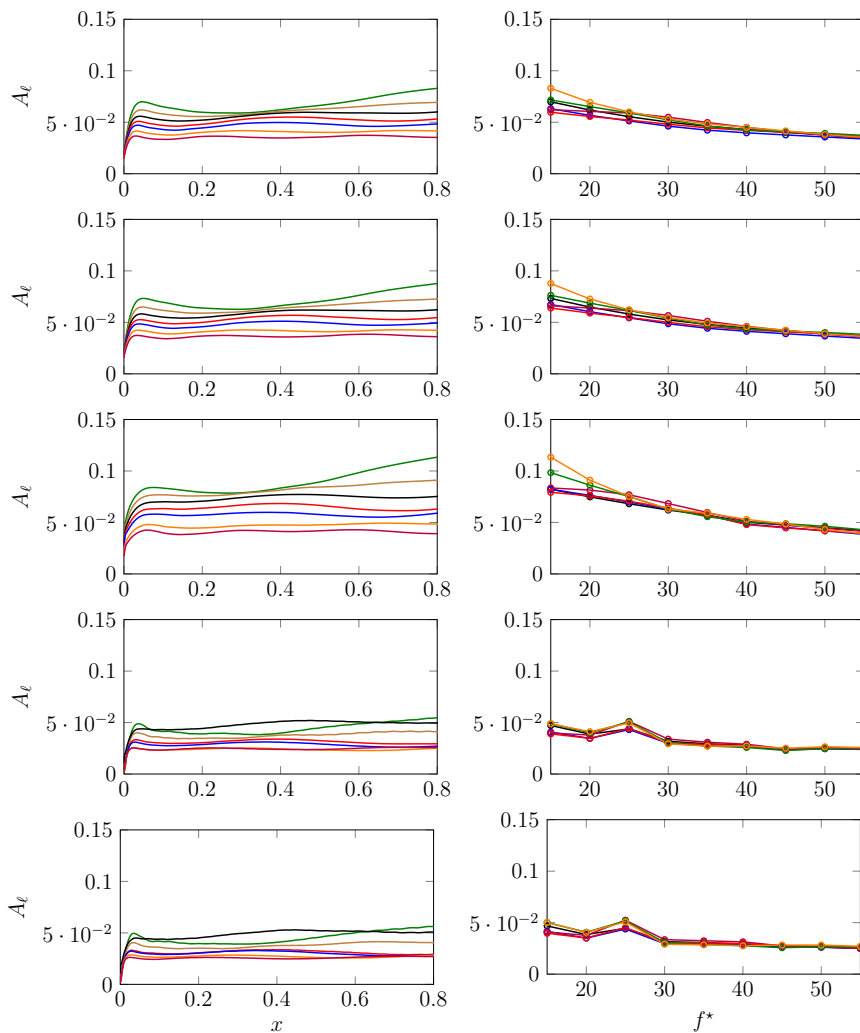


Figure 4.31. Reynolds number Re effect on the meanline maximum oscillation amplitude A_ℓ as a function of the streamwise direction x at different forcing frequencies f^* (left column) and of the forcing frequency at different streamwise stations (right column). Left column: $f^* = 15$ (green curve); 20 (brown); 25 (black); 30 (red); 35 (blue); 45 (orange); 55 (purple) Hz. Right column: $x = 0.05$ (black); 0.13 (blue); 0.2 (red); 0.4 (purple); 0.6 (green); 0.8 (orange). Natural frequency predicted by the theoretical model: $f_n^* = 26.26$ Hz. From top to bottom: $Re = 20, 40, 400, 800, 1600$.

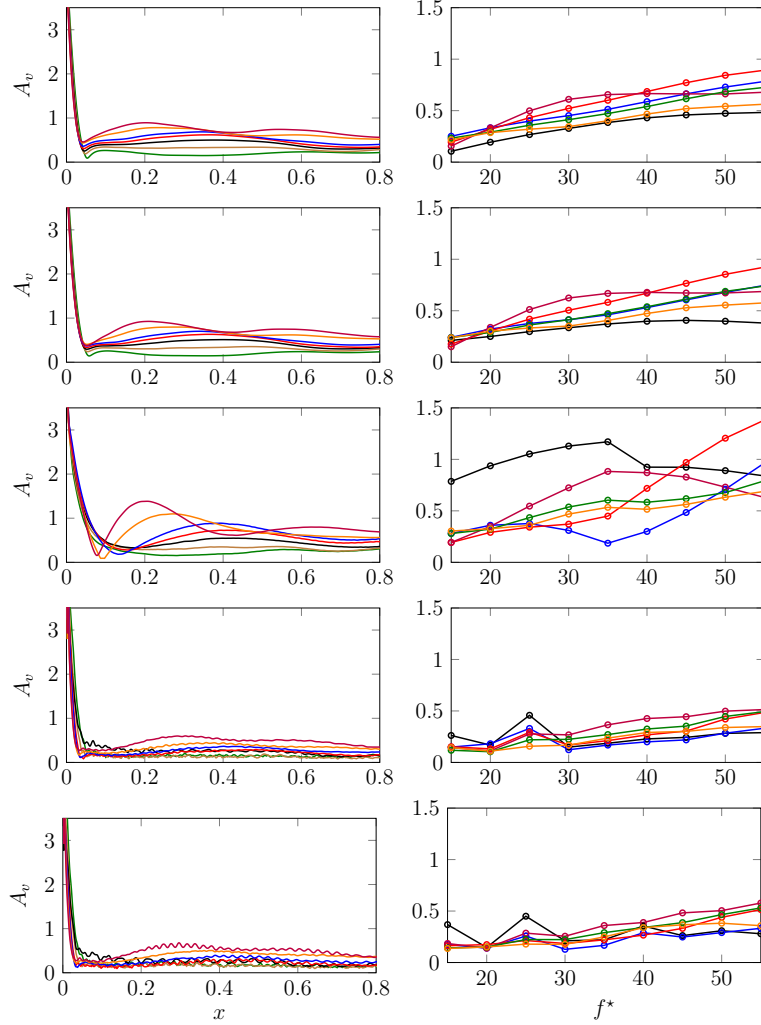


Figure 4.32. Reynolds number Re effect on the maximum oscillation amplitude of transverse velocity component A_v as a function of the streamwise direction x at different forcing frequencies f^* (left column) and of the forcing frequency at different streamwise stations (right column). Left column: $f^* = 15$ (green curve); 20 (brown); 25 (black); 30 (red); 35 (blue); 45 (orange); 55 (purple) Hz. Right column: $x = 0.05$ (black); 0.13 (blue); 0.2 (red); 0.4 (purple); 0.6 (green); 0.8 (orange). Natural frequency predicted by the theoretical model: $f_n^* = 26.26$ Hz. From top to bottom: $Re = 20, 40, 400, 800, 1600$.

analysis of Fig. 4.32, right panels, reveals that at $Re = 400$ a local peak of A_v at $f^* = 25$ Hz (i.e. in practice at the leading natural frequency) appears in correspondence of the critical station predicted by the simplified theoretical model, $x_s = 0.13$, while at lower Reynolds numbers the function $A_v(f^*)$ monotonically increases at the critical station. It is interesting to note that the peak frequency $f^* = 25$ Hz, which has a local character at $Re = 400$, becomes global further increasing the Reynolds number up to 1600. As matter of fact, the resonance peaks at the various streamwise stations synchronize with each other at this frequency for $Re \geq 800$ (while at $Re = 400$ they depend on the x station considered). The A_v synchronization of all the streamwise locations at the resonance frequency as the Reynolds number increases, approaching the almost inviscid conditions, allows one to state that $f^* = 25$ Hz is a global natural frequency of the system, thus recovering the considerations previously made. From another point of view, one can argue that the various x stations synchronize with the critical station as the Reynolds number increases, and therefore it forces the global oscillations of the entire flow field. This behaviour of the critical station x_s resembles the concept of wavemaker, which has been characterized both through local (Pier and Huerre [115]) and global (Giannetti and Luchini [116]) stability studies for unstable flows. Pier and Huerre [115] studied the self-sustained oscillations of wake flows applying the local spatio-temporal stability analysis, and they were able to identify the non-linear wake oscillation frequency with the local frequency of the convective/absolute transition station, which therefore imposes its own frequency over the entire flow field. Giannetti and Luchini [116] analyzed the stability properties of the flow past an infinitely long circular cylinder in the context of linear theory. The core of the instability was identified by inspecting the spatial structure of the product between the direct and adjoint eigenfunctions. This quantity takes into account the feedback which is at the origin of the self-excited oscillation and which is located in a region of the flow which acts as a wavemaker. In the context of gravitational liquid sheet flows, de Luca and Costa [14]

found that the critical station separates the upstream subcritical region, where the flow is absolutely unstable, from the supercritical downstream one, where the flow is convectively unstable. It is worth pointing out that analyzing the flow field structure to obtain information about the mechanisms underlying the global oscillations of flow systems has been so far applied to study unstable flows, which exhibit self-sustained oscillations. In the present case, such a kind of investigation is performed on a forced globally stable flow system.

Sinuuous-varicose modes interaction in resonance conditions

To shed light on the liquid curtain flow behaviour in subcritical resonance conditions, a SPOD analysis of VOF data obtained at $We = 0.75$ for the different Reynolds number Re values is performed. The state vector $\mathbf{q}(\mathbf{x}, t)$ is obtained by stacking the fluctuations of the velocity components (u' and v') and of the volume fraction (C') in a column vector for a given time instance. $N = 2500$ snapshots have been considered, dividing the data in $N_b = 12$ blocks of equal length ($N_f = 374$). The Strouhal number $St = f^* H_i^* / U_i^*$ ranges from 0 to 0.30, with a resolution of $\Delta St = 0.0017$; $St = 0.076$ corresponds to the forcing frequency $f^* = 25$ Hz. The normalized SPOD spectra at various Re are reported in Fig. 4.33. The flow presents a clear modal separation at the forcing frequency and its harmonics at all Reynolds numbers. At the highest Reynolds number ($Re = 1600$), a peak occurring at the sub-harmonic frequency $St = 0.038$ is also detectable, this being a typical behaviour of nonlinear phenomena (Hayashi [117]), associated with the quadratic phase coupling (Schmidt [118]).

Fig. 4.34 shows the normalized cumulative energy distribution of SPOD C' modes at various Reynolds numbers for a driving frequency close to the natural one. At low Re , the first 10 modes contribute for approximately 99% to the total energy of the flow. As the Reynolds number increases, due to nonlinear effects, higher modes are excited and about 100 modes are needed to capture the same amount of

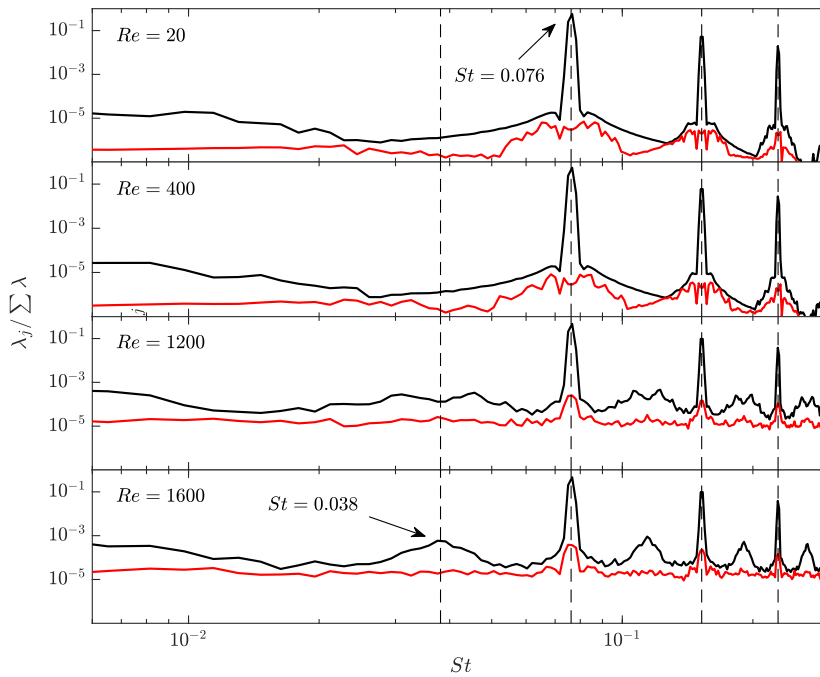


Figure 4.33. Normalized SPOD spectra at $We = 0.75$ for different Reynolds number Re values. The spectra report only the frequency content of the first 2 modes. Forcing frequency $f^* = 25$ Hz ($St = 0.076$).

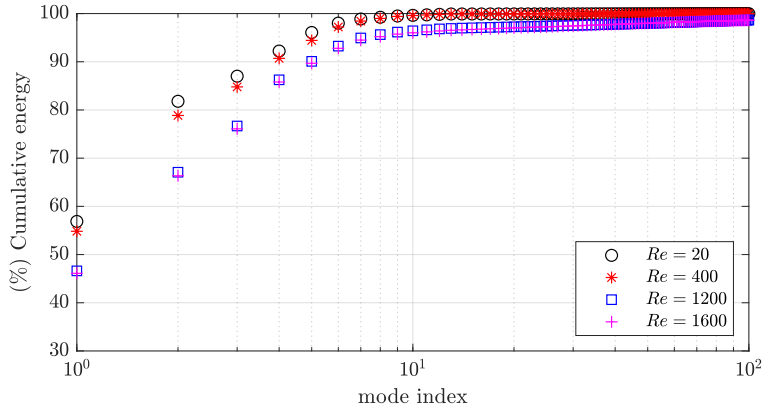


Figure 4.34. Cumulative energy distribution of SPOD modes at $We = 0.75$ for different Reynolds number Re values.

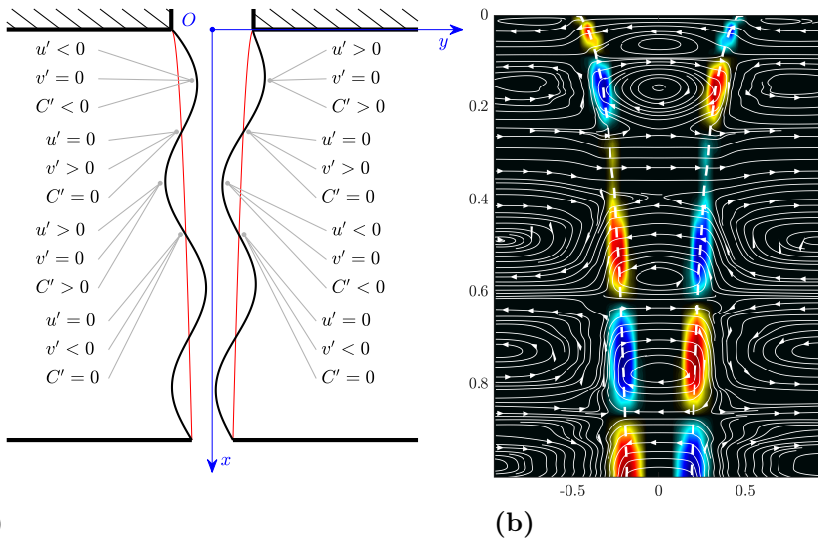


Figure 4.35. Panel (a): sketch of sinuous disturbance. The red lines denote the interface of the mean field. Panel (b): streamlines pattern as viewed by an observer moving with the mean flow. The colour map refers to $C'(x, y)$ mode ($0 < x < 1$, $-1 < y < 1$).

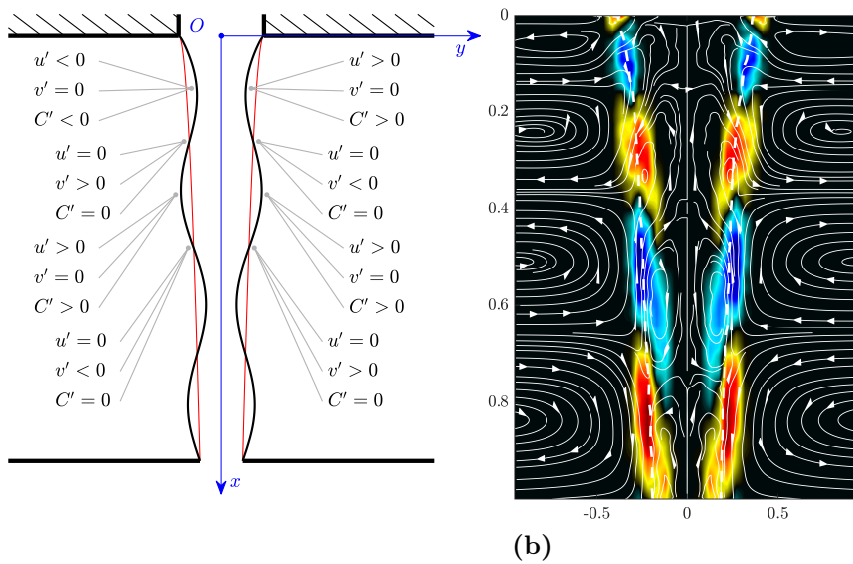


Figure 4.36. Panel (a): sketch of varicose disturbance. The red lines denote the interface of the mean field. Panel (b): streamlines pattern as viewed by an observer moving with the mean flow; the colour map refers to the varicose part of $C'(x, y)$ mode ($0 < x < 1$, $-1 < y < 1$).

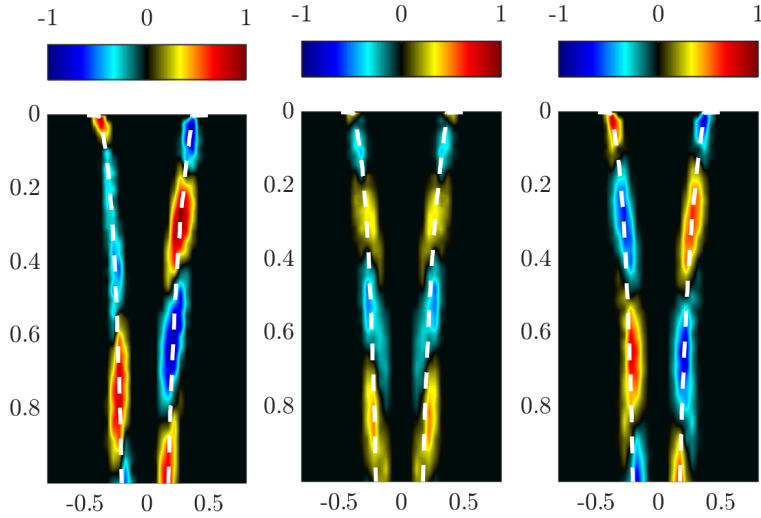


Figure 4.37. Decomposition in sinuous and varicose components of the flow field at $We = 0.75$, $Re = 1600$. $C'(x, y)$ mode (left panel) and its varicose (middle panel) and sinuous (right panel) components ($0 < x < 1$, $-0.75 < y < 0.75$).

energy at $Re > 1000$. The same results are retrieved when applying the POD technique (not reported).

A main result coming from the SPOD of the flow fields is the nonlinear behaviour of the system approaching the inviscid regime, revealed by the appearance of secondary varicose modes when the curtain is sinusoidally forced in resonance conditions, which superpose on the main sinuous deformation of the sheet shape. The sinuous contributions show an antisymmetric behaviour for $u'(x, y)$ and $C'(x, y)$ and a symmetric one for $v'(x, y)$ (Fig. 4.35, $x = x^*/L^*$ and $y = y^*/H_i^*$), whereas the opposite holds for the varicose contributions, as sketched in Fig. 4.36(a). The panel (b) depicts the streamlines pattern as viewed by an observer moving with the mean flow. The colour map reports the spatial distribution of varicose part of C' mode. To recover sinuous and varicose structures, any mode φ_j can be decomposed according to Eq. (4.8). Fig. 4.37 reports the varicose

and sinuous components extracted for the C' mode at $Re = 1600$, where φ_j^s and φ_j^v are defined as:

$$\varphi_{C'}^s(x, y) = [\varphi_{C'}(x, y) - \varphi_{C'}(x, -y)]/2, \quad (4.14a)$$

$$\varphi_{C'}^v(x, y) = [\varphi_{C'}(x, y) + \varphi_{C'}(x, -y)]/2. \quad (4.14b)$$

Further details regarding the sinuous-varicose modes interaction in resonance conditions, including a parametric analysis of the flow behaviour at different We and St numbers, and the flow field low-order reconstruction by means of SPOD modes, are given in Colanera, Della Pia, Chiatto, de Luca and Grasso [119].

Subcritical unstable behaviour

Numerical simulations of the curtain dynamics excited by means of the impulse perturbation (4.5) are performed for $We < 1$, following the same approach used in supercritical regime (Section 4.1.2). Two Weber number values are considered, respectively greater and lower than We_{th} (Eq. (2.24) in Section 2.1.3), namely $We = 0.8$ and $We = 0.4$. Results of the spatio-temporal evolution of the transverse velocity perturbation $v(x, t)$ are reported in Fig. 4.38(a)-(b). As theoretically recalled in Section 2.1.3, the velocity signal splits into two travelling waves with opposite directions (i.e. left and right travelling waves) for $We < 1$. Following the temporal evolution of the meanline perturbation (black line is for $t = 0.25$, blue line for $t = 2.5$, red line for $t = 7.5$), it is clearly evident that at $We = 0.8$ the flow is asymptotically globally stable; the spatial oscillations amplitude tends to vanish at every station of the curtain at $t = 7.5$ (Fig. 4.38(a)). The analysis of Fig. 4.38(b) reveals instead an unstable growth of the perturbation superposed on the base flow at $We = 0.4$, with consequent temporal amplification of spatial oscillations on the whole domain. To shed light on the physical mechanisms determining the flow instability outlined above, the energy budgets temporal evolution (Eq. (2.33) in Section 2.1.3) is reported in Fig. 4.39 for $We = 0.8$

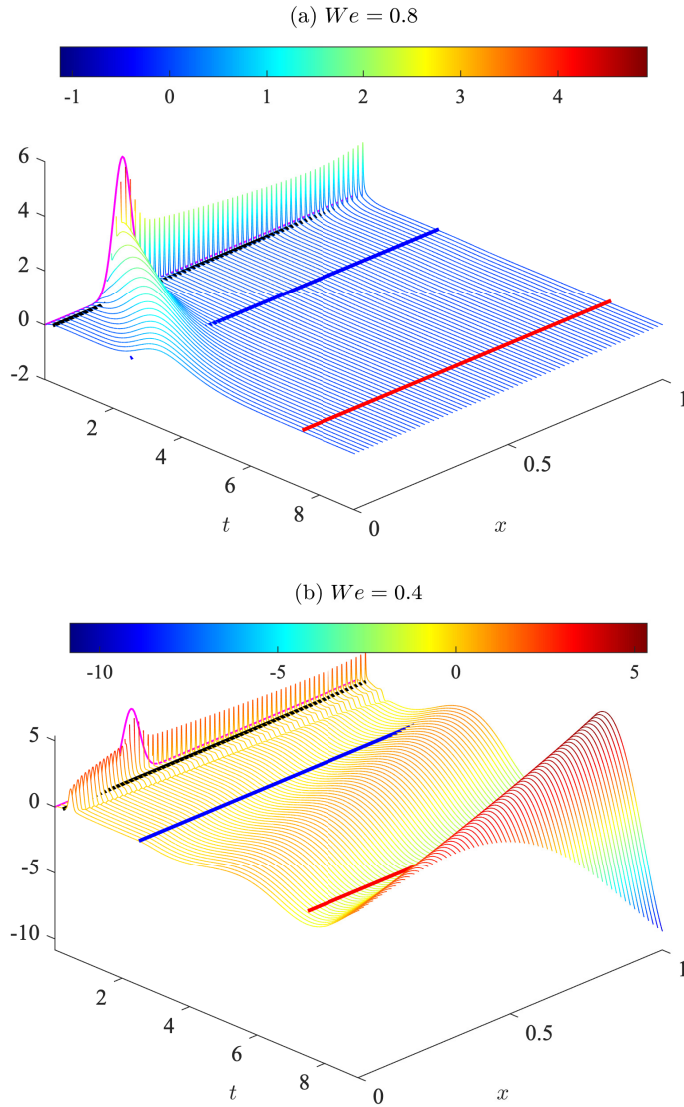


Figure 4.38. Spatio-temporal evolution of the transverse velocity perturbation $v(x,t)$ for $We = 0.8$ (panel (a)) and $We = 0.4$ (panel (b)): $t = 0.25$ (black line), 2.5 (blue line) and 7.5 (red line). The magenta curve in both panels represents the initial perturbation (4.5). $We_{th} = 0.63$.

(panels (a)-(d)) and $We = 0.4$ (panels (e)-(h)). The sum of kinetic and surface tension energies E_t reveals, as expected, an asymptotic decreasing behaviour for $We = 0.8$, while an unstable growth occurs for $We = 0.4$ (black curves). Both the energy exchanges through the domain boundaries, ΔF_c and ΔF_σ (blue curves), and the viscous D and inviscid P dissipation terms (magenta curves), play a stabilizing role on the subcritical flow dynamics, regardless of the Weber number value. On the other hand, it is found that the surface tension, through the work per unit time L_σ , is the physical mechanism driving the flow instability when We is progressively reduced, as can be clearly appreciated by the temporal amplification of oscillations in L_σ when We is reduced from $We = 0.8$ to $We = 0.4$ (dashed green curves). The latter result confirms the crucial role of surface tension in the destabilization of gravitational liquid curtains, which was outlined in previous stability analyses by de Luca and Costa [14] and Barlow *et al.* [17]. Note that Tammisola *et al.* [51] and Schmidt *et al.* [52] also found a surface tension-induced global instability of two-dimensional planar jet and wake flows of two immiscible fluids with different velocities. It is also interesting to observe that the pressure term L_p (green solid curve in Fig. 4.39), which has been found to play the main destabilizing role in supercritical regimes (Section 4.1.2), is almost not involved in the energy balance in subcritical conditions.

The instability onset occurring as the Weber number progressively decreases is further elucidated in Fig. 4.40, which shows the temporal evolution of the meanline oscillations amplitude at $x = x_p$, that is the station where the perturbation is introduced, respectively for $We = 0.8$ (panel (a)) and $We = 0.4$ (panel (b)). The numerical analysis is performed for three different values of Reynolds number ($Re = 41.3, 413$ and ∞). In asymptotically stable conditions ($We = 0.8$), the meanline amplitude undergoes a transient growth in the initial time instants, which is well fitted by the power law $t^{\frac{1}{3}}$. When the Weber number decreases down to $We = 0.4$, after an initial ($t < 0.5$) transient growth characterized by the same algebraic trend observed at $We = 0.8$ (i.e., $t^{\frac{1}{3}}$), the perturbation amplitude

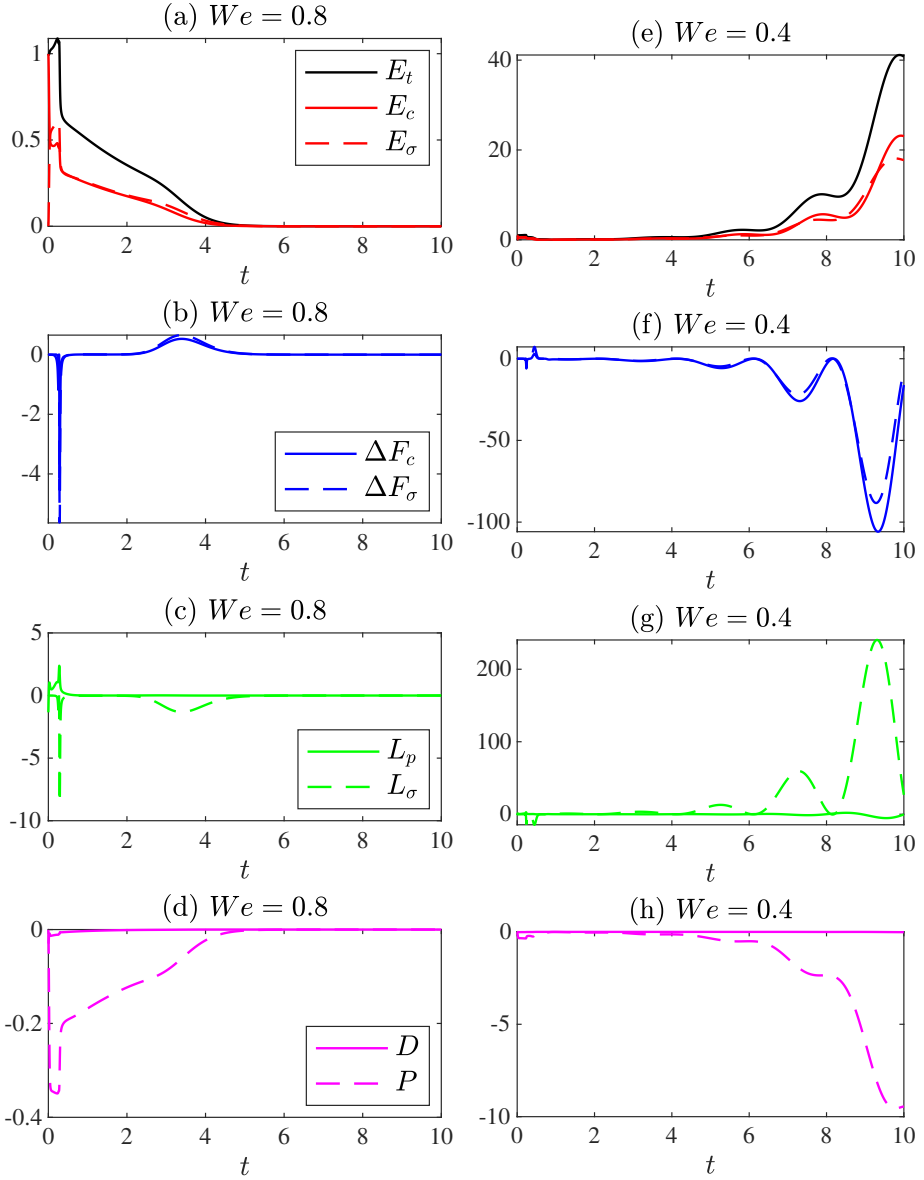


Figure 4.39. Temporal evolution of the energy budgets for $We = 0.8$ (panels (a)-(d)) and $We = 0.4$ (panels (e)-(h)). All the terms are scaled with respect to the initial total energy E_{t0} . For a detailed explanation of the terms, see Eq. (2.33) in Section 2.1.3. $We_{th} = 0.63$.

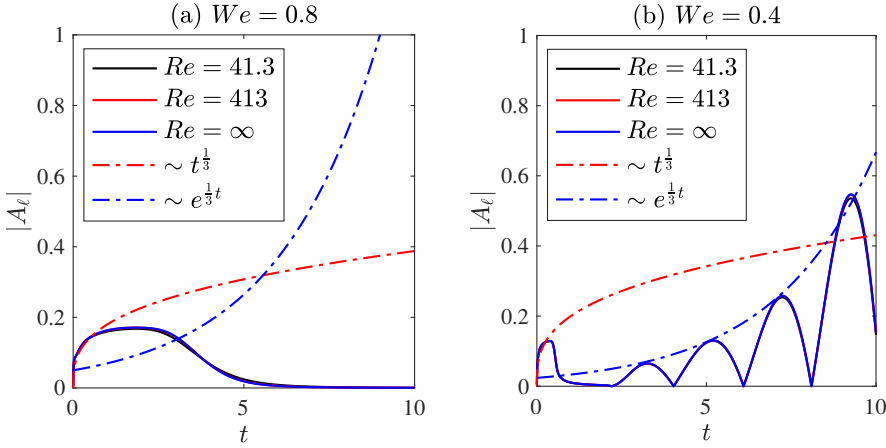


Figure 4.40. Temporal evolution of meanline oscillations amplitude at $x = x_p$ for $We = 0.8$ (panel (a)) and $We = 0.4$ (panel (b)): $Re = 41.3$ (continuous black curve); 413 (continuous red curve); ∞ (continuous blue curve). The dot-dashed curves represent algebraic ($\sim t^{\frac{1}{3}}$, red) and exponential ($\sim e^{\frac{1}{3}t}$, blue) growths. $We_{th} = 0.63$.

exhibits an unstable evolution described by the exponential trend $e^{\frac{1}{3}t}$ (Fig. 4.40(b)). It is also worth noting that results obtained by varying the Weber number are not dependent on the particular value of the Reynolds number considered, as shown by the perfect superposition of solid curves in Fig. 4.40 (panels (a)-(b)), namely the viscosity does not play any key role.

The previous findings agree with the results by de Luca and Costa [14] and Barlow *et al.* [17]. These authors employed a local spatio-temporal stability approach, and found an absolute algebraic unstable growth of disturbances for liquid sheets in subcritical regime, described by the power law $t^{\frac{1}{3}}$. Analyzing the sheet flow on a finite domain from a global perspective, an initial transient algebraic growth of the perturbation ($\sim t^{\frac{1}{3}}$) in asymptotically stable conditions ($We = 0.8$) is found herein, while in unstable conditions ($We = 0.4$) the initial algebraic amplification is followed by an asymptotic expo-

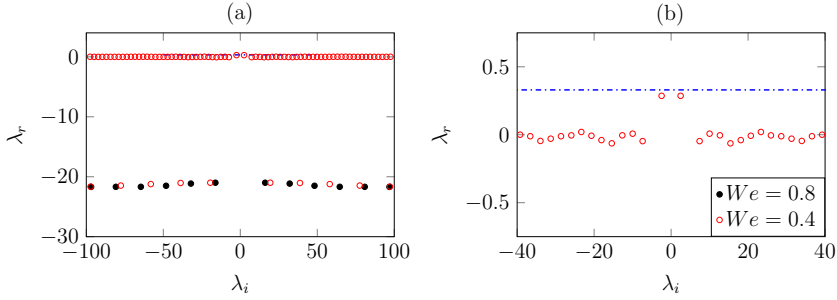


Figure 4.41. Inner eigenvalues of the spectrum (panel (a)) with a zoom on the unstable part (panel (b)). The curve $\lambda_r = 1/3$ (dot-dashed blue line) is also reported. $Re = \infty$, $We_{th} = 0.63$.

nential growth. The latter result is confirmed by the linear stability analysis: the spectra calculated in inviscid conditions ($Re = \infty$) and reported in Fig. 4.41 reveal that the leading eigenvalue (i.e., with maximum growth rate λ_r) becomes unstable at $We = 0.4$, with a growth rate close to the value $\lambda_r = 1/3$ arising from numerical simulations (relative spread of 12.12 %). Note also that two branches of spectrum are obtained for $We < We_{th}$, as predicted in Section 2.1.3. Further details regarding the Froude and Weber number effects on the flow subcritical instability are given in Della Pia *et al.* [120].

4.2 Two-phase mixing layers

The experimental characterization of the planar air-water mixing layer represents the aim of the present section. The two-phase mean (time-averaged) flow is characterized for several injection conditions in Section 4.2.1 (an overview is summarized in Fig. 4.42). Insights into the unsteady flow dynamics are gained through the velocity component fluctuations spectral analysis (Section 4.2.2), and the global oscillatory behaviour of the flow is finally discussed in Section 4.2.3.

4.2.1 Mean flow field characterization

The mean flow topology is first presented and discussed for a selected case defined as the REF case, which is characterized by values of the flow quantities reported in Table 4.11. Later on, the effect of injection conditions on the two-phase flow field will be investigated by means of a parametric analysis involving the following dimensionless parameters

$$Re_g = \frac{\rho_g U_g \delta_g}{\mu_g}, \quad We_l = \frac{\rho_l U_l^2 \delta_l}{\sigma}, \quad M = \frac{\rho_g U_g^2}{\rho_l U_l^2}, \quad (4.15)$$

whose values are reported in Table 4.12 for the main cases considered in the analysis. The Reynolds number based on the gas vorticity thickness Re_g varies from 256 to 768. The inlet liquid vorticity thickness δ_l , which is defined analogously to δ_g and is obtained from the PIV measured velocity profiles in water, is used to define the liquid Weber number We_l , which varies from 0.19 to 2.97. Note also that, being the ratio e/δ_g greater than unity for all the cases examined (last row in Table 4.12), the present investigation lies within the so called *injector-influenced* regime outlined by Fuster *et al.* [48].

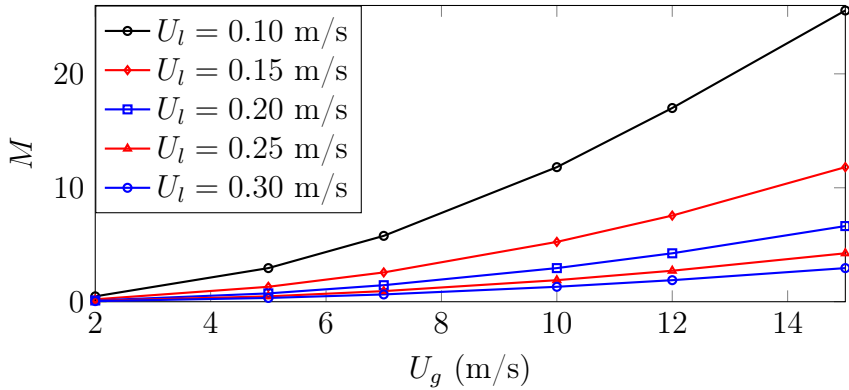


Figure 4.42. Overview of the air-water mixing layer testing conditions in terms of M values as a function of the gas velocity U_g , at different values of the liquid velocity U_l .

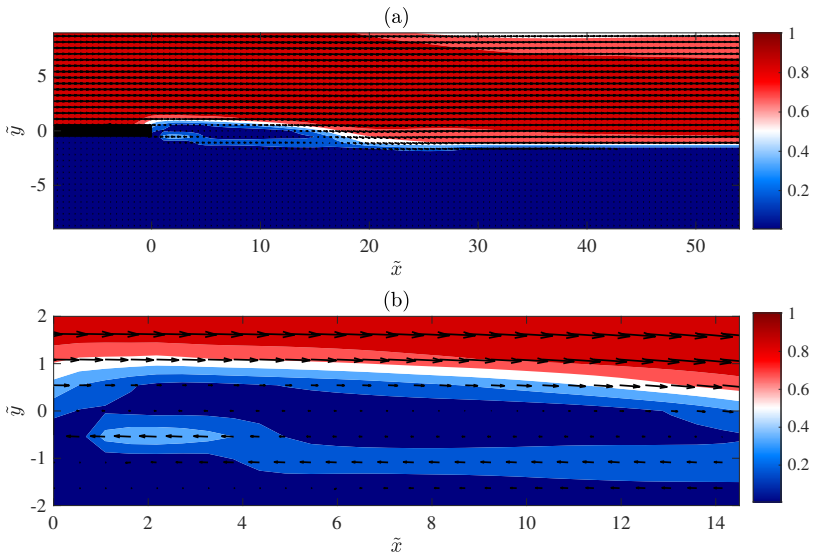


Figure 4.43. Time-averaged velocity magnitude \bar{V}/U_g contour (a) with zoom next to the nozzle exit section (b). In both panels, the splitter plate location is highlighted in black, and velocity vectors are reported. REF case of Table 4.12.

Name	Variable	Value	Unit
Gas density	ρ_g	1.177	Kg m^{-3}
Liquid density	ρ_l	997	Kg m^{-3}
Gas viscosity	μ_g	$1.84 \cdot 10^{-5}$	$\text{Kg m}^{-1} \text{s}^{-1}$
Liquid viscosity	μ_l	$8.90 \cdot 10^{-4}$	$\text{Kg m}^{-1} \text{s}^{-1}$
Surface tension	σ	$72.5 \cdot 10^{-3}$	N m^{-1}
Inlet liquid velocity	U_l	0.15	m s^{-1}
Inlet gas velocity	U_g	7	m s^{-1}
Gas vorticity thickness	δ_g	$1.1 \cdot 10^{-3}$	m
Liquid vorticity thickness	δ_l	$2.7 \cdot 10^{-3}$	m
Splitter plate thickness	e	$2.0 \cdot 10^{-3}$	m

Table 4.11. Dimensional quantities corresponding to the REF case.

Case	REF	WElo	WEme	WEhi	RElo	REtr	REme	REhi	REgl
Re_g	493	493	493	493	384	704	714	768	768
We_l	0.84	0.19	1.27	2.97	0.84	0.84	0.84	0.84	0.19
M	2.57	5.78	1.45	0.64	1.31	5.25	7.56	11.81	25.56
e/δ_g	1.81	1.81	1.81	1.81	1.62	1.83	2.15	2.60	2.60

Table 4.12. Overview of the main cases considered in the analysis. Dimensionless parameters are defined in Eq. (4.15).

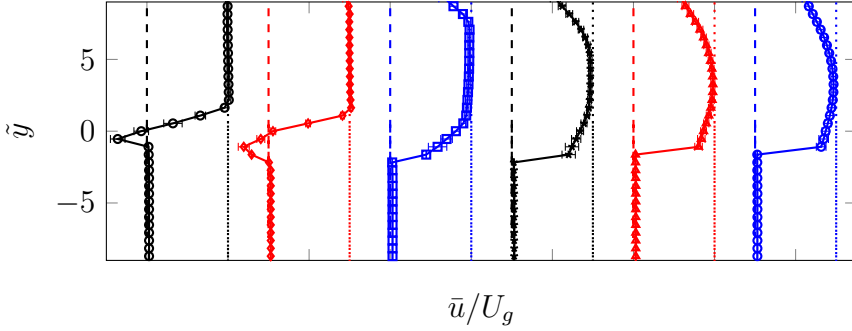


Figure 4.44. Time-averaged streamwise $\bar{u}(\tilde{y})/U_g$ velocity component profiles at different \tilde{x} stations: $\tilde{x} = 0.55$ (\blacklozenge); 10.88 (\blacklozenge); 21.76 (\blacksquare); 32.10 (\blackstar); 42.98 (\blacktriangle); 53.31 (\blacklozenge). The dashed and dotted lines represent the values $\bar{u}/U_g = 0$ and 1 , respectively, while error bars denote the average measurement uncertainty. REF case of Table 4.12.

Base case

The time-averaged velocity magnitude \bar{V} contour is shown in Fig. 4.43(a) together with the velocity vectors distribution, and a zoom around the splitter plate immediately downstream of the nozzle exit section is provided in Fig. 4.43(b). For all cases discussed within this work, the mean quantities \bar{u} and \bar{v} are computed as

$$\bar{u}(x, y) = \frac{1}{T} \int_0^T u(x, y, t) dt, \quad \bar{v}(x, y) = \frac{1}{T} \int_0^T v(x, y, t) dt, \quad (4.16)$$

where u and v are the instantaneous measured velocity components along x and y directions, respectively, and the averaging time T spans 8000 temporal realizations of the flow ($T = 4.0$ s). Note that in Fig. 4.43 the velocity magnitude has been scaled with respect to U_g , and the spatial coordinates have been made dimensionless by means of the splitter plate thickness, i.e. $\tilde{x} = x/e$ and $\tilde{y} = y/e$.

After issuing from the injection section ($\tilde{x} = 0$), the air and water flows meet downstream of the splitter plate. By moving along the

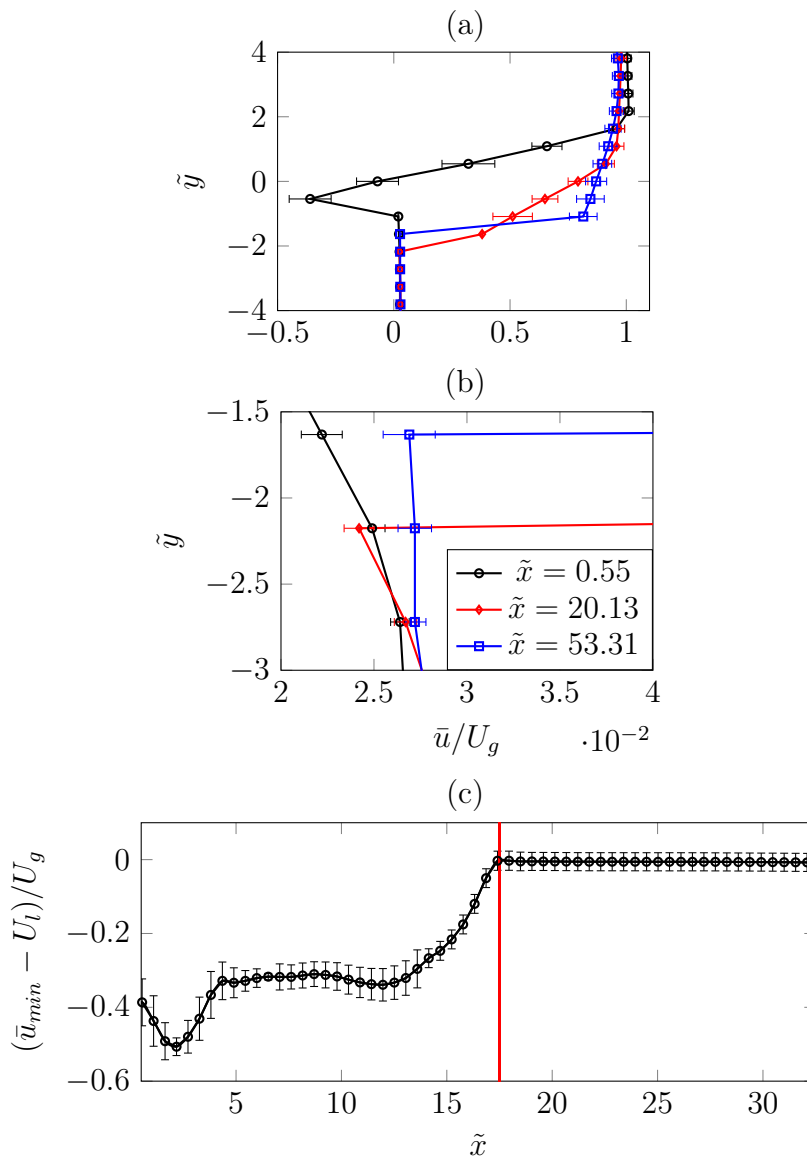


Figure 4.45. Velocity profiles $\bar{u}(\tilde{y})/U_g$ at different \tilde{x} stations (a) with zoom near the liquid phase (b) and velocity defect $(\bar{u}_{min} - U_l)/U_g$ streamwise distribution (c). The vertical red line in panel (c) denotes the wake region length \tilde{x}_w , while error bars represent the average measurement uncertainty. REF case of Table 4.12.

streamwise direction, two distinct regions can be detected: a wake flow region ($0 < \tilde{x} < \tilde{x}_w$), and a pure mixing layer region ($\tilde{x} > \tilde{x}_w$), with $\tilde{x}_w = x_w/e = 17.5$. The wake region length \tilde{x}_w has been calculated as the last streamwise station (starting from $\tilde{x} = 0$) where $\bar{u}(\tilde{y}) < 0$ (i.e. $\bar{u} > 0$ for $\tilde{x} > \tilde{x}_w$). The spatial development of the mixing layer is more clearly quantified in Fig. 4.44, which reports $\bar{u}(\tilde{y})$ profiles at different streamwise stations spanning both air and water streams, together with the corresponding average measurement uncertainty. The reverse flow component within the wake region is highlighted by the negative values of \bar{u} for \tilde{y} around zero. Far from $\tilde{y} = 0$, the velocity profile is characterized by an almost uniform distribution in both air ($\tilde{y} > 2$) and water ($\tilde{y} < -1.1$) streams, while it undergoes strong spatial variations within the region $-1.1 < \tilde{y} < 2$. Downstream of the wake region, the velocity profile is influenced by the air-air shear layer forming between the injected gas stream and the still ambient, with consequent reduction of the local \bar{u} value by increasing \tilde{y} (phenomenon of jet expansion, see Descamps *et al.* [65]).

By moving along \tilde{x} , the momentum exchange between the faster gas and slower water stream leads to the progressive reduction of the velocity defect, namely the difference between the minimum local velocity and the free-stream value, $\bar{u}_{min} - U_l$. This aspect is clarified in Fig. 4.45, which shows the velocity profile at three selected downstream stations, respectively inside ($\tilde{x} = 0.55$, black curve), just outside ($\tilde{x} = 20.13$, red) and far from ($\tilde{x} = 53.31$, blue) the wake region (panels (a)-(b)), and the velocity defect streamwise distribution (c), together with the corresponding average measurement uncertainty.

The different regions characterizing the flow topology are further highlighted by $\bar{u}(\tilde{x})$ and $\bar{v}(\tilde{x})$ velocity profiles, respectively shown in Fig. 4.46(a)-(b), for vertical stations spanning both air and water streams. The distribution $\bar{u}(\tilde{x}, \tilde{y} = 0)$ highlights the strong spatial variation characterizing the flow field in the wake region (blue curve in panel (a)), while $\bar{v}(\tilde{x})$ profiles reveal the downward deviation of the gas stream (i.e. negative values of $\bar{v}(\tilde{x})$) in the near-field region, as a result of the combination of water jet contraction (Ag-

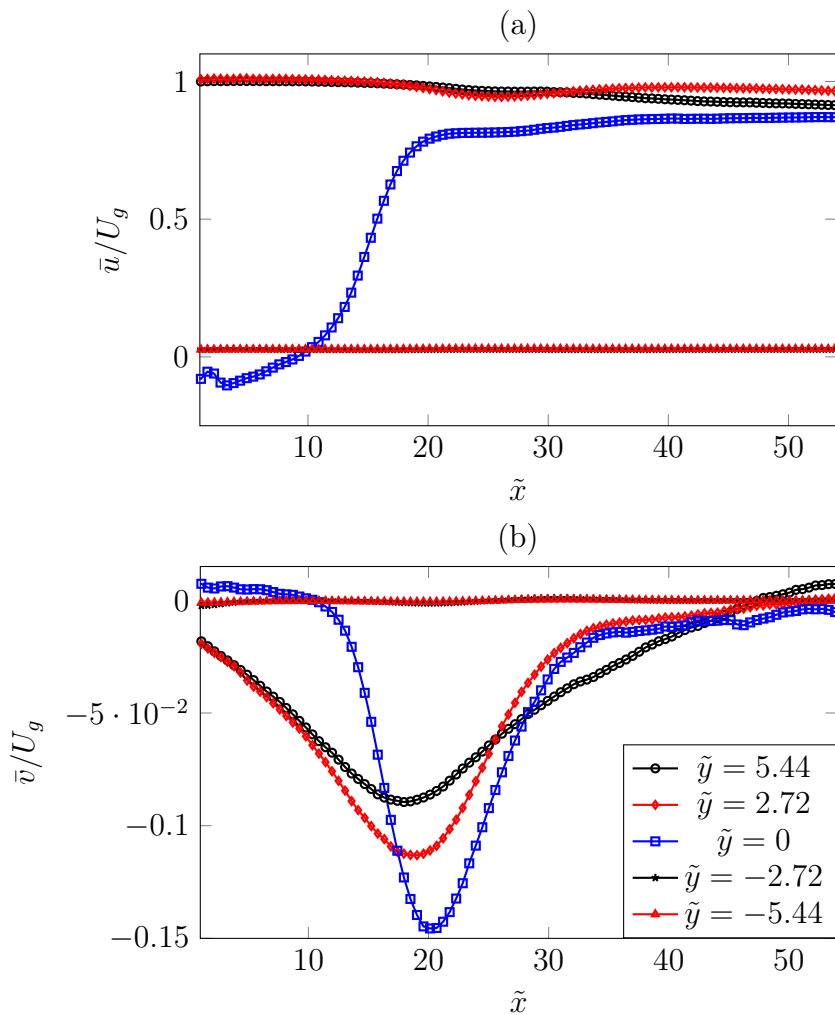


Figure 4.46. Time-averaged streamwise $\bar{u}(\tilde{x})/U_g$ (a) and vertical $\bar{v}(\tilde{x})/U_g$ (b) velocity component profiles at different \tilde{y} stations. REF case of Table 4.12.

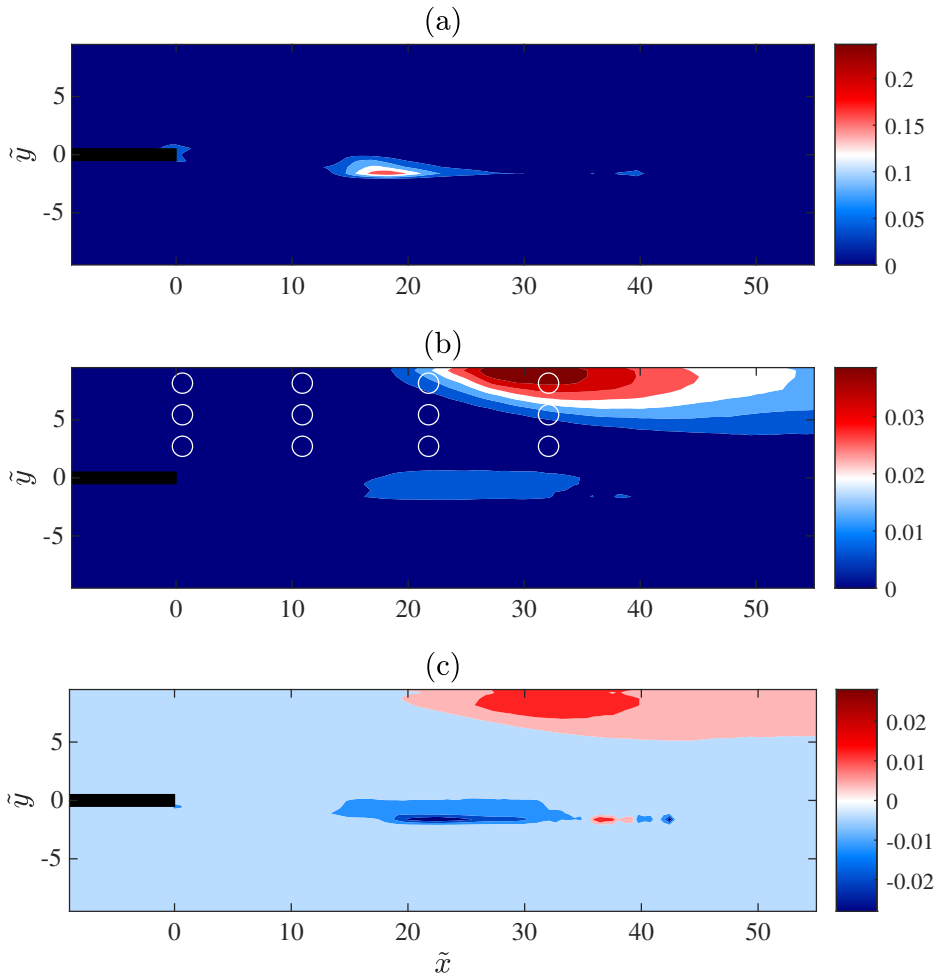


Figure 4.47. Contour of $\overline{u'u'}/U_g^2$ (a), $\overline{v'v'}/U_g^2$ (b) and $\overline{u'v'}/U_g^2$ (c). The white circles in panel (b) denote monitoring locations employed for the analysis of unsteady velocity fluctuations in Section 4.2.2. REF case of Table 4.12.

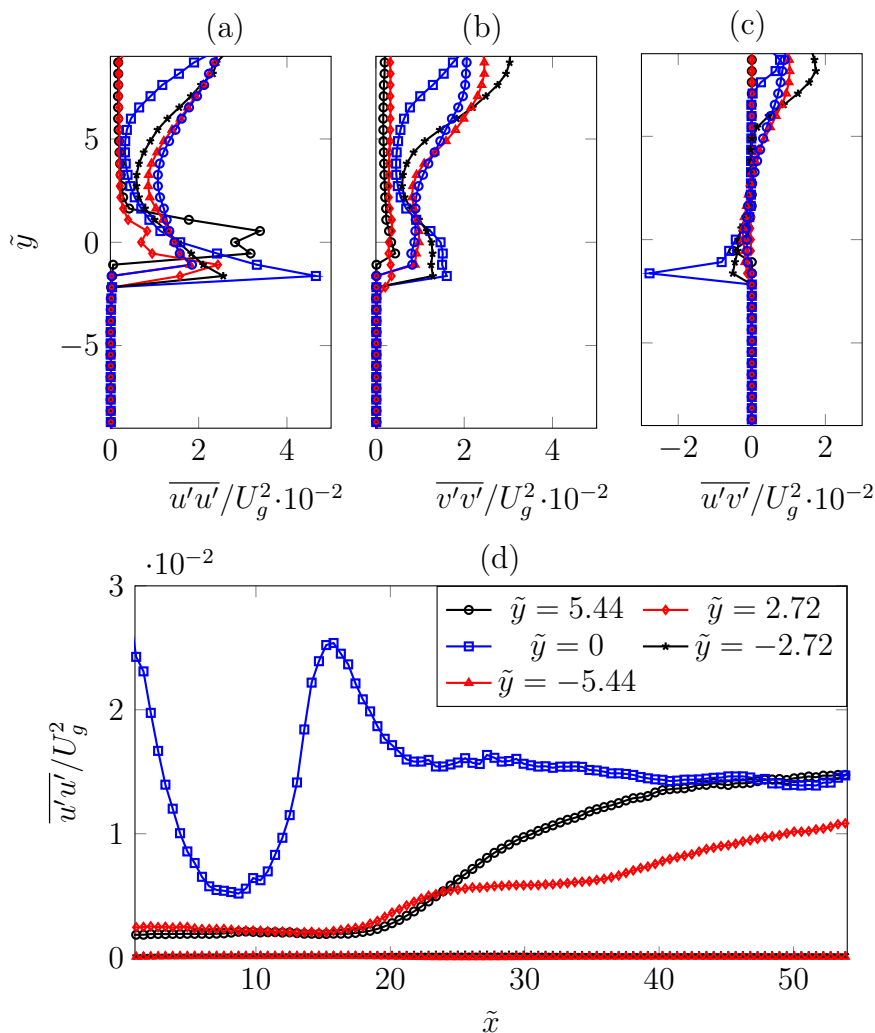


Figure 4.48. Profiles of $\overline{u'u'}/U_g^2$ (a), $\overline{v'v'}/U_g^2$ (b) and $\overline{u'v'}/U_g^2$ (c) at different streamwise stations: $\tilde{x} = 0.55$ (\circ); 10.88 (\diamond); 21.76 (\square); 32.10 (\star); 42.98 (\blacktriangle); 53.31 (\circ). Panel (d) reports $\overline{u'u'}/U_g^2$ profiles at different vertical stations \tilde{y} . REF case of Table 4.12.

baglah *et al.* [57]) and air recirculation within the wake. Furthermore, Figs. 4.47 and 4.48 show the Reynolds stress tensor components $\overline{u'u'}$ (panels (a)), $\overline{v'v'}$ (b) and $\overline{u'v'}$ (c) in terms of contour representations and \tilde{y} -profiles, respectively. Note that the white circles in Fig. 4.47(b) represent monitoring locations, which will be used for the analysis of unsteady velocity fluctuations in Section 4.2.2. The \tilde{x} -velocity component fluctuation is evaluated as $u' = u - \bar{u}$, and the same applies for v' . The $\overline{u'u'}(\tilde{y})$ distribution (panels (a)) is characterized by larger peaks than the others (panels (b) and (c)), as also found by Ling *et al.* [58] by means of three-dimensional direct numerical simulations. Moreover, all the distributions are peaked in correspondence of the maximum momentum exchange locations, namely at the air-water and air-air mixing layers interfaces (see also Jiang and Ling [94]). Similarly, the streamwise $\overline{u'u'}(\tilde{x})$ distribution reported in Fig. 4.48(d) reveals two peaks; the first one immediately downstream of the splitter plate, and the second one at $\tilde{x}_w = 17.5$, namely at the end of the recirculation region. It is also possible to appreciate that, for each \tilde{y} location, a constant value is asymptotically reached as \tilde{x} increases, revealing that the mixing layer progressively achieves a self-similar state moving far from the wake flow region (Mehta [121]).

Theoretical-experimental comparison

The analysis of the REF case is concluded by reporting a comparison between the velocity profiles here measured and the theoretical base flows proposed by Otto *et al.* [46] and Fuster *et al.* [48] in the context of linear stability analysis. The comparison is performed at two distinct streamwise stations: a first one inside the wake region ($\tilde{x} < \tilde{x}_w$, panels (a)-(b) in Fig. 4.49), and a second one just outside it ($\tilde{x} > \tilde{x}_w$, panels (c)-(d)). Note that the measured profiles (black curves) have been vertically shifted in such a way that the air-water interface is located at $y = 0$, to facilitate the comparisons with theoretical formula (red curves) hereafter provided.

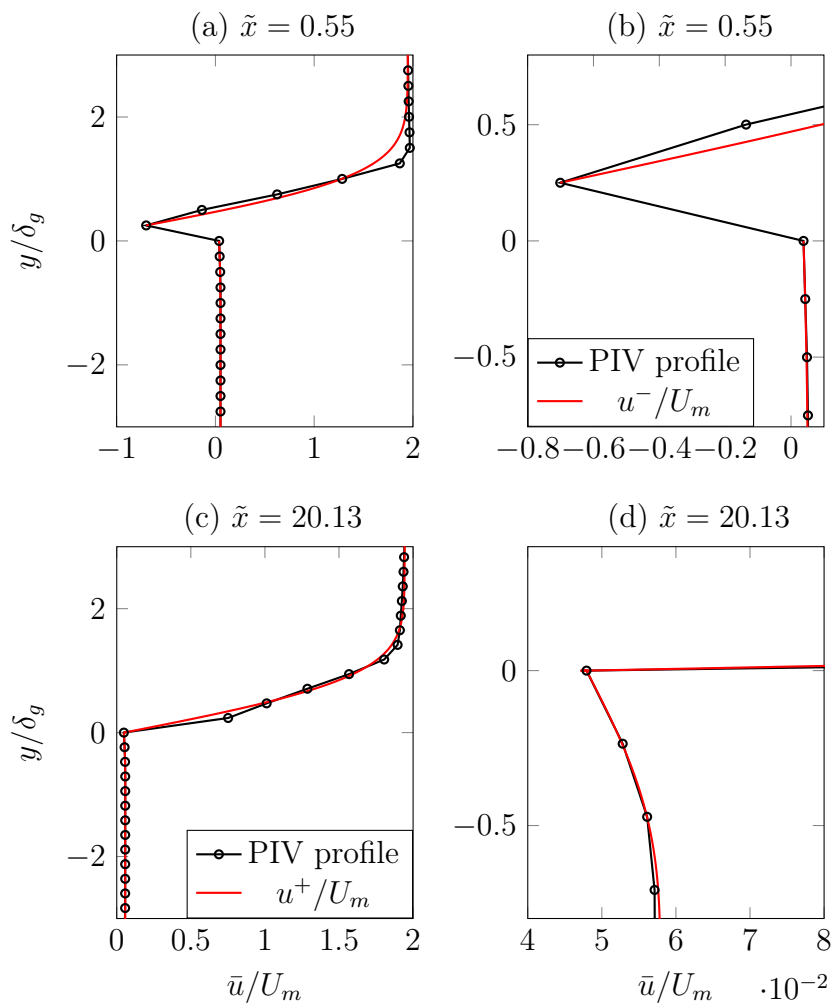


Figure 4.49. Theoretical-experimental comparison of velocity profiles inside (panels (a)-(b)) and outside ((c)-(d)) the wake region of length $\tilde{x}_w = 17.5$. REF case of Table 4.12.

The analytical velocity profile used in Fig. 4.49(c)-(d) reads as

$$\frac{u^+}{U_m} = \begin{cases} -\frac{U_l}{U_m} \operatorname{erf}\left(\frac{y}{\delta_l}\right) + \frac{\bar{u}_0}{U_m} \left[1 + \operatorname{erf}\left(\frac{y}{\delta_d}\right)\right], & y \leq 0, \\ \frac{U_g}{U_m} \operatorname{erf}\left(\frac{y}{\delta_g}\right) + \frac{\bar{u}_0}{U_m} \left[1 - \operatorname{erf}\left(\frac{y}{\delta_d}\right)\right], & y \geq 0, \end{cases} \quad (4.17)$$

which is the same as that reported by Fuster *et al.* [48] once small notational differences are rectified, while a modified version (discontinuous at $y = 0$) is adopted for comparisons in the wake region (Fig. 4.49(a)-(b)),

$$\frac{u^-}{U_m} = \begin{cases} -\frac{U_l}{U_m} \operatorname{erf}\left(\frac{y}{\delta_l}\right) + \frac{\bar{u}_0}{U_m} \left[1 + \operatorname{erf}\left(\frac{y}{\delta_d}\right)\right], & y \leq 0, \\ \frac{U_g}{U_m} \operatorname{erf}\left(\frac{y - y_{min}}{\delta_g}\right) + \frac{\bar{u}_{min}}{U_m} \left[1 - \operatorname{erf}\left(\frac{y - y_{min}}{\delta_d}\right)\right], & y > 0. \end{cases} \quad (4.18)$$

In Eqs. (4.17)-(4.18), the error function $\operatorname{erf}(y)$ is employed, $U_m = (U_g + U_l)/2$, \bar{u}_0 is the measured velocity at the air-water interface (an analytical estimation based on continuity of shear stresses across the interface was used by Fuster *et al.* [48]), \bar{u}_{min} is the minimum (negative) measured value within the wake region (at the vertical location $y = y_{min}$), and δ_d is an adjustable parameter introduced by Otto *et al.* [46] to mimic experimental velocity profiles in the near-field region of the mixing layer.

Results of the comparison reveal a strict agreement between the measured and theoretical velocity profiles, both inside (i.e. negative value of velocity defect) and outside the wake region. Values of the ratio δ_d/δ_g giving the best match with experimental data are respectively equal to 0.75 (for $\tilde{x} < \tilde{x}_w$) and 0.78 ($\tilde{x} > \tilde{x}_w$). According to Otto *et al.* [46], δ_d/δ_g is found to be less than the unity in both cases, due to the presence of a velocity defect in the mean flow profile.

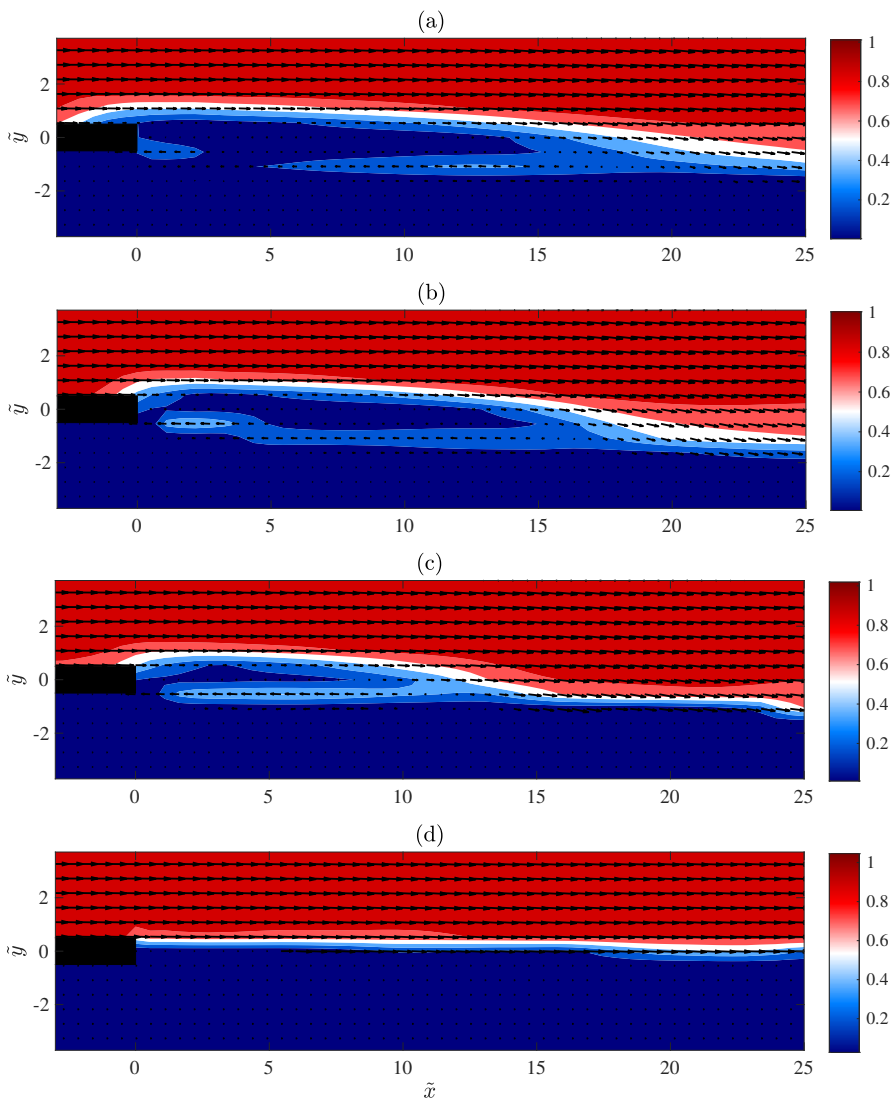


Figure 4.50. Weber number We_l effect on \bar{V}/U_g flow field. The splitter plate is highlighted in black, and velocity vectors are reported. WEL0 (a), REF (b), WEme (c) and WEhi (d) cases of Table 4.12.

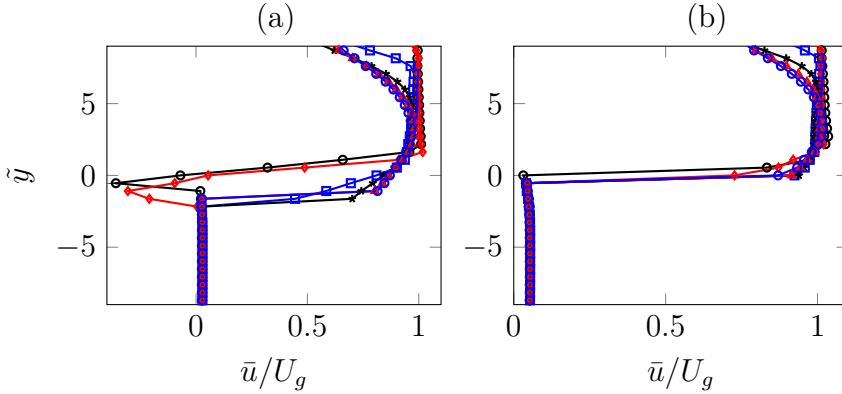


Figure 4.51. Weber number We_l effect on the time-averaged streamwise $\bar{u}(\tilde{y})/U_g$ velocity component at different \tilde{x} stations: $\tilde{x} = 0.55$ (\blacklozenge); 10.88 (\blacklozenge); 21.76 (\blacksquare); 32.10 (\blackcross); 42.98 (\blacktriangle); 53.31 (\blacklozenge). REF (a) and WEhi (b) cases of Table 4.12.

Effect of liquid Weber number

The effect of Weber number We_l variation on the two-phase flow topology at fixed Re_g is investigated by modifying the injection velocity U_l . Results are shown in Fig. 4.50 in terms of time-averaged velocity magnitude contour and velocity vectors distribution; the Weber number varies between $We_l = 0.19$ (WElo case, panel (a)) and $We_l = 2.97$ (WEhi case, panel (d)). The gas Reynolds number is equal to $Re_g = 493$, as in the REF case previously discussed.

The recirculation region characterizing the flow downstream of the injection section progressively reduces as We_l increases, and it vanishes in the WEhi case. The increase in inlet momentum reduces the relative importance of capillary to inertia forces, thus leading to an almost unperturbed air-water interface at the splitter plate edge in the last case. For the WEhi case, the liquid velocity field is basically not influenced by the co-flowing gaseous phase, developing parallel to the streamwise direction and to the injected air stream.

The wake flow region reduction when the Weber number increases

is quantified in Fig. 4.51, where $\bar{u}(\tilde{y})$ distributions at different streamwise stations are reported for REF (a) and WEhi (b) cases. In the latter configuration, the absence of the wake flow component determines an almost spatially invariant flow along the streamwise direction up to $\tilde{y} = 5$, where slight differences among the velocity profiles are due to the air-air mixing layer development.

Effect of gas Reynolds number

Results of the investigation performed by varying the gas Reynolds number are first shown in Figs. 4.52-4.53, respectively in terms of velocity magnitude contours with superposed vectors distributions, and $\bar{u}(\tilde{y})$ profiles at different streamwise locations; the liquid velocity is kept constant and equal to that of the REF case, so that $We_l = 0.84$.

By looking at the two-dimensional flow fields, it can be seen that the wake region progressively shortens by increasing the Reynolds number from the RElo (a) to the REme (c) case, with \tilde{x}_w decreasing from 21.2 to 9.8. Accordingly, the peak of the Reynolds stress component $\overline{u'u'}$ is shifted towards lower \tilde{x} values, and it achieves its maximum at $Re = 704$, as reported in Fig. 4.54. The liquid phase development is strongly affected by the gas Reynolds number: the increase in Re_g augments the momentum transferred by shear from the gas to the liquid stream, with consequent stronger acceleration and contraction of the water jet in the near-field region (Agbaglah *et al.* [57]). Fig. 4.52 shows the liquid jet progressive contraction when Re_g increases: moving along \tilde{x} , the gas flow appears deflected upwards due to interactions with liquid waves developing along the streamwise direction (Matas *et al.* [43], Fuster *et al.* [48], Ling *et al.* [58]). The momentum flux difference in the air-air mixing layer also increases with increasing Re_g , leading to a reduction in $\bar{u}(\tilde{y})$ moving towards the top of the domain, as shown by the evolution of velocity profiles in Fig. 4.53, from panel (a) to (c).

For the highest value of Reynolds number considered (REhi case, Figs. 4.52-4.53(d)), the wake region vanishes, i.e. $\tilde{x}_w = 0$; as a conse-

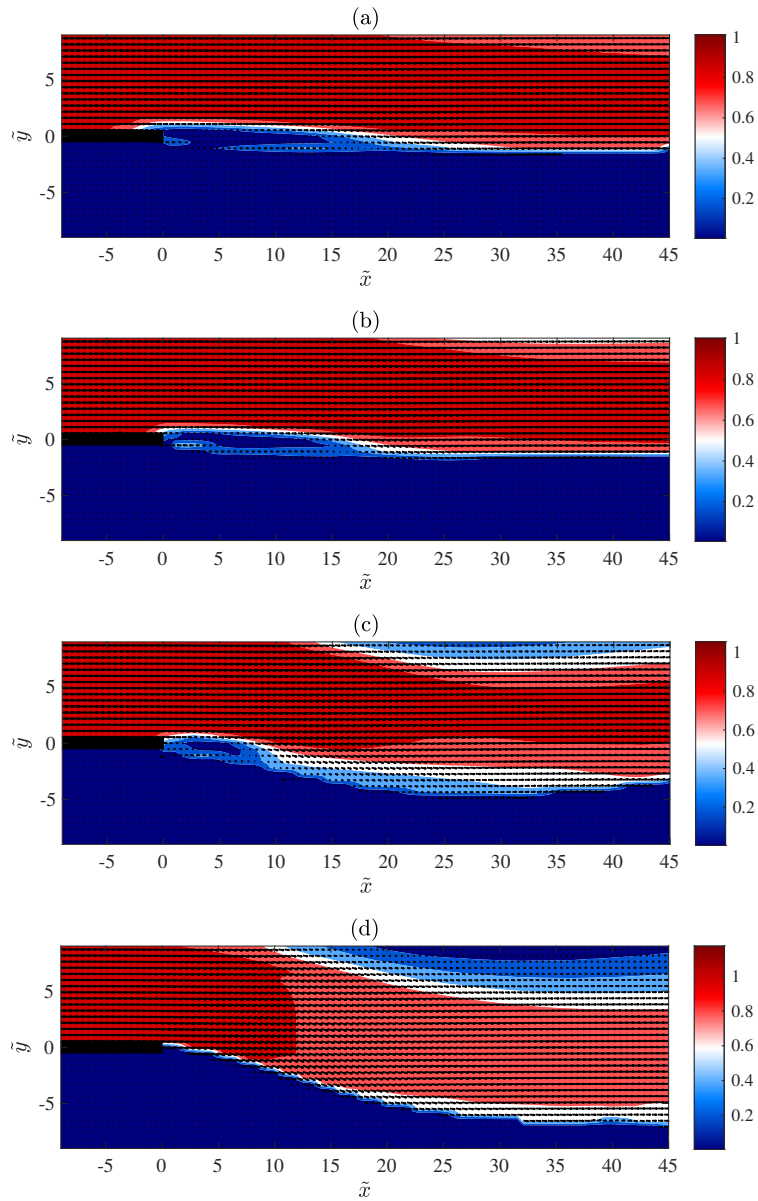


Figure 4.52. Reynolds number Re_g effect on the time-averaged velocity magnitude \bar{V}/U_g . The splitter plate is highlighted in black, and velocity vectors are reported. RElo (a), REF (b), REme (c) and REhi (d) cases of Table 4.12.

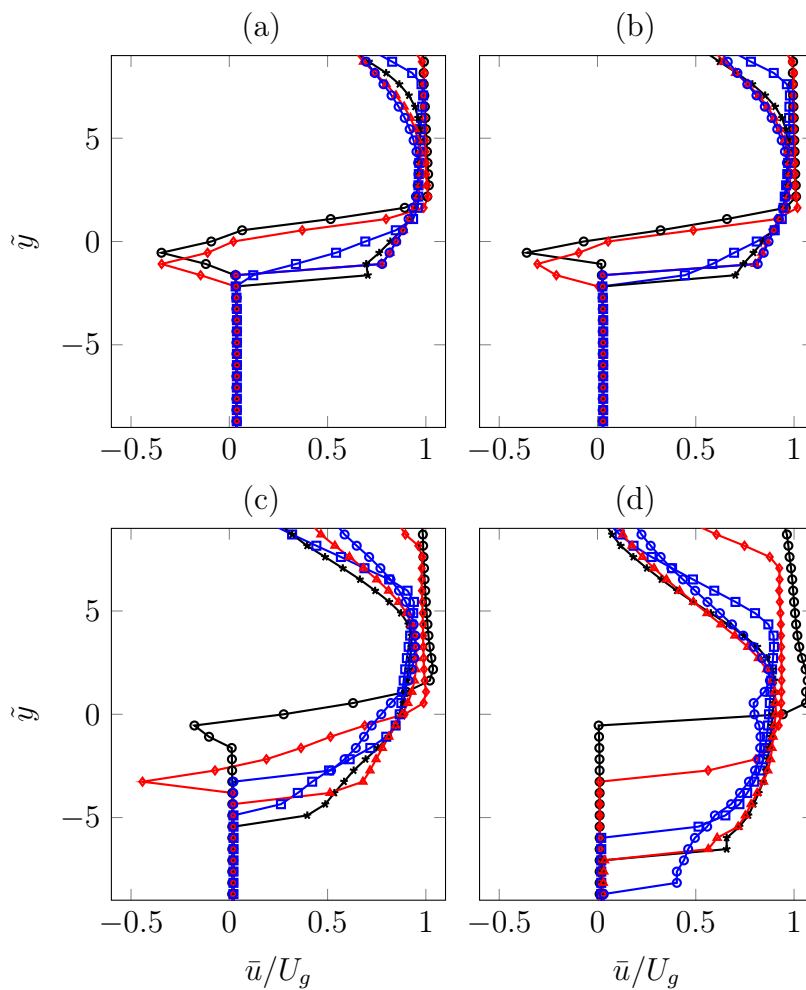


Figure 4.53. Reynolds number Re_g effect on the time-averaged streamwise $\bar{u}(\tilde{y})/U_g$ velocity component at different \tilde{x} stations: $\tilde{x} = 0.55$ (\bullet); 10.88 (\blacklozenge); 21.76 (\blacksquare); 32.10 (\blackstar); 42.98 (\blacktriangleright); 53.31 (\blacklozenge). RElo (a), REF (b), REme (c) and REhi (d) cases of Table 4.12.

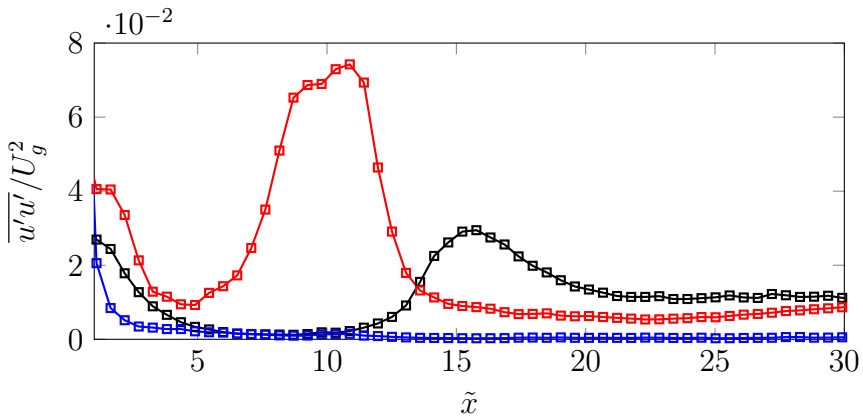


Figure 4.54. Profiles of $\overline{u'u'}/U_g^2$ at $\tilde{y} = 0$ for different values of the Reynolds number. REF (black curve), REtr (red curve) and REhi (blue curve) cases of Table 4.12.

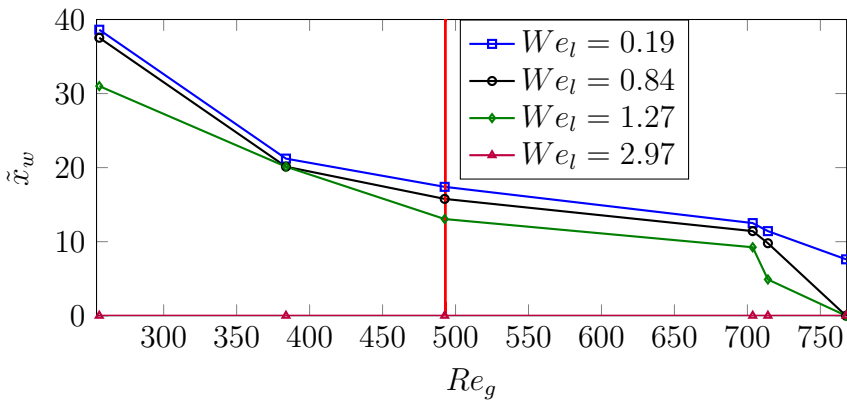


Figure 4.55. Reynolds number Re_g effect on the wake region length \tilde{x}_w at different We_l values. The vertical red line corresponds to $Re_g = 493$.

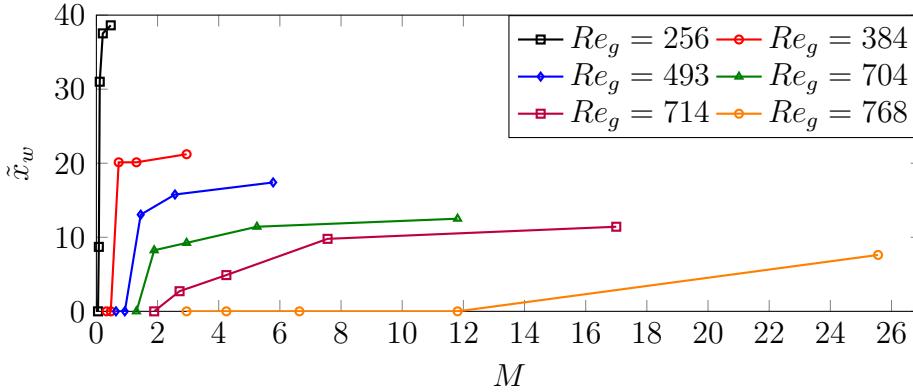


Figure 4.56. Dynamic pressure ratio M effect on the wake region length \tilde{x}_w at different values of the Reynolds number Re_g .

quence, no peak in the Reynolds stress component $\overline{u'u'}$ distribution can be detected (blue curve in Fig. 4.54). To shed light on this aspect, the curve $\tilde{x}_w(Re_g)$ is reported in Fig. 4.55 for different values of the Weber number We_l . Four cases are reported: $We_l = 0.19$ (blue curve), 0.84 (black), 1.27 (green) and 2.97 (magenta), corresponding to the flow fields shown in Fig. 4.50(a)-(d) for $Re_g = 493$ (vertical red line in Fig. 4.55). It can be seen that the progressive decreasing of the recirculation region with Re_g is enhanced by increasing the liquid Weber number, in agreement with the We_l effect at fixed Re_g previously outlined. In particular, at $We_l = 2.97$ no wake is detected at any Re_g value.

Effect of gas-to-liquid dynamic pressure ratio

The trend of the wake length as a function of the gas-to-liquid dynamic pressure ratio $\tilde{x}_w(M)$ is finally summarized in Fig. 4.56, for different values of the gas Reynolds number. It can be seen that, for a fixed Re_g , relatively low M values (high liquid velocities) promote a reduction of the wake, which eventually vanishes. This is analogous to the We_l effect outlined in Fig. 4.55 and by the velocity contours

reported in Fig. 4.50. Moreover, the M value denoting the transition from a wake regime to a purely mixing layer regime increases as Re_g increases. Therefore, only at relatively high values of the gas Reynolds number the flow behaves as a pure mixing layer in a wide range of liquid injection velocities (i.e. wide range of M values).

4.2.2 Unsteady dynamics analysis

The air-water mixing layer oscillatory dynamics is first analyzed by applying a Fast Fourier Transform (FFT) algorithm to the PIV measured vertical velocity component fluctuations v' , considering different streamwise \tilde{x} and normal-to-plate \tilde{y} locations (see Fig. 4.47(b) in Section 4.2.1). The effects of Weber (We_l) and Reynolds (Re_g) numbers on the signals frequency spectra are first examined; note that the dynamic pressure ratio M also varies by changing both We_l and Re_g values. Results are shown in Fig. 4.57, where two We_l (0.19 and 1.27) and three Re_g (493, 714 and 768) values are considered, and a monitoring station immediately after the splitter plate in air flow is selected, i.e. $(\tilde{x}, \tilde{y}) = (0.55, 5.44)$. Note that the fluctuation amplitudes $A_{v'}$ are made dimensionless by the inlet gas velocity value U_g for each case.

At relatively low Reynolds number (panels (a)-(b)), the spectra appear noisy and the order of magnitude of peak frequencies is equal to $\mathcal{O}(f) = 10^2$ Hz. By fixing We_l and increasing Re_g (i.e. by moving from top to bottom in each column of Fig. 4.57), the noise significantly reduces, and at the same time the peak frequency is lowered down to $\mathcal{O}(f) = 1$ Hz. For the higher Weber number value ($We_l = 1.27$) the peak frequency depends on the specific Re_g considered: it increases from $f = 6.42$ Hz to $f = 8.94$ Hz for Re_g going from 714 (panel (d)) to 768 (f). The peak frequencies ratio between the latter and former case is equal to 1.39, and it is in close agreement with the scaling $(U_{g(f)}/U_{g(d)})^{\frac{3}{2}} = 1.40$, where $U_{g(f)} = 15$ m/s and $U_{g(d)} = 12$ m/s. This scaling was also found in the experimental analyses by Raynal *et al.* [39] and Marmottant and Villermaux [42]

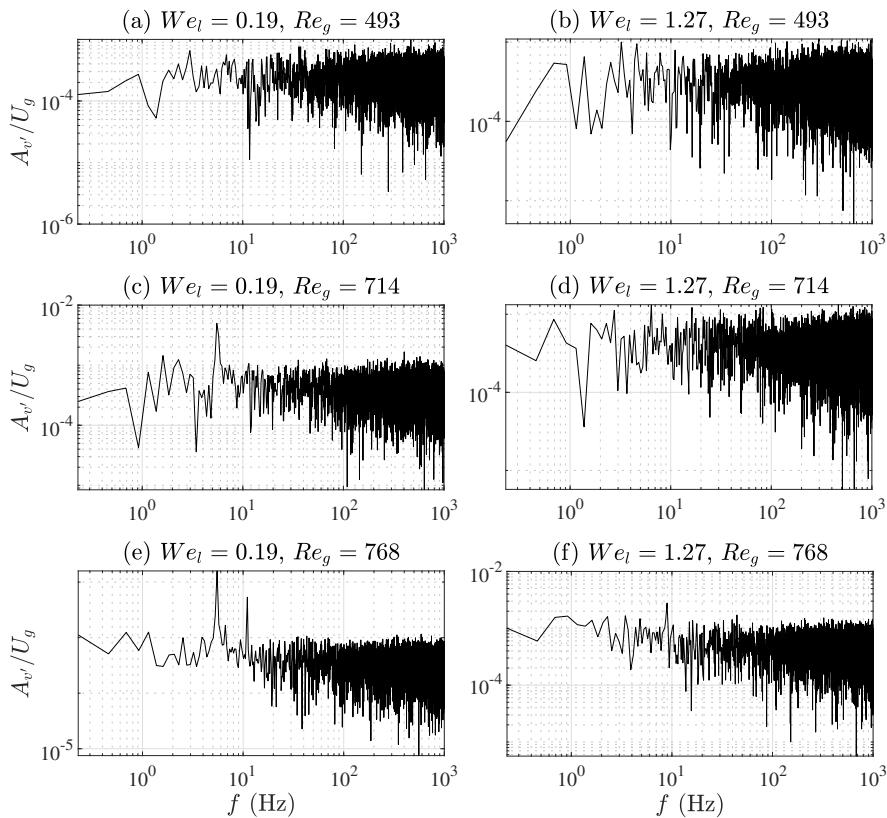


Figure 4.57. We_l and Re_g effects on the FFT of vertical velocity component fluctuation $v'(t)/U_g$ at $(\tilde{x}, \tilde{y}) = (0.55, 5.44)$, i.e. in air flow immediately downstream of the splitter plate. $M = 5.78$ (a), 1.45 (b), 17.00 (c), 4.25 (d), 25.56 (e), 6.64 (f).

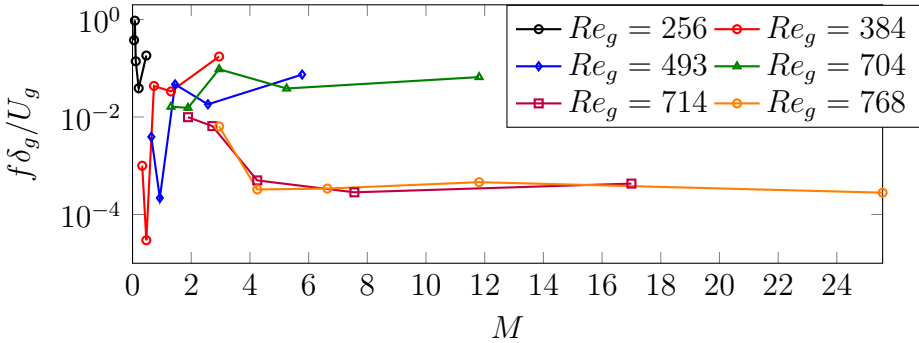


Figure 4.58. Dynamic pressure ratio M effect on the peak (dimensionless) frequency of the FFT of $v'(t)$ at $(\tilde{x}, \tilde{y}) = (0.55, 5.44)$ for different values of the Reynolds number Re_g .

for a multitude of gas injection velocities U_g . On the other hand, when We_l reduces to 0.19, the peak frequency is not dependent on the specific Re_g value, and it is equal to $f = 5.51$ Hz (panels (c) and (e), respectively).

A more significant data reduction is reported in Fig. 4.58, where the dimensionless peak frequencies $f\delta_g/U_g$ are shown as a function of the dynamic pressure ratio M . This representation of data allows the comparison between present results and theoretical predictions from local spatio-temporal stability analyses and direct numerical simulations of literature (Fuster *et al.* [48], Otto *et al.* [46], Bozonnet *et al.* [49]). In particular, Otto *et al.* [46] pointed out that, at relatively low M and Re_g values, the flow behaves like a noise amplifier, being characterized by convective instability. In this case, numerical simulations performed by Fuster *et al.* [48] and lately by Bozonnet *et al.* [49] have shown that frequency spectra of the gas-liquid interface oscillatory dynamics strongly depend on the injected noise level (e.g. the turbulence fluctuations within the gas phase, characterized by high frequency values) and on the selected streamwise station. This behaviour is analogous to the one previously outlined at $Re_g = 493$ in Fig. 4.57(a)-(b), and it is summarized in Fig. 4.58 for a wider

range of Reynolds number values ($Re_g \leq 493$, black, red and blue curves). On the other hand, at relatively high Re_g , Otto *et al.* [46] and Fuster *et al.* [48] outlined a transition from convective to absolute instability of the flow when M increases beyond a critical threshold M_c ($M_c = \mathcal{O}(1)$ for $\rho_g/\rho_l = 0.001$ in Fuster *et al.* [48]). In the latter case, the flow acts as an oscillator, driving the unsteady dynamics at a specific forcing frequency not related to the noise perturbations spectrum. This result is also analogous to what previously shown in Fig. 4.57, panels (c) and (e), respectively corresponding to $M = 17$ and 25.56 for $Re_g \geq 714$. Moreover, Fuster *et al.* [48] found that at relatively high Re_g the most unstable frequency is characterized by a monotonic decreasing trend as M increases, approaching the value $f\delta_g/U_g = 5 \cdot 10^{-4}$ as M increases and the instability becomes absolute. This finding is retrieved in Fig. 4.58 for $Re_g \geq 714$ (magenta and orange curves), where $f\delta_g/U_g = \mathcal{O}(10^{-4})$ for $M > 4.25$. Finally, it can be noted that the case $Re_g = 704$ (green curve) is similar to the two highest Re_g cases previously discussed, but it is characterized by a higher peak frequency $f\delta_g/U_g = \mathcal{O}(10^{-2})$ beyond the value $M = 4.25$.

4.2.3 Global oscillatory behaviour

For the highest M value here investigated, corresponding to the REgl case of Table 4.12, Fig. 4.59 shows the frequency spectra at different stations along the streamwise direction, spanning the range $\tilde{x} \in [0.55, 32.10]$ (from panel (a) to (d)). Each panel reports three curves, corresponding to three different monitoring vertical locations within the air flow. It can be seen that the measured peak frequency does not vary moving along the streamwise and/or vertical direction. In this respect, it can be inferred that the flow features global mode oscillations, i.e. temporal velocity fluctuations synchronized over a large spatial extent at the flow natural frequency. It can be also noted that the unsteady dynamics in presence of global oscillations is characterized by a low-order behaviour, i.e. the flow oscillates at

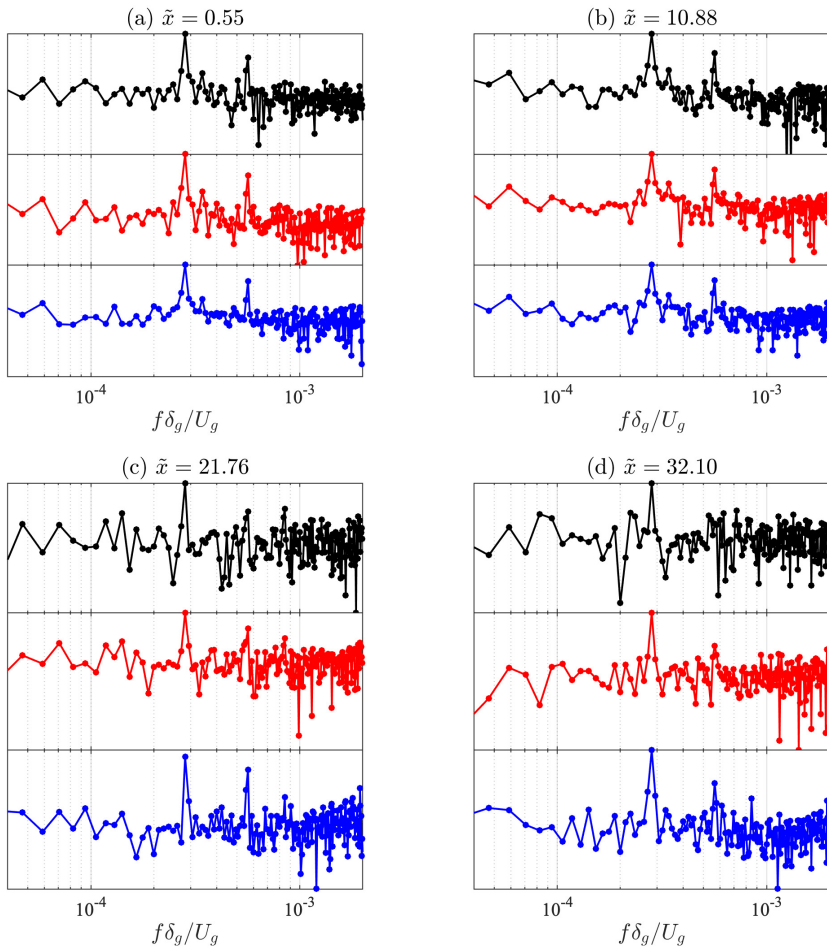


Figure 4.59. FFT of $v'(t)$ at different (\tilde{x}, \tilde{y}) locations: $\tilde{y} = 8.16$ (black curve); 5.44 (red); 2.72 (blue). REgl case of Table 4.12.

the peak (dimensionless) frequency $f\delta_g/U_g = 2.8 \cdot 10^{-4}$ and its first super-harmonic $5.6 \cdot 10^{-4}$, the energy content at other frequencies being negligible. An analogous behaviour has been recently outlined for one-phase mixing layers formed between parallel streams of different velocities by Dutta *et al.* [122]. The measured peak frequency $f\delta_g/U_g = 2.8 \cdot 10^{-4}$ is in close agreement with various experimental literature findings reported in Table 5 on page 171 by Fuster *et al.* [48].

To shed light on the spatio-temporal flow dynamics in presence of global mode oscillations, the analysis of the REgl case is concluded by performing the proper orthogonal decomposition (POD) of u' velocity fluctuations,

$$u'(\tilde{x}, \tilde{y}, t) = u(\tilde{x}, \tilde{y}, t) - \bar{u}(\tilde{x}, \tilde{y}) = \sum_{j=1}^{\infty} a_j(t) \varphi_j(\tilde{x}, \tilde{y}). \quad (4.19)$$

The Gappy POD iterative algorithm (Everson and Sirovich [123], Venturi and Karniadakis [124], Gunes *et al.* [125]) is applied to denoise the data and extract the leading modes, with a spatial weight matrix (defining the state vector norm) accounting for the different densities of gas and liquid phases.

The POD energy distribution is reported in Fig. 4.60(a), while panels (b)-(f) show the first five POD modes. The first mode (panel (b)) denotes a normal-to-flow oscillatory (flapping) dynamics of the interface, while the couples of modes $2^{nd} - 3^{th}$ and $4^{th} - 5^{th}$ represent spatially coherent structures advected along the streamwise direction, each couple being characterized by the typical shift of modes along the \tilde{x} axis. The power spectral density (PSD) of the temporal coefficients a_i associated to the leading modes is finally reported in Fig. 4.61. All the modes are peaked at the (dimensionless) frequency $f\delta_g/U_g = 2.8 \cdot 10^{-4}$, which is the same value outlined by the local spectral analyses previously shown in Fig. 4.59. Moreover, the product between the second POD mode wavelength, $\tilde{\lambda} = \lambda/e = 25$ (see Fig. 4.60(c)), and the secondary peak frequency of $PSD(a_2)$,

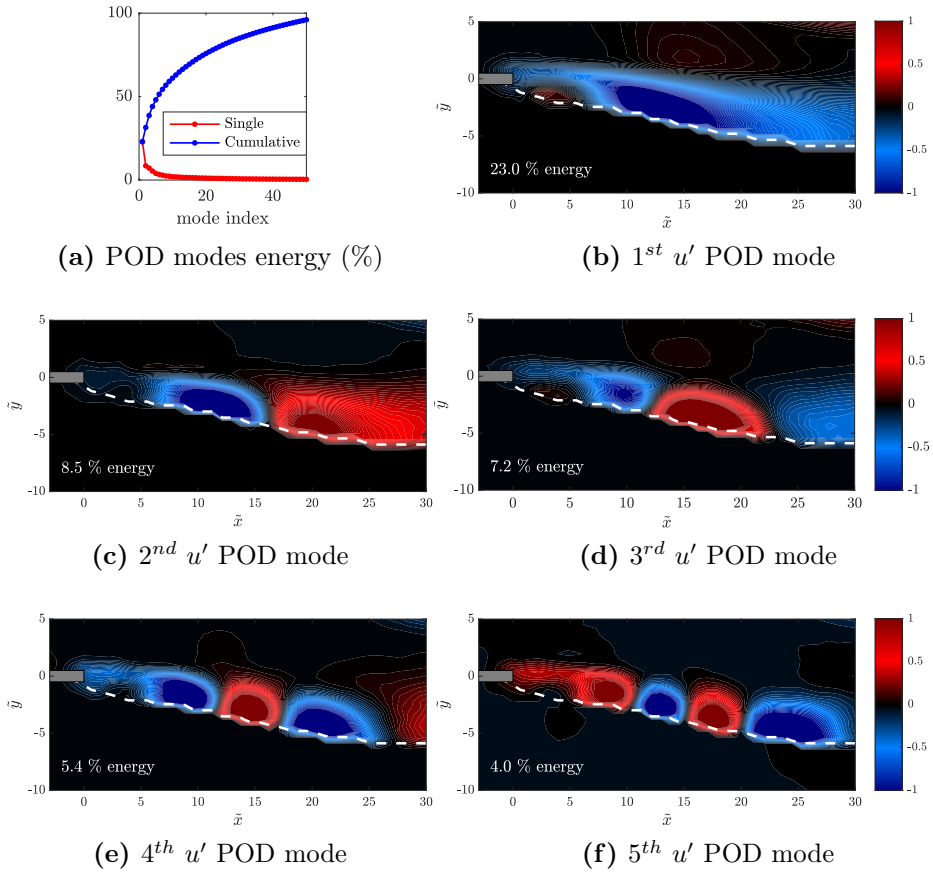


Figure 4.60. POD analysis of the REgl case of Table 4.12. Energy distribution (panel (a)); leading u' modes (each scaled with respect to its maximum, panels (b)-(f)). In each panel, the splitter plate is highlighted in grey, and the mean interface location is denoted by the white dashed line.

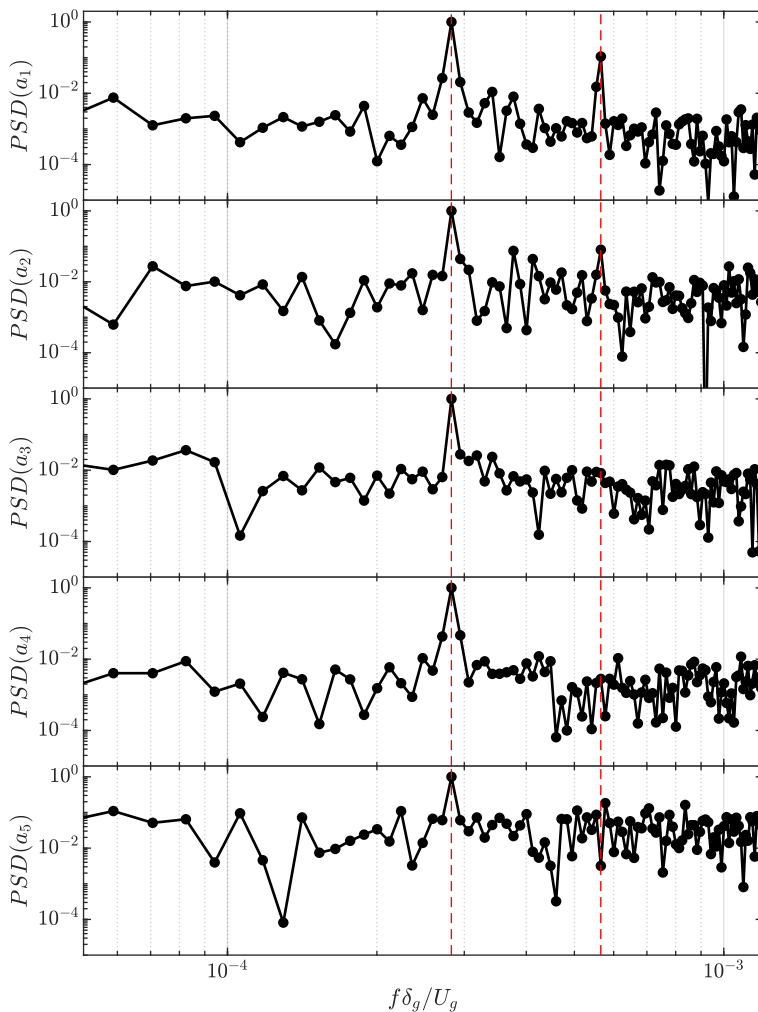


Figure 4.61. Power spectral density (PSD) of the temporal coefficients a_i associated to the leading POD modes shown in Fig. 4.60. The vertical red dashed lines denote the peak frequency $f\delta_g/U_g = 2.8 \cdot 10^{-4}$ and its first super-harmonic $f\delta_g/U_g = 5.6 \cdot 10^{-4}$.

$f\delta_g/U_g = 5.6 \cdot 10^{-4}$ (Fig. 4.61), yields a dimensional velocity of the disturbance travelling wave equal to $U = \lambda f = 0.55$ m/s. This value is in close agreement with the interfacial wave propagation speed given by Dimotakis [126], $U_D = (\sqrt{\rho_l}U_l + \sqrt{\rho_g}U_g)/(\sqrt{\rho_l} + \sqrt{\rho_g}) = 0.59$ m/s (relative spread of 6.78% for $U_l = 0.1$ m/s and $U_g = 15$ m/s, corresponding to the REgl case here analyzed), which was obtained assuming the gas and liquid dynamic pressures in balance in a reference frame moving with the wave speed. These last findings highlight the relationship between the global mode velocity oscillations measured within the flow field and the gas-liquid interfacial spatio-temporal dynamics.

Conclusion

The main goal of the work described in this thesis is twofold: i) to advance towards a more complete understanding of the physical mechanisms underlying gravitational liquid curtains unsteady dynamics; and ii) to provide an experimental characterization of two-phase mixing layer flows simultaneously in gas and liquid phases, preparing the way towards a global stability analysis in the next future.

To accomplish these objectives, theoretical, numerical and experimental methodologies have been developed and employed, including volume-of-fluid direct numerical simulations, linear stability analysis, data-driven modal decomposition techniques, and time-resolved particle image velocimetry (Chapter 3). The last methodology has been applied for the experimental characterization of the two-phase mixing layer velocity field, as a result of the collaboration between the research group in which the candidate worked in Naples and the Flow Stability & Control research group at Delft University of Technology, where the candidate spent a Visiting Scholar period of one year during his Ph.D. Program.

The main conclusions that can be drawn from this work are hereafter summarized, separately for the two gas-liquid interfacial flow systems investigated. Recommendations for possible future developments of the work are finally reported.

5.1 Conclusions

5.1.1 Gravitational liquid curtains

The unsteady dynamics of gravitational liquid curtain flows crucially depends on the Weber number We , namely the ratio between inertia and capillary forces within the liquid phase. Three flow regimes with different peculiar features can be distinguished depending on the Weber number value: supercritical ($We > 1$), transcritical ($We = \mathcal{O}(1)$), and subcritical ($We < 1$) regimes.

In supercritical conditions (Sections 4.1.1 and 4.1.2), the major novel finding is that the sheet becomes unstable for relatively high values of the gas-to-liquid density ratio r_ρ , as predicted by a simplified theoretical linear model of the curtain dynamics and confirmed by two-dimensional fully nonlinear numerical simulations. Since the oscillatory dynamics of the average sheet displacement resembles that of a tensional string forced by terms containing the lateral velocity, and it is subjected to a total damping coefficient which can assume negative values, it can be argued that the distribution of the transverse velocity component of the ambient gaseous phase represents such a forcing term, which leads the system towards the instability. The role of the gaseous ambient phase on the sheet instability has been thus quantified by means of an energy budget analysis, shedding light on the physical mechanisms underlying the curtain dynamics. The energetic analysis has revealed that the key term driving the instability is the work per unit time made by the atmospheric environment on the liquid phase by means of pressure perturbations; the weight of this energy budget overwhelms progressively all other budgets as the density ratio is increased.

When the Weber number traverses the critical threshold $We = 1$ (transcritical regime, Section 4.1.3), experimental measurements of the curtain oscillatory dynamics reveal an original discontinuous behaviour of the flow system, namely its natural frequency abruptly increases going from supercritical to subcritical conditions. The theo-

retical predictions of the flow natural frequency and its *jump* when the supercritical-to-subcritical flow transition occurs remarkably agree with experimental measurements, and strongly rely on two features of the simplified curtain model employed: accounting for the liquid sheet–air ambient interaction, and considering a sheet of finite length. As a matter of fact, if one neglects the pressure term in case of a finite length curtain, the linear stability analysis yields an empty spectrum, i.e. no natural frequency is detected, and consequently no frequency discontinuity. On the other hand, if a curtain of infinite length is considered, the natural frequency predicted by the theoretical analysis vanishes.

In subcritical conditions (Section 4.1.4), direct numerical simulations show a nonlinear sinuous-varicose modes interaction when forcing the liquid curtain at its natural frequency, namely when the sheet oscillates in resonance conditions. Although the linear inviscid theory (accounting for sinuous modes only) is able to quantitatively predict the natural frequency also in presence of sinuous–varicose modes interaction, it is obviously not able to foresee the varicose distortions. The latter modes can be instead predicted by a data-driven approach based on the dynamic mode decomposition of random perturbations superposed on the base flow, which has been employed to obtain the two-dimensional global (BiGlobal) spectrum of the flow in both supercritical and subcritical conditions. The role of sinuous and varicose contributions in the dynamics and topology of the subcritical flow has been further clarified by means of the spectral proper orthogonal decomposition of numerical data. In resonance conditions, the varicose component of the leading SPOD mode becomes progressively more important (energy-wise) as We decreases, attaining a maximum at $We = 0.75$, whereas the sinuous contribution increases with We . The excitation of the varicose mode when the Weber number is decreased, with a progressive shift from higher harmonics towards the leading frequency, can be interpreted as a prelude to the rupture experienced by the liquid sheet, experimentally observed when We is reduced (by progressively reducing the inlet

flow rate). Finally, the energy budget decomposition shows that the work per unit time done by the surface tension is the physical mechanism responsible for the flow instability in subcritical conditions, as the Weber number is progressively decreased down to We_{th} , with We_{th} being the inlet We number for which the sheet is entirely subcritical (local Weber number less than the unity everywhere along the curtain). In these conditions, a transient algebraic growth of perturbations is found in both asymptotically stable ($We_{th} < We < 1$) and unstable ($We < We_{th}$) regimes. In the latter case, the temporal evolution of disturbances eventually follows an asymptotic modal growth, which is also recovered in the eigenvalues spectra evaluated by the linear stability analysis.

5.1.2 Two-phase mixing layers

The time-averaged flow topology and the unsteady dynamics of air-water mixing layer flows past a finite thickness splitter plate are affected by both gas and liquid physical parameters, related to the air U_g and water U_l injection velocities. In particular, the effects of the gas Reynolds number Re_g , the liquid Weber number We_l , and the gas-to-liquid dynamic pressure ratio M are the most relevant, and have been investigated through two-phase time-resolved particle image velocimetry measurements, for the first time performed simultaneously in gaseous and liquid streams. The experiments have been designed so as to work at a relatively high plate-to-air vorticity thickness ratio, e/δ_g , i.e. in the so called injector-influenced regime.

The analysis of a selected base case configuration ($Re_g = 493$, $We_l = 0.84$) reveals that the mean two-phase flow is affected by the presence of a recirculation wake region behind the splitter plate located at the injection section ($\tilde{x} = 0$), whose extension \tilde{x}_w depends on the interplay between liquid Weber and gas Reynolds numbers. A very good agreement between the experimental data $\bar{u}(\tilde{x}, \tilde{y})$ and theoretical velocity profiles provided in literature is obtained, both in the pure mixing layer region ($\tilde{x} > \tilde{x}_w$) and inside ($\tilde{x} < \tilde{x}_w$) the wake

region, where a negative value of the velocity defect (i.e. difference between the minimum and free-stream liquid velocity, $\bar{u}_{min} - U_l$) is found.

A parametric analysis of the flow behaviour has been then performed by varying separately the governing parameters We_l and Re_g , and thus the gas-to-liquid dynamic pressure ratio M . By fixing $Re_g = 493$, the wake region vanishes as We_l increases up to 2.97, and the air-water mixing layer becomes parallel, namely spatially invariant along the streamwise direction \tilde{x} . Analogously, the wake progressively shortens as Re_g increases at fixed We_l , and for the highest value of Reynolds number considered ($Re_g = 768$) it vanishes in a wide range of M values ($0 < M < 12$). Therefore, it is found that only at relatively high values of the gas Reynolds number the flow behaves as a pure mixing layer in a wide range of liquid injection velocities.

The unsteady flow dynamics is initially investigated through the frequency spectra of velocity fluctuations, evaluated at different locations within the air phase. In agreement with spatio-temporal local linear stability predictions of literature, the spectral analysis reveals that the flow amplifies random noise (e.g. generated by free stream turbulence) at low Re_g and M values, while for high Re_g a clear peak frequency $f\delta_g/U_g = 2.8 \cdot 10^{-4}$ arises as M progressively increases beyond the threshold value $M = 4.25$. In this case, the flow exhibits a global mode behaviour, namely the temporal velocity fluctuations are synchronized with the peak frequency over a large extent in the spatial domain. The proper orthogonal decomposition of velocity fluctuations finally gives insights onto the dominant structures of the flow, and reveals the relationship between global mode oscillations measured within the gaseous phase and the gas-liquid interfacial spatio-temporal dynamics.

5.2 Recommendations for future work

This work has successfully given insights on the physical mechanisms underlying the unsteady dynamics of two typical gas-liquid interfacial flow configurations, namely gravitational liquid curtain flows and two-phase mixing layers.

A combined theoretical-numerical-experimental investigation has shed light on the curtain two dimensional flow stability properties in supercritical ($We > 1$), transcritical ($We = \mathcal{O}(1)$) and subcritical ($We < 1$) regimes. The numerical simulation and data-driven modal decomposition methodologies used and developed herein apply straightforward to three-dimensional scenarios. Future work should thus aim at providing comparisons and establishing the connections between present two-dimensional results and three-dimensional curtain configurations of real occurrence, focusing in particular on the subcritical sheet dynamics and the related breakup mechanisms. Preliminary work in this direction is reported in Section 4.1.2 and in the Master Thesis of M. R. Acquaviva "Hole-induced dynamics of a gravitational liquid curtain: a numerical approach" (Unina, 2022), and it has been also presented at the European Congress on Computational Methods in Applied Science and Engineering 2022 (Della Pia *et al.* [127] and Colanera *et al.* [128]).

On the experimental side, the major contribution of this work is certainly represented by the air-water mixing layer velocity field characterization through time-resolved particle image velocimetry. The measurements here provided may represent the starting point to perform a data-driven global stability analysis of the flow by application of modal decomposition techniques (SPOD/DMD) to the experimental data.

Insights into liquid curtains numerical treatment

A.1 Boundary conditions in subcritical regime

Dividing Eq. (2.17) (Section 2.1.3) by U and enforcing the temporal modes position (Section 3.2) leads to the following Sturm-Liouville-like eigenvalue integro-differential equation:

$$\frac{d}{dx} \left[\left(U - \frac{1}{We} \right) \frac{d\hat{\ell}}{dx} \right] + 2\lambda \frac{d\hat{\ell}}{dx} + \lambda^2 \left[\frac{1}{U} - R \int_0^1 (\cdot) \ln|x - \xi| d\xi \right] \hat{\ell} = 0. \tag{A.1}$$

The equation is singular since the second order term coefficient vanishes at the location where the flow, accelerating due to gravity, reaches a critical velocity equal to $1/We$. The procedure developed to remove this singularity, inspired by Finnicum *et al.* [19] and Girfoglio *et al.* [13], is hereafter described.

Integrating Eq. (A.1) from the inlet location ($x = 0$) to the generic location x and resolving for $d\hat{\ell}/dx$ (by taking into account the kinematic boundary condition, Eq. (2.13) in Section 2.1.3), yield an expression for the local slope of the sheet centreline, which depends on

the slope value at the inlet location

$$\begin{aligned} \left(U - \frac{1}{We}\right) \frac{d\hat{\ell}}{dx} = & -\lambda\hat{\ell} - \lambda \int_0^x \left(\frac{v}{U} - RFd\xi + RG\right) d\xi + \\ & + \left(U - \frac{1}{We}\right) \frac{d\hat{\ell}}{dx} \Big|_0, \end{aligned} \quad (\text{A.2})$$

where $F(x) = \int_0^1 \hat{v} \ln|x - \xi| d\xi$ and $G(x) = \int_0^1 U d\hat{\ell}/dx \ln|x - \xi| d\xi$, respectively.

Note that in a supercritical regime the coefficient $U - \frac{1}{We}$ at left hand side does not vanish in any location. The scenario entirely changes in subcritical regime since at the critical station, where the local Weber number $We_l = UWe$ is unity, this coefficient vanishes. Since for inlet Weber numbers weakly less than unity the sheet can survive without rupture, one can hypothesize that the sheet assumes an initial slope which is able to eliminate the singularity (Finnicum *et al.* [19]). As made for the nappe problem by Girfoglio *et al.* [13], one can evaluate the initial slope $d\hat{\ell}/dx|_0$ which nullifies the right hand side of Eq. (A.2) and substitute it into the equation itself, so as to obtain an undetermined equation:

$$\frac{d\hat{\ell}}{dx} = \frac{\lambda \left(\hat{\ell}(x_s) - \hat{\ell}(x) \right) - \lambda \int_{x_s}^x v/U d\xi + R\lambda \int_{x_s}^x F d\xi - R\lambda \int_{x_s}^x G d\xi}{U - \frac{1}{We}}, \quad (\text{A.3})$$

where x_s is the critical station introduced in Section 2.1.3 (Eq. (2.25)). Applying de L'Hôpital's rule allows one to calculate the singular limit as

$$\frac{d\hat{\ell}}{dx} \Big|_{x_s} = \frac{-\lambda\hat{v}(x_s)/U + \lambda R[F(x_s) - G(x_s)]}{\lambda + We/Fr}. \quad (\text{A.4})$$

Therefore, for subcritical inlet, the boundary conditions to be enforced in solving the eigenvalue problem (3.8) (see Section 3.2) are expressed by Eq. (A.4) together with the condition $\hat{\ell}(0) = 0$.

A.2 Viscous modification of the eigenvalues analysis

The matrix operators \mathcal{M} and \mathcal{A} introduced in Section 3.2 modify for viscous conditions ($Re \neq \infty$) as follows:

$$\mathcal{M} \equiv \begin{pmatrix} \mathcal{I} - RU \cdot \mathcal{I} \mathcal{N} \mathcal{I} & RU \cdot \mathcal{I} \mathcal{N} \mathcal{I} \cdot U \cdot \mathcal{D} \\ \mathcal{O} & \mathcal{I} \end{pmatrix},$$

$$\mathcal{A} \equiv \begin{pmatrix} -U \cdot \mathcal{D} + \frac{\varepsilon}{2Re} \mathcal{D}^2 & \frac{U}{We} \mathcal{D}^2 \\ \mathcal{I} & -U \cdot \mathcal{D} \end{pmatrix}.$$

All symbols are analogous to those of Eq. (3.8) in Section 3.2, except for the viscous modification (depending on the Reynolds number Re) of \mathcal{A}_{11} (see Eq. (2.27) in Section 2.1.3). The eigenvalue integro-differential equation (A.1) accordingly modifies as

$$\begin{aligned} & \frac{d}{dx} \left[\left(U - \frac{1}{We} \right) \frac{d\hat{\ell}}{dx} \right] + \left(2\lambda - \frac{\varepsilon}{2URe} \frac{d^2U}{dx^2} \right) \frac{d\hat{\ell}}{dx} = \\ & -\lambda^2 \left[\frac{1}{U} - R \cdot \mathcal{I} \mathcal{N} \mathcal{I} \right] \hat{\ell} + \frac{\varepsilon\lambda}{2URe} \frac{d^2\hat{\ell}}{dx^2} + \frac{\varepsilon}{2Re} \frac{d^3\hat{\ell}}{dx^3} + \\ & + \frac{\varepsilon}{URe} \frac{dU}{dx} \frac{d^2\hat{\ell}}{dx^2}. \end{aligned} \tag{A.5}$$

It is evident that the presence of the viscous term removes the singularity exhibited by the flow in inviscid conditions; in fact, at the critical station x_s , namely where $U = 1/We$, the second order term of Eq. (A.5) does not vanish. From the other hand, one can still manipulate the equation using the same approach adopted in Appendix A.1, thus determining the second boundary condition to be

applied in subcritical viscous regime:

$$\left. \frac{d\hat{\ell}}{dx} \right|_{x_s} = \frac{-\lambda W e \hat{v}(x_s) + \lambda [RF(x_s) - RG(x_s) + SI(x_s)]}{\lambda + We/Fr} + \frac{S[H(x_s) + L(x_s) + M(x_s)]}{\lambda + We/Fr}, \quad (\text{A.6})$$

where the following parameters have been defined:

$$S = \frac{\varepsilon}{2Re}, \quad F(x) = \mathcal{I} \mathcal{N} \mathcal{T} \cdot \hat{v}, \quad G(x) = \mathcal{I} \mathcal{N} \mathcal{T} \cdot \left(U \frac{d\hat{\ell}}{dx} \right),$$

$$H(x) = \frac{1}{U} \frac{d^2 U}{dx^2} \frac{d\hat{\ell}}{dx}, \quad I(x) = \frac{1}{U} \frac{d^2 \hat{\ell}}{dx^2}, \quad L(x) = \frac{d^3 \hat{\ell}}{dx^3}, \quad M(x) = \frac{2}{U} \frac{dU}{dx} \frac{d^2 \hat{\ell}}{dx^2}.$$

Details of the mixing layer experimental apparatus

B.1 Experiment core

A three dimensional sketch (realized in CATIA V5) of the air-water wind tunnel representing the core part of the mixing layer experimental apparatus is reported in Fig. B.1, together with the corresponding block diagram representation. The main components of the (hereafter called) *experiment core* are:

- 2 ducts; 1 splitter plate; 2 nozzles,

and are respectively described in Tables B.1, B.2 and B.3. Honeycombs are placed in the liquid tunnel, and a combination of honeycombs and anti-turbulence screens is employed in the gas tunnel (see Section 3.5 for details about the flow conditioners design). The components dimensions are expressed as a function of four parameters:

- $l = 500$ mm; $h = w = 100$ mm; $e = 2$ mm.

Both liquid and gas channels have a 100×100 mm² cross-section, and the contraction ratio of the nozzles is 5:1. Fig. B.2 shows the main views of the experiment core; the occupied space is approximatively

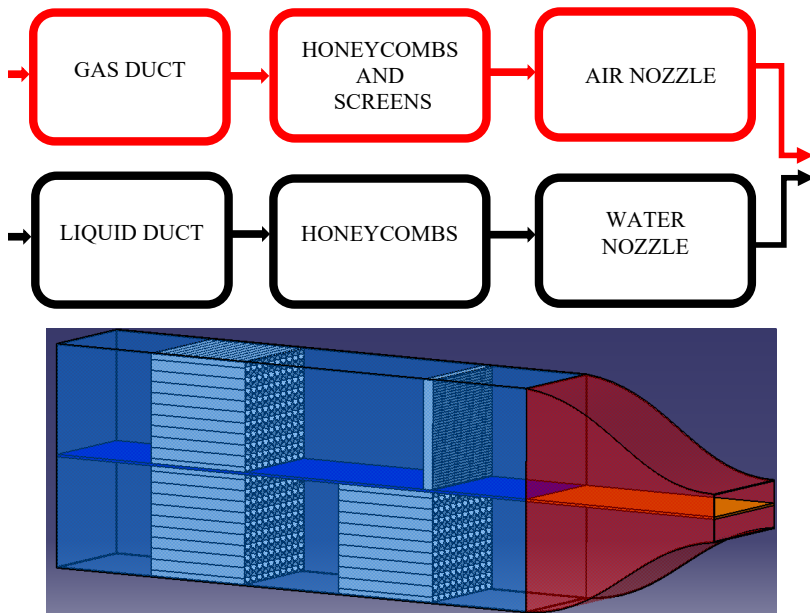


Figure B.1. Block diagram representation (top) and three dimensional sketch (bottom) of the experiment core components. The splitter plate separates the gas and liquid ducts.

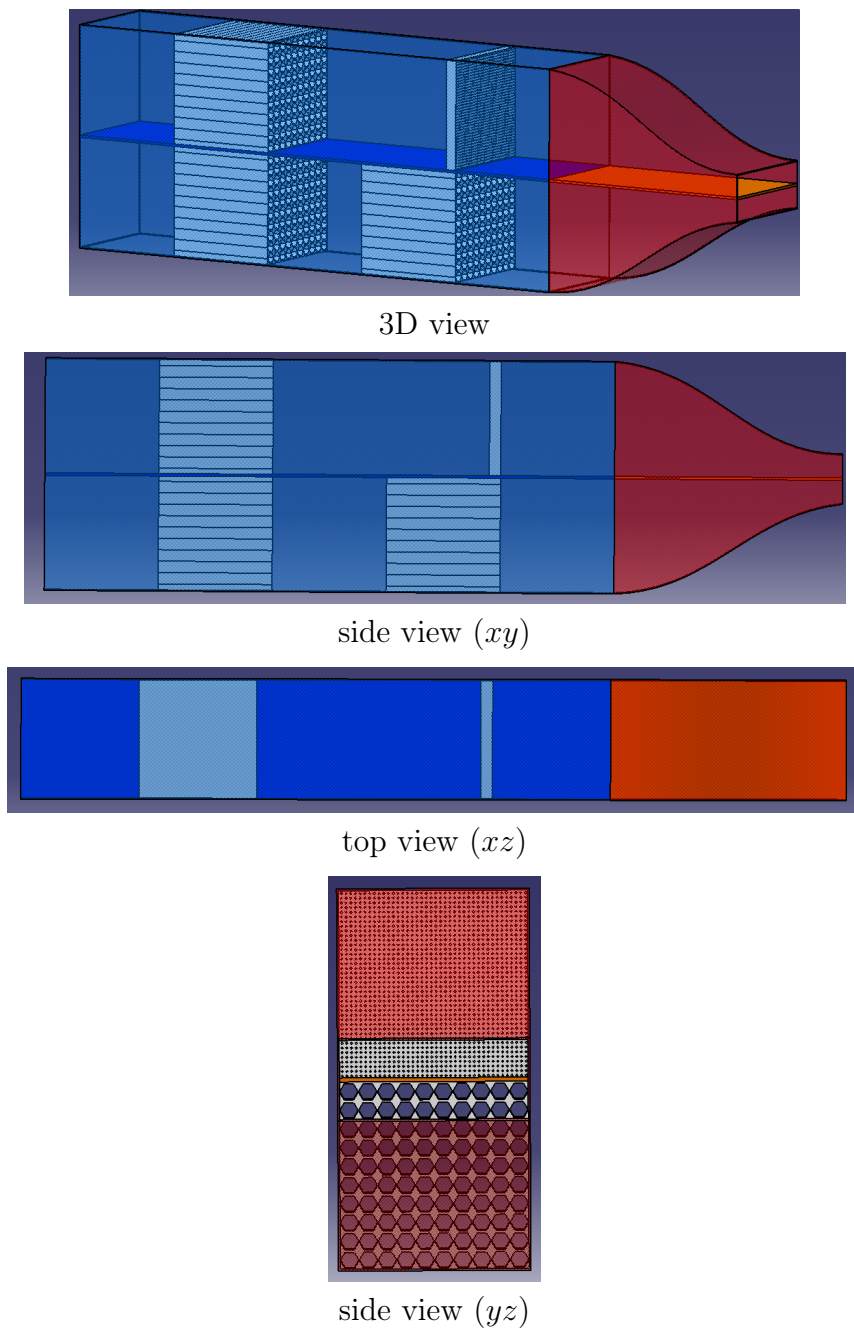


Figure B.2. Main views of the experiment core components.



Figure B.3. Picture of the experiment core realized in Plexiglas. The test section is also shown (on the right).

Table B.1. Gas and liquid ducts dimensions. Each duct has a rectangular cross section (in yz plane); the area occupied by each phase (gas or liquid) is $A_{yz} = h \cdot w$.

Name	Variable	Expression	Value (mm)
Length (x axis)	L_D	l	500
Height (y axis)	H_D	h	100
Width (z axis)	W_D	w	100

equal to $x \times y \times z = 700 \times 202 \times 100 \text{ mm}^3$. All the components have been realized in Plexiglas; a picture is reported in Fig. B.3.

B.2 Air circuit

A three-dimensional sketch of the main air circuit components is shown in Fig. B.4, together with the corresponding block diagram representation. The core assembly is also reported. The components added to the experiment core are:

- 1 blower; 1 connection duct; 1 connection flange.

Table B.2. Splitter plate dimensions. It has a $e \times w$ rectangular cross section (in yz plane). Parameters values: $l = 500$ mm; $h = w = 100$ mm; $e = 2$ mm.

Name	Variable	Expression	Value (mm)
Length (x axis)	L_E	$l + 2/5 \cdot l$	700
Height (y axis)	H_E	e	2
Width (z axis)	W_E	w	100

Table B.3. Gas and liquid nozzles dimensions. Each nozzle has a contoured cross section (in yz plane) with contraction ratio $H^i/H^f = 5$. Parameters values: $l = 500$ mm; $h = w = 100$ mm; $e = 2$ mm.

Name	Variable	Expression	Value (mm)
Length (x axis)	L_N	$2/5 \cdot l$	200
Max height (y axis)	H_N^i	h	100
Min height (y axis)	H_N^f	$H^f/H^i \cdot h$	20
Width (z axis)	W_N	w	100

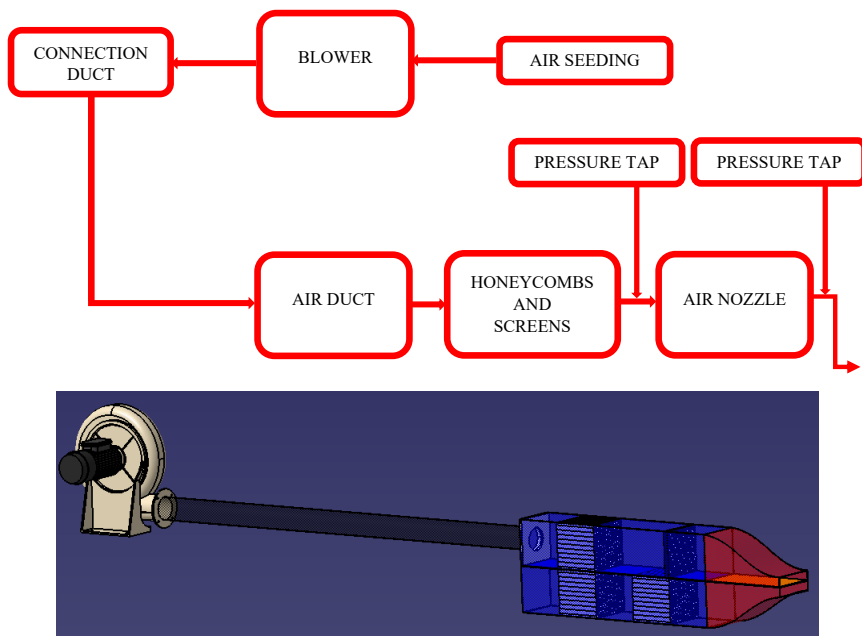


Figure B.4. Block diagram representation (top) and three dimensional sketch (bottom) of the gas circuit (plus the core) components. The air flow seeding and the pressure taps are not represented.



Figure B.5. Picture of the connection component between the blower (on the right) and the air duct (on the left).

The blower accelerates the gas flow from quiescent conditions ($U_g = 0$) up to a maximum velocity $U_{g,max}$: the required power is calculated in Section B.2.1. The connection between the blower and the duct has been schematized as a pipe with diameter $D_1 = 315$ mm, equal to the blower exit section, and length $L_1 = 500$ mm. Finally, a flange connects the pipe to the gas duct. Note that a more sophisticated blower-duct connection with variable cross-sectional area has been designed and employed in the realized apparatus (see Fig. B.5).

B.2.1 Air blower power estimation

The power required to accelerate the gas flow up to $U_{g,max} = 30$ m/s (higher than the maximum velocity designed for the PIV measurements, see Section 3.5.1) can be estimated starting from the energy conservation equation applied between section a and b :

$$\frac{p_a}{\rho g} + \frac{v_a^2}{2g} + z_a = \frac{p_b}{\rho g} + \frac{v_b^2}{2g} + z_b + h_f + \sum h_i - h_e, \quad (\text{B.1})$$

Table B.4. Minor losses coefficients for the air circuit: data from Munson *et al.* [129] and White [130]. In particular, the estimation $K = 4$ is taken from Chapter 8 of [129].

Loss coefficient	K
Sharp entrance (gas duct entrance)	0
Honeycomb	4
Anti-turbulence screens	4
Nozzle	0

Table B.5. Gas circuit head losses varying the working velocity U_g . The required power P_e is calculated assuming a precautionary value of $\eta = 0.75$ for the blower efficiency.

Head losses (m)	$U_g = 10$ m/s	$U_g = 30$ m/s
h_p	0	0
h_v	5.1 (75.11%)	46 (74.92%)
h_z	0	0
h_f	0.06 (0.89%)	0.4 (0.65%)
$\sum h_i$	1.63 (24.0%)	15 (24.43%)
$h_e(\text{total})$	6.79 (100%)	61.40 (100%)
Head losses (Pa)	78.36	704
Blower power (hp)	0.003	0.08

where section a is the blower inlet and section b is the gas nozzle outlet. The total head loss h_e can thus be determined from Eq. (B.1),

$$h_e = h_p + h_v + h_z + h_f + \sum h_i = 61.40 \text{ m}, \quad (\text{B.2})$$

where the different terms have been evaluated as:

- $h_p = \frac{p_b - p_a}{\rho g} = 0;$
- $h_v = \frac{v_b^2 - v_a^2}{2g} = 46 \text{ m};$
- $h_z = z_b - z_a = 0 \text{ m};$
- $h_f = h_{f_1} + h_{f_2} = \frac{f_1 L_1}{D_1} \cdot \frac{v_1^2}{2g} + \frac{f_2 L_2}{D_2} \cdot \frac{v_2^2}{2g} = 0.20 \text{ m} + 0.20 \text{ m} = 0.40 \text{ m};$
- $\sum h_i = K_1 \frac{v_1^2}{2g} + K_2 \frac{v_2^2}{2g} + K_3 \frac{v_3^2}{2g} = 0.0 \cdot \frac{v_1^2}{2g} + (4 + 4) \cdot \frac{v_2^2}{2g} = 15 \text{ m}.$

The kinetic head (h_v) is determined assuming the gas at rest outside the blower ($v_a = 0$) and evaluating the velocity at the nozzle exit section as $v_b = Q/A_b$, with the flowrate $Q = v_b \cdot A_b = 0.06 \text{ m}^3/\text{s}$ estimated in section b , where both the required velocity $v_b = 30 \text{ m/s}$ and the cross-section area $A_b = 2 \cdot 10^{-3} \text{ m}^2$ are known. With the flowrate Q assigned, the fluid velocity at the different stations is evaluated as $v_i = Q/A_i$. The term h_p is assumed equal to zero, because sections a and b are both considered at atmospheric pressure ($p_a = p_b$). The term h_z is also assumed equal to 0 m, because the blower exit section is supposed to be horizontally aligned with the duct inlet section. The friction losses in the pipe, h_{f_1} , and in the gas duct, h_{f_2} , are both estimated as $h_f = fL/D \cdot v^2/(2g)$, where $D_2 = 0.1 \text{ m}$ is the equivalent (hydraulic) diameter of the duct rectangular cross-section, and $L_2 = L_D = 0.5 \text{ m}$ is its length (see Table B.1). Note that the Darcy friction factor $f_i = f(Re_{D_i}, \epsilon/D_i)$ is evaluated with the well-known

Colebrook formula, assuming a roughness coefficient $\epsilon = 0.0015$ mm: $f_1 = 0.022$ and $f_2 = 0.022$, respectively. Finally, the minor losses in the gas circuit are estimated as $h_i = K_i \cdot v_i^2 / (2g)$, with the coefficients K_i taken from [129], [130] and reported in Table B.4. The friction losses in the nozzle have been neglected (Chapter 8 of Munson *et al.* [129]).

The required power P_e of the blower is thus calculated as

$$P_e = \rho g Q h_e / \eta \approx 56 \text{ W (0.08 hp)}, \quad (\text{B.3})$$

where $\rho = 1.177 \text{ Kg/m}^3$, $g = 9.81 \text{ m/s}^2$, and a precautionary value equal to $\eta = 0.75$ has been assumed for the blower efficiency. The head losses estimation at $U_g = U_{g,max}$ is summarized in Table B.5, including also a lower working velocity case ($U_g = 10 \text{ m/s}$). Based on this performance estimation, a ruck Ventilatoren RS315LEC has been chosen as the air blower of the experimental apparatus.

B.3 Liquid circuit

A sketch of the experimental apparatus including the liquid circuit is reported in Fig. B.6. The liquid circuit components added to the experiment core are:

- 2 tanks; 4 pipes; 1 connection flange; 1 test section; 1 liquid collector; 1 pump; 1 regulating valve; 1 flowmeter.

An overflowing tank is positioned 0.5 m above the liquid channel and is schematized as a $500 \times 500 \times 500 \text{ mm}^3$ cube. A 50 mm diameter pipe allows the liquid to flow from the tank to the channel entrance, where it is constrained through a properly designed flange to the duct. A regulating valve is positioned upstream of the liquid channel entrance, allowing to regulate the (constant) flowrate during each experiment. After the channel, the liquid enters the test section, which is schematized as a $500 \times 42 \times 100 \text{ mm}^3$ parallelepiped open on the top, left and right sides (yellow component in Fig. B.6). A

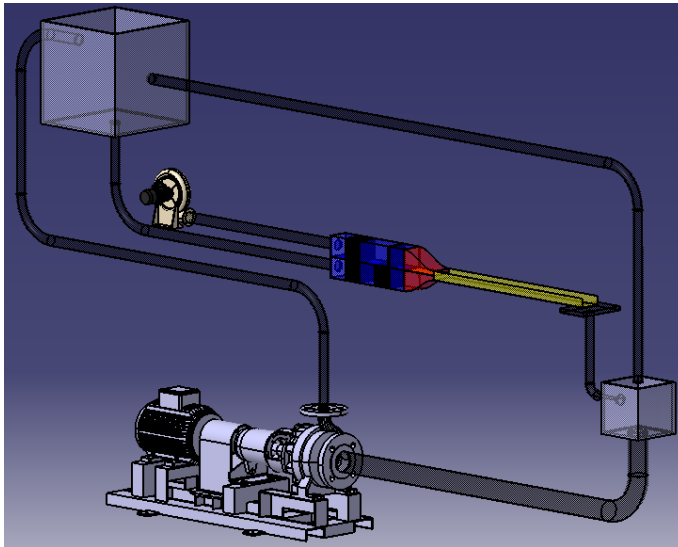
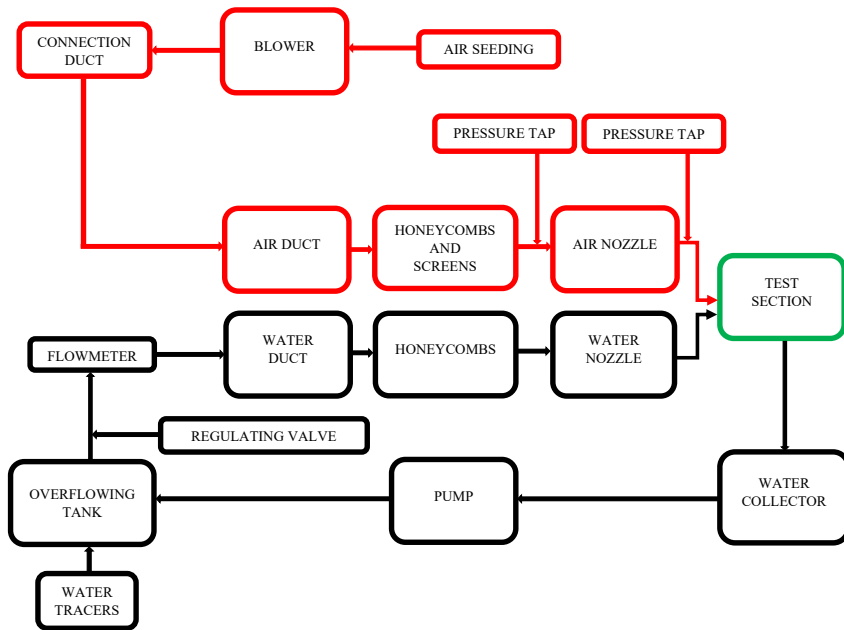


Figure B.6. Block diagram representation (top) and three dimensional sketch (bottom) of the final version of the experimental apparatus. The flowmeter, the pressure taps, the regulating valve and the flows seeding are not represented.

collector is positioned below the final part of the test section: it discharges the liquid into a second tank positioned 400 mm below the test section. A pump thus allows the liquid to flow back from the second to the first (overflowing) tank through two different pipes 38.1 mm (1 + 1/2 in.) in diameter.

B.3.1 Overflowing tank design

The driving force in the liquid circuit is gravity acting on the fluid. The gravitational energy $\rho g(z_b - z_a)$ required to obtain an injection velocity equal to $U_{l,max} = 1$ m/s (higher than the maximum velocity designed for the PIV measurements, see Section 3.5.1) can be estimated starting from Eq. (B.1) applied between section a and b ,

$$\frac{p_a}{\rho g} + \frac{v_a^2}{2g} + z_a = \frac{p_b}{\rho g} + \frac{v_b^2}{2g} + z_b + h_f + \sum h_i.$$

In this case, section a is the liquid free surface in the tank, and section b is the nozzle outlet connected to the liquid channel. The unknown quantity $h_z = z_b - z_a$ can thus be determined from Eq. (B.1),

$$h_z = h_p + h_v + h_f + \sum h_i = 695 \text{ mm.} \quad (\text{B.4})$$

The different terms have been evaluated as

- $h_p = \frac{p_b - p_a}{\rho g} = 0;$
 - $h_v = \frac{v_b^2 - v_a^2}{2g} = 51 \text{ mm};$
 - $h_f = h_{f_1} + h_{f_2} = \frac{f_1 L_1}{D_1} \cdot \frac{v_1^2}{2g} + \frac{f_2 L_2}{D_2} \cdot \frac{v_2^2}{2g} = 44 \text{ mm} + 0 \text{ mm} = 44 \text{ mm};$
-

$$\bullet \sum h_i = K_1 \frac{v_1^2}{2g} + K_2 \frac{v_2^2}{2g} + K_3 \frac{v_3^2}{2g} = (0.5 + 0.5 + 10 + 0.05) \cdot \frac{v_1^2}{2g} + (4 + 4) \cdot \frac{v_2^2}{2g} = 600 \text{ mm.}$$

The kinetic head, h_v , is determined assuming a constant liquid level in the tank during the entire experiment ($v_a = p_a = 0$) and evaluating the velocity at the nozzle exit section as $v_b = Q/A_b$, with the flowrate $Q = v_b \cdot A_b = 0.002 \text{ m}^3/\text{s}$ estimated in section b , where both the required velocity $v_b = 1 \text{ m/s}$ and the cross-section area $A_b = 2 \cdot 10^{-3} \text{ m}^2$ are known. With the flowrate Q assigned, it is easy to determine the velocity in the different sections of the gas circuit as $v_i = Q/A_i$. The term h_p is zero because both sections a and b are assumed at atmospheric pressure. The friction losses in the pipe, h_{f_1} , and in the liquid duct, h_{f_2} , are both estimated as $h_f = fL/D \cdot v^2/(2g)$. In particular, $D_1 = 0.05 \text{ m}$, $L_1 = 2 \text{ m}$, $D_2 = 0.1 \text{ m}$ is the equivalent (hydraulic) diameter of the duct rectangular cross-section, and $L_2 = L_D = 0.5 \text{ m}$ is its length (see Table B.1). Note that the Darcy friction factor $f_i = f(Re_{D_i}, \epsilon/D_i)$ is evaluated with the well-known Colebrook formula, assuming a roughness coefficient $\epsilon = 0.0015 \text{ mm}$: $f_1 = 0.02$ and $f_2 = 0.025$, respectively. The minor losses between the overflowing tank and the nozzle are estimated as $h_i = K_i \cdot v_i^2/(2g)$, with the coefficients K_i taken from [129], [130], [131] and reported in Table B.6. Note that the friction losses in the nozzle have been neglected (Chapter 8 of Munson *et al.* [129]).

Therefore, assuming $\rho = 997 \text{ Kg/m}^3$, $g = 9.81 \text{ m/s}^2$, and the overflowing tank bottom located $Z = 500 \text{ mm}$ above the channel, a liquid level equal to $h_z - Z = 195 \text{ mm}$ is obtained. The corresponding pressure head has allowed to realize the PIV measurements in the designed U_l operative range (see Section 3.5.1).

B.3.2 Liquid pump power estimation

The pump allows the liquid to flow back from the waste to the overflowing tank, thus creating a continuous system which avoids the

Table B.6. Minor losses coefficients relative to the first part of the liquid circuit (from the overflowing tank to the nozzle): data from Munson *et al.* [129], White [130]. * The ball valve head loss coefficient $K = 0.05$ is taken from Chapter 8 of [129]. ** The head loss coefficient $K = 10$ is purely indicative; it can vary in a range [1;100] depending on the type of flowmeter and the operating conditions [131]. *** The honeycomb head loss coefficient $K = 4$ is taken from Chapter 8 of Munson *et al.* [129].

Loss	K
Sharp exit (tank exit section)	0.5
Regulating valve	0.05*
Flowmeter	10**
Sharp entrance (liquid duct entrance)	0.5
Honeycombs	8***
Nozzle	0.2

waste of PIV tracers. A preliminary estimation of the required pump power at $U_{l,max} = 1$ m/s can be realized by employing the following equation:

$$\frac{p_a}{\rho g} + \frac{v_a^2}{2g} + z_a = \frac{p_b}{\rho g} + \frac{v_b^2}{2g} + z_b + h_f + \sum h_i - h_{pump}.$$

In this case, sections a and b are the liquid free surfaces in the waste and overflowing tanks, respectively. The total head loss h_{pump} can thus be determined as

$$h_{pump} = h_p + h_v + h_z + h_f + \sum h_i = 2084 \text{ mm}, \quad (\text{B.5})$$

where the different terms have been evaluated as

- $h_p = \frac{p_b - p_a}{\rho g} = 0;$
- $h_v = \frac{v_b^2 - v_a^2}{2g} = 0;$

- $h_z = z_b - z_a = 1500$ mm;
- $h_f = h_{f_1} + h_{f_2} = \frac{f_1 L_1}{D_1} \cdot \frac{v_1^2}{2g} + \frac{f_2 L_2}{D_2} \cdot \frac{v_2^2}{2g} = 278$ mm;
- $\sum h_i = K_1 \frac{v_1^2}{2g} + K_2 \frac{v_2^2}{2g} = 0.5 \cdot \frac{v_2^2}{2g} + (0.5 + 0.95) \cdot \frac{v_3^2}{2g} = 306$ mm.

The head losses h_v and h_p are both zero, because the liquid is assumed at rest in both the tanks. With a flowrate equal to $Q = 0.06$ m³/s known, it is easy to determine the velocity in the two pipes (see Fig. B.6): $v_1 = v_2 = 1.75$ m/s ($D_1 = D_2 = 38.1$ mm). The friction losses in the pipes, h_{f_1} and h_{f_2} , are both estimated as $h_f = fL/D \cdot v^2/(2g)$. Note that the Darcy friction factor $f_i = f(Re_{D_i}, \epsilon/D_i)$ is evaluated with the well-known Colebrook formula, assuming a roughness coefficient $\epsilon = 0.0015$ mm for both the pipes: $f_1 = f_2 = 0.02$. The minor losses reduce to the sharp exit/entrance of the two tanks ($K = 0.5$), but a further coefficient equal to $K = 0.95$ has been considered, to account for head losses due to any bending of the longer (flexible) pipe.

The required power P_{pump} that the pump must supply is thus calculated as ($\rho = 997$ Kg/m³, $g = 9.81$ m/s²)

$$P_{pump} = \rho g Q h_{pump} / \eta \approx 55 \text{ W (0.07 hp)}, \quad (\text{B.6})$$

where a value of $\eta = 0.75$ has been assumed for the pump efficiency. Based on this performance estimation, a T.I.P. TVX 12000 Dompelpomp has been chosen as the water pump of the experimental apparatus.

B.4 Final assembly

A picture of the final assembly of the experimental apparatus components is shown in Fig. B.7. Note that for practical convenience the water pump has been positioned inside the waste tank (on the bottom in Fig. B.7).



Figure B.7. Picture of the final assembly of the experimental apparatus components.

Bibliography

- [1] G. Tryggvason, R. Scardovelli, and S. Zaleski, *Direct Numerical Simulations of Gas-Liquid Multiphase Flows*. Cambridge University Press, 2011.
- [2] S. J. Weinstein and K. J. Ruschak, “Coating flows,” *Annual Review of Fluid Mechanics*, vol. 36, pp. 29–53, 2004.
- [3] L. D. Soderberg and P. H. Alfredsson, “Experimental and theoretical stability investigations of plane liquid jets,” *European Journal of Mechanics - B/Fluids*, vol. 17, pp. 689–737, 1998.
- [4] M. Lodomez, B. M. Crookston, B. P. Tullis, and S. Erpicum, “Mitigation techniques for nappe oscillations on free-overfall structures,” *Journal of Hydraulic Engineering*, vol. 145, no. 2, p. 04018086, 2019.
- [5] A. H. Lefebvre, *Atomization and Sprays*. Emisphere Publishing, 1989.
- [6] H. B. Squire, “Investigation of the instability of a moving liquid film,” *British Journal of Applied Physics*, vol. 4, no. 6, pp. 167–169, 1953.
- [7] D. L. Chubb, F. D. Calfo, M. W. McConley, M. S. McMaster, and A. A. Afjeh, “Geometry of thin liquid sheet flows,” *AIAA Journal*, vol. 32, pp. 1325–1328, 1994.
- [8] N. S. Barlow, S. J. Weinstein, and B. T. Helenbrook, “On the response of convectively unstable flows to oscillatory forcing with ap-

- plication to liquid sheets,” *Journal of Fluid Mechanics*, vol. 699, pp. 115–152, 2012.
- [9] S. J. Weinstein, D. S. Ross, J. R. Kenneth, and N. S. Barlow, “On oblique liquid curtains,” *Journal of Fluid Mechanics*, vol. 876, pp. 1–9, 2019.
- [10] D. J. Duke, D. Honnery, and J. Soria, “The growth of instabilities in annular liquid sheets,” *Experimental Thermal and Fluid Science*, vol. 68, pp. 89–99, 2015.
- [11] A. Zandian, W. A. Sirignano, and F. Hussain, “Planar liquid jet: early deformation and atomization cascades,” *Physics of Fluids*, vol. 29, no. 6, p. 062109, 2017.
- [12] H. Lhuissier, P. Brunet, and S. Dorbolo, “Blowing a liquid curtain,” *Journal of Fluid Mechanics*, vol. 795, pp. 784–807, 2016.
- [13] M. Girfoglio, F. De Rosa, G. Coppola, and L. de Luca, “Unsteady critical liquid sheet flows,” *Journal of Fluid Mechanics*, vol. 821, pp. 219–247, 2017.
- [14] L. de Luca and M. Costa, “Instability of a spatially developing liquid sheet,” *Journal of Fluid Mechanics*, vol. 331, pp. 127–144, 1997.
- [15] O. Tammisola, A. Sasaki, F. Lundell, M. Matsubara, and L. Soderberg, “Stabilizing effect of surrounding gas flow on a plane liquid sheet,” *Journal of Fluid Mechanics*, vol. 672, pp. 5–32, 2011.
- [16] F. De Rosa, M. Girfoglio, and L. de Luca, “Global dynamics analysis of nappe oscillation,” *Physics of Fluids*, vol. 26, no. 12, p. 122109, 2014.
- [17] N. S. Barlow, B. T. Helenbrook, and S. P. Lin, “Transience to instability in a liquid sheet,” *Journal of Fluid Mechanics*, vol. 666, pp. 358–390, 2011.
- [18] L. de Luca, “Experimental investigation of the global instability of plane sheet flows,” *Journal of Fluid Mechanics*, vol. 399, pp. 355–376, 1999.
-

-
- [19] D. S. Finnicum, S. J. Weinstein, and K. J. Rushak, “The effect of applied pressure on the shape of a two-dimensional liquid curtain falling under the influence of gravity,” *Journal of Fluid Mechanics*, vol. 255, pp. 647–665, 1993.
- [20] S. P. Lin and W. Y. Jiang, “Absolute and convective instability of a radially expanding liquid sheet,” *Physics of Fluids*, vol. 15(6), pp. 1745–1754, 2003.
- [21] L. D. Soderberg, “Absolute and convective instability of a relaxational plane liquid jet,” *Journal of Fluid Mechanics*, vol. 493, pp. 89–119, 2003.
- [22] B. Torsey, S. J. Weinstein, D. Ross, and N. Barlow, “The effect of pressure fluctuations on the shapes of thinning liquid curtains,” *Journal of Fluid Mechanics*, vol. 910, pp. 1–14, 2021.
- [23] D. R. Brown, “A study of the behaviour of a thin sheet of moving liquid,” *Journal of Fluid Mechanics*, vol. 10, pp. 297–305, 1961.
- [24] L. de Luca and C. Meola, “Surfactant effects on the dynamics of a thin liquid sheet,” *Journal of Fluid Mechanics*, vol. 300, pp. 71–85, 1995.
- [25] J. Roche, N. Le Grand, P. Brunet, L. Lebon, and L. Limat, “Perturbations on a liquid curtain near break-up: wakes and free edges,” *Physics of Fluids*, vol. 18, no. 8, p. 082101, 2006.
- [26] A. Kacem, Y. Le Guer, K. El Omari, and P. Bruel, “Experimental investigations of planar water sheets flowing under gravity,” *WIT Transactions on Engineering Sciences*, vol. 115, pp. 97–107, 2017.
- [27] S. J. Weinstein, A. Clarke, A. Moon, and E. Simister, “Time-dependent equations governing the shape of a two-dimensional liquid curtain, part 1: Theory,” *Physics of Fluids*, vol. 9, no. 12, pp. 3625–3636, 1997.
- [28] S. Erpicum, B. Dewals, P. Archambeau, M. Piroton, and B. Blancher, “Discussion of “Modeling and prototype testing of flows
-

- over flip-bucket aerators"; by Penghua Teng and James Yang," *Journal of Hydraulic Engineering*, vol. 146, no. 5, p. 07020005, 2020.
- [29] M. Lodomez, B. Tullis, P. Archambeau, V. Kitsikoudis, M. Pirotton, B. Dewals, and S. Erpicum, "Nappe oscillations on free-overfall structures, data from laboratory experiments," *Scientific Data*, vol. 7, p. 180, 2020.
- [30] N. Le Grand-Piteira, P. Brunet, L. Lebon, and L. Limat, "Propagating wave pattern on a falling liquid curtain," *Physical Review E*, vol. 74, p. 026305, 2006.
- [31] S. P. Lin, "Stability of a viscous liquid curtain," *Journal of Fluid Mechanics*, vol. 104, pp. 111–118, 1981.
- [32] S. P. Lin and G. Roberts, "Waves in a viscous liquid curtain," *Journal of Fluid Mechanics*, vol. 112, pp. 443–458, 1981.
- [33] A. Kornecki, E. H. Dowell, and J. O'Brien, "On the aeroelastic instability of two-dimensional panels in uniform incompressible flow," *Journal of Sound and Vibration*, vol. 47, no. 2, pp. 163–178, 1976.
- [34] F. De Rosa, "Dinamiche instazionarie ed instabilità lineare globale di getti liquidi," in *PhD thesis, Università di Napoli Federico II*, <http://www.fedoa.unina.it/9459>, 2013.
- [35] P. J. Olsson and D. S. Henningson, "Optimal disturbance growth in watertable flow," *Studies in Applied Mathematics*, vol. 94, pp. 183–210, 1995.
- [36] S. P. Lin, Z. W. Lian, and B. J. Creighton, "Absolute and convective instability of a liquid sheet," *Journal of Fluid Mechanics*, vol. 220, pp. 673–689, 1990.
- [37] H. Helmholtz, "On discontinuous movements of fluids," *The London, Edinburgh, and Dublin Philosophical Magazine and Journal of Science*, vol. 36, no. 244, pp. 337–346, 1868.
- [38] W. Thomson, "Hydrokinetic solutions and observations," *The London, Edinburgh, and Dublin Philosophical Magazine and Journal of Science*, vol. 42, pp. 362–377, 1871.
-

-
- [39] L. Raynal, E. Villermaux, J. C. Lasheras, and E. J. Hopfinger, “Primary instability in liquid-gas shear layers,” in *11th Symposium on Turbulent Shear Flows*, vol. 3, pp. 27.1–27.5, 1997.
- [40] F. Ben Rayana, A. Cartellier, and E. Hopfinger, “Assisted atomization of a liquid layer: investigation of the parameters affecting the mean drop size prediction,” in *Proceedings ICLASS 2006, August 27 - September 1, Kyoto Japan. Academic, ISBN4-9902774-1-4.*, 2006.
- [41] J. Eggers and E. Villermaux, “Physics of liquid jets,” *Reports on Progress in Physics*, vol. 71, no. 036601, 2008.
- [42] P. Marmottant and E. Villermaux, “On spray formation,” *Journal of Fluid Mechanics*, vol. 498, pp. 73–111, 2004.
- [43] J. P. Matas, S. Marty, and A. Cartellier, “Experimental and analytical study of the shear instability of a gas-liquid mixing layer,” *Physics of Fluids*, vol. 23, p. 094112, 2011.
- [44] P. Yecko, S. Zaleski, and J. M. Fullana, “Viscous modes in two-phase mixing layers,” *Physics of Fluids*, vol. 14, no. 12, pp. 4115–4122, 2005.
- [45] T. Boeck and S. Zaleski, “Viscous versus inviscid instability of two-phase mixing layers with continuous velocity profile,” *Physics of Fluids*, vol. 17, p. 032106, 2005.
- [46] T. Otto, M. Rossi, and T. Boeck, “Viscous instability of a sheared liquid-gas interface: dependence on fluid properties and basic velocity profile,” *Physics of Fluids*, vol. 25, p. 032103, 2013.
- [47] P. Huerre and P. A. Monkewitz, “Local and global instabilities in spatially developing flows,” *Annual Review of Fluid Mechanics*, vol. 22, no. 1, pp. 473–537, 2005.
- [48] D. Fuster, J. P. Matas, S. Marty, S. Popinet, J. Hoepffner, A. Cartellier, and S. Zaleski, “Instability regimes in the primary breakup region of planar coflowing sheets,” *Journal of Fluid Mechanics*, vol. 736, pp. 150–176, 2013.
-

-
- [49] C. Bozonnet, J. P. Matas, G. Balarac, and O. Desjardins, “Stability of an air-water mixing layer: focus on the confinement effect,” *Journal of Fluid Mechanics*, vol. 933, no. A14, pp. 1–27, 2022.
- [50] J. P. Matas, A. Delon, and A. Cartellier, “Shear instability of an axisymmetric air-water coaxial jet,” *Journal of Fluid Mechanics*, vol. 843, pp. 575–600, 2018.
- [51] O. Tammisola, F. Lundell, and L. Soderberg, “Surface tension-induced global instability of planar jets and wakes,” *Journal of Fluid Mechanics*, vol. 713, pp. 632–658, 2012.
- [52] S. Schmidt, O. Tammisola, L. Lesshafft, and K. Oberleithner, “Global stability and nonlinear dynamics of wake flows with a two-fluid interface,” *Journal of Fluid Mechanics*, vol. 915, p. A96, 2021.
- [53] J. P. Matas, “Inviscid versus viscous instability mechanism of an air-water mixing layer,” *Journal of Fluid Mechanics*, vol. 768, pp. 375–387, 2015.
- [54] M. P. Juniper, “The full impulse response of two-dimensional jet/wake flows and implications for confinement,” *Journal of Fluid Mechanics*, vol. 590, pp. 163–185, 2007.
- [55] M. P. Juniper, “The effect of confinement on the stability of non-swirling round jet/wake flows,” *Journal of Fluid Mechanics*, vol. 605, pp. 227–252, 2008.
- [56] C.-S. Yih, “Instability due to viscosity stratification,” *Journal of Fluid Mechanics*, vol. 27, no. 2, pp. 337–352, 1967.
- [57] G. Agbaglah, R. Chiodi, and O. Desjardins, “Numerical simulation of the initial destabilization of an air-blasted liquid layer,” *Journal of Fluid Mechanics*, vol. 812, pp. 1024–1038, 2017.
- [58] Y. Ling, D. Fuster, G. Tryggvason, and S. Zaleski, “A two-phase mixing layer between parallel gas and liquid streams: multiphase turbulence statistics and influence of interfacial instability,” *Journal of Fluid Mechanics*, vol. 859, pp. 268–307, 2019.
-

-
- [59] Y. Ling, D. Fuster, S. Zaleski, and G. Tryggvason, “Spray formation in a quasiplanar gas-liquid mixing layer at moderate density ratios: a numerical closeup,” *Physical Review Fluids*, vol. 2, no. 1, p. 014005, 2017.
- [60] A. Sanchis and A. Jensen, “Dynamic masking of PIV images using radon transform in free surface flows,” *Experiments in Fluids*, vol. 51, pp. 871–880, 2011.
- [61] A. A. Ayati, J. Kolaas, A. Jensen, and G. W. Johnson, “A PIV investigation of stratified gas-liquid flow in a horizontal pipe,” *International Journal of Multiphase Flow*, vol. 61, pp. 129–143, 2014.
- [62] M. A. Andr e and P. M. Bardet, “Interfacial shear stress measurements using high spatial resolution multiphase PIV,” *Experiments in Fluids*, vol. 56, no. 132, 2015.
- [63] M. P. Buckley and F. Veron, “Airflow measurements at a wavy air-water interface using PIV and LIF,” *Experiments in Fluids*, vol. 58, no. 161, 2017.
- [64] W. Kosiwczuk, A. Cessou, M. Trinit e, and B. Lecordier, “Simultaneous velocity field measurements in two-phase flows for turbulent mixing sprays by means of two-phase PIV,” *Experiments in Fluids*, vol. 39, pp. 895–908, 2005.
- [65] M. Descamps, J. Matas, and A. Cartellier, “Gas-liquid atomisation: gas phase characteristics by PIV measurements and spatial evolution of the spray,” in *2nd colloque INCA, Initiative en Combustion Avanc e, Rouen: France*, 2008.
- [66] H. Li, S. Ji, X. Tan, Z. Li, Y. Xiang, P. Lv, and H. Duan, “Effect of Reynolds number on drag reduction in turbulent boundary layer flow over liquid–gas interface,” *Physics of fluids*, vol. 32, no. 122111, 2020.
- [67] R. Scardovelli and S. Zaleski, “Direct numerical simulation of free-surface and interfacial flow,” *Annual Review of Fluid Mechanics*, vol. 31, no. 1, pp. 567–603, 1999.
-

-
- [68] S. Popinet, “Gerris: a tree-based adaptive solver for the incompressible Euler equations in complex geometries,” *Journal of Computational Physics*, vol. 190, no. 2, pp. 572–600, 2003.
- [69] S. Popinet, “An accurate adaptive solver for surface-tension-driven interfacial flows,” *Journal of Computational Physics*, vol. 228, no. 16, pp. 5838–5866, 2009.
- [70] C. W. Hirt and B. D. Nichols, “Volume of fluid (VOF) method for the dynamics of free boundaries,” *Journal of Computational Physics*, vol. 39, no. 1, pp. 201–225, 1981.
- [71] M. M. Francois, S. J. Cummins, E. D. Dendy, D. B. Kothe, J. M. Sicilian, and M. W. Williams, “A balanced-force algorithm for continuous and sharp interfacial surface tension models within a volume tracking framework,” *Journal of Computational Physics*, vol. 213, no. 1, pp. 141–173, 2006.
- [72] S. J. Cummins, M. M. Francois, and D. B. Kothe, “Estimating curvature from volume fractions,” *Computers & Structures*, vol. 83, no. 6, pp. 425–434, 2005.
- [73] J. A. van Hooft, S. Popinet, C. C. van Heerwaarden, S. J. A. van der Linden, S. R. de Roode, and B. J. H. van de Wiel, “Towards adaptive grids for atmospheric boundary-layer simulations,” *Boundary-Layer Meteorology*, vol. 167, no. 3, pp. 421–443, 2018.
- [74] O. T. Schmidt and T. Colonius, “Guide to spectral proper orthogonal decomposition,” *AIAA Journal*, vol. 58, no. 3, pp. 1023–1033, 2020.
- [75] C. W. Rowley and S. T. M. Dawson, “Model reduction for flow analysis and control,” *Annual Review of Fluid Mechanics*, vol. 49, no. 1, pp. 387–417, 2017.
- [76] K. Taira, S. L. Brunton, S. T. M. Dawson, C. W. Rowley, T. Colonius, B. J. McKeon, O. T. Schmidt, S. Gordeyev, V. Theofilis, and L. S. Ukeiley, “Modal analysis of fluid flows: an overview,” *AIAA Journal*, vol. 55, no. 12, pp. 4013–4041, 2017.
-

-
- [77] A. Towne, O. T. Schmidt, and T. Colonius, “Spectral proper orthogonal decomposition and its relationship to dynamic mode decomposition and resolvent analysis,” *Journal of Fluid Mechanics*, vol. 847, pp. 821–867, 2018.
- [78] G. Berkooz, P. Holmes, and J. L. Lumley, “The proper orthogonal decomposition in the analysis of turbulent flows,” *Annual Review of Fluid Mechanics*, vol. 25, no. 1, pp. 539–575, 1993.
- [79] P. J. Schmid, “Dynamic mode decomposition of numerical and experimental data,” *Journal of Fluid Mechanics*, vol. 656, pp. 5–28, 2010.
- [80] J. Tu, C. Rowley, D. Luchtenburg, S. Brunton, and J. Kutz, “On dynamic mode decomposition: theory and applications,” *Journal of Computational Dynamics*, vol. 1, pp. 391–421, 11 2013.
- [81] P. A. Kadu, Y. Sakai, Y. Ito, K. Iwano, M. Sugino, T. Katagiri, T. Hayase, and K. Nagata, “Application of spectral proper orthogonal decomposition to velocity and passive scalar fields in a swirling coaxial jet,” *Physics of Fluids*, vol. 32, no. 1, p. 015106, 2020.
- [82] B. Zhang, R. Ooka, and H. Kikumoto, “Identification of three-dimensional flow features around a square-section building model via spectral proper orthogonal decomposition,” *Physics of Fluids*, vol. 33, no. 3, 2021.
- [83] M. Chiatto, J. K. Shang, L. de Luca, and F. Grasso, “Insights into low Reynolds flow past finite curved cylinders,” *Physics of Fluids*, vol. 33, no. 3, p. 035150, 2021.
- [84] M. Chiatto, L. de Luca, and F. Grasso, “Modal analysis of actively controlled flow past a backward facing ramp,” *Physical Review Fluids*, vol. 6, p. 064608, 2021.
- [85] P. Welch, “The use of fast Fourier transform for the estimation of power spectra: a method based on time averaging over short, modified periodograms,” *IEEE Transactions on Audio and Electroacoustics*, vol. 15, no. 2, pp. 70–73, 1967.
-

-
- [86] A. Nekkanti and O. T. Schmidt, “Frequency-time analysis, low-rank reconstruction and denoising of turbulent flows using SPOD,” *Journal of Fluid Mechanics*, vol. 926, no. A26, pp. 1–35, 2021.
- [87] V. Theofilis, “Globally unstable basic flows in open cavities,” in *6th Aeroacoustics Conference and Exhibit*, American Institute of Aeronautics and Astronautics, 2000.
- [88] S. Bagheri, E. Akervik, L. Brandt, and D. S. Henningson, “Matrix-free methods for the stability and control of boundary layers,” *AIAA Journal*, vol. 47, no. 5, p. 1057 – 1068, 2009.
- [89] F. Gomez, R. Gomez, and V. Theofilis, “On three-dimensional global linear instability analysis of flows with standard aerodynamics codes,” *Aerospace Science and Technology*, vol. 32, no. 1, p. 223 – 234, 2014.
- [90] R. Ranjan, S. Unnikrishnan, and D. Gaitonde, “A robust approach for stability analysis of complex flows using high-order navier-stokes solvers,” *Journal of Computational Physics*, vol. 403, 2020.
- [91] B. T. Chu, “On the energy transfer to small disturbances in fluid flow (part i),” *Acta Mechanica*, vol. 1, pp. 215–234, 1965.
- [92] B. Herrmann, P. J. Baddoo, R. Semaan, S. L. Brunton, and B. J. McKeon, “Data-driven resolvent analysis,” *Journal of Fluid Mechanics*, vol. 918, p. A10, 2021.
- [93] D. Jiang and Y. Ling, “Destabilization of a planar liquid stream by a co-flowing turbulent gas stream,” *International Journal of Multiphase flows*, vol. 122, pp. 103–121, 2020.
- [94] D. Jiang and Y. Ling, “Impact of inlet gas turbulence on the formation, development and breakup of interfacial waves in a two-phase mixing layer,” *Journal of Fluid Mechanics*, vol. 921, no. A15, 2021.
- [95] R. D. Mehta and P. Bradshaw, “Design rules form small low speed wind tunnels,” *The Aeronautical Journal of the Royal Aeronautical Society*, 1979.
-

-
- [96] R. D. Marshall, “Performance requirements and preliminary design of a boundary layer wind tunnel facility,” *U S. Department of Commerce NBSIR*, vol. 85-3168, 1985.
- [97] J. Groth and A. V. Johansson, “Turbulence reduction by screens,” *Journal of Fluid Mechanics*, vol. 197, pp. 139–155, 1988.
- [98] F. Scarano and M. L. Riethmuller, “Advances in iterative multi-grid PIV image processing,” *Experiments in Fluids*, vol. 29, no. 7, pp. S051–S060, 2000.
- [99] J. Westerweel and F. Scarano, “Universal outlier detection for PIV data,” *Experiments in Fluids*, vol. 39, no. 6, p. 1096–1100, 2005.
- [100] J. Kim, P. Moin, and R. Moser, “Turbulence statistics in fully developed channel flow at low Reynolds number,” *Journal of Fluid Mechanics*, vol. 177, pp. 133–166, 1987.
- [101] A. Colanera, A. Della Pia, and M. Chiatto, “Data-driven global stability of vertical planar liquid jets by DMD on random perturbations,” *Physics of Fluids*, vol. 34, p. 122101, 2022.
- [102] A. Kacem, “Étude expérimentale et numérique d’une nappe liquide en écoulement gravitaire,” in *Thèse de doctorat en Mécanique des fluides, Université de Pau et des Pays de l’Adour*, <http://www.theses.fr/2017PAUU3052>, 2017.
- [103] G. G. Agbaglah, “Breakup of thin liquid sheets through hole-hole and hole-rim merging,” *Journal of Fluid Mechanics*, vol. 911, p. A23, 2021.
- [104] D. L. Chubb and K. A. White, “Liquid sheet radiator,” *AIAA Paper*, pp. 87–1525, 1987.
- [105] D. L. Chubb and F. D. Calfo, “Scaling results for the liquid sheet radiator (lsr),” *NASA TM-102100*, 1989.
- [106] D. L. Chubb, M. W. McConley, M. S. McMaster, and A. A. Afjen, “A study of thin liquid sheet flows,” *NASA TM-106323*, 1993.
-

-
- [107] A. Jaber and M. Tadjfar, “Experimental investigation on flow and breakup of two-dimensional liquid jets,” *WIT Transactions on Engineering Sciences*, vol. 115, pp. 97–107, 2017.
- [108] G. Sunderhauf, H. Raszillier, and F. Durst, “The retraction of the edge of a planar liquid sheet,” *Physics of Fluids*, vol. 14, no. 1, pp. 198–208, 2002.
- [109] N. Savva and J. W. M. Bush, “Viscous sheet retraction,” *Journal of Fluid Mechanics*, vol. 626, pp. 211–240, 2009.
- [110] J.-L. Pierson, J. Magnaudet, E. J. Soares, and S. Popinet, “Revisiting the taylor-culick approximation: Retraction of an axisymmetric filament,” *Physical Review Fluids*, vol. 5, p. 073602, 2020.
- [111] H. Deka and J.-L. Pierson, “Revisiting the taylor-culick approximation. ii. retraction of a viscous sheet,” *Physical Review Fluids*, vol. 5, p. 093603, 2020.
- [112] A. M. Karim, W. J. Suszynski, and S. Pujari, “Liquid film stability and contact line dynamics of emulsion liquid films in curtain coating process,” *Journal of Coatings Technology and Research*, vol. 18, no. 6, pp. 1531–1541, 2021.
- [113] F. E. C. Culick, “Comments on a ruptured soap film,” *Journal of Applied Physics*, vol. 31(6), pp. 1128–1129, 1960.
- [114] M. Chiatto and A. Della Pia, “Natural frequency discontinuity of vertical liquid sheet flows at transcritical threshold,” *Journal of Fluid Mechanics*, vol. 945, p. A32, 2022.
- [115] B. Pier and P. Huerre, “Nonlinear self-sustained structures and fronts in spatially developing wake flows,” *Journal of Fluid Mechanics*, vol. 435, pp. 145–174, 2001.
- [116] F. Giannetti and P. Luchini, “Structural sensitivity of the first instability of the cylinder wake,” *Journal of Fluid Mechanics*, vol. 581, pp. 167–197, 2007.
- [117] C. Hayashi, “Subharmonic oscillations in nonlinear systems,” *Journal of Applied Physics*, vol. 24, no. 5, pp. 521–529, 1953.
-

-
- [118] O. Schmidt, “Bispectral mode decomposition of nonlinear flows,” *Nonlinear Dynamics*, vol. 102, p. 2479–2501, 2020.
- [119] A. Colanera, A. Della Pia, M. Chiatto, L. de Luca, and F. Grasso, “Modal decomposition analysis of unsteady viscous liquid sheet flows,” *Physics of Fluids*, vol. 33, p. 092117, 2021.
- [120] A. Della Pia, A. Colanera, and M. Chiatto, “Surface tension-induced instability in spatially developing subcritical liquid curtains,” *Physics of Fluids*, vol. 34, p. 042122, 2022.
- [121] R. D. Mehta, “Effect of velocity ratio on plane mixing layer influence of the splitter plate wake,” *Experiments in Fluids*, vol. 10, pp. 194–204, 1991.
- [122] D. Dutta, I. Kanshana, S. S. Gopalakrishnan, and A. C. Mandal, “Experimental studies on the frequency selection in flat plate wakes: mean-flow stability analyses and low-dimensional modeling,” *Physical Review Fluids*, vol. 7, p. 044102, 2022.
- [123] R. M. Everson and L. Sirovich, “Karhunen–Loève procedure for gappy data,” *Journal of The Optical Society of America A-optics Image Science and Vision*, vol. 12, pp. 1657–1664, 1995.
- [124] D. Venturi and G. Karniadakis, “Gappy data and reconstruction procedures for flow past a cylinder,” *Journal of Fluid Mechanics*, vol. 519, p. 315–336, 2004.
- [125] H. Gunes, S. Sirisup, and G. Karniadakis, “Gappy data: To Krig or not to Krig?,” *Journal of Computational Physics*, vol. 212, no. 1, pp. 358–382, 2006.
- [126] P. E. Dimotakis, “Two-dimensional shear layer entrainment,” *AIAA Journal*, vol. 24, no. 11, pp. 1791–1796, 1986.
- [127] A. Della Pia, L. Grande, A. Colanera, M. Chiatto, and L. de Luca, “Volume-of-fluid simulation of three-dimensional gravitational liquid sheet flows,” *European Congress on Computational Methods in Applied Sciences and Engineering*, Oslo (Norway), 5-9 June 2022.
-

- [128] A. Colanera, A. Della Pia, M. R. Acquaviva, M. Chiatto, and L. de Luca, "Modal analysis of a three-dimensional gravitational liquid sheet," *European Congress on Computational Methods in Applied Sciences and Engineering*, Oslo (Norway), 5-9 June 2022.
 - [129] B. R. Munson, D. F. Young, T. H. Okiishi, and W. W. Huebsch, *Fundamentals of Fluid Mechanics*. Hoboken, NJ: J. Wiley & Sons, 2006.
 - [130] F. M. White, *Fluid Mechanics*. Boston, Mass: WCB/McGraw-Hill, 1999.
 - [131] B. S. Institution, "Measurement of fluid flow by means of pressure differential devices inserted in circular cross-section conduits running full - part 3: nozzles and venturi nozzles," *BS EN ISO 5167-3*, 2003.
-